Long-term cyclic oxidation behavior of wrought commercial alloys

at high temperatures

by

Bingtao Li

A dissertation submitted to the graduate faculty

in partial fulfillment of the requirements for the degree of

DOCTOR OF PHILOSOPHY

Major: Materials Science and Engineering

Program of Study Committee:
Brian Gleeson, Major Professor
Soma Chaudhuri
Dan Sordelet
Iver Anderson
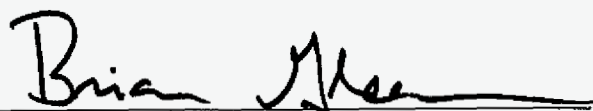David Cann

Iowa State University

Ames, Iowa

2003

Graduate College
Iowa State University

This is to certify that the doctoral dissertation of

Bingtao Li

has met the dissertation requirements of Iowa State University

_____
Major Professor

TABLE OF CONTENTS

viii

LIST OF FIGURES

LIST OF TABLES

ABSTRACT

The oxidation resistance of a high-temperature alloy is dependent upon sustaining the formation of a protective scale, which is strongly related to the alloying composition and the oxidation condition. The protective oxide scale only provides a finite period of oxidation resistance owing to its eventual breakdown, which is especially accelerated under thermal cycling conditions.

This current study focuses on the long-term cyclic oxidation behavior of a number of commercial wrought alloys. The alloys studied were Fe- and Ni-based, containing different levels of minor elements, such as Si, Al, Mn, and Ti. Oxidation testing was conducted at 1000 and 1100 °C in still air under both isothermal and thermal cycling conditions (1-day and 7-days). The specific aspects studied were the oxidation behavior of chromia-forming alloys that are used extensively in industry. The current study analyzed the effects of alloying elements, especially the effect of minor element Si, on cyclic oxidation resistance. The behavior of oxide scale growth, scale spallation, subsurface changes, and chromium interdiffusion in the alloy were analyzed in detail. A novel model was developed in the current study to predict the life-time during cyclic oxidation by simulating oxidation kinetics and chromium interdiffusion in the subsurface of chromia-forming alloys.

From cyclic oxidation kinetics, Fe-base alloys generally showed poorer oxidation resistance than Ni-base alloys. All Fe-base alloys showed a large amount of spallation during cyclic oxidation at 1000 °C. The Ni-base alloys also showed dramatic variability in their oxidation behavior, from negative weight change (large spallation) to stable positive weight gain (small spallation) during cyclic oxidation. The variation in oxidation behavior was mainly attributed to the alloying elements. The alumina-forming alloys, 214 and 602CA, showed excellent oxidation resistance during cyclic oxidation at 1000 and 1100 °C The chromia-forming alloy 45TM also showed excellent oxidation resistance, which is attributed to the beneficial effect of SiO_2 particles within subsurface region formed during cyclic oxidation and to the presence of a minor amount of reactive element (*i.e.*, Ce).

Minor alloying elements were to found to play significant role on cyclic oxidation behavior. Manganese was generally detrimental to oxidation resistance. Most alloys with Mn

addition larger than 0.2 wt.% formed an $MnCr_2O_4$ outer oxide layer, which is less-protective and prone to spall. The effect of Si depended on alloy composition. Increasing the Si content in the SM alloys (<1 wt.%) resulted in improved oxidation resistance. Formation of Si-rich oxide particles at the alloy/scale interface was believed to aid by impeding the diffusion of oxygen and chromium, thus decreasing oxidation kinetics of the 800 alloys. A higher silicon content facilitated the formation of oxide protrusions, such as Cr_2O_3 and TiO_2, at the alloy/scale interface of the Ti-containing alloys, which could result in larger stresses and poorer spallation resistance. Ti could oxidize at the alloy/scale interface, which would induce complex stresses and initiate the formation of cracks along the alloy/scale interface. A relatively high minor alloying element content of Ti or Al also increased the extent of internal oxidation, which could offset the beneficial effect of silicon.

The high-Si (>2 wt.%) Ni-base alloys in the current study showed different oxidation behavior. Silicon oxidized and formed what was inferred to be a continuous SiO_2 layer at the alloy/scale interface or a dispersion of SiO_2 particles in the subsurface region of the alloys. The formation of a disperse distribution of SiO_2 particle in the vicinity of the scale/alloy interface in the 45TM alloy apparently caused a decrease in the growth rate of the Cr_2O_3 scale. The silicon in 160-HR oxidized to form a continuous SiO_2 layer, which partially blocked oxygen diffusion inward and resulted in less internal oxidation attack. The development of a continuous silica layer initiated the formation of cracks within the scale and a general weakening of scale strength during cyclic oxidation.

Addition of Fe and Co to a cast NiCr-based alloy increased the chromia-scale growth rate and resulted in poorer cyclic oxidation resistance, while addition of Si decreased scale growth rate, and thus improved cyclic oxidation resistance. The effect of Si on decreasing scale growth rate was believed to eliminate the detrimental effect of Fe and Co on increasing scale growth rate, and hence improved cyclic oxidation resistance.

The average effective interdiffusion coefficient, $\tilde{D}_{Cr}^{eff}$, was found to be very sensitive to the alloy composition. Higher Si content may increase the value of $\tilde{D}_{Cr}^{eff}$. A larger $\tilde{D}_{Cr}^{eff}$ could supply sufficient chromium to compensate the chromium consumption due to the formation of chromia scale, and thus facilitate the re-formation of chromia scale and improve oxidation

resistance. Addition of Fe and Co to a NiCr-based alloy decreased the $\tilde{D}_{Cr}^{eff}$ and increased the scaling kinetics, thus resulting in poorer oxidation behavior.

The numerical model used in this study gives an advanced method to predict the subsurface depletion profile under cyclic oxidation conditions. The results showed good agreement with measured depletion profiles; although, this agreement depended significantly on the value of $\tilde{D}_{Cr}^{eff}$ used. The life-time prediction for oxidation resistance was obtained by comparing the predicted interfacial chromium content with the critical chromium level for the formation of protective scale, and the result could show good agreement with experiment.

CHAPTER 1 INTRODUCTION

High-temperature corrosion plays an important role in the selection of materials in modern industry. Numerous commercial processes operate at temperatures exceeding about 500 °C, such as electric power generating plants, aerospace, gas turbines, heat-treating, and mineral and metallurgical processing [1]. Oxidation is often the most important high-temperature corrosion reaction in commercial processes. Most metals and alloys readily oxidize in air or a mixed process gas having a relatively low oxygen partial pressure, P_{O_2}. Moreover, most high-temperature alloys are designed to react with the oxidizing environment in such a way that a protective oxide scale forms [2]. The degradation resistance of a high-temperature alloy is dependent upon sustaining the formation of this protective scale.

The properties of the scale determine the extent to which protection can be provided. Ideally, the scale should exhibit a slow growth rate, good adherence to the alloy substrate, a high stability, and be continuous and free of defects such as microcracks or large voids. In general, a chromia, alumina, or silica scale can meet these requirements for high-temperature oxidation resistance, with chromia-forming alloys being the most extensively used in high-temperature industrial applications.

Almost all commercial alloys designed for high-temperature application have the additional constraints of requiring adequate strength, toughness, thermal stability, creep resistance, formability, machinability, weldability, etc. Thus, commercial alloys are typically based on Fe, Co, or Ni and contain judicious additions of Cr, Mo, Al, Mn, Si, Ti, W, and/or reactive elements (RE) for obtaining their comprehensive properties. Minor alloying additions can greatly influence oxidation behavior, especially under thermal cycling conditions. For example, the oxides of Mn, Ti, Al and Si are more stable thermodynamically than that of chromium and, consequently, have a strong tendency to oxidize in the subsurface regions of the alloy and scale, thus possibly adversely affecting scale adhesion. The nature of this internal oxidation process depends critically on the concentration of the minor additions.

At high temperature, initial scale growth is usually very rapid; however, the reaction rate will eventually decrease when scale thickness reaches about 0.5 µm and the transport of reacting species through the scale becomes rate controlling. In accordance with diffusion-

controlled kinetics, the scale usually thickens with time at a parabolic rate under isothermal conditions, *i.e.*,

$$x = \sqrt{k_p t} \qquad (1.1)$$

where x is the scale thickness, k_p is the parabolic rate constant, and t is time.

A continuous scale of α-Al_2O_3 is more stable and generally more protective than a scale of Cr_2O_3. However, aluminum reacts with iron (and nickel) to form brittle intermetallic phases which can weaken the alloy and decrease fabricability and weldability [3]. As a consequence, the aluminum concentration in a commercial wrought alloy is restricted to an allowable level. Further, in some commercial processes involving mixed oxidants (e.g., O and S) the temperatures are too low for the slow-growing Al_2O_3 scale to become kinetically established. In such cases, the alumina-forming alloy may exhibit poor corrosion resistance. Nevertheless, the addition of a few percent aluminum to a chromia-forming alloy is generally found to improve the oxidation resistance [4].

The formation of a continuous chromia scale requires that the alloy contains a critical chromium content, N_{Cr}^*. This critical content is dictated by kinetics and is dependent upon such variables as the alloy's composition, structure and the oxidizing conditions. The growth of a chromia scale requires the selective removal of chromium from the alloy and, consequently, results in the development of a chromium depletion region in the subsurface of the alloy. The nature and extent of subsurface depletion are influenced by the oxidizing conditions, the resistance of the scale to cracking and spalling, and the diffusion properties of the alloy. Clearly, the greater the extent of subsurface depletion, the less likely it will be for the chromia scale to heal or even reform in the event of spallation. The ability to predict the subsurface depletion profile of chromium would be required for any life-time assessment model of chromia-forming alloys.

An important parameter for predicting the depletion profile is the interdiffusion coefficient, which typically depends on composition and, hence, position in the profile. Since data on the composition dependence of interdiffusion coefficients in commercial alloys are virtually non-existent, the utilization of an average "effective" interdiffusion coefficient to

characterize diffusivity in a multi-component alloy system would offer the advantage of simplifying calculations of the subsurface depletion profiles.

Protective oxide scales provide only a finite period of oxidation resistance owing to their eventual breakdown, which is especially accelerated under thermal cycling conditions. The formation of a less protective scale follows breakdown. Breakdown therefore marks the end of the useful service life of an alloy and, for a chromia former, is a consequence of chromium depletion at the scale/alloy interface below the critical concentration [5]. The time for scale breakdown is typically accelerated under thermal cycling conditions because thermal stresses are induced during a thermal cycle on account of the scale having a lower coefficient of thermal expansion (CTE) than the alloy subsurface on which it forms [6]. Thus, it is the combination of thermal stresses and poor scale adherence that cause the scale to fail and eventually breakdown under thermal cycling conditions.

This thesis reports a detailed study on the oxidation behavior of the long-term, cyclic oxidation behavior of a number of commercial chromia-forming alloys which have different chemical compositions and microstructures. The alloys studied were Fe- and Ni-base, and contained different levels of minor elements, such as Si, Al, Mn, Ti. Despite the great amount of literature on isothermal and cyclic oxidation, a definite need exists to comprehensively understand the long-term, cyclic oxidation behavior of commercial alloys and the effects of composition. The specific aims of this study were to:

(a) Characterize the subsurface microstructural and compositional changes in wrought commercial alloys during the oxidation process.

(b) Determine the effects of specific minor additions on cyclic oxidation behavior of a given alloy, particularly the effect of silicon.

(c) Develop a phenomenological model to calculate the effective average interdiffusion coefficient that, in turn, can be used to predict subsurface depletion profiles.

The alloys studied were oxidized in air at 1000 °C and 1100°C for oxidizing cycles of one and seven days. The minor additions were found to have a large effect on subsurface structure and scale phase constitution resulting from cyclic oxidation exposure, which contributed to different oxidation behaviors. The nature of the scale/alloy interface and the

phases present at this interface can affect scale adhesion, diffusion rates, and ultimately cyclic oxidation resistance.

This thesis is not only of fundamental interest, but is also of practical relevance to alloy design. All commercial alloys studied were obtained in wrought form. The results from this study will also contribute significantly to the ultimate goal of predicting subsurface diffusion behavior during cyclic oxidation and relating the prediction to the working life of the component; such predictability would be of significant practical importance.

CHAPTER 2 LITERATURE REVIEW

2.1 Oxidation of Metals

2.1.1 Introduction

Basically, the formation of an oxide is a reaction of a metal and oxygen. An oxide scale may be a single layer or may consist of a series of oxide layers of varying compositions that depend on the temperature and oxidizing conditions. However, oxidation reactions are not random. There are two important factors in discussing the oxidation of metals: thermodynamics and kinetics. Metallic elements react with oxygen to form oxides if it is energetically feasible. Thermodynamics show whether or not a reaction can take place. When the oxidation reaction is possible, kinetics tell how fast the reaction will be. In practical applications, kinetics are of more importance because they determine the extent of metal consumption and, hence, lifetimes. Oxidation theory of pure metals provides the foundation for understanding the more complicated processes associated with the oxidation of alloys.

2.1.2 Thermodynamics of Metal Oxidation

Consider the high-temperature reaction of a metal, M, with an oxidant gas, in this case oxygen. The metal initially absorbs oxygen and then chemical reaction ensues to form an oxide. For the metals of interest to this study, the resulting oxide is solid. Thus, the oxide can nucleate and grow to form a scale on the metal surface. Depending on its growth kinetics, the scale may or may not protect the underlying metal.

The formation of an oxide may be generally described by the reaction

$$\frac{2x}{y}M + O_2 = \frac{2}{y}M_xO_y \tag{2.1}$$

The high temperature oxidation of metals may seem to be among the simplest of reactions, but the reaction path and behavior may involve a large number of phenomena and processes which depend on a variety of factors [7,8].

Under equilibrium conditions, the law of mass action gives

$$K = \frac{a_{M_xO_y}^{2/y}}{a_M^{2x/y} \cdot a_{O_2}} \tag{2.2}$$

where K is the temperature-dependent equilibrium constant and a_i is the thermodynamic activity of species i. In most cases, the solids (metal and oxide) are assumed to be in their standard state, so that their activities are defined as unity. At relatively high temperatures and moderate pressures, the oxidant gas can be treated as being ideal; that is, the activity of oxygen can be approximated by its partial pressure in atmospheres. Thus, equation (2.2) simplifies to

$$K = \frac{1}{P_{O_2}} \tag{2.3}$$

where P_{O_2} is the partial pressure of oxygen.

Thermodynamically, reaction (2.1) for any metal can take place spontaneously from left to right when the Gibbs free energy, ΔG, is negative. For the reaction (2.1), the Gibbs free energy change is:

$$\Delta G = \Delta G_f^o + RT \ln K \tag{2.4}$$

where ΔG_f^o is the standard free energy of formation of the oxide at absolute temperature T and R is the gas constant. If $\Delta G = 0$, the system is at equilibrium, and if $\Delta G > 0$, the reaction is thermodynamically unfavorable. At equilibrium ($\Delta G = 0$),

$$\Delta G_f^o = -RT \ln K = RT \ln P_{O_2} \tag{2.5}$$

Thus, knowing that at equilibrium both the forward and reverse reaction rates are equal, the dissociation pressure of the oxide can be defined as:

$$P_{O_2}^{diss} = \exp\left(\frac{\Delta G_f^o}{RT}\right) \tag{2.6}$$

The metal M can only be oxidized to the oxide M_xO_y if the ambient partial pressure of oxygen is larger than the dissociation pressure.

The Gibbs energy change, ΔG, is the driving force for oxidation reaction. For the usual conditions of constant temperature and pressure, ΔG is described by the auxiliary function as:

$$\Delta G = \Delta H - T\Delta S \tag{2.7}$$

where ΔH is the enthalpy of reaction and ΔS is the entropy change. Equation (2.7) shows that a plot of ΔG versus T approximates as a straight line, which would change in slope when a new phase forms (*i.e.*, at melting or boiling temperature). A Gibbs energy-temperature diagram, usually called an Ellingham diagram (Figure 2.1) [9], summarizes the temperature dependence of ΔG_f^o for various common oxidation reactions at standard state (P_{O_2} =1atm).

The Ellingham diagram in Fig. 2.1 shows the relative thermodynamic stability of the indicated oxides. The lower the line on the diagram, the more negative the standard free energy of formation and the more stable the oxide. For example, the lines for Al_2O_3, SiO_2 and Cr_2O_3 are lower than those for FeO, NiO and CoO in the Ellingham diagram (see Fig. 2.1), so the former oxides are more stable and therefore meet an important criterion for being protective scales. The P_{O_2} can be read directly from Figure 2.1 by using of the P_{O_2} scale along the bottom and right side of the diagram. A straight line drawn from the index point labeled O at the upper left of the diagram, through a specific temperature point on an oxide line, intersects the P_{O_2} scale at the dissociation oxygen partial pressure for that oxide at that temperature ($P_{O_2}^{diss}$). Any oxygen partial pressure above $P_{O_2}^{diss}$ will oxidize the metal; and any below it will reduce the oxide to metal at that temperature. The oxides lower on the diagram are more stable and consequently have lower $P_{O_2}^{diss}$ values. For instance, from Figure 2.1, it is found that the dissociation pressure for NiO is 10^{-10} atm at 1000°C, while that for Cr_2O_3 is 10^{-22} atm, and for SiO_2 and Al_2O_3 are 10^{-26} and 10^{-34} atm, respectively. Thus, the metal elements with lower dissociation pressures for their oxides may form internal oxide precipitates.
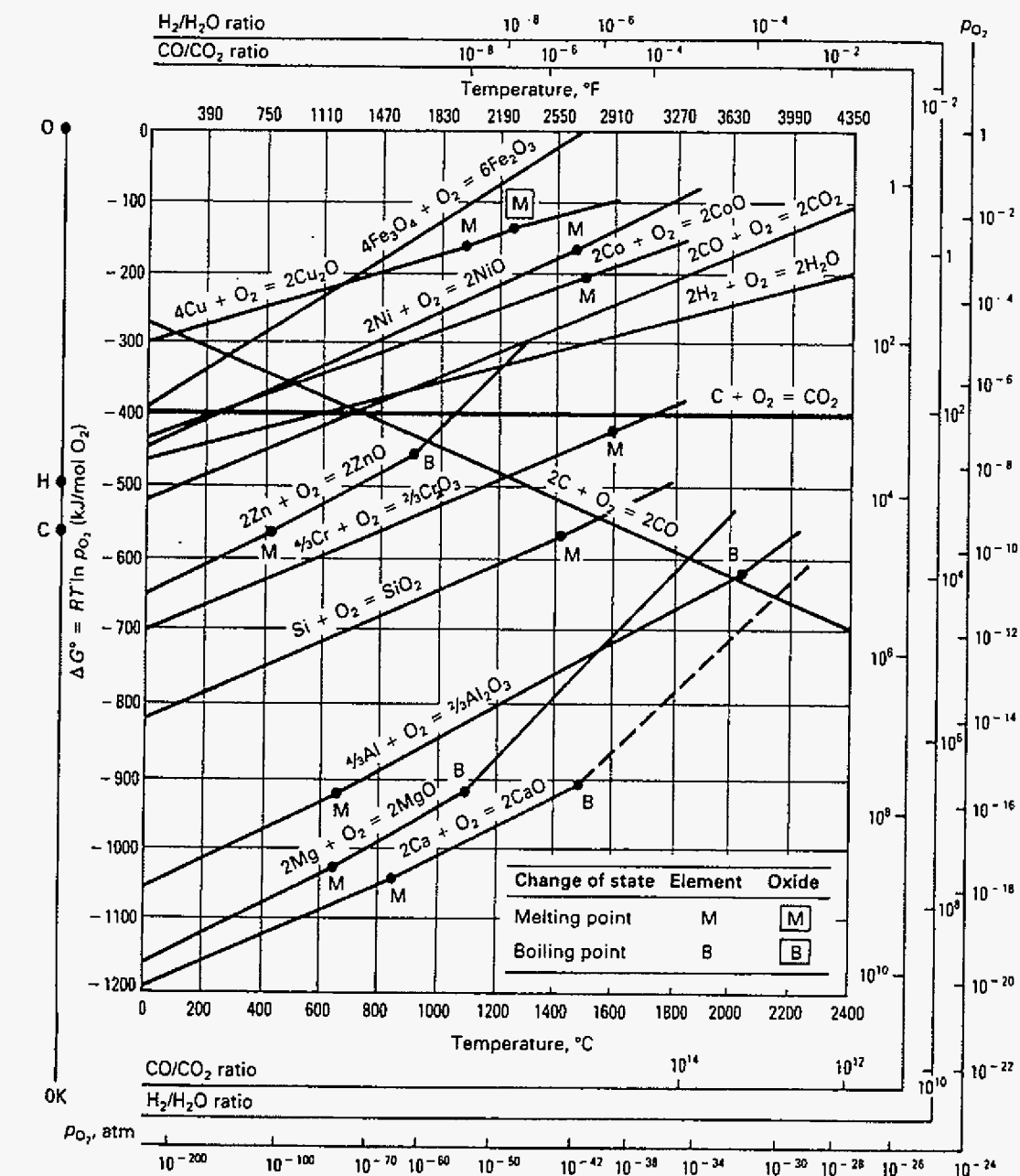
Figure 2.1. Ellingham diagram showing the standard Gibbs energies of formation of selected oxides as a function of temperature.

Low oxygen partial pressures are in practice achieved using oxygen-bearing gas mixtures. The most common gas mixtures are H_2O/H_2 and CO_2/CO. The partial pressures of oxygen are established from the equilibria:

$$H_2O = H_2 + \frac{1}{2}O_2 \tag{2.8}$$

and

$$CO_2 = CO + \frac{1}{2}O_2 \tag{2.9}$$

For controlled laboratory experiment, the equilibrium is often facilitated using a platinized ceramic catalyst in the reaction zone of the furnace. Reaction (2.9) is known to be particularly sluggish in the absence of a catalyst. In addition to the direct oxidation with oxygen, the overall metal oxidation reactions in these gas mixtures are:

$$xM + yH_2O = M_xO_y + yH_2 \tag{2.10}$$

and

$$xM + yCO_2 = M_xO_y + yCO \tag{2.11}$$
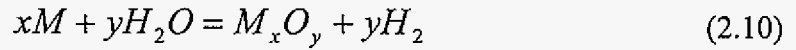
From Figure 2.1, the H_2O/H_2 and CO/CO_2 ratios can be obtained by using the same method as for determining $P_{O_2}^{diss}$, using the index points labeled H and C at the left of the diagram instead of point O.

2.1.3 Kinetics of Metal Oxidation

When a metal is exposed to air, the oxygen typically reacts to form an oxide scale on the surface and the metal consequently gains weight (i.e., grams of oxygen gained). The oxidation rate may be described by the change in the oxide thickness, x (cm), or the sample's weight, ΔW (mg/cm^2). These two parameters are directly related by the equation

$$x = \frac{V_{oxide}}{y \cdot M_o} \times \Delta W \tag{2.12}$$

where V_{oxide} is the molar volume of oxide in cm^3/mol, y is the stoichiometric amount of oxygen in oxide M_xO_y, and M_o is the atomic weight of oxygen.

The formation of oxide scale is related to consumption of metal, and the relationship between weight change (ΔW) and thickness of metal consumed (X), is given by

$$X = \frac{V_m}{\gamma \cdot M_o} \times \Delta W \tag{2.13}$$

where V_m is the molar volume of metal in cm^3/mol and γ is the stoichiometric factor for the oxide scale product (i.e., $\gamma = y/x$ for M_xO_y). For most metals, the oxidation rates follow one or more of three possible kinetic laws: linear, logarithmic, and parabolic. These kinetics laws are discussed in the following section.

2.1.3.1 Kinetic Laws

Formation of an oxide scale will separate the two reactants, metal and gaseous oxygen. In order for the reaction to proceed further, at least one of the reactants must penetrate the scale to form more oxide at the oxide/gas, oxide/metal, or both interfaces. The mechanisms by which the reactants penetrate the scale can therefore be an important part of the overall mechanism and kinetics by which high temperature oxidation occur. Another aspect of the oxidation process, which can sometimes be rate controlling, are the kinetics of the interfacial reaction steps.

(i) Parabolic rate law

When the rate-controlling step in the oxidation process is the diffusion of reactant(s) through the oxide layer with chemical potential gradients being the driving force, the scaling kinetics will follow the parabolic rate law. Parabolic kinetics result from the fact that the scale thickness, x, increases with time, t, and, since this corresponds to the diffusion distance increasing, the oxidation rate decreases. The instantaneous oxidation rate is quite simply inversely proportional to the oxide thickness:

$$\frac{dx}{dt} = \frac{k_p'}{x} \tag{2.14}$$

where k_p' is a proportionality constant. Integration of equation (2.14) gives

$$x^2 = k_p t + C \tag{2.15}$$

where k_p is the parabolic constant ($k_p = 2\,k_p{}'$) with typical units of cm^2/s. Another form of the parabolic rate equation is given by the weight gain (g/cm^2):

$$\Delta W^2 = k_p t + C \tag{2.16}$$

where the units of k_p in this case are g^2/cm^4·s.

The parabolic rate law is the standard for analysis of high-temperature oxidation kinetics, in which diffusion through the relatively thick scale controls reaction rates. Deviations are generally analyzed in terms of chemical and metallurgical effects on the rates of the relevant diffusing process(es). The parabolic rate law may not hold in early stages of oxidation before the scale has developed sufficient continuity and thickness.

Since the parabolic oxidation rate is a diffusion-controlled process and, hence, thermally activated, it increases exponentially with temperature, following the Arrhenius equation:

$$k_p = k_o \exp(\frac{-Q}{RT}) \tag{2.17}$$

where k_o is a constant that is a function of the oxide composition and the gas pressure, and Q is the activation energy for oxide growth. Figure 2.2 shows the temperature dependence of the k_p values for the oxides of Fe, Co, Ni, Cr, Al, and Si. The figure shows a range of k_p values for Al_2O_3 and Cr_2O_3 growth because these oxides do not show intrinsic behavior.

In the case of hafnium and zirconium, the exponent in equation (2.15) is found to be 3 (cubic law) rather than 2 (parabolic law) at high temperatures. This has been attributed to the simultaneous dissolution of oxygen into the substrate metal during oxidation [9].
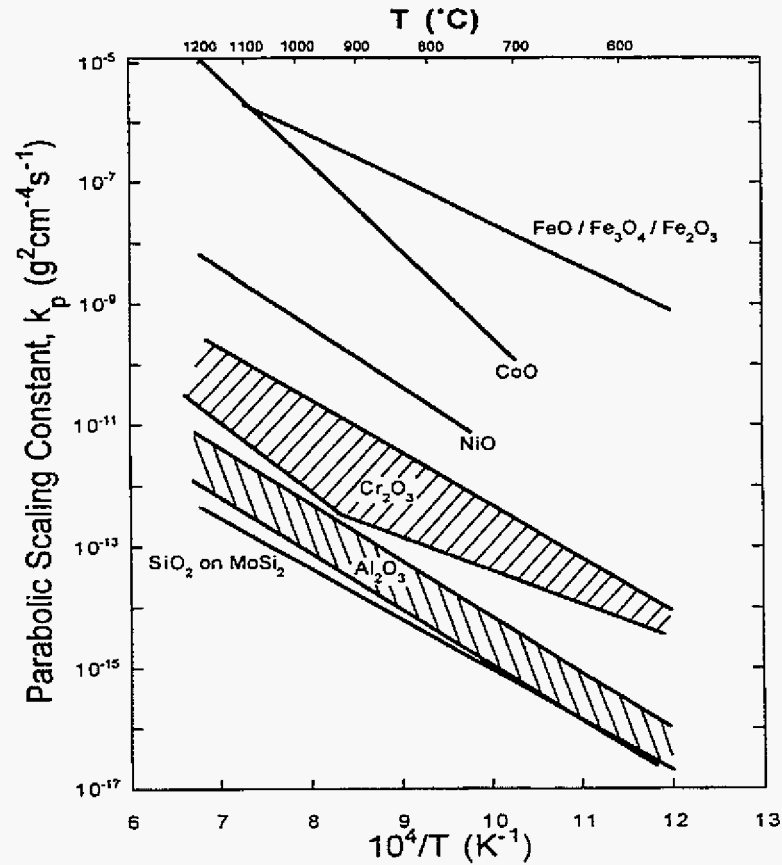
Figure 2.2. Parabolic oxidation rate constant for various oxide scales
as a function of temperature [1].

(ii) Linear rate law

Under certain conditions, the oxidation of a metal proceeds at a constant rate according to
a linear rate law, *i.e.*,

$$x = k_l t \qquad (2.18)$$

where x is the scale thickness and k_l is the linear rate constant. A linear rate law may result
when a phase-boundary reaction controls the kinetics rather than a transport process. An
example is CO_2 dissociation at the scale surface controlling the oxidation kinetics of steel in
a CO_2-rich atmosphere [10].

Linear kinetics are also possible if the oxide is volatile or molten, if the scale spalls or cracks, or if a porous, non-protective oxide forms on the metal [11]. Since the rate of oxidation never slows down, consumption of the metal occurs in a relatively short time in comparison to a metal scaling according to parabolic kinetics.

In the early stages of a metal oxidation process, the scale may be sufficiently thin that linear oxidation kinetics prevail. As the scale thickens, a transition to parabolic kinetics will usually eventuate. Conversely, micro-cracking and porosity may develop as the scale thickens, reducing the protectiveness of the oxide. The parabolic rate law may then fail and the kinetics approach linearity at some time after the start of reaction and scale growth. That is, a constant oxidation rate can develop after a period of parabolic behavior, as shown in Figure 2.3 for the case of magnesium oxidation. The oxidation curve shows that in the region of the point A, i.e., at "breakaway", the rate abruptly alters from a value which is initially very small to one which is both large and constant which no longer decrease with time. When an oxide scale undergoes physical or chemical transformation, the transition from parabolic to linear kinetics may also occur [12].
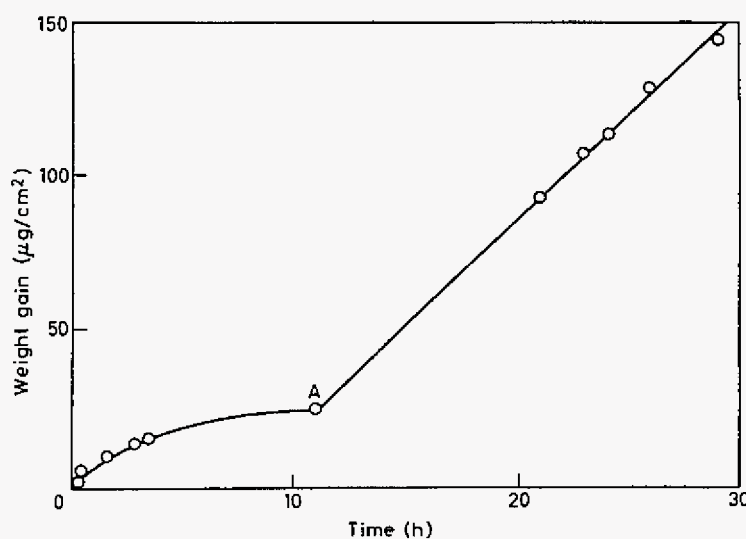
Figure 2.3. Transition of kinetics from parabolic to linear for early stages

of magnesium oxidation at 525 °C [12].

(iii) Logarithmic rate law

At low temperatures (*e.g.*, T < 300-400 °C), oxidation rates are often inversely proportional to time, *i.e.*,

$$\frac{dx}{dt} = \frac{k}{t} \tag{2.19}$$

where k is a constant. Integration of (2.17) leads to the logarithmic rate law

$$x = k_a \log(k_b t + 1) \tag{2.20}$$

where k_a and k_b are constants. Logarithmic oxidation is usually obeyed for relatively thin scales at low temperatures.

2.1.3.2 Transport Properties of Metal Oxides

(i) Defects in Oxides

All metal oxides are to some extent ionic in nature, and it is practicable to consider transport through the oxide scale in terms of ions with the constraint of electroneutrality. Thus, under conditions of diffusion-controlled growth, the oxidation process can be treated as ionic transport through a growing oxide scale. Stoichiometric ionic compounds can have appreciable ionic conductivity due to Schottky defects and/or Frenkel defects (Figure 2.4). Schottky defects are combinations of cation vacancies and anion vacancies in the proper ratio necessary to maintain charge balance. Frenkel defects are a combination of a cation vacancy and an interstitial cation. Metal cations are generally much smaller than the oxygen anions. Limited ionic conductivity is therefore realistically possible in stoichiometric crystals by diffusion of cations interstitially or substitutionally, or by anions substitutionally.
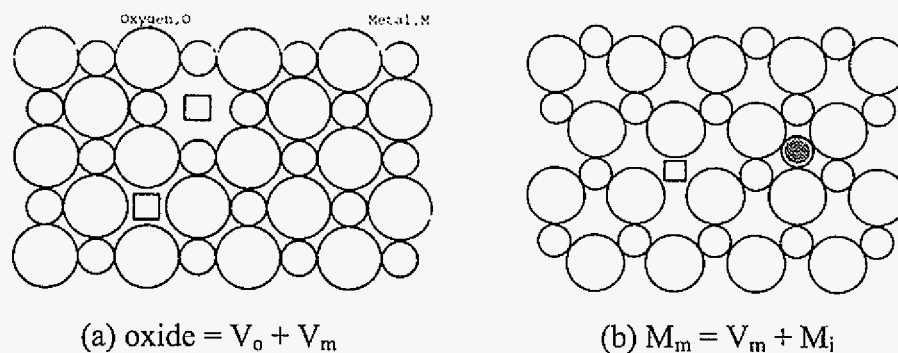
Figure 2.4. Defects in stoichiometric ionic crystals (a) Schottky defect (b) Frenkel defect. In these schematics, $\square$ = vacancy and $\bullet$ = metal interstitial

Metallic oxides are seldom stoichiometric and therefore cannot grow by mere diffusion of Schottky and Frenkel defects. By non-stoichiometry, it is implied that the metal to non-metal atom ratio is not exactly that given by the stoichiometric chemical formula, even though the compound is electrically neutral. Non-stoichiometric ionic compounds can be classified as electrical semiconductors because there is electronic disorder in addition to ionic disorder in order to attain local electrical neutrality.

Electronic semiconductors are classified as n-type (excess of electrons) or p-type (excess of electron holes). The n-type oxides may be either cation excess or anion deficient. Some examples of n-type oxides are TiO_2, Fe_2O_3, $NiFe_2O_4$, ZnO, Al_2O_3, and SiO_2 [13]. For n-type oxides, the defect (i.e., cation interstitial or oxygen vacancy) vacancy concentration is proportional to the negative power of the oxygen partial pressure as [13]:

$$C \propto P_{O_2}^{-1/n} \tag{2.21}$$

where C is the ionic defect concentration, n is a positive integer which depends upon the charge of the ionic defect in the oxide and the oxide stoichiometry.

The p-type oxides may be cation deficient or anion excess. Some common p-type oxides include NiO, CoO, FeO, $FeCr_2O_4$, $CoCr_2O_4$, and $NiAl_2O_4$. The ionic defect (i.e., cation vacancy or oxygen interstitial) concentration is related to the oxygen partial pressure by [13]:

$$C \propto P_{O_2}^{1/n} \tag{2.22}$$

During the oxidation process, ions transport by two ways: the cation migrates outwards to scale/gas interface and the anion migrates inwards to metal/scale interface (Figure 2.5). Two reactions could potentially happen at two interfaces and result in scale growth; however, it is typically found that one reaction predominates.
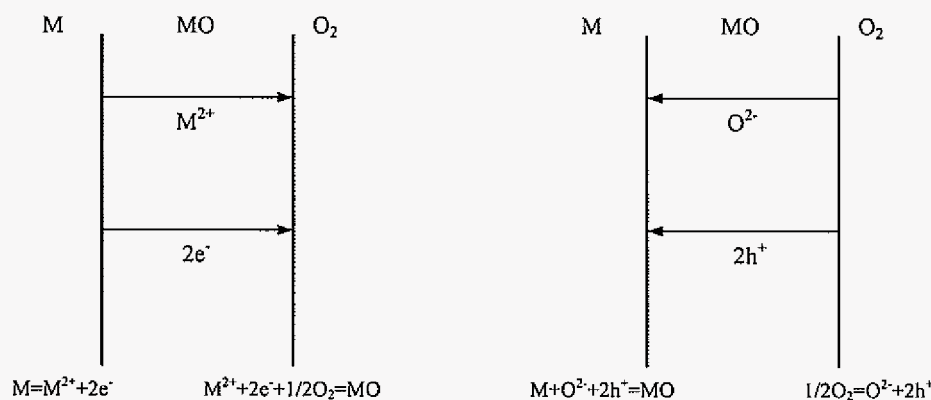
Figure 2.5. Ion transport processes and interfacial reactions
in a non-stoichiometric oxide scale.

(ii) Doping of Oxides

For the defect structures treated so far it has been assumed that the oxides are pure; however, it is thermodynamically impossible to produce perfectly pure compounds or materials. It is therefore necessary to consider the effects of impurities on the defect structure of oxides. It is noted, however, that the presence of impurities can sometimes be neglected if the intrinsic defect concentration in the most oxide is relatively large. For an oxygen-deficient oxide MO_{1-x}, the pure oxide is an n-type conductor, and the following rules are found [14]:

- When a lower valence cation is substitutionally dissolved, the oxygen vacancy concentration increases, and the electron concentration decreases.
- When a higher valence cation is substitutionally dissolved, the electron concentration increases, and the oxygen vacancy concentration decreases.

For a metal-deficient oxide $M_{1-x}O$, the pure oxide is p-type and it is found that:

- The addition of substitutionally dissolved lower valence foreign cations increases the concentration of holes and decreases the concentration of cation vacancies.

- The addition of substitutionally dissolved higher valence foreign cations decreases the concentration of holes and increases the concentration of cation vacancies.

2.1.4 Wagner's Theory of Metal Oxidation

Carl Wagner's theory of metal oxidation [15] provides a fundamental understanding of the essential features of the high-temperature growth of dense scales. The model ideally assumes that the scale is dense, single-phase, continuous, and adheres to the metal over the entire metal surface [15-17]. The basic assumption of the theory is that lattice diffusion of the reacting atoms or ions through the dense scale is rate controlling (i.e., the microstructure of the oxide scale was not considered). Figure 2.6 gives a set-up of the model.

Metal   M   Oxide MO   Gas   O$_2$

cations →

anions →

← electrons

$a'_M = 1$

P''_{O_2}

$P'_{O_2} = \exp(\Delta G^o_{MO}/RT)$

$a''_M = \dfrac{\exp(\frac{\Delta G^o_{MO}}{2RT})}{(P''_{O_2})^{1/2}}$

$M = M^{2+} + 2e^-$ or
$M + O^{2-} = MO + 2e^-$

$M^{2+} + 2e^- + 1/2O_2 = MO$ or
$1/2O_2 + 2e^- = O^{2-}$
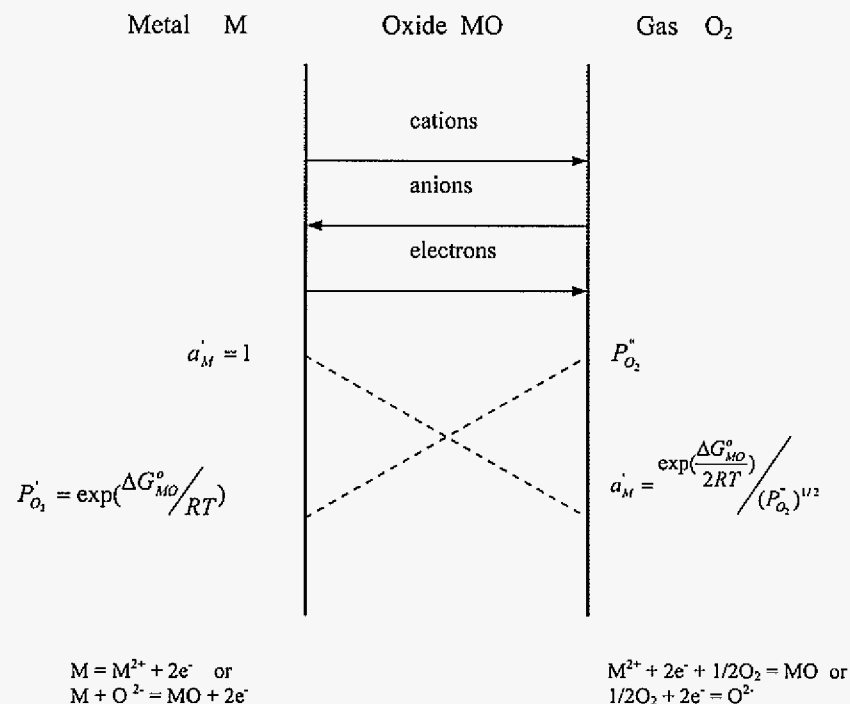
Figure 2.6. Transport processes according to Wagner's theory [15].

The migration of ionized species, as indicated in Figure 2.5, will cause an electric field to be established across the scale, consequently resulting in the transport of electrons across the scale from metal to atmosphere. The fluxes of these diffusing species are determined by the gradients both in the chemical potential and electric field, which together provide the net driving force for ionic migration. The relative migration rates of cations, anions, and electrons must also be balanced such that no net charge build-up occurs within the scale.

Wagner derived an expression for the parabolic rate constant in terms of the electronic and ionic conductivity of the oxide or, alternatively, in terms of the self-diffusion coefficients of the reacting ions in which parameters can be measured relatively easily. Limiting cases of Wagner's derivation are as follows:

$$k' = \frac{1}{RT} \int_{\mu_M''}^{\mu_M'} D_M \, d\mu_M \qquad (2.23)$$

and

$$k' = \frac{1}{RT} \int_{\mu_X''}^{\mu_X'} D_X \, d\mu_X \qquad (2.24)$$

where k' is the parabolic rate constant with unit of $cm^2 s^{-1}$, D_M and D_X are the self-diffusion coefficients for metal, M, and non-metal, X, through the scale, respectively, and μ_M and μ_X are the chemical potentials for metal and non-metal. Equation (2.23) is valid when cation diffusion predominates and Equation (2.24) is valid when anion diffusion predominates.

The good agreement between parabolic rate constants calculated from conductivities or diffusivities and the rate constants measured in oxidation experiments provide strong validation for Wagner's theory [18,19]. Because the diffusion flux within the oxide is proportional to the defect concentration, for a p-type oxide, the oxidation rate can be related as:

$$k' \propto [(P_{O_2}^o)^{1/n} - (P_{O_2}^i)^{1/n}] \qquad (2.25a)$$

where $P_{O_2}^o$ and $P_{O_2}^i$ are the oxygen pressures at the scale/gas interface and metal/scale interface respectively; n is the integer related to the cation vacancy or oxygen interstitial charge. For an n-type oxide, the oxidation rate is:

$$k' \propto [(P_{O_2}^i)^{-1/n} - (P_{O_2}^o)^{-1/n}] \qquad (2.26a)$$

where in this case n is related to the oxygen vacancy or cation interstitial charge. In most cases, the ambient oxygen pressure $P_{O_2}^o$ is much greater than the oxide dissociation pressure $P_{O_2}^i$, so that equations (2.25a) and (2.26a) can be approximated to give

$$k' \propto (P_{O_2}^o)^{1/n} \quad \text{for a p-type scale} \qquad (2.25b)$$

and

$$k' \propto (P_{O_2}^i)^{-1/n} \quad \text{for a n-type scale} \qquad (2.26b)$$

Oxides formed in practice are usually more complex than what was assumed by Wagner. There exist several treatments that extend Wagner's theory [17]. Firstly, a multi-layer scale may form on a number of metals, such as Fe, Cu and Co. For instance, a three-layered $FeO/Fe_3O_4/Fe_2O_3$ scale forms on iron above about 560 °C at atmospheric pressure [20-23]. The overall oxidation behavior is determined by the nature and intrinsic growth kinetics of the oxides in the different layers. Secondly, scales forming on metal surfaces are usually polycrystalline in structure, and in many cases, these structures are fine-grained. Grain-boundary diffusion can greatly alter the overall diffusion characteristics of scales at relatively lower temperatures. Figure 2.7 shows an Arrhenius plot of the parabolic rate constant for the oxidation of high-purity nickel to NiO. The increasing values at low temperatures are due to the more rapid short-circuit diffusion of nickel in polycrystalline scales.

As indicated above, Wagner's theory considered the ideal case of scale formation in which the scale is assumed to be a compact and perfectly adherent barrier, *i.e.*, free of voids, pores, and fissures. The assumption made by Wagner were indeed appropriate; however, deviations from Wagner's theory have been shown [17,24,25]. Oxide scales dynamically grow, and tend to buckle and detach through their growth. Many studies have shown that pores form and develop preferentially along grain boundaries in the scale [26,27]. The presence of voids in scales clearly represents a deviation from ideal scale growth. In some extreme cases, it may be necessary to take into account the void volume fraction in Wagner's

model. Often, however, void formation is considered to be a secondary process that does not significantly affect the overall scaling kinetics.
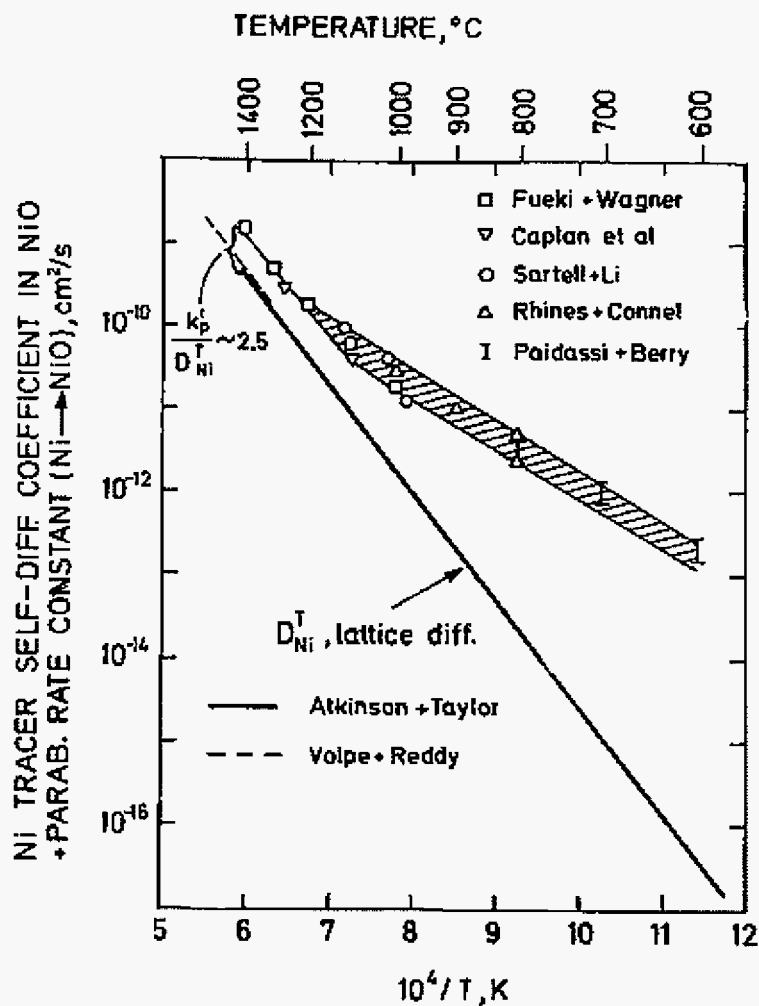
Figure 2.7. Parabolic rate constants varied according to grain boundary and lattice diffusion models [14].

As the scale grows, stresses develop due to differences in the molar volume of metal and oxide(s). The resulting growth stresses are typically compressive. More significant stresses can develop under thermal cycling conditions due to a CTE mismatch between oxide scale and metal, as will be discussed in more detail in section 2.1.6. Increasing stresses may

eventually result in crack formation and even scale detachment [28-30]. Cracking of a protective oxide scale results in the parabolic oxidation being interrupted by a sudden increase in rate when the gas can react directly with the metal surface. As oxide begins to cover the metal surface again, parabolic oxidation is resumed. The overall oxidation of the metal becomes approximately a linear process for the periodic cracking and healing of a protective oxide [11].

2.1.5 Properties of Metal Oxide Scales

As discussed in the previous section, when a dense scale forms, the reaction may only proceed via the solid-state diffusion of the reactant(s) through the scales. The overall reaction will then be governed by the solid-state transport of the reactant ions. However, the protective scale may eventually spall if porosity, microcracks, or stresses develop in the scale. An understanding of the various possible scaling behaviors requires knowledge of high-temperature properties of the metal oxides.

2.1.5.1 Ideal Crystal Structures of Metal Oxides

The crystal structure of most structural metals may be divided into three main types: body-centred cubic, face-centred cubic and hexagonal close-packed. For the simple metal oxides, their crystal structures can be considered to consist of a hexagonal or cubic close-packing of oxygen ions, with the metal ions occupy interstitial sites in the close-packed structures. The interstitial sites in close-packed structures are of two types: (i) sites surrounded by four oxygen ions, the so-called tetrahedral sites, and (ii) sites surrounded by six oxygen ions, the octahedral sites. There are two tetrahedral sites and one octahedral site per close-packed structure. Many studies [31-33] have shown that the cations often occupy the tetrahedral and/or octahedral interstices in regular patterns for the simple metal oxides.

(i)   The Rocksalt (NaCl) Structure

In the rocksalt structure the anions are cubic close-packed and the smaller cations occupy the octahedral interstices (Figure 2.8). The oxides CoO, NiO, FeO, TiO possess this crystal

structure. It may be noted that the NiO, FeO, TiO oxides may be highly nonstoichiometric and as such their NaCl structures are highly defective.
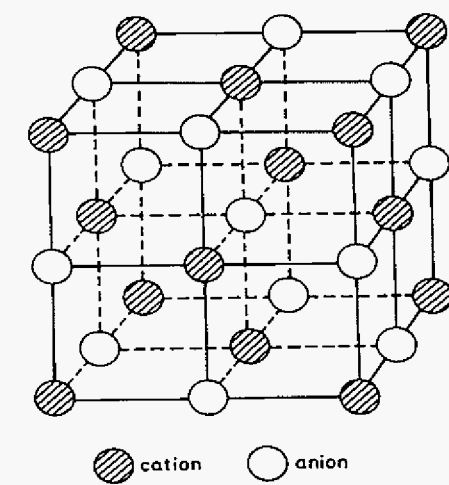
Figure 2.8. The Rocksalt (NaCl) structure.

(ii)   The Rutile (TiO_2) Structure

In the rutile structure, the metal ions are octahedrally coordinated, and the structure can be viewed as consisting of TiO_6 octahedra which share edges and corners in such a way that each oxygen ion belongs to three neighboring octahedra (Figure 2.9). The oxides MnO_2, VO_2, NbO_2, MoO_2, WO_2 also have a rutile structure.
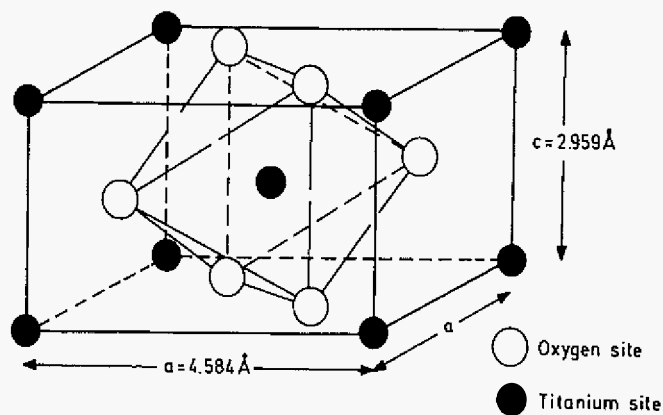
Figure 2.9. The Rutile (TiO_2) Structure.

(iii)   The Corundum (Al_2O_3) Structure

The corundum structure can be regarded as a close-packing of oxygen ions with the trivalent metal atoms occupying 2/3 of the octahedral sites. As the metal atoms occupy the octahedral sites, each metal atom is surrounded by six oxygen atoms, while each oxygen atom is surrounded by four metal atoms. In addition to Al_2O_3, the oxides Fe_2O_3, Cr_2O_3, Ti_2O_3, V_2O_3 have the corundum structure.
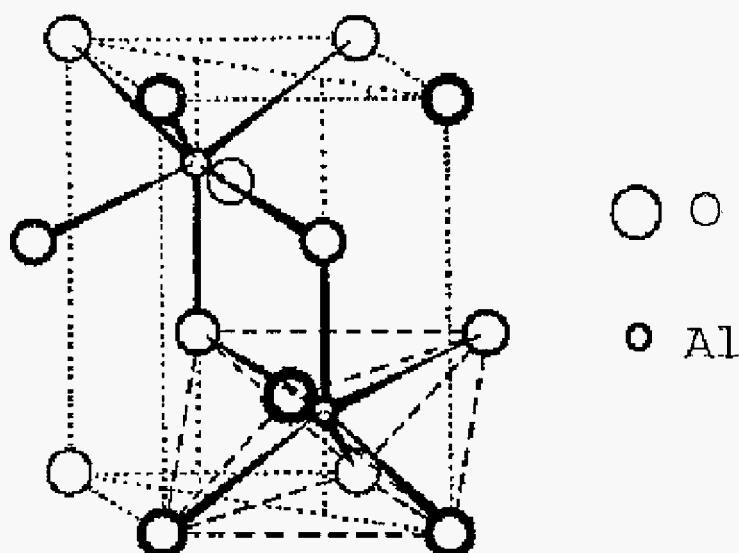
Figure 2.10. The Corundum (Al_2O_3) Structure.

(iv)   The Spinel ($MgAl_2O_4$) Structure

In the spinel structure, the oxygen atoms are cubic closed-packed, and the metal ions occupy both the tetrahedral and octahedral sites. The unit cell consists of 32 oxygen atoms and accordingly the structure contains 32 octahedral and 64 tetrahedral sites. Some relevant spinel oxides are $FeCr_2O_4$, $NiCr_2O_4$, and $MnCr_2O_4$.

Spinels are a class of ionic compounds formed from strongly electropositive metal ions and strongly electronegative non-metal ions [34]. Stoichiometric formulas of spinels can be AB_2O_4, A_2BO_4, or A_3O_4. The first of these represents the normal spinel structure in which divalent cation A is in a tetrahedral site, trivalent cation B is in an octahedral site, and

divalent anion O is in a normal anion site. When the starting oxides are placed in contact along a planar interface, the reaction

$$AO + B_2O_3 = AB_2O_4 \tag{2.27}$$

proceeds, a layer of spinel forms between the starting oxides.

2.1.5.2 Mechanical Properties of Oxide Scales

The protective effect of oxide scales may be impaired if intrinsic or extrinsic stresses lead to cracking or spalling. Therefore, the mechanical properties of the scales play a vital role in protection, in particular under service conditions where the presence of stresses cannot be avoided. The mechanical properties of scales represent parameters for ultimately characterizing scale cohesion and adhesion, but which are also used directly to evaluate deformation and fracture. The mechanical properties of concern are elastic (Young's modulus, shear modulus, Poisson ratio), and plastic and creep (ductile-brittle transition temperature, stress-strain relationship).

A great number of publications [35-39] exists on the mechanical behavior of oxide scales. For compressive failure, there are two models. One model (Figure 2.11 (a)) assumes that the oxide-metal interface is intrinsically strong and has not been weakened by void formation or segregation of trace elements. Initial failure occurs by shear cracking, followed by the nucleation and propagation of a crack along the oxide-metal interface. The critical strain, $\varepsilon_{c,s}$, for spallation is calculated from this model to be [40]

$$\varepsilon_{c,s} = \left[\frac{2\gamma_o}{xE_{ox}(1-v)} \right]^{1/2} \tag{2.28}$$

with γ_o being the fracture energy of the oxide-metal interface, x the scale thickness, E_{ox} the Young's modulus of the oxide, and v the Poisson ratio. The other model (Figure 2.11 (b)) assumes spallation is the result of preceding decohesion at the scale-metal interface and buckling of the oxide layer leading to through-thickness cracks or unstable growth of the interfacial decohesion zone. The calculated failure strain, ε_c', from this decohesion model is associated with the beginning of crack deflection from the interface on the perimeter of the buckled configuration through the scale toward the surface [41]:

$$\varepsilon_{c,d}' = 3.6 E_{ox} \left(\frac{x}{R}\right)^2 \qquad (2.29)$$

where R is the initial radius of the zone of decohesion.
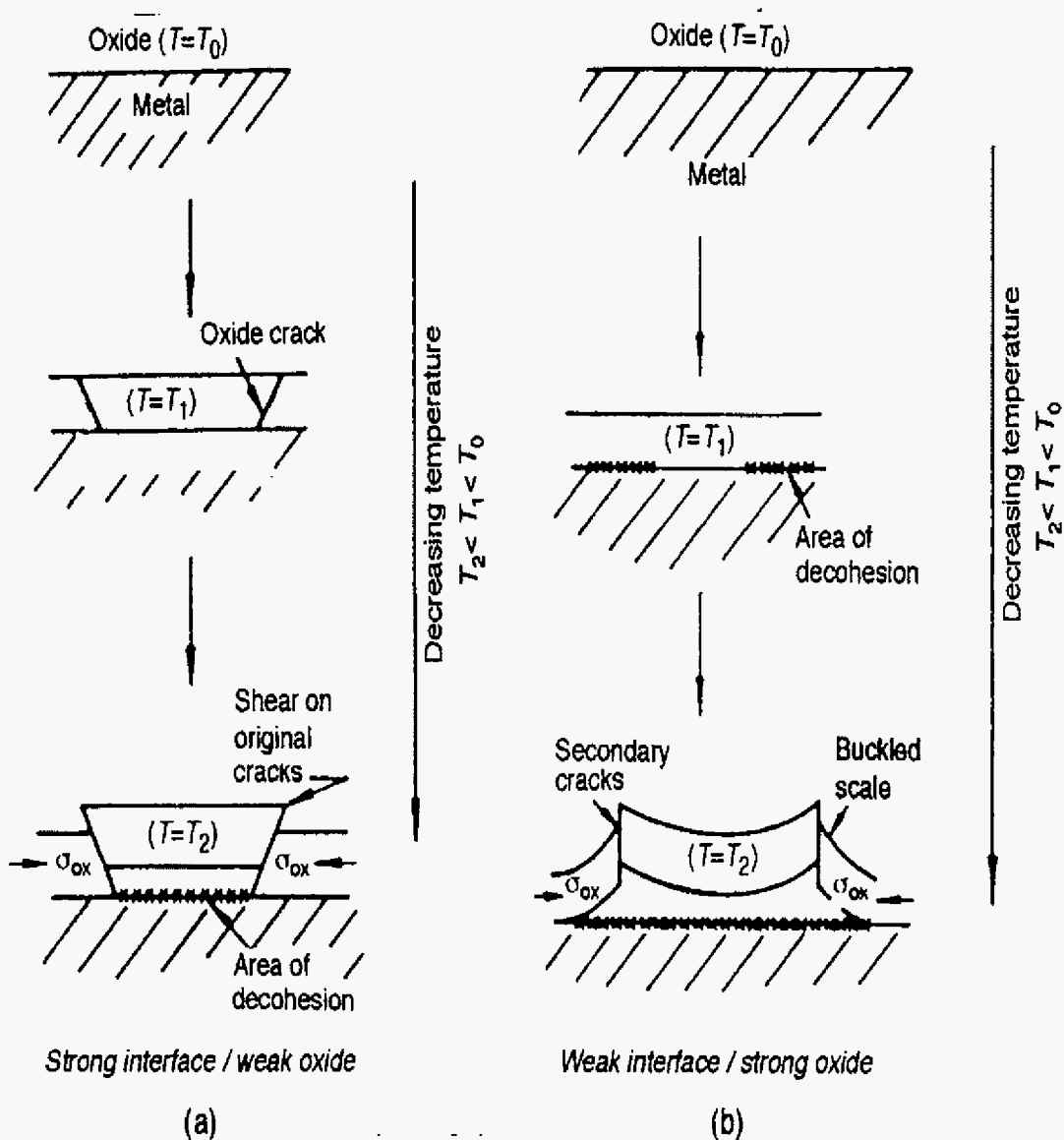
Figure 2.11. Schematic representation of the steps in the oxide spallation process [40].

Tensile failure of a scale layer is easier to deal with than compressive failure, and the relatively simple fracture mechanics of the former gives [42,43]:

$$\varepsilon_c^T = \frac{K_{Ic}}{fE_{ox}\sqrt{\pi c}} \tag{2.30}$$

where ε_c^T is the critical strain for through-scale cracking, K_{Ic} is the fracture toughness of the oxide, f is a constant, and c is half the length of an embedded defect or the whole length of a surface defect. K_{Ic} can be calculated from the fracture energy of the oxide according to

$$K_{Ic} = \sqrt{2\gamma_o E_{ox}} \tag{2.31}$$

Table 2.1 lists some data on room-temperature mechanical properties for various oxides [43]. The high-temperature data ($\sim$ 700 or 800 °C) are close to the room-temperature values in Table 2.1 [44].

Table 2.1. Surface fracture energies and elastic moduli and calculated fracture toughness values of some oxides [43].

Oxide	γ_o (J/m^2)	E_{ox} (GPa)	K_{Ic} (m$^{1/2}$MPa)
FeO	3.0	130	0.9
CoO	3.0	156	1.0
NiO	3.6	191	1.2
MnO	2.7	148	0.9
Fe$_3$O$_4$	4.5	208	1.4
FeCr$_2$O$_4$	5.0	233	1.5
Fe$_2$MnO$_4$	3.0	108	0.8
Al$_2$O$_3$	7.7	419	2.5
Cr$_2$O$_3$	5.8	283	1.8
Fe$_2$O$_3$	6.0	219	1.6
Y$_2$O$_3$	4.8	123	1.1
SiO$_2$	4.4	85.6	0.9

2.1.6 Stresses in Oxide Scales

Stresses in oxide scales may play a key role in the oxidation resistance of materials. As analyses of practical damage cases show, the failure of components is often initiated by stresses either resulting from the oxidation process itself or from operation of the component. There are generally three types of stresses which have to be considered: growth stress, thermally induced stress, and external stresses from operation [45].

2.1.6.1 Stresses from Oxide Growth

The earliest model to explain growth stresses in oxide scales is that by Pilling and Bedworth [46]. This model describes the volume change involved in the transition from the metal lattice to the oxide when only oxygen anions are diffusing. The ratio of the volume per metal ion in the oxide to the volume per metal atom in the metal is termed the Pilling-Bedworth ratio (PBR). The PBR for some important oxides and metal substrates are given in Table 2.2.

Oxide scales which grow inwards should be compressively stressed if the PBR were greater than unity, while tensile stresses would develop if the PBR were less than unity. It is seen that for most oxide/metal systems, PBR values are greater than unity. Thus, most oxides may be expected to grow with developing compressive stresses. However, if oxide scales grow by outward diffusion of metal ions, the oxide scale must in contrast remain free of growth stresses, as the oxide grows freely on the scale surface. This is clearly not the case, as there are geometric constraints. Such a free growth is rarely possible.

It is noted that there is no obvious relationship between PBR values and the magnitude of the stresses in the scale. According to Stringer [48], the volume expansion accompanying oxidation can be accommodated by the higher mobility of metal ions at the interface, so that growth stresses are minimized.

Table 2.2. Typical PBR values for some important oxides and metal substrates [14,47,48].

Oxide/Metal	PBR
Al_2O_3/Al	1.28
NiO/Ni	1.65
$FeO/\alpha\text{-Fe}$	1.68
CoO/Co	1.86
Cr_2O_3/Cr	2.07
$Cr_2O_3/Fe\text{-}25Cr\text{-}20Ni$	2.1
$Fe_3O_4/\alpha\text{-Fe}$	2.1
$Fe_2O_3/\alpha\text{-Fe}$	2.14
$Fe(FeCr)_2O_4/Fe\text{-}Cr$	2.1
$FeCr_2O_4/Fe\text{-}18Cr\text{-}8Ni$	2.1
Fe_3O_4/FeO	1.2
Fe_2O_3/Fe_3O_4	1.02
TiO_2/Ti	1.73
SiO_2/Si	2.15

The PBR is simply based on the volumetric constraint of a molar volume change. However, growth stress is much more complex and requires a detailed consideration of oxide growth mechanism. An oxide may grow laterally as well as thickening with time during an oxidation process. Constrained by the underlying alloy, the lateral strain would produce a compressive stress in the scale. Rhines and Wolf [49] introduced a conceptual model (Rhines-Wolf model) for the origin of growth strain and stress. They pointed out that no lateral stress/strain would develop in following three cases:

- The oxide grows by inward diffusion of oxygen at the oxide/alloy interface (B in Fig. 2.12),
- The oxide grows by outward diffusion of the metal ions at the top of the oxide scale (C in Fig. 2.12),
- New oxide forms at grain boundaries lying parallel to the oxide/alloy interface.

In all these three instances, the volume change accompanying the oxidation reaction can be accommodated by a rigid body displacement of the oxide parallel to the oxide/alloy interface. When new oxide forms along grain boundaries lying perpendicular to the oxide/alloy interface (A in Fig. 2.12), a lateral stress/strain would be generated and the process would require concurrent inward diffusion of oxygen and outward diffusion of metal ions. If fully constrained by the underlying alloy, the stress in the oxide generated by this growth strain would simply be:

$$\sigma = \frac{E}{(1-v)}\varepsilon = \frac{E}{(1-v)}\frac{b}{d} \tag{2.32}$$

where E, v, b, and d are the elastic modulus, the Poisson's ratio, Burgers vector, and lateral size of grain, respectively. Any concurrent stress relaxation processes will reduce this value, but the estimate vividly shows how very large stresses can be created by insertion of relatively few molecules per grain boundary.
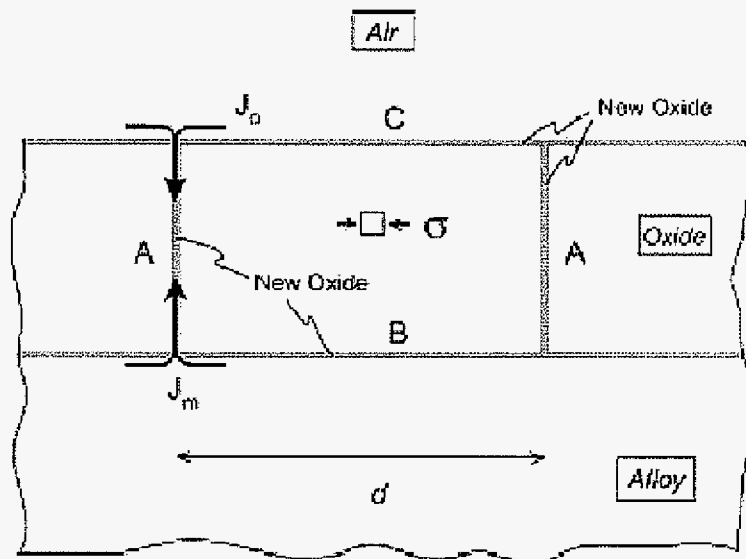
Figure 2.12. Possible location of new oxide formed as a result of the inward flux oxygen, J_o, and the outward flux of metal ions, J_m [49].

2.1.6.2 Stresses from Temperature Change

The difference in the coefficient of thermal expansion (CTE) between the substrate metal and the oxide scale results in the stresses in the scale on cooling from the oxidation temperature. The mismatch in CTE is particularly important under thermal cycling oxidation conditions. Further, the phase transformation that may occur in both the oxide and in the substrate during a temperature change can lead to the development of stresses in the scales. Table 2.3 lists CTE values of some important oxides. The CTE values of some substrate materials are shown in Table 2.4.

Table 2.3. Typical CTE values for some important oxides [43,47,50,51].

Oxide	CTE ($10^6 K^{-1}$)	Temperature range(°C)
Al_2O_3	8.1	400-800
NiO	17.1	20-1000
FeO	12.2	100-1000
Fe_2O_3	12.2	100-1000
CoO	15.0	20-900
Cr_2O_3	7.3	100-1000
SiO_2	7.4-30.0	0-730[a]
TiO_2	7.2-10.6	25-277[a]
Y_2O_3	8.9	400-800

[a]Measured on single crystal. CTE values depend on orientation and temperature.

It is worth noting that CTE of a given material will change with temperature usually in a non-linear manner. However, accurate temperature dependences are difficult to obtain.

Table 2.4. CTE values for some substrate materials [47,50].

Material	CTE $(10^6 K^{-1})$	Temperature range(°C)
Fe	15.3	0-900
Ni	17.6	0-1000
Co	14.0	25-350
Cr	9.5	0-1000
12Cr1Mo steel	10.8-13.3	20-600
Alloy 800	16.2-19.2	20-1000
Alloy 617	13.6	20-300
Alloy X	13.7-20.0	20-1000

The stress which arises from the different CTE values of the oxide (α_{ox}) and metal (α_m) can be calculated for an adherent oxide scale for a temperature change ΔT as follows [47]:

$$\sigma_{ox} = \frac{-E_{ox}\Delta T(\alpha_m - \alpha_{ox})}{(1-v)(1+\frac{E_{ox}}{E_m}\frac{d_{ox}}{d_m})} \qquad (2.33)$$

where E, v, and d are the elastic module, the Poisson's ratio, and thickness respectively. The subscription m and ox respect metal and oxide. Equation (2.33) is obtained by assuming metal and oxide have close Poisson's ratio. It is shown that temperature change affects linearly the stress in the oxide scale.

2.1.6.3 External Stresses

For the external stresses, the stress level in the scale can be calculated from the operating conditions. Depending on the strain distribution in the component and its geometry, the stresses in the scale can most often be derived from the strain that is imposed at the surface of the component [47].

2.1.7 Oxidation of Common Metals in Commercial Alloys

(1) Oxidation of Iron

The principal solid oxide phases that form below 570 °C are Fe_3O_4 (magnetite) and Fe_2O_3 (hematite), which form as an inner layer and an outer layer of the oxide scale, respectively. At temperatures above eutectoid temperature of 570 °C, an additional inner scale forms adjacent to the metal, consisting of the fast-growing FeO (Wüstite).

As shown by the Ellingham in Figure 2.1, the oxide phase stable at the lowest P_{O_2} is found closest to the metal surface (FeO at T > 570 °C), whereas the phase stable at highest P_{O_2} (Fe_2O_3) is found closest to the oxidizing environment. Upon cooling below 570 °C, the FeO in thermodynamically unstable with respect to a mixture of Fe and Fe_3O_4.

For iron oxidizing at a temperatures between 350 and 500 °C, Fe_3O_4 nucleates first and grows laterally over the surface [52]. Once complete coverage is achieved, the Fe_2O_3 thickens parabolically. Ultimately nucleation and lateral overgrowth by Fe_2O_3 occur, slowing the growth rate of the Fe_3O_4 appreciably, due to the lower effective P_{O_2} at the Fe_3O_4 surface. Specially The P_{O_2} falls from that of the environment to that governed by the equilibrium between Fe_3O_4 and Fe_2O_3 at the prevailing temperature. Both FeO and Fe_3O_4 are purported to nucleate first and grow out of the surface of pure Fe at 700 to 800 °C in low oxygen pressure (10^{-3} Pa) [53-54].

(2) Oxidation of Nickel

Perhaps the simplest case of oxidation is presented by nickel, which forms only one oxide (NiO) under ordinary conditions [55]. Nickel, in comparison with metals such as iron, cobalt and copper, has a relatively good resistance to oxidation at high temperature. Further, the CTE values of NiO and Ni are similar (17.1 and 17.6 x 10^{-6} K^{-1}, respectively), so that the effects of thermal cycling can be largely neglected [56].

(3) Oxidation of Chromium

The oxidation of pure chromium is a simple process because a single solid oxide Cr_2O_3 forms. Cr_2O_3 is a continuous and highly protective scale. The two most important complicating features are scales thinning by CrO_3 evaporation and scale buckling as a result of compressive stress development. However, Cr_2O_3 is normally protective in air or oxygen up to approximately 1000 °C, volatile CrO_3 may form at higher temperatures [53,57].

(4) Oxidation of Aluminum

Aluminum is a very reactive metal with a high affinity for oxygen. Aluminum oxide scale (Al_2O_3) which forms on the metal surface is relatively inert and protective in character, so that aluminum is highly resistant to most atmospheres and to a great variety of chemical agents. Due to its very high stability, the establishment of an Al_2O_3 scale can suppress the oxidation of most other elements in the alloy.

(5) Oxidation of Silicon

The formation of SiO_2 on silicon or silicon-containing alloys results in very slow oxidation rates. However, this system is also one which can be influenced markedly by oxide vapor species. Whereas the oxidation of chromium is influenced by vapor-species formation at high oxygen pressures, the effect for silicon is important at low oxygen pressures. At oxygen pressures near the dissociation pressure of SiO_2, a significant pressure of SiO develops in equilibrium with SiO_2 (s) and Si (s) [9]. This can result in a rapid flux of SiO_2 away from the metal surface and the subsequent formation of SiO_2 "smoke". The formation of the SiO_2 as a smoke rather than as a continuous layer causes continued rapid oxidation reaction.

(6) Oxidation of Titanium

Titanium is intrinsically very reactive, so that whenever the metal surface is exposed to air, or to any environment containing available oxygen, a thin tenacious surface scale of oxide is formed, which gives excellent corrosion resistance at temperature below about 500 °C. On fabricated titanium surfaces at normal or slightly elevated temperatures, the oxide

formed is rutile, which is a tetragonal form of titanium oxide (TiO_2). A strong bond between metal and oxide results from the favorable spacing between titanium ions in the rutile lattice and the titanium atoms in the metal structure. This explanation, however, does not account for the fact that other oxides of titanium, such as broolite (orthorhombic structure) and anatase (tetragonal structure) are also protective [56]. Above about 600 °C, penetration of oxygen and nitrogen occurs. The presence of these elements renders the titanium brittle. This feature must be taken into account when considering the use titanium at elevated temperatures.

(7) Oxidation of Cobalt

Cobalt forms two oxides: CoO and Co_3O_4. Below about 900 °C, only CoO is produced under standard conditions of temperature and pressure. A higher temperature oxide layer is also formed, which shows the oxide CoO close the base metal and the oxide Co_3O_4 outside close to environment [58].

(8) Oxidation of Molybdenum

The volatilization of oxide is particularly important in the oxidation of Mo at high temperature and high oxygen pressure. The effects of oxide volatility on the oxidation of Mo have been observed at temperatures as low as 475 °C and the rate of oxide evaporation above 725 °C was such that gas-phase diffusion became the rate-controlling process [59,60]. Molybdenum begins to noticeably oxidize in air at 300 °C and oxidation becomes rapid at 500 °C, and the rate of attack is very rapid by 1200 °C [61]. Below 500 °C, oxidation proceeds according to the parabolic rate law, showing some degree of protection. The oxidation proceeds by a two-step process with molybdenum dioxide (MoO_2) as the inner oxide layer and molybdenum trioxide (MoO_3) as the outer layer. Above 500 °C, MoO_3 begins to volatilize and at 600 °C the rate of evaporation of MoO_3 becomes significant. At about 700 °C, the rate of vaporization of MoO_3 equals its rate of formation, and so temperature increases, the volatilization rate becomes extremely rapid.

2.2 Oxidation of Alloys

2.2.1 Introduction

The oxidation theory of metals offers a basic understanding of alloy oxidation. However, alloy oxidation is generally much more complex as a result of some, or all, of the following [9]:

(a) The various metal components in an alloy will have different affinities for oxygen.

(b) More oxides may be formed.

(c) A degree of solid solubility may exist between the oxides.

(d) The various metal ions will have different mobilities in the oxide phases.

(e) The various metals will have different diffusivities in the alloy.

(f) Dissolution of oxygen into the alloy may result in sub-surface precipitation of oxides of one or more of the alloying elements (*i.e.*, internal oxidation).

When it is considered that scales can crack, contain voids, spall, sinter and even give multiple layers of irregular thickness, the situation becomes even more complex. For example, practical operation of components is generally under cyclic conditions, which result in thermal stresses which, in turn, greatly affect the integrity of the oxide scale and its adhesion to the alloy.

2.2.2 Thermodynamics of Alloy Oxidation

2.2.2.1 Chemical activity

As in the case of a pure metal (section 2.1.2), alloy oxidation thermodynamically requires a decrease in free energy. However, the chemical activities of the alloy components are not unity.

For dilute solution, the average solvent atom exists essentially in the same chemical surrounding environment as in the pure state, with only a small number of solute atoms

neighboring the solvent atoms. Thus, the solvent atoms act as if they were in ideal solutions and Raoult's law applies to the solvent [62]:

$$\lim_{N_A \to 1} a_A = N_A \qquad (2.34)$$

where a_A and N_A are the activity and mole fraction of solvent A. Also, according to Henry's law, the activity of solute B is given as:

$$\lim_{N_B \to 0} a_B = \gamma_B N_B \qquad (2.35)$$

where γ_B is the activity coefficient of solute B for the solute/solvent system. For a binary system A-B, it is not necessary to find the activities of both components. Rather, as long as the activity of one of the components is known, the activity of the other can be found using the Gibbs-Duhem equation [62] for the activity coefficients:

$$N_A d \ln \gamma_A + N_B d \ln \gamma_B = 0 \qquad (2.36)$$

The integrated form of equation (2.36) is given by:

$$\ln \gamma_A = -\int_{\ln \gamma_B \; at \; x_A = 0}^{\ln \gamma_B \; at \; x_A = x_A} d \ln \gamma_B \qquad (2.37)$$

2.2.2.2 Selective Oxidation

For a binary alloy A-B (where B is the less noble metal), the scale growth will depend on the alloy composition. On the sole basis of thermodynamic stability, the binary alloy will show transition from AO to BO formation (Figure 2.13) at some critical activity ratio determined from the reaction

$$AO + \underline{B} = BO + \underline{A} \qquad (2.38)$$

for which

$$\left(\frac{a_A}{a_B} \right)_{Crit.} = K = \exp(\frac{-\Delta G}{RT}) \qquad (2.39)$$

In reaction (2.38), $\underline{A}$ and $\underline{B}$ correspond to A and B in the alloy. The reaction will proceed to the right if $\left(\dfrac{a_A}{a_B}\right)_{Crit.} < K.$
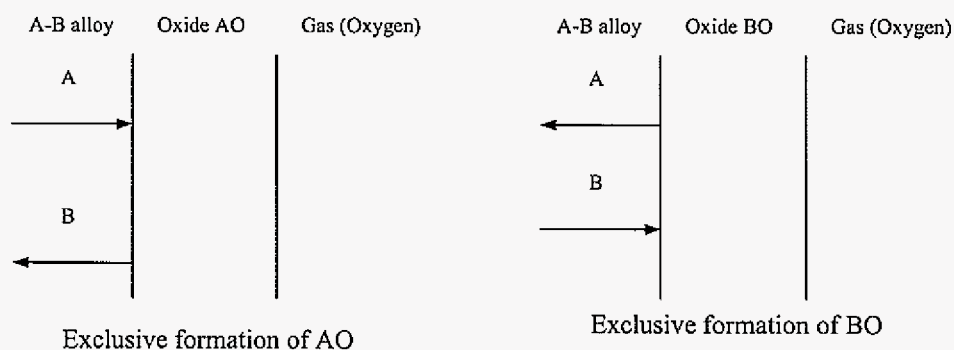
Figure 2.13. Selective oxidation of an binary A-B alloy.

For a sufficiently high concentration N_B in the alloy, only BO will be formed if BO has extremely low permeability to A, and A will diffuse into the alloy from the alloy/scale interface. The oxidation reaction will be

$$B \text{ (at the scale/interface)} + \tfrac{1}{2} O_2 = BO \qquad (2.40)$$
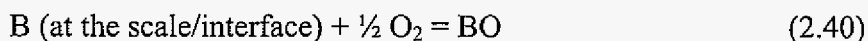
Assuming that the BO scale is compact and pore free, Wagner [63] showed that the critical concentration of B, N_B^c, necessary to sustain BO formation, is given by

$$N_B^c = \frac{V_A}{\upsilon M_o} \left(\frac{\pi k_p}{2D}\right)^{1/2} \qquad (2.41)$$

where V_A is the molar volume of the alloy, υ is the ratio of oxygen ions to metal cations in the oxide BO_υ, M_o is the atomic weight of oxygen, k_p is the parabolic rate constant for BO growth, and D is the alloy interdiffusion coefficient.

For the formation of exclusive oxide scale BO, the concentration of B in the alloy is required to be larger than the critical concentration, N_B^c. When BO is exclusively formed as an external scale, the alloy is depleted in B, as shown in Figure 2.14. Equation (2.41) was

arrived at by assuming that the concentration of B in the alloy at the alloy/scale interface, N_B^i, is zero.
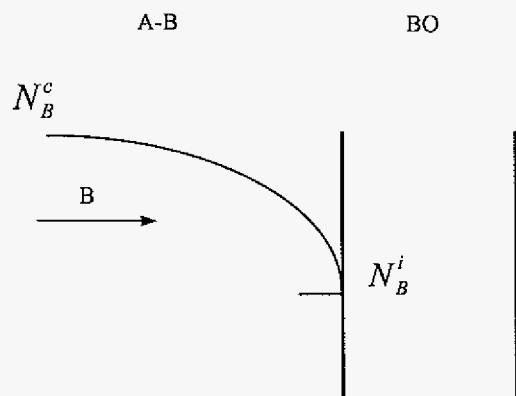
Figure 2.14. Depletion of B in a binary A-B alloy.

With the depletion of B, the concentration of B at the scale/interface could eventually become lower than that necessary to maintain equilibrium with BO. As a consequence, reaction (2.40) cannot be maintained and less-protective oxide AO will form (*i.e.*, the reverse of reaction 2.38), which will result in protective-scale breakdown on the alloy [64].

At an intermediate concentration of B in the alloy, both AO and BO may form as an external scale product. Various alternative situations may arise depending upon the properties of AO and BO: the two oxides may be completely miscible and form an oxide solid solution - (A,B)O, e.g., Ni-Co alloys; they may be partly or completely immiscible, e.g., Cu-Ni alloy; or they may react to form another oxide - ABO_2, e.g. Ni-Cr alloy. In addition, internal oxidation may take place.

2.2.3 Growth of Oxide Scales

When a binary alloy A-B is exposed to oxygen, the establishment of a protective scale is a time-dependent process. The very initial stages of a gas/alloy reaction are collectively referred to as the transient stage. The transient stage is typically followed by steady-state

scaling behavior. Virtually all thermodynamically stable products are formed during the transient stage [65]. However, as the reaction progresses a gradient in the oxidant activity develops, such that the least stable products dissociate or are displaced, leaving only the most stable product(s) closest to the alloy. The steady-state scales for heat-resisting alloys are generally alumina or chromia.

2.2.3.1 Initial Stages of Oxidation

When the clean surface of a binary alloy A-B is exposed to oxygen gas, the surface atoms of both alloy components react with oxygen. As a result, a thin oxide film consisting of small crystallites of both oxides (AO and BO) is initially formed on the surface. Initial oxidation stages can be divided into three main stages [14]:

  (i)   adsorption of oxygen gas on the surface,
  (ii) formation of individual oxide nuclei which grow laterally to form a continuous oxide film, and
  (iii) further growth of the oxide film normal to the surface.

During oxygen adsorption, the oxygen molecules dissociate and are adsorbed as atoms. These atoms initially adsorb at sites where the atom is in contact with the maximum number of surface atoms in the alloy substrate. Therefore, in polycrystalline materials, grains of preferential orientation exist where the number of adsorbed oxygen atoms is highest [66].

When the oxygen-saturated alloy is further exposed to oxygen, the oxygen may dissolve in the alloy and nuclei of the oxidation product are formed on the surface. These nuclei grow laterally and form a continuous surface film, as indicated in the Figure 2.15. Generally, nucleation and the growth of the nuclei are dependent on the composition of the substrate, grain orientation, temperature, and gas partial pressure.
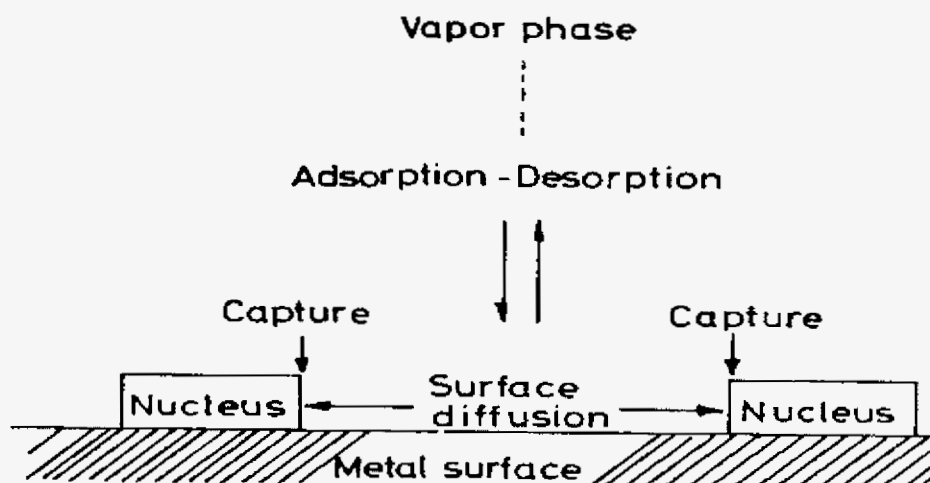
Figure 2.15. Lateral growth of the nuclei leading to
the formation of an oxide film[14].

The two oxides will grow at different rates, and as such the fast-growing oxide (AO), which generally is thermodynamically less-stable, will tend in the early stages of oxidation to overgrow the slower-growing oxide (BO). The establishment of the fast-growing oxide scale decreases the oxygen activity at the scale/alloy interface; however, if the B content is sufficient, the thermodynamically more-stable oxide (BO) can eventually develop into a continuous layer at the scale/alloy interface. As a consequence, the continued growth of the less-stable transient products above the established more-stable oxide layer is essentially terminated if rates of diffusion and/or solubilities are low in the latter. The initial stages of oxidation are shown schematically in Figure 2.16 for a nickel-copper alloy. Cu_2O is a faster growing oxide and less stable compared to NiO. Due to the different stabilities of the two oxides, the NiO nuclei are stable at the low oxygen partial pressure beneath the outer, fast-growing Cu_2O layer, and thus can develop a continuous NiO layer by lateral growth if nickel content is high enough (in the left side of Figure 2.16). The slower growing NiO partial layer can, from this stage on, act as a barrier for copper diffusion and thus slow down the oxidation rate of the Cu_2O layer. The right side of Figure 2.16 represents the case where the amount of nickel in the alloy is insufficient to form a continuous NiO layer, and thus further Cu_2O growth is not suppressed to any measureable extent.
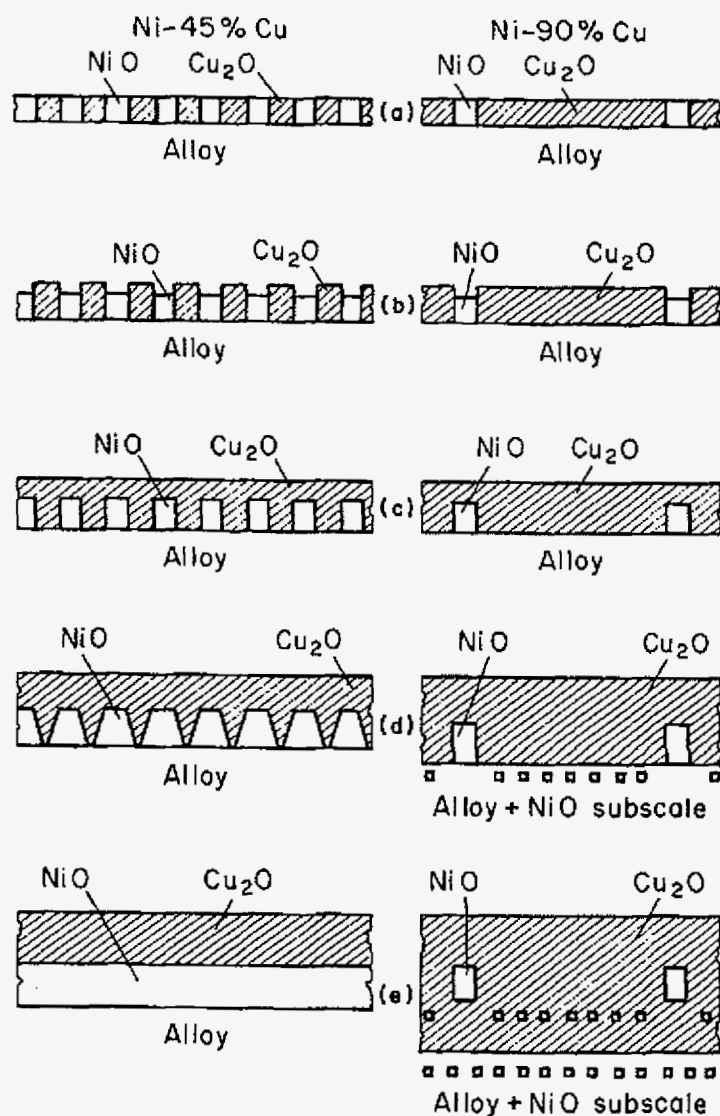
Figure 2.16. Schematic representation of approach for initial stages
of oxide growth in Ni-Cu alloys [67].

If oxide layers further grow, the less-stable products eventually detach and spall due to
poor adhesion. The duration of the transient stage can vary significantly from alloy to alloy;
for some alloys, it may be on the order of seconds, while for others it may be on the order of

days. In general, the duration decreases with increasing content of the protective-scale-forming element [1].

2.2.3.2 Later Stages of Oxidation

After the initial stage of oxidation, which is determined by the nucleation and growth behaviors, growth of the continuous scale occurs in the thickness direction. For dense oxide scales, this growth is typically determined by solid-state diffusion. The growth of external scales may be limited by the diffusion through the scale or by the interdiffusion of the alloy components in the alloy phase. Oxidation of Ni-Pt alloys, for which NiO is the only stable oxide, provides a simplified case to illustrate these aspects. This is summarized in Figure 2.17.
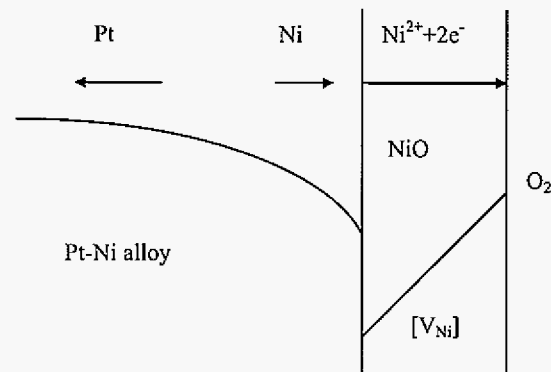
Figure 2.17. Schematic representation of diffusion processes
during oxidation of a Ni-Pt alloy [68].

In the external scale, there is an oxygen partial pressure gradient which is determined by the two boundaries conditions of the oxide scale and by the scale thickness. At outside of the oxide scale, the oxygen pressure remains constant if the environment us stable and constant, and the oxygen pressure at the alloy/scale interface also remains constant by the metal-oxide equilibrium (e.g. Equation 2.40). This oxygen gradient results in a defect concentration gradient across the scale which enables the diffusion across the external scale.

The formation of an external scale on an alloy results in a subsurface depletion profile of element B (Ni in Fig. 2.17). It is important that B diffuses to the alloy/scale interface from the alloy matrix to sustain the external scale growth. There are two limiting cases in the selective formation of the external scale [14]:

(i) If the interdiffusion in the alloy is fast compared with the rate at which B is consumed by the scale growth, zone of B depletion in the alloy at the alloy/scale interface would be very marginal. The scale formation is then determined by the rate of diffusion through the scale.

(ii) If the rate of B diffusion in the alloy is much slower than the diffusion through the scale, a significant subsurface zone of B would result and the oxidation would be determined by the rate of arrival of B at the alloy/scale interface.

These different situations can result in differences in the stability of the alloy/scale interfaces as shown in Figure 2.18. If interdiffusion in the alloy is faster than the scale growth rate (case (i)), the scale growth would be most rapid in the thin-scale region because the chemical potential through the scale is steepest in this region. This tends to cause the alloy/scale interface to become planar (a in Fig. 2.18). For case (ii), the rate of diffusion of the less-noble B in the alloy determines the reaction rate. In this case, B is being selectively oxidized. Thus the concentration gradient of B in the alloy would be steepest in front of any oxide protrusions into the alloy matrix, and consequently the oxide protrusion grows at an accelerated rate. This situation favors a non-planar alloy/scale interface. Thus, instability of the interface is favored by slow intermetallic diffusion and rapid scale formation.
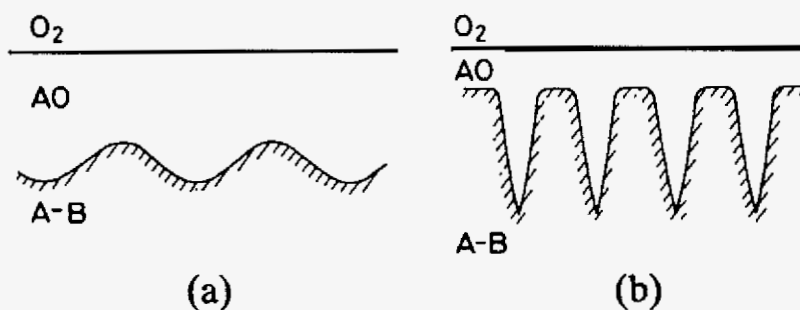
Figure 2.18. Stability/instability of an alloy/scale interface [62,69].

Protective scale growth will eventually end due to mechanical or thermal stresses, as discussed in section 1.6, or due to excessive volatile oxide formation at high temperatures, such as gaseous CrO_3 formation at temperature above about 1000 °C. Thus protective oxide scales only improve the oxidation resistance, but they cannot inhibit oxidation, especially under long-term and thermal-cycling conditions. In the meantime, alloy oxidation often undergoes subsurface degradation in the form of internal oxidation and void formation which may worsen the properties of the alloy's oxidation resistance. These effects will be discussed in later sections.

2.2.4 Subsurface Degradation

For pure metals and alloys rich in the protective-scale-forming element, weight gain in Equation 2.16 is directly related to the amount of metal consumed, which, in turn, reflects oxidation resistance. However, the situation is more complex for alloys which undergo subsurface degradation in the form of internal oxidation and subsurface void formation. John [70] studied the oxidation behavior of a variety of high-temperature alloys over the temperature range 760-1093 °C for times up to one year, and found that more than 80% of the metal attack incurred by most alloys was a result of internal oxidation and subsurface void formation. Harper et al. [71] and Gleeson and Harper [72] reported the long-term, cyclic oxidation behavior of various wrought alloys over the temperature range 982-1204 °C. It was found that, depending on temperature and alloy composition, internal attack accounted for 14-98% of the average metal affected by the oxidation process. Moreover, the amount of internal attack was higher than 85% for almost all alloys oxidized at 982 °C. Thus, it is very important to consider subsurface degradation in evaluating oxidation resistance.

2.2.4.1 Internal Oxidation

Internal oxidation is used here in a generic sense to represent a process in which a diffusing oxidant from the surface reacts with a less-noble solute component in the alloy to form discrete particles [73]. Internal oxidation is not desired because it changes the optimized mechanical properties of an alloy and may result in internal stress and grain-boundary

weakening, thus decreasing the high-temperature properties. For example, internal Al_2O_3 formation at grain boundaries in Al-containing high-temperature alloys promotes crack initiation if tensile stresses are present in the subsurface [74]. Such types of crack initiation can soon lead to failure of the component by crack growth by creep or fatigue.

Rapp [75] gave the following prerequisites for internal oxidation of a binary alloy A-B in which A is the base metal:

(1) The alloy must be able to dissolve the oxidant X.

(2) The free energies of formation must be lower for the oxidation product BX than for the oxidation product AX, which means that B must have a higher affinity to X than A.

(3) Oxidant X must diffuse faster into the alloy than metal B from the inside of the alloy to the surface.

(4) B must not exceed a minimum critical concentration, beyond which a continuous external scale of BX forms.

(5) No initial surface layer is present that would prevent the dissolution of X into the alloy.

For a binary alloy A-B, the dissolved oxygen atoms react with less-noble B atoms in the alloy,

$$B(diss) + vO(diss) = BO_v \qquad (2.42)$$
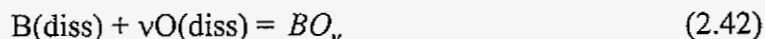
Thus, the necessary condition for formation of BO_v in the alloy may be formulated in terms of the equilibrium solubility product K_{sp} for formation of BO_v in a dilute alloy:

$$[a_B][a_O]^v = K_{sp} \qquad (2.43)$$

where v is the stoichimetric factor for the internal oxide BO_v. An a_i represents the chemical activity of reacting component i. For an ideal solution, $a_B = N_B$ (mole fractions of B in the alloy) and $a_O = N_O$ (mole fraction of oxygen in the alloy). Laflamme and Morral [76] formulated a criterion showing that internal oxidation occurs for values falling between zero and unity:

$$0 < {K_{sp}}\Big/{N_B N_O^v} < 1 \tag{2.44}$$

Thus, when the product $N_B N_O^v$ is greater than the equilibrium solubility product for BO_v, internal oxidation should occur.

The greater the stability of BO_v, the lower will be its K_{sp} value [1]. It is for this reason that the internal precipitates commonly observed in oxidized high-temperature alloys are of the stable oxides Al_2O_3, SiO_2, TiO_2, and Cr_2O_3 [72,77,78]. Multiple internal oxidation zones can also develop if more than one reaction product is stable [79,80]. The sequence of the thermodynamically possible phases progresses from metal-rich in the innermost zone of the alloy to oxidant-rich at the surface.

The internal oxidation zone extends to the depth at which the activity of dissolved oxygen becomes too small for formation of the oxide BO_v. The kinetics of internal oxidation are generally found to be diffusion-controlled. The depth of the internal oxidation zone, ξ, in an alloy undergoing no external scale formation can be described by the following kinetic expression, assuming no enrichment of B in the internal oxidation zone [9,74,81]:

$$\xi = \left(\frac{2N_O^s D_O t}{v N_B^O} \right)^{1/2} \tag{2.45}$$

where N_O^s is the solubility of the oxidant in the alloy, D_O is the diffusivity of the oxidant in the alloy, N_B^O is the initial solute concentration, and t is time. The product $N_O^s D_O$ is called the oxygen permeability in alloy. The solubility of oxygen in the alloy depends upon the partial pressure P_{O_2} of oxygen at the alloy surface according Sievert's law [82]:

$$N_O^s \propto P_{O_2}^{1/2} \tag{2.46}$$

The above discussion considers only internal precipitation in the absence of external scale formation. In the case of external AO_v scale formation, the value of N_O^s is no longer fixed by the environment but is instead fixed by the equilibrium between at the alloy/scale interface (assuming no through-scale access by the oxidant), *i.e.*,

$$\underline{A} + \frac{v}{2} O_2 = AO_v \tag{2.47}$$

The effective thickness of the internal precipitation zone decreases in a most pronounced manner from that predicted in the absence of an external scale at large values of k_p and N_B^O [83]. A large k_p value corresponds to a large amount of metal recession, which means the total attack is still high, even though the internal precipitation zone is relatively low.

The preceding theoretical considerations are based on models assuming predominant lattice diffusion of both oxygen and the alloying element. As such, the theoretical treatments are only expected to apply to relatively high temperatures or to very large-grained materials (with the extreme being single crystals). As the temperature is reduced, grain boundary effects will become increasingly important. This is due to relatively rapid diffusion along grain boundaries, enhanced concentration or segregation of oxidant and the alloying element at grain boundaries, and a preferred tendency for nucleation at grain boundaries [14,72,78].

2.2.4.2 Transition from Internal Oxidation to External Scale Formation

The transition from internal to external oxide formation typically occurs with a relatively small increase in the alloy content of the less-noble component B in the A-B alloy, at which oxidation leads to the formation of a surface scale of BO_v and the alloy is no longer oxidized internally. Considering the alloy system A-B, there are two situations to be considered: One is when only one of the components can oxidize and the other is when both of the component can oxidize.

For the first case, if the oxygen partial pressure is low (i.e., below the stability of AO_v), the component B in the alloy surface nucleates as BO_v in a A-rich matrix. If B can diffuse fast enough to reach the surface and keep supplying B for BO_v formation, a complete surface layer of BO_v is produced. If this condition is not met, however, then BO_v will precipitate as internal particles within the alloy. So, the internal or external formation of BO_v depends on the balance between the outward flux of B and the inward flux of atomic oxygen into the alloy.

Wagner [81] proposed that the condition for the transition from internal to external BO_ν formation occurs when a critical volume fraction of BO_ν, f*, is attained. Under this condition the influx of oxygen is so restricted that sideways growth of the BO_ν precipitates is kinetically favorable and BO_ν eventually forms as a continuous layer on the alloy surface. Under conditions of no or a negligibly small rate of metal recession, the following criterion for the transition from internal to external BO_ν formation is obtained:

$$N_{B^*}^O \geq \left[f^* \left(\frac{V_m}{V_{ox}} \right) \pi \frac{N_O^S D_O}{2\nu D_B} \right]^{1/2} \tag{2.48}$$

where $N_{B^*}^O$ is the critical mole fraction of B in the alloy, V_m is molar volume of the alloy, V_{ox} is molar volume of the oxide, and D_B is the diffusion coefficient of solute B in the alloy. Rapp [74] reported excellent agreement between experimental and predicted values of N_{In}^O as a function of oxygen partial pressure in Ag-In alloys oxidized at 550 °C. The value of f* is usually taken to be 0.3 according to the results from this study by Rapp.

It is important to distinguish equation (2.41) and (2.48). Equation (2.41) has been used by some in the past for a bare alloy to form an exclusive BO_ν scale layer. However, this is not a completely correct use of this criterion, since its derivation was based on supply rather than establishment. The criterion in equation (2.41) gives only the minimum possible B content in the alloy necessary to supply B at a sufficient rate to the alloy/scale interface for the sustained growth of an established BO_ν scale layer. The actual B content necessary for both the establishment and sustained growth of a BO_ν scale will very likely be higher than the value obtained from equation (2.41) owing to transient and kinetic effects [1]. Equation (2.48) gives the critical B content for the transition from internal to external oxidation. This value reflects the local criterion to form an exclusive scale. For example, if the B content at the scale/alloy interface is lower than the critical value, it is not kinetically possible to form an exclusive scale, and internal oxidation may occur instead.

2.2.4.3 Subsurface Void Formation

Many commercial alloys develop voids and porosity in the subsurface region after more extended oxidation. There are at least three possible mechanisms to explain subsurface void formation during the oxidation of unstressed metals and alloys [1,84,85]:

(i)   Vacancy injection resulting from the fact that the outward diffusive flux of metal undergoing oxidation must be counterbalanced by an inward flux of vacancies. This is generally referred to as the Kirkendall effect, and it is possible for the injected vacancies to eventually supersaturate the alloy matrix and coalesce to form voids. The Kirkendall effect may also operate for the diffusion of the surface-enriched, non-reacting elements back into the alloy (e.g., Ni in the alumina-forming NiAl [3]).

(ii)   Gas-bubble formation due to the carbon in the alloy reacting with inward-diffusing oxygen to form CO and CO_2 gases of sufficiently high pressures to induce the nucleation and growth of voids.

(iii)   Creep cavitation due to tensile stresses in the underlying alloy accompanying scale growth. The stresses are a consequence of the volume change between the alloy and the oxide.

The first two of these three mechanisms are probably the most viable [1].

The tendency for void formation in the alloy is also a function of the shape of specimens and their surface-to-volume ratio (radius of curvature) [86,87]. For example, if non-uniform oxidation takes place and when specimens have finite dimensions, constraints are imposed on the system, particularly at edges and corners, and this produces voids and cavities in these regions.

Subsurface void formation affects the oxidation mechanism and the alloy's properties. For example, the accumulation of voids along grain boundaries in the subsurface region of alloy may severely affect the mechanical integrity and properties of the alloy.

2.2.5 Factors Affecting Alloy Oxidation

A large number of factors may affect and control the high-temperature oxidation behavior of alloys. The combination of such factors further makes the behavior more complex. This

section only reviews effects of the most important factors, and some of them are directly relevant to the main aims of the current study.

2.2.5.1 Surface Preparation

When a bare alloy surface is exposed to an oxidizing environment, oxides of the alloy components nucleate at the surface. Different oxides have different thermodynamic and kinetic properties, and thus show different oxidation behaviors. For example, in the case of Fe-Cr alloys, chromia is thermodynamically the most stable oxide that can form as an exclusive scale layer at chromium content exceeding about 18 wt%, but iron oxides are the fastest growing. For a borderline chromia-forming alloy, to exhibit protective oxide behavior, the initially formed, faster-growing iron oxides have to be undercut by a chromia layer which forms initially as internal precipitates within the alloy [88]. Thus, the state of the initial surface will greatly affect oxide nucleation and further affect the alloy's oxidation behavior.

To produce a complete scale layer of Cr_2O_3, for example, a certain minimum concentration (Equation 2.50) and therefore a certain minimum flux of chromium is needed. The Fe-Cr alloy grain boundaries, being high diffusivity paths, can supply more chromium to undercut the faster growing iron oxides in the regions where the grain boundaries intersect the alloy surface. However, in regions far from grain boundaries where the flux of chromium is governed by a slower bulk diffusion (at lower temperatures), the flux may not be enough to form a continuous chromia scale in the early stages of oxidation. In these regions, the faster growing iron oxides will continue to grow, leading to the formation of iron-oxide nodules on the alloy surface. Eventually the faster growing iron oxides may become undercut by a healing layer of Cr_2O_3, which causes a decrease in the oxidation rate.

Decreasing the alloy grain size has been shown to eliminate the formation of iron-rich nodules on the surface of Fe-Cr alloys containing a near-critical chromium content [88]. The reason is that the grain boundaries, which offer fast diffusion paths, can maintain a sufficient supply of chromium to the alloy/scale interface, which helps to quickly undercut any fast growing transient oxides.

Concerning the different methods of grain size reduction, cold deformation is the most common. This can be introduced by straining a sample prior to oxidation (*e.g.*, in a tensile

machine, or cold rolling [89,90]) or superficially deforming the sample surface by, for example, shot peening, sand blasting [91] and machining [92,93].

There is also a potentially detrimental effect related to surface condition. Theoretical [94,95] and experimental [96,97] studies have shown that geometrical surface irregularities generate additional stresses which can facilitate defect formation. The stresses are believed to cause extension of the defects and thus a deterioration in scale integrity. Guttmann *et al.* [98] studied ODS alloy MA956 with different surface pre-treatments: sand-blasted surface with 1.45 μm average roughness, lathe-turned surface with 1.32 μm average roughness, and 800-grit SiC ground surface with 0.28 μm average roughness. The results showed that the scale exhibited very good adherence for the flat surface provided by the 800-grit treatment, other two surface conditions showed spallation earlier at 1100 °C (Figure 2.19). Tensile stresses acted perpendicular to the interface if the sample surface was not absolutely flat.
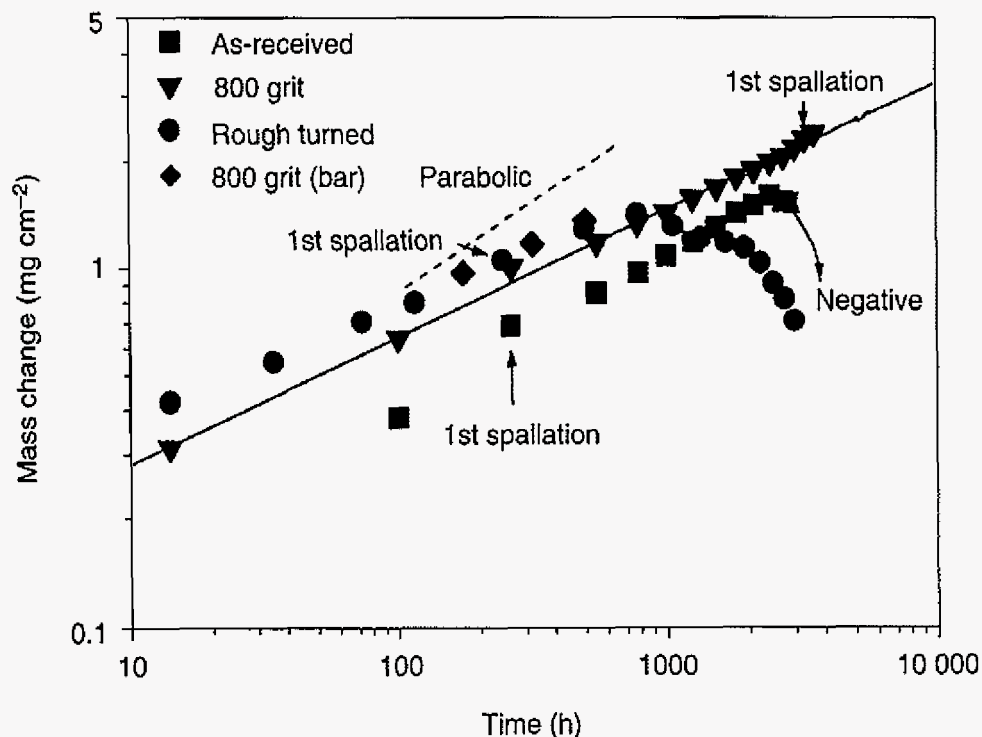
Figure 2.19. Mass change vs exposure time at 1100 °C after different surface treatments. 800-grit sample showed subparabolic oxidation kinetics [98].

It is noted that the main objective of surface finishing is to eliminate any differences in surface conditions such as residual cold work, surface contamination and oxidation, and/or near-surface depletion, which can be introduced during secondary processing of a given alloy [99].

Figure 2.20 shows the influence of specimen microstructure and experimental procedure on the oxidation of chromium [100]. In one run, polished and electrolytically prepared chromium was lowered into a furnace pre-heated to 1200 °C and having an atmosphere of 1 atm O_2. Recording of the weight gain was started within 30s. The metal was found to oxidize relatively rapidly due to the formation of microcrystalline oxide and because the growth predominantly occurs by grain-boundary diffusion. In the other two cases shown in Fig. 2.20, the chromium was annealed and thermally etched and the resulting specimens had large, well-developed grains. In one run the oxidation was started by adding oxygen to the system while chromium was evaporating from the surface ("thermally etched"). In another run the specimen was held out of the hot zone of the furnace, the appropriate oxygen pressure was established and the specimen was then lowered into the furnace ("thermally etched, cold started"). In the latter case an adherent Cr_2O_3 scale formed as the specimen was lowered into the furnace, yielding a lower oxidation rate at temperature.
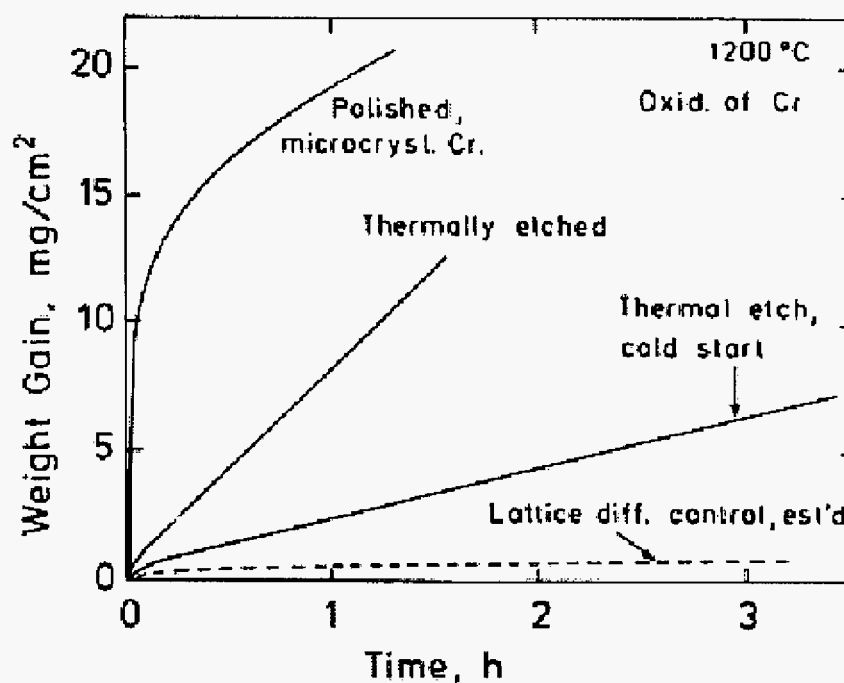
Figure 2.20. Influence of specimen microstructure and
experimental procedure on the oxidation of chromium [100].

2.2.5.2 Matrix Crystal Structure

Large differences in scale growth have been found for oxidation of chromia-forming
alloys depending upon the crystal structure of the matrix [101-106]. Stott *et al.* [101]
examined the oxidation of single-phase ferrite (BCC) Fe-Cr alloys at 1000 °C. They found
that an Fe-14Cr alloy oxidized in a protective manner at 1000 °C, forming an adherent Cr_2O_3
scale with localized areas of iron-rich nodules. By contrast, Kumar and Douglass [102]
conducted a series of oxidation experiments on a single-phase austenitic (FCC) alloy of
composition Fe-14Cr-14Ni at 1000 °C. Instead of forming a thin, protective Cr_2O_3 scale, the
austenitic alloy was found to develop a thick oxide scale consisting of a thick and porous
outer layer and an internally oxidized zone. There was also delamination between the outer
oxide and the internally oxidized zone. The difference in scaling behavior was attributed to
the significantly lower diffusivity of chromium in austenite compared to that in ferrite [103-

106]. Interestingly, when Kumar and Douglass added 4 wt.% silicon to their austenitic alloy, it subsequently oxidized to form a very thin, but adherent oxide scale. Electron probe microanalysis showed that the outer scale was chromia, with a very thin silica layer adjacent to the alloy surface.

2.2.5.3 Minor Additions

As has been established in the previous sections, alloys depend on the formation of a dense, slow-growing external scale for protection against oxidation at high temperature. However, beyond certain temperature or duration, these scales are susceptible to breakdown and are less effective. Minor alloying additions, such as aluminum and silicon, can significantly influence oxidation behavior, particularly under thermal cycling conditions.

Cyclic oxidation behavior is dictated mainly by alloying factor which determines the scale adherence. The scale adherence plays the most important role on spallation behavior and is affected by both scale morphology, scale compositions [141], which largely depend on chemical elements of alloys. Minor alloying additions can be beneficial or detrimental to the oxidation behavior of the alloy, depending upon such factors as their amount, the alloy system, and the oxidation condition [108-126]. For example, depending on concentration, aluminum and silicon can play an effective role in aiding Cr_2O_3 nucleation at the alloy surface. The oxides of Al and Si are more stable than that of chromium; thus, precipitates of the former should form preferentially at the alloy surface in the very early stages of oxidation [108]. Such precipitates can thus act as nucleation sites for Cr_2O_3, since Cr_2O_3 grows more rapidly than alumina and silica, facilitating establishment of the Cr_2O_3-rich scale and preventing formation of significant amount of iron-rich oxides. At same time, aluminum and silicon should getter oxygen, reducing its ingress into the alloy. Once the protective scale has been established, development of a healing layer of the slower-growing Al_2O_3 and/or SiO_2 oxides provides an even more effective barrier to oxidation. This requires formation of a high population density of the minor-element oxide particles at, or close to, the alloy/scale interface and a reasonable rapid rate of growth and coalescence of these particles to establish the complete healing layer [109]. According to Stott *et al.* [100], the formation of silica precipitates during the early-stages of oxidation facilitates the development of a Cr_2O_3 scale

on an Fe-14Cr-10Si alloy oxidized at 1000 °C in air. The continuous inner scale layer of silica that eventually developed on this alloy improved isothermal resistance compared to Fe-26Cr-1Si and Fe-14Cr-3Si alloys, but did result in more extensive scale spallation on cooling.

For commercial chromia-forming alloys, main minor additions are Si, Ti, Al, and Mn in the amount of 0.1-0.3 wt.%, and perhaps a reactive element such as Ce, La, and Zr in the amount of 0.005-0.3 wt.% [110]. The following section will briefly review the effects of these elements on the oxidation behavior of chromiua-forming alloys.

2.2.5.3.1 Manganese

Manganese is generally found to be detrimental to the oxidation behavior of chromia-forming alloys. For stainless steels and Fe-base superalloys the maximum specified manganese level is typically 1.5-2.0 wt.%, while for Ni-base superalloys the maximum is no more than about 0.5 wt.% [110]. As a consequence, manganese is primarily found to be an issue in Fe-base alloys.

Manganese forms a more stable oxide (MnO) than chromium. However, the manganese tends to diffuse through the Cr_2O_3 layer and establish an outer $MnCr_2O_4$ spinel scale [111,112]. As shown by Lobnig *et al.*[113], the lattice diffusivity of manganese in Cr_2O_3 is about two orders of magnitude faster than both nickel and iron at 900 °C, thus explaining the increased tendency for manganese to oxidize at the outer surface. The spinel is less protective than Cr_2O_3 and therefore tends to decrease oxidation resistance [112, 114].

2.2.5.3.2 Silicon

The silicon content in high-temperature alloys is usually limited to less than 3% because of mechanical, weldability, and thermal-stability constraints. Silica is thermodynamically more stable than chromia and will consequently tend to form beneath or at the alloy/chromia-scale interface.

Lower silicon contents of 0.05-1.0% may or may not be sufficient to form a continuous SiO_2 layer at the alloy/scale interface, but are sufficient to have a beneficial effect on

oxidation kinetics, particularly by facilitating exclusive Cr_2O_3 scale formation [100, 115]. Jones and Stringer [115] showed that the oxidation mode for the Co-25Cr alloy changes from the development of a fast-growing duplex structure to the formation of a protective Cr_2O_3 scale with the presence of as little as 0.05% silicon in the alloy.

Evans *et al.* [116] reported the influence of silicon additions on the oxidation resistance of 20Cr-20Ni stainless steels with 0.05-2.35 wt.% silicon in a CO_2-based atmosphere at 850 °C. They found that the rate of scale growth (primarily Cr_2O_3) was a minimum for an alloy containing about 0.9 % silicon, Figure 2.21. The minimum in the rate constant coincided with the presence of a continuous SiO_2-rich layer at the alloy/scale interface, which was inferred to act as a barrier to chromium diffusion. Localized internal protrusion of SiO_2 developed in alloys containing more than 0.9 % silicon.
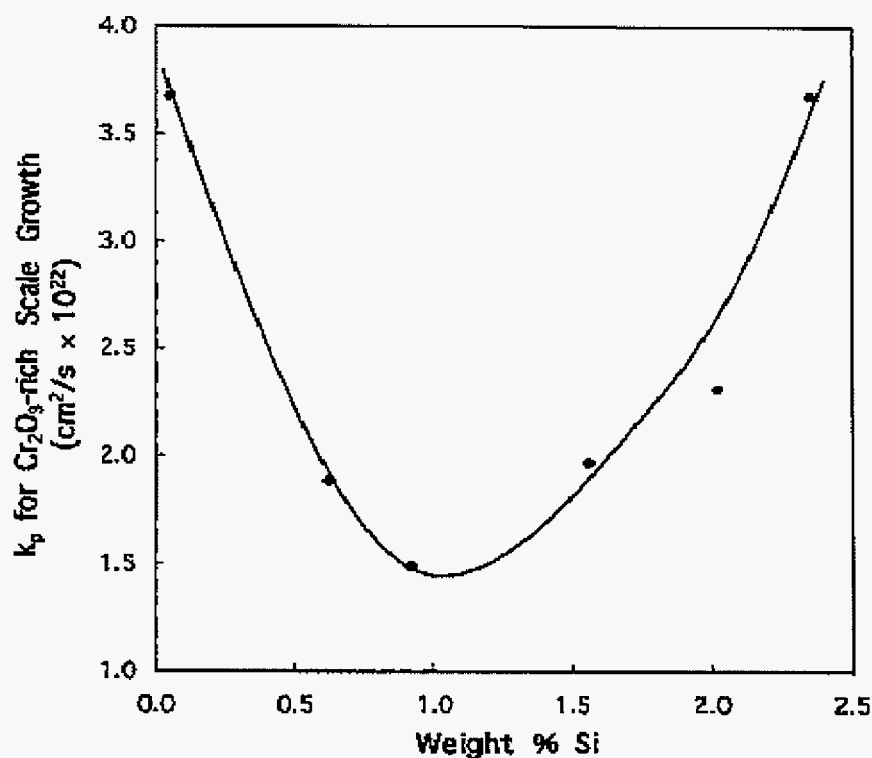
Figure 2.21. Variation of the parabolic rate constant for Cr_2O_3-rich scale growth on alloys of different silicon contents at 850 °C in a CO_2-based atmosphere.

As shown previously, high silicon content facilitates the formation of a continuous silica layer at the alloy/scale interface [100], which improves isothermal oxidation resistance by suppressing cation transport through Cr_2O_3 scale. However, an inner SiO_2 layer can also greatly worsen the extent of scale spallation under thermal cycling conditions [100, 114, 116]. From Figure 2.22, about 0.25 wt.% silicon showed the smallest spallation under cyclic condition at 900 °C, while higher silicon caused large spallation [117]. Stott *et al.* [101] also found the consistent silicon effects on Fe-Cr-Si alloys oxidized at 1000 °C. The early-stage formation of silica precipitates during the early stage of oxidation facilitates the development of a Cr_2O_3 scale on an Fe-14Cr-10Si alloy. The continuous inner scale layer of silica that eventually developed on this alloy improved isothermal oxidation resistance compared to Fe-26Cr-1Si and Fe-14Cr-3Si alloys but result in more extensive scale spallation on cooling.
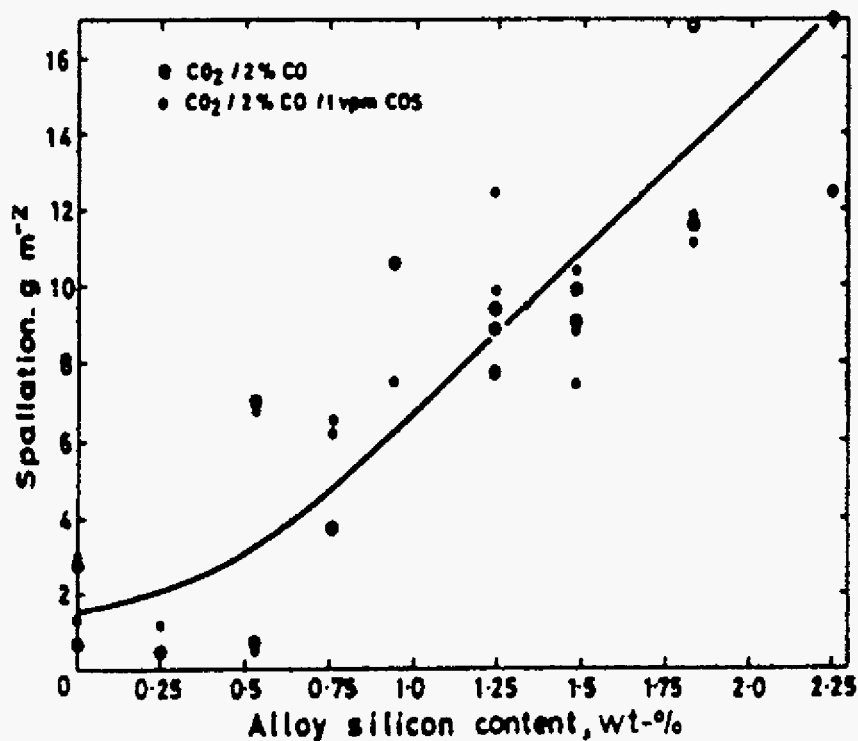
Figure 2.22. Effect of silicon content on the oxidation behavior of Fe-20Cr-25Ni-based steels [117].

2.2.5.3.3 Aluminum

Aluminum is added to improve high-temperature strength by the mechanism of precipitation hardening via formation of the coherent Ni_3Al-based γ' phase. Too high an aluminum content, and hence too high a γ' volume fraction, makes alloys difficult to deform by hot or cold rolling and also degrades the weldability of the alloy. These factors limit the amount of aluminum that can be added to wrought alloys, with commercial alumina-forming alloys containing only up to about 5 wt.% Al. Al_2O_3 is thermodynamically more stable than chromia. Furthermore, a continuous alumina scale grows more slowly than a chromia scale, and thus alumina scales formed through selective oxidation provide considerably better oxidation than corresponding chromia scales [8]. For chromia-forming alloys, the aluminum must be at level above about 0.4 % to have a beneficial effect. Such an Al level is sufficient to establish an Al_2O_3–rich inner layer at the base of the Cr_2O_3 scale; however, this depends on temperature and the amount of other elements in the alloy. The Al_2O_3–rich inner layer, which acts to decrease the thickening kinetics of the Cr_2O_3 scale by reducing the outward migration of chromium cations, does not need to be continuous to confer a beneficial effect [111].

2.2.5.3.4 Titanium

Titanium is added to Ni-base superalloys to increase the extent of strengthening brought about by γ'-$Ni_3(Al,Ti)$ precipitates [1]. However, titanium is generally detrimental to the oxidation resistance of chromia-forming alloys [118-121]. Titania, TiO_2, is more stable thermodynamically than Cr_2O_3, thus TiO_2 may develop below an external chromia scale as internal oxide. However, in the case of chromia-forming alloys, titanium tends to oxidize at both the scale surface and the alloy/scale interface [119-122]. As internal oxide, the TiO_2 tends to form at grain boundaries. Internal TiN has also been found when the environments are reducing (i.e., low oxygen potentials) or if the alloy is oxidized in air at a sufficiently high temperature [2]. The formation of TiN gives further internal attack, deeper into the substrate, which is detrimental to the performance of the alloy.

2.2.5.3.5 Reactive Elements

The addition of a small amount (0.005-0.3%) of reactive elements (RE), such as yttrium, lanthanum, cerium, zirconium, or hafnium, can considerably improve the resistance of protective scales to spallation [123]. For M-Cr alloys containing RE, there is reportedly a reduction in the concentration of chromium in the alloy necessary to form a continuous, protective chromia layer [124-126]. Moreover, the growth rate of that layer, once established, is reduced and the resistance of the scale to spallation is improved very significantly in comparison to if the alloy containing no RE. Figure 2.22 shows the RE effect for the case of the Ni-base alloy René N5, with and without addition of 100-150 ppm yttrium, and oxidized in air at 1150 °C in one-hour thermal cycles [127]. When a small amount of RE is added, it tends to segregate to the alloy-scale interface and scale grain boundaries, and have the apparent effect of suppressing cation diffusion in the scale [128]. An additional, and perhaps coinciding effect is for the RE to react with sulfur in the alloy to form sulfides or S-RE-containing complexes, thus preventing the interfacial segregation of free sulfur and consequential weakening of the alloy-scale interfacial bond strength. In support of this latter effect, Figure 2.23 also shows that removal of alloy sulfur content to a level below *ca.* 0.1 ppm w/w by hydrogen annealing results in good adhesion of the Al_2O_3-rich scale formed on a Ni-base superalloy containing no RE [129]. Alloys containing high concentrations (>1%) of RE tend to form intermetallic phases which are prone to preferential oxidation, thus reducing the oxidation resistance of the alloy [130].
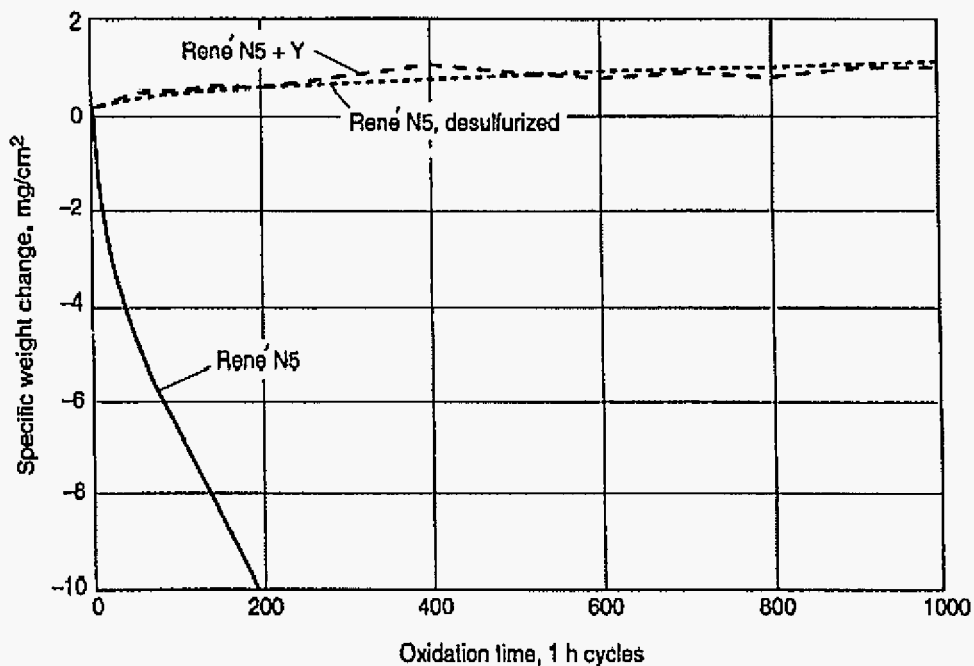
Figure 2.23. The effect of addition of Yttrium or desulfurizing pre-treatment on 1150 °C cyclic oxidation behavior of the cast, Ni-base superalloy René N5.

This is clearly illustrated in Figure (2.24) where NiAl+Hf is observed to show every similar mass gains up to 1000h at 1100 °C, independent of cycle frequency [131]. While René N5B (NiAl alloy) showed cycle-dependent spallation behaviors. The good cyclic oxidation resistance for NiAl+Hf is due to the excellent scale adhesion, which contributes to exist of Hf at the alloy/scale interface.
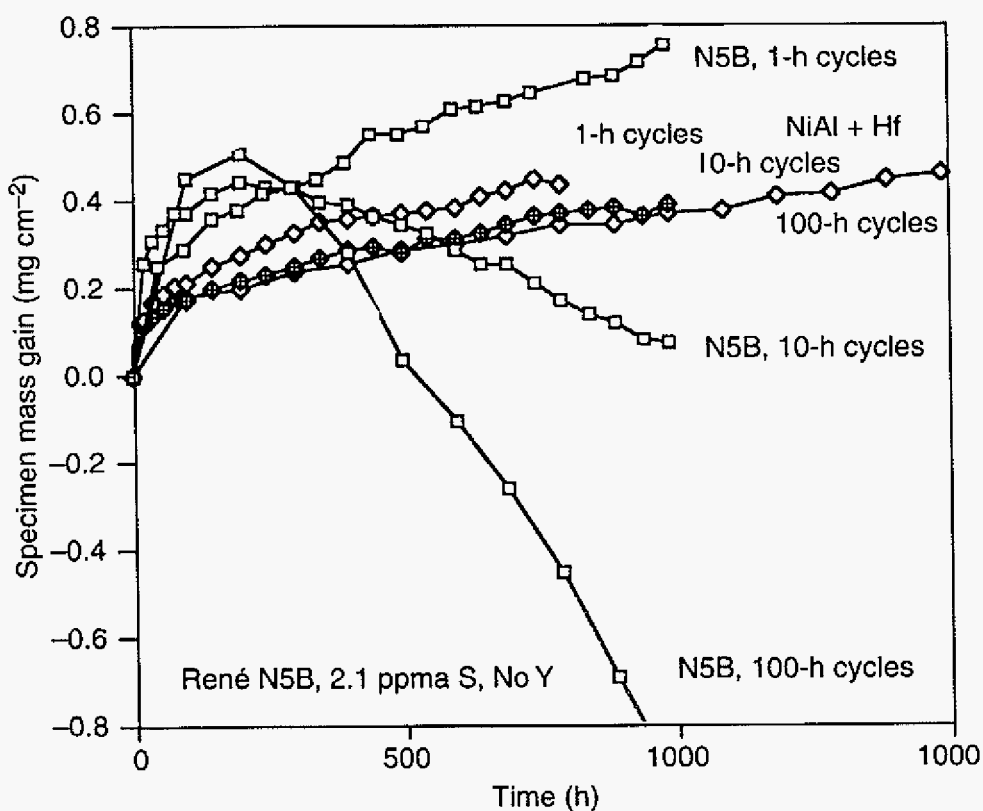
Figure 2.24. Mass gain for various cycle times at 1100 °C for René N5B and NiAl+Hf alloys.

2.2.6 Diffusion Processes Associated with Alloy Oxidation

The formation of a Cr_2O_3-rich scale on an alloy results in the development of a subsurface depletion profile of chromium. The depth and shape of the profile depend on the diffusivity of chromium in the alloy which, in turn, depends in a complex manner on the thermodynamic interactions between the various alloying elements and chromium. The ability to predict the subsurface depletion profile of chromium would be required for any life-time assessment model of chromia-forming alloys. The utilization of a interdiffusion coefficient to characterize the diffusivity of chromium in an alloy system offers a method to calculate the subsurface depletion profiles.

For binary and commercial alloys, multiple alloying elements show interdiffusion effects between chromium and other elements, specially, the diffusion characteristics of chromium can depend very much on the concentrations and gradients of other elements. With the selective depletion of chromium to form a Cr-rich scale, the concentration of Cr in the subsurface region of the alloys will change with time, which means that the chromium interdiffusion coefficient may change with time at a given position. The effective interdiffusion coefficient is obtained by measuring the subsurface depletion profile, which is the result of interdiffusion. Thus, the utilization of an effective interdiffusion coefficient, D^{eff}, to characterize the diffusivity of chromium in a multi-component alloy system offers the advantage of simplifying calculations of the subsurface depletion profiles.

2.2.6.1 Effective Interdiffusion Coefficient

Diffusion is the movement of a given species from a region of high chemical activity to a region of low activity and for solid-solution systems that are not prone to clustering, the rate of diffusion of a given species is found to be proportional to and in a direction that is down its concentration gradient. Figure 2.25 shows a hypothetic concentration gradient of chromium in the subsurface region of an alloy that has undergone a given period of selective Cr_2O_3 formation. As can be inferred from the previous sections, the establishment of a protective chromia scale, requires initially a transient stage which produces all thermodynamically stable products. Then, as the reaction progresses a gradient in the oxidant activity develops, such that the least stable products dissociate or are displaced, leaving only the most stable product, Cr_2O_3, as the protective scale in contact with the alloy (assuming the chromium content in the alloy is sufficiently high). Under ideal conditions, a steady state is then established, in which the scaling behavior can be used to predict the oxidation lifetime. Upon reaching a steady state, the chromium content in the alloy at the scale/alloy interface will lower to a fix value of N_{Cr}^{i}, as shown in Figure 2.23. The unaffected alloy has a higher chromium concentration, N_{Cr}^{o}, which will continuously diffuse to the alloy/scale interface to sustain the continuous chromia scale growth.
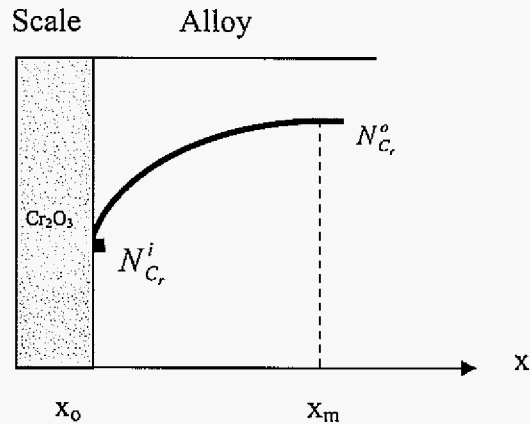
Figure 2.25. Chromium depletion profile in an oxidized chromia-forming alloy.

The rate equation for diffusion at a given position within the concentration gradient may be approximated from Fick's first law [132]:

$$J = -D\frac{dN}{dx}$$

(2.49)

where J is the interdiffusion molar flux of chromium in the x-direction, in typical units of $mol \cdot cm^{-2} \cdot s^{-1}$, N is molar concentration, in units of $mol \cdot cm^{-3}$, x is specific position, in cm, and D is the diffusion coefficient, in units of $cm^2 \cdot s^{-1}$.

For n-multicomponent alloy system, such as commercial alloys, the interdiffusion flux of component i is expressed on the basis of Fick's first law as [133,134]

$$\widetilde{J}_i = -\sum_{j=1}^{n-1} \widetilde{D}_{ij}^n \frac{\partial N_j}{\partial x} \qquad (i = 1,2,...,n\text{-}1)$$

(2.50)

where $\widetilde{D}_{ij}^n$ correspond to the $(n\text{-}1)^2$ interdiffusion coefficients and it is a function of compositions, and $\dfrac{\partial N_j}{\partial x}$ is the gradient of concentration of component j. The equation (2.50) can be written as:

$$\tilde{J}_i = -\tilde{D}_i^{e\!f\!f} \frac{\partial N_i}{\partial x} \tag{2.51}$$

where an effective interdiffusion coefficient is defined as

$$\tilde{D}_i^{e\!f\!f} = \tilde{D}_{ii}^n + \sum_j \frac{\tilde{D}_{ij}^n \frac{\partial N_j}{\partial x}}{\frac{\partial N_i}{\partial x}} \tag{2.52}$$

Thus, the interdiffusion coefficients can be simplified as an effective interdiffusion coefficient that can be obtained from Equation (2.51) after the interdiffusion flux, $\tilde{J}_i$, and the gradient of concentration of component i, $\frac{\partial N_i}{\partial x}$, are obtained. The interdiffusion flux can be determined as a function of a distance x directly from the concentration profile. As shown by Dayananda [135,136], the interdiffusion flux can also be given by the relationship:

$$\tilde{J}_i = \frac{1}{2t} \int_{N_i^o}^{N_i^l} (x - x_o) dN_i \tag{2.53}$$

where x_o corresponds to the position of the alloy/scale interface.

Dayananda [135-136] further developed a model to calculate the average effective interdiffusion coefficient of a component from its concentration profile. The specifics of this and other proposed models for determining $\tilde{D}^{e\!f\!f}$ are discussed in the following.

I. Model I – Dayananda's model

Dayananda developed a model for obtaining the effective interdiffusion coefficient, which utilized the integration of Equation 2.51. Figure 2.26 shows a concentration profile through a diffusion couple after some period of diffusion. The Matano interface, x_o, represents the interface of mass balance for the diffusing component, i. In the case of an oxidized alloy, the scale/alloy interface is approximately equal to the position of the Matano interface.
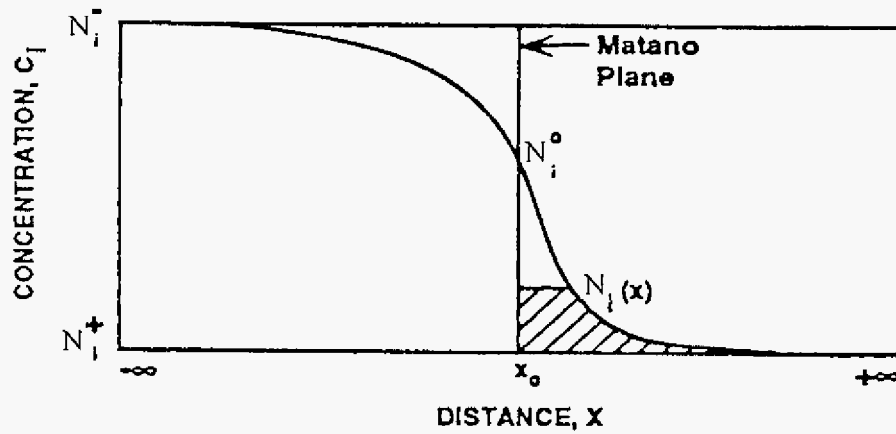
Figure 2.26. Schematic concentration profile for component i

in an infinite, solid-solid diffusion couple.

Integrating the interdiffusion flux J given by Equation (2.51) over the depletion region from x_1 to x_2, gives

$$\int_{x_1}^{x_2} \tilde{J} dx = \int_{x_1-x_o}^{x_2-x_o} \tilde{J} d(x-x_o) = \tilde{J}(x-x_o)|_{x_1}^{x_2} - \int_{\tilde{J}(x_1)}^{\tilde{J}(x_2)} (x-x_o) d\tilde{J} \qquad (2.54)$$

Because $dJ=(x-x_o)dN/2t$ from Equation (2.53), Equation (2.54) becomes:

$$\int_{x_1}^{x_2} \tilde{J} dx = \tilde{J}(x_2)(x_2 - x_o) - \tilde{J}(x_1)(x_1 - x_o) - \frac{1}{2t} \int_{N(x_1)}^{N(x_2)} (x-x_o)^2 dN \qquad (2.55)$$

From $\tilde{J} dx = - \tilde{D}^{eff} dN$, Equation (2.55) can be written as

$$\int_{x_1}^{x_2} \tilde{D}^{eff} dN = \tilde{J}(x_1)(x_1 - x_o) - \tilde{J}(x_2)(x_2 - x_o) + \frac{1}{2t} \int_{N(x_1)}^{N(x_2)} (x-x_o)^2 dN \qquad (2.56)$$

Thus, an average effective interdiffusion coefficient for the range from x_1 to x_2 can be obtained by:

$$\tilde{D}^{eff} = \frac{\tilde{J}(x_1)(x_1 - x_o) - \tilde{J}(x_2)(x_2 - x_o)}{N(x_2) - N(x_1)} + \frac{\int_{N(x_1)}^{N(x_2)} (x - x_o)^2 dN}{2t(N(x_2) - N(x_1))} \qquad (2.57)$$

In the case of a depletion profile after selective oxidation (Figure 2.25), concentration range changes from the alloy/scale interface ($x_1=x_0$), Matano plane if omitting the interface

movement) to unaffected matrix ($x_2=x_m$). Thus, $x_1-x_o=0$ and $\tilde{J}(x_2)=\tilde{J}(x_m)=0$ in the first part of right side of Equation 2.57, then Equation (2.57) can be re-written as

$$\tilde{D}^{eff} = \frac{\int_{N^i}^{N^o}(x-x_o)^2 dN}{2t(N^o-N^i)} \tag{2.58}$$

where N^o is concentration in bulk of the alloy, and N^i is concentration at the scale/alloy interface, and x_o is the scale/alloy interface.

Dayananda's model thus obtains an average effective interdiffusion coefficient by mathematic transformation for Fick's first law over a concentration range. In the following, two alternative models are developed in the current study to determine the effective interdiffusion coefficient.

II. Model II - Average-slope model

Combining Equations (2.51) and (2.53), the effective interdiffusion coefficient can be obtained as

$$\tilde{D}^{avs} = -\frac{\tilde{J}}{dN/dx} = -\frac{\int_{N^o}^{N^i}(x-x_o)dN}{2t} \cdot \frac{1}{dN/dx} \tag{2.59}$$

where dN/dx can be defined as the average slope along the chromium depletion profile, which can be obtained by

$$\frac{dN}{dx} = \frac{\int_{x_o}^{x_m} N' dx}{x_m - x_o} \tag{2.60}$$

where x_m is the position of the depletion front, as shown in Fig. 2.25.

III. Model III - Average-D model

This method considers the local interdiffusion coefficients along the subsurface chromium depletion profile. Specially local interdiffusion coefficients, $\tilde{D}_{N_{x(n)}}$, are calculated at different

compositions along the profile, and the effective interdiffusion coefficient is then determined for whole depletion region.

Fick's second law can be written as

$$\frac{\partial N}{\partial t} = \frac{\partial}{\partial x}(D\frac{\partial N}{\partial x})$$ (2.61)

In this equation, the position variable x and the time variable t can be combined into one variable $\lambda = x / t^{1/2}$, so that N may be considered to be a function of only one variable, λ [132]. Then, Equation (2.61) may be transformed as:

$$\frac{\partial N}{\partial t} = \frac{\partial \lambda}{\partial t}(\frac{\partial N}{\partial \lambda}) = -\frac{1}{2}\frac{x}{t^{3/2}}(\frac{dN}{d\lambda}) = -\frac{\lambda}{2t}(\frac{dN}{d\lambda})$$ (2.62a)

and

$$\frac{\partial N}{\partial x} = \frac{\partial \lambda}{\partial x}(\frac{\partial N}{\partial \lambda}) = \frac{1}{t^{1/2}}(\frac{dN}{d\lambda})$$ (2.62b)

Substituting Equations (2.62) into Equation (2.61), one obtains:

$$-\frac{\lambda}{2t}(\frac{dN}{d\lambda}) = \frac{\partial}{\partial x}[\frac{D}{t^{1/2}}(\frac{dN}{d\lambda})] = \frac{1}{t}\frac{d}{d\lambda}(D\frac{dN}{d\lambda})$$ (2.63)

Simplifying the following equation is obtained

$$-\frac{\lambda}{2}(\frac{dN}{d\lambda}) = \frac{d}{d\lambda}(D\frac{dN}{d\lambda})$$ (2.64)

Consider the boundary condition in Figure 2.23:

$$N = N^o \qquad \text{for } \lambda = \infty$$ (2.65)

where N^o is the bulk content of the selectively oxidized component in the alloy. Integrating Equation (2.65), one obtains

$$-\frac{1}{2}\int_{N^o}^{N} \lambda dN = D\frac{dN}{d\lambda}\Big|_{N^o}^{N}$$ (2.66)

Since the concentration gradient goes to zero as N approaches N°, the right-hand side of Equation (2.66) is simply $D(dN/d\lambda)$. Then the local interdiffusion coefficient at N'' can be obtained as

$$D_{N''} = -\frac{1}{2t(dN''/d\lambda)} \int_{N^0}^{N''} \lambda dN'' \qquad (2.67a)$$

At some constant time t and x_o as interface position, (2.67a) can be written as

$$D_{N''} = -\frac{1}{2t(dN''/dx)} \int_{N^0}^{N''} (x - x_o)dN'' \qquad (2.67b)$$

The effective interdiffusion coefficient is thus obtained by determining the average of all the local interdiffusion coefficients:

$$\widetilde{D}^{avd} = \frac{\sum_{n=1}^{n_t} \Sigma D_{N''}}{n_t} \qquad (2.68)$$

where n is the number of measurements along the depletion profile (from 1 to n_t). This model shall be called the average-D model.

2.2.6.2 Depletion Profile Prediction

Wagner [68] analyzed binary alloy oxidation by assuming that the process was diffusion controlled and that scale growth was ideal (*i.e.*, there was no cracking or spallation of the scale). The expression for the subsurface depletion profile of chromium was determined from this analysis to be given by,

$$N_{Cr}(x,t) = N_{Cr}^i + (N_{Cr}^o - N_{Cr}^i)\frac{erf[\frac{x}{2(Dt)^{1/2}}] - erf[\frac{k_c}{2D}]^{1/2}}{1 - erf[\frac{k_c}{2D}]^{1/2}} \qquad (2.69)$$

where x is the distance from the alloy/scale interface to matrix, N_{Cr}^o and N_{Cr}^i are the chromium content in the bulk and alloy/scale interface, and k_c is corrosion constant that is related to k_p, *i.e*,

$$k_c = \left(\frac{V_{metal}}{v \cdot M_o}\right)^2 \cdot k_p \qquad (2.70)$$

where V_{metal} is the molar volume of metal and M_o is the atomic weight of oxygen, and k_p is parabolic rate constant for the growth of oxide BO_y.

The assumptions used derive Equation (2.69) limit the application of this equation under conditions of thermal cycling during which spallation may occur during cooling. Spallation would cause a departure form steady-state conditions and result in accelerated subsurface and metal recession. Both of these consequential factors would negatively affect the alloy life during high-temperature operation. A further limitation of Equation (2.69) is that the chromium content at the alloy/scale interface is required to calculate the depletion profile. From a practical standpoint, it would be desired to predict N^i, especially under thermal cycling conditions.

Whittle [64] considered the case of reformation of the protective oxide layer if the first layer spalls after a thermal cycle. The concentration at the alloy/scale interface is specifically important if repeated losses of the protective oxide are expected, as sufficient time must elapse between successive losses of oxide in order for the concentration at the alloy/scale interface to return to a value that is close to what had before the loss of the first oxide. An approximate solution for the depletion profile after complete spallation was obtained as (for chromia-former)

$$N_{Cr} = N_{Cr}^o - \frac{N_{Cr}^*}{1-N_{Cr}^*}(1-N_{Cr}^o)erfc\frac{x}{2[D(t-t^*)]^{1/2}}$$
$$\times[1+\frac{N_{Cr}^*}{1-N_{Cr}^*}\times\frac{2}{\pi}\sin^{-1}(t/t^*)^{1/2}]+\frac{2}{\pi}\int_0^{(t'/t-t^*)^{1/2}}\exp[-\frac{x^2(1+u^2)}{4Dt}]\frac{du}{1+u^2} \quad (2.71)$$

where t^* is the time at which the loss of the protective oxide occured, and N_{Cr}^* is the critical concentration of chromium to form the protective chromia scale,

$$N_{Cr}^* = \left(\frac{\pi k_c}{2D}\right)^{1/2} \quad (2.72)$$

The ratio of k_c/D is a characteristic alloy parameter and directly relates to the alloy's ability to form a protective chromia scale. The concentration of chromium at the alloy-oxide interface is then obtained by applying x=0 in Equation 2.71 when t>t*, as

$$N_{Cr}^i = \frac{N_{Cr}^*}{1-N_{Cr}^*}\left[N_{Cr}^o - N_{Cr}^* - \frac{N_{Cr}^*}{1-N_{Cr}^*}(1-N_{Cr}^o)\frac{2}{\pi}\sin^{-1}(t^*/t)^{1/2}\right] \quad (2.73)$$

Figure 2.27 shows that the variation of interfacial chromium concentration with time for an alloy with N_{Cr}^o=0.25 at.% and k_c/D=10^{-2}. The value of N_{Cr}^* is also shown as a dashed line

with a value of 0.125. From Fig. 2.27, the interfacial concentration of chromium decreases abruptly when chromia layer re-forms immediately after spalling of the initial layer. With increasing time beyond t^*, the interfacial chromium concentration increases, rapidly at first, eventually approaching the value slightly lower than what it had before the initial layer spalled from the surface. Only after the time when N_{Cr}^i becomes greater than N_{Cr}^* (0.125), a protective chromia scale can be reformed.
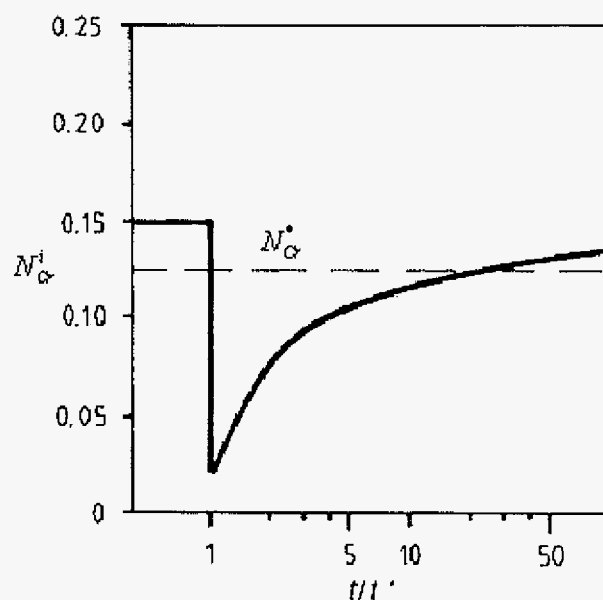
Figure 2.27. Variation of interfacial concentration of Cr with time.

The ratio of k_c/D and the value of N_{Cr}^* can be used to ascertain whether an alloy can resist repeated spallings of the scale at short time intervals. Consequently, alloys can be divided into the four groups (Figure 2.28):

1. $N_{Cr}^o < N_{Cr}^*$:   Insufficient chromium to form the protective oxide.

2. $N_{Cr}^* < N_{Cr}^o < (1 - N_{Cr}^*)^2$:   Sufficient chromium to form the protective oxide initially, but insufficient to re-form it.

3. $1 - (1 - N_{Cr}^*)^2 < N_{Cr}^o < (1 - N_{Cr}^*)^3$:   Sufficient chromium for healing of the protective oxide, but not sufficient for repeated spalling at high frequency.

4. $N_{Cr}^o > (1 - N_{Cr}^*)^2$:   Sufficient chromium to resist rapid spalling possible.
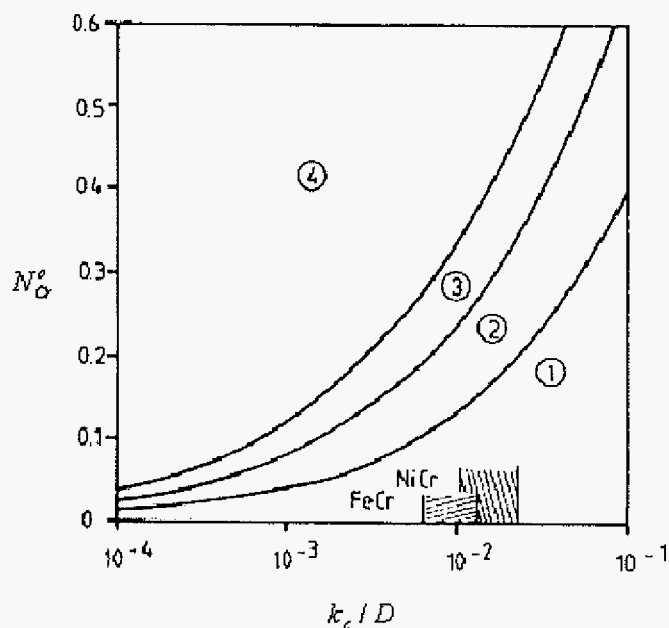
Figure 2.28. Critical mole fractions for alloys to withstand repeated spalling of the protective oxide as a function of k_c/D.

Whittle considered short-term cyclic oxidation, in which the movement of the alloy/scale interface can be neglected. Thus, it limits the application in long-term cycling oxidation, in which the interface movement must be considered for most chromia-forming alloys.

Nesbitt [137, 138] developed a numerical model to predict the depletion profile during a selective oxidation process. As oxidation proceeds, the weight gain, which comes from the oxidation reaction, and weight loss, which results from the scale spallation, happen at the same time. Thus, the finite difference process (Figure 2.29) is used to calculated the concentration change in a given small time interval Δt by considering the weight gain in term of k_p and weight loss in term of spallation constant Q_o to predict the rate of solute consumption associated with partial scale spallation.
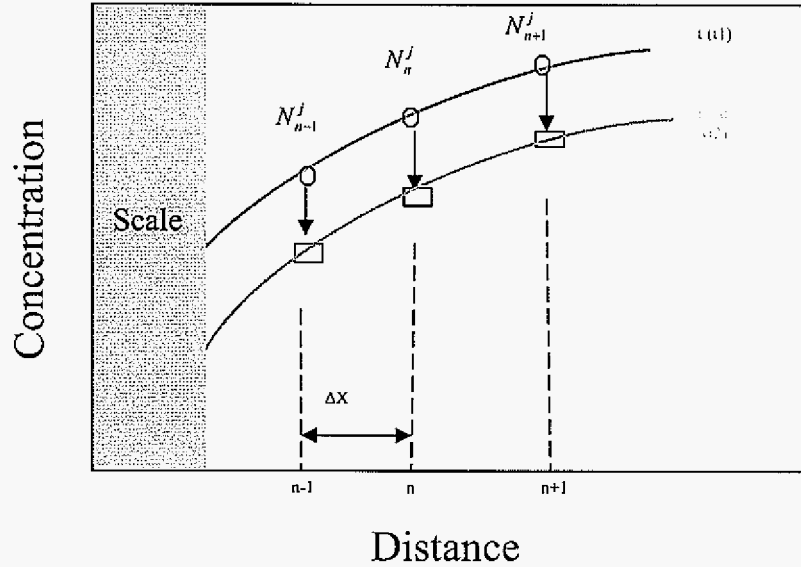
Figure 2.29. Schematic diffusion zone for time t and time t+Δt.

In order to predict the depletion profiles with time, Nesbitt used Fick's second law to describe diffusion in a ternary alloy,

$$\frac{\partial N_{Cr}}{\partial t} = \frac{\partial\left(D_{Cr,Cr}\left(\frac{\partial N_{Cr}}{\partial x}\right)\right)}{\partial x} + \frac{\partial\left(D_{Cr,M}\left(\frac{\partial N_M}{\partial x}\right)\right)}{\partial x} \qquad (2.74)$$

where M is another metal component. Equation (2.74) can be developed as

$$\frac{\partial N_{Cr}}{\partial t} = D_{Cr,Cr}\frac{\partial^2 N_{Cr}}{\partial x^2} + \left(\frac{\partial D_{Cr,Cr}}{\partial N_{Cr}}\frac{\partial N_{Cr}}{\partial x} + \frac{\partial D_{Cr,Cr}}{\partial N_M}\frac{\partial N_M}{\partial x}\right)\frac{\partial N_{Cr}}{\partial x} +$$
$$D_{Cr,M}\frac{\partial^2 N_M}{\partial x^2} + \left(\frac{\partial D_{Cr,M}}{\partial N_{Cr}}\frac{\partial N_{Cr}}{\partial x} + \frac{\partial D_{Cr,M}}{\partial N_M}\frac{\partial N_M}{\partial x}\right)\frac{\partial N_M}{\partial x} \qquad (2.75)$$

As shown in Figure (2.29), the following finite-difference equivalents can be used to resolve Equation (2.75):

$$\frac{\partial N_{Cr}}{\partial t} = \frac{N^{i+1}_{Cr,n} - N^{i}_{Cr,n}}{\Delta t} \tag{2.76}$$

$$\frac{\partial N_{Cr}}{\partial x^2} = \frac{N^{i}_{Cr,n+1} - 2N^{i}_{Cr,n} + N^{i}_{Cr,n-1}}{(\Delta x)^2} \tag{2.77}$$

and $$\frac{\partial N_{Cr}}{\partial x} = \frac{N_{Cr,n+1} - N_{Cr,n-1}}{2\Delta x} \tag{2.78}$$

Thus, Equation (2.75) can be determined by resolving the equivalents in (2.76-2.78), which are computed in an iterative manner by establishing a nodal concentration grid over a diffusion-affected region after establishing the boundary conditions.

Boundary condition for solute Cr at the alloy surface is that the alloy surface recedes as Cr diffuses to interface. Considering the alloy recession (Figure 2.30) due to the alloy/scale interface movement occurring during oxidation, a coefficient α ($\alpha > 1$), which is related to spallation parameter Q_o, is used to obtain the chromium flux,

$$J^{oxide}_{Cr}\Big|_{x=x_o} = \alpha J^{alloy}_{Cr}\Big|_{x=x_o} \tag{2.79}$$

with

$$\alpha = 1/(1 - V_{Cr}N^{i}_{Cr}) \tag{2.80}$$
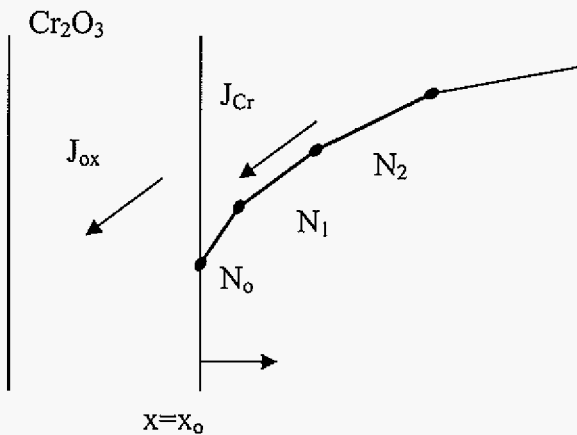
Figure 2.30. Binary conditions at the alloy surface.

where J_{Cr}^{oxide} is flux of chromium entering the oxide (i.e., the amount of chromium being consumed by oxidation), J_{Cr}^{alloy} is flux of chromium within the alloy at the alloy/scale interface, V_{Cr} is the partial molar volume of chromium in the scale, and C_{Cr}^{i} is the chromium content at the scale/alloy interface. Therefore, J_{Cr}^{oxide} is greater than J_{Cr}^{alloy} at the alloy/scale interface due to the interface movement. The flux of chromium diffusing to the alloy/scale interface can be determined by

$$J_{Cr}^{alloy}\bigg|_{x=x_o} = -D_{Cr,Cr}\left(\frac{\partial N_{Cr}}{\partial x}\right)_{x=x_o} - D_{Cr,M}\left(\frac{\partial N_M}{\partial x}\right)_{x=x_o} \tag{2.81}$$

with boundary condition (Fig. 2.30)

$$\left(\frac{\partial N_{Cr}}{\partial x}\right)_{x=x_o} = \frac{-N_2 + 4N_1 - 3N_0}{2\Delta x} \tag{2.82}$$

The flux of chromium entering the oxide (i.e., the amount of Cr being consumed by oxidation), J_{ox}, can be obtained by applying the Cyclic Oxidation Spalling Program (COSP), which was developed at NASA [139, 140]. The COSP tracks weight of oxide scale which grows and spalls in each cycle. In order to consider the spallation during thermal cycling, the faction, f, of scale spalled in a given cycle is defined as:

$$f = W_s / W_f \tag{2.83}$$

where W_s is the specific weight of spall in mg/cm^2, and W_f is the specific weight of total scale present before cooling in mg/cm^2. Then, the premise is given by as:

$$f = Q_o W_f \tag{2.84}$$

where Q_o is a proportionality constant in units of cm^2/mg and is also called as spallation constant. Combing Equations (2.83) and (2.84):

$$W_s = Q_o (W_f)^2 \tag{2.85}$$

Thus, Equation (2.85) gives a relation between the amount of scale present and the amount of scale spalled. Then, at any point in time, the observed overall weight change of a sample undergoing cyclic oxidation is the weight gained by scale formation to the time, minus the weight of scale lost by spalling. If t is the duration of one thermal cycle, then the final specific weight change of the sample after the first cycle is given by:

$$\Delta W = (k_p t)^{1/2} - Q_o (W_f)^2 \tag{2.86}$$

The above equation gives the predicted cyclic oxidation kinetics assuming parabolic scaling kinetics. Figure 2.31 shows hypothetical COSP results for an alloy with different possible spallation constants. Clearly, the alloy exhibits more severe weight loss and consequently less oxidation resistance with increasing Q_o.
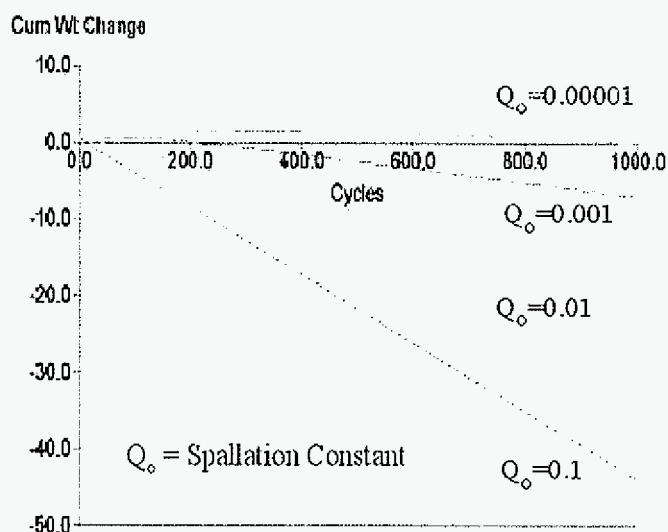
Figure 2.31. Kinetics of cyclic oxidation for different spallation constants.

The model developed by Nesbitt to predict the depletion profile is called OxDiff (Oxidation and Diffusion) Diffusion Model and the program is written in FORTRAN. For given alloy system, three parameters are required to predict the depletion profile: oxide growth rate (k_p), oxide spallation constant (Q_o), and interdiffusion coefficient (D_{Cr}). Based on previous discussion, k_p can be obtained by TGA test, Q_o by the COSP program, and $\tilde{D}^{eff}$ by one of the models presented in section 2.2.6.1.

2.2.7 Cyclic Oxidation

Isothermal oxidation testing is often used in laboratory studies to assess oxidation mechanisms and to obtain what could be termed "ideal" oxidation data. However, most high-temperature material systems are used under thermal cycling conditions. The kinetics of

isothermal and cyclic oxidation may be very different due scale cracking or even spallation during cyclic oxidation. Figure 2.32 [139, 141] shows the significant effect of thermal cycling on surface recession of Ni-Cr alloys at 1200 °C for 50 one-hour cycles. Thus, determining the oxidation behavior of a given alloy under thermal cycling condition gives a much more representative description of the restiance of that alloy to high-temperature degradation under actual service conditions. According, cyclic oxidation is one of the most important and frequently used testing procedures.
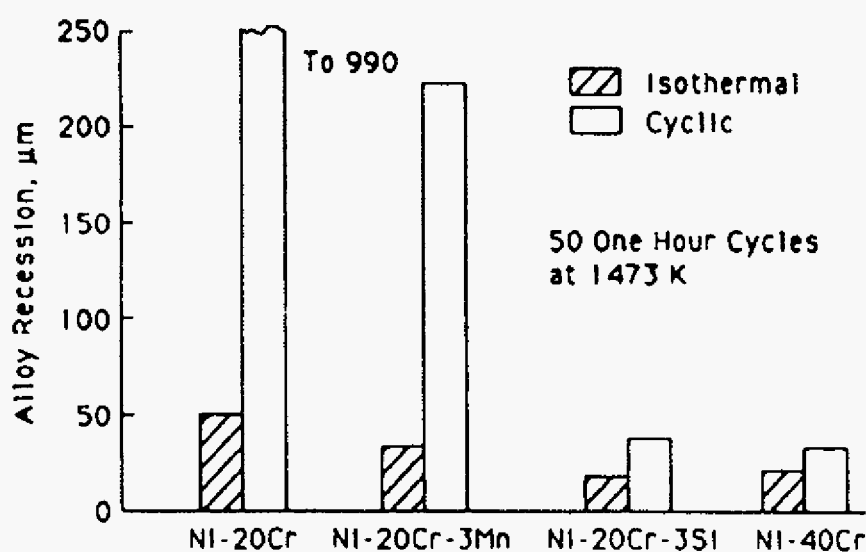
Figure 2.32. Enhanced metal recession as a result of cyclic oxidation. Alloy recession is defined as the loss of metal thickness per side.

Scale spallation usually takes place during the cooling period of a thermal cycle. With a change in temperature, the difference in thermal expansion coefficient between the scale and the underlying alloy causes the generation of a thermal stress. Oxides that are ductile at high temperature are often brittle at lower temperatures, and the thermal stress generated could lead to scale cracking and possibly even scale spallation. Obviously, if some scale is lost during a thermal cycle, there remains a less protective scale on the alloy as the next cycle begins. If after longer oxidation time, the chromium content at the alloy/scale interface decreases below a critical level, N_{Cr}^*, reformation of the chromia scale is not kinetically possible, leading to the formation of a more rapidly growing, and hence less protective scale.

This transition to more rapid scale growth is called breakdown. Therefore, the alloy would undergo more rapid oxidation attack (*i.e.*, selective subsurface depletion) during the subsequent cycle.

The spallation of oxide scales generally involves the separation of cracked scale either by de-cohesion at the alloy/scale interface or by fracture on planes within the scale itself [142,143]. Moon and Lee [144] attempted to quantify the fraction, F, of spalled scale resulting from a temperature drop, ΔT, by the expression

$$F = [\frac{\eta X (\Delta T)^2}{\beta}]^m \tag{2.87}$$

where X is the scale thickness before spalling, η is a factor that converts scale thickness to weight gain, m is a positive number which depends on the mechanical properties of the scale, and β is a constant which is dependent upon the strength of adhesion at the alloy/scale interface. Equation (2.87) shows that the fraction of scale spallation increases with a thicker oxide scale, larger temperature drop, and weaker scale adhesion at the alloy/scale interface.

Equation (2.87) provides a semi-quantitative description of scale spallation; however, it should be realized that there are many factors that affect the cyclic oxidation behavior of an alloy, including alloy composition and thermal cycling schedule. The oxidative effects of minority elements in the alloy were discussed in Section 2.2.5.3. The following part discusses in more detail the effect of thermal cycling schedule.

Thermal-cycling schedule can greatly affect the extent and even mode of scale spallation. The main parameters include cycle frequency and cooling rate. The effect of cycle frequency on oxidation behavior is complex and depends on the scale adherence, the type of defects controlling spallation, the total test time, and the test temperature [131]. Because an oxide scale has a lower coefficient of thermal expansion (CTE) than the alloy matrix on which it forms, thermal stresses are induced during temperature variation. However, scale defects, which can increase spallation, may develop during each cycle. Thus, the change of cycle frequency could yield a positive or negative effect on the extent of scale spallation. For example, decreasing the cycle frequency could decrease the induced thermal stresses, which is beneficial to scale spallation resistance; however, because a decrease in the cycle

frequency could correspond to a longer hold time at high temperature, the scale would be thicken and may have time to develop defects, thus resulting in a larger amount of spallation. However, the more expected result is that scale damage and, hence, extent of spallation should increase with increasing cycle frequency. Figure 2.33 shows the effect of cycle duration Δt on mass change curves generated by COSP [145]. It is seen that decrease of cycle duration, which corresponds to increase of cycling frequency, resulted in larger mass loss.
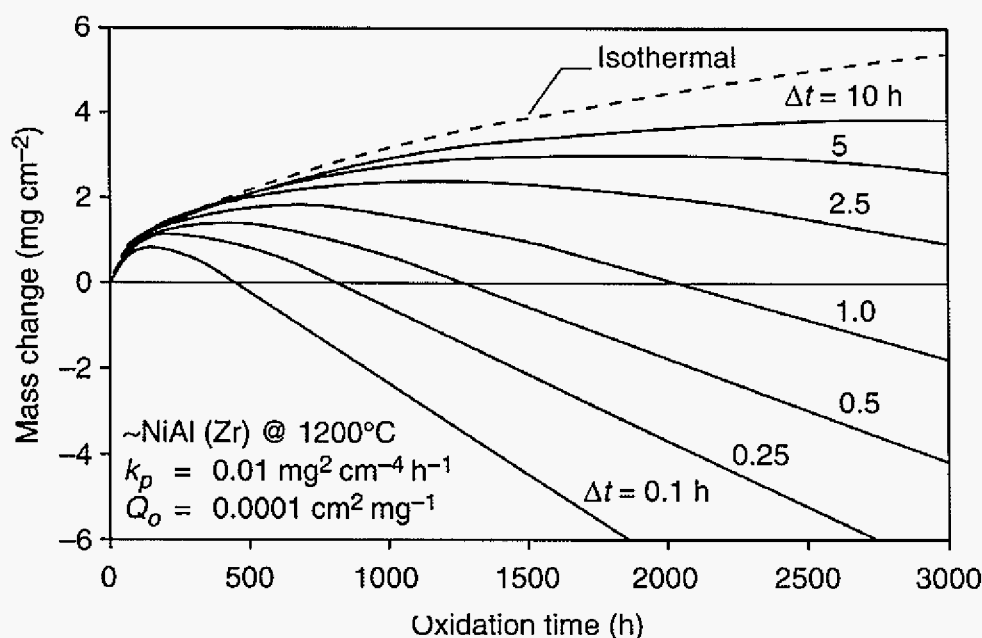
Figure 2.33. The effect of cycle duration Δt on mass change curves.

It had been widely assumed that a higher cooling rate should induce greater thermal stress from a thermal shock component, but Smialek and Lowell *et al.* [145,146] reported that a higher cooling rate actually decreases the mass loss rate and extent of scale spallation. Rather than inducing a thermal gradient in thin scales, fast cooling by water quenching was found to induce large thermal gradients in the metal subsurface. This resulted in the contraction of the outer subsurface layer, which was opposed by the inner core, causing a tensile deformation of the metal surface. Thus, the scale is deformed along with the metal surface and may actually form cracks normal to the surface. This situation provides much more resistance to scale spallation than intact scales subject to high compressive stresses.

2.3 Commercial High-Temperature Alloys

2.3.1 Introduction

High temperature materials have additional design constraints in comparison with those materials which are used at or near room temperature. There are three important constraints for the design of high-temperature alloys: creep; thermal stability of microstructure; and high-temperature corrosion resistance. Other factors that often must be considered include cost, mechanical properties, machinability, fabricability, and weldability. Thus, the design of high-temperature alloys is more complicated than what may be inferred from the precious sections of this chapter. For example, for model iron- or nickel-base binary alloys, an alumina or silica scale forms at approximately 15 wt.% Al or 5 wt.% Si respectively. But these levels of aluminum and silicon result in brittle alloys that would have limited use for practical applications [147]. Commercial alloys used at high temperatures include stainless steels, the Fe-, Ni-, and Co-base superalloys, and various metallic coating compositions. The Fe-base superalloys are an extension of stainless steel technology and generally are wrought, whereas Ni-base superalloys may be wrought or cast depending upon the application/composition involved. The current study focuses on wrought iron- and nickel-base commercial superalloys.

Fe- and Ni-base superalloys can be strengthened by the following mechanisms: solid-solution strengthening, precipitation hardening and oxide-dispersion strengthening [148]. The Fe-base alloys can be strengthened the least and Ni-base alloys the most. Figure 2.34 shows the stress-rupture strength as a function of temperature for various alloy systems [149]. It is seen that the high-temperature strength increases with increase of alloying elements. For example, carbon steels do not have strength above about 500 °C, while Ni-base alloys have high strength almost above 1000 °C.
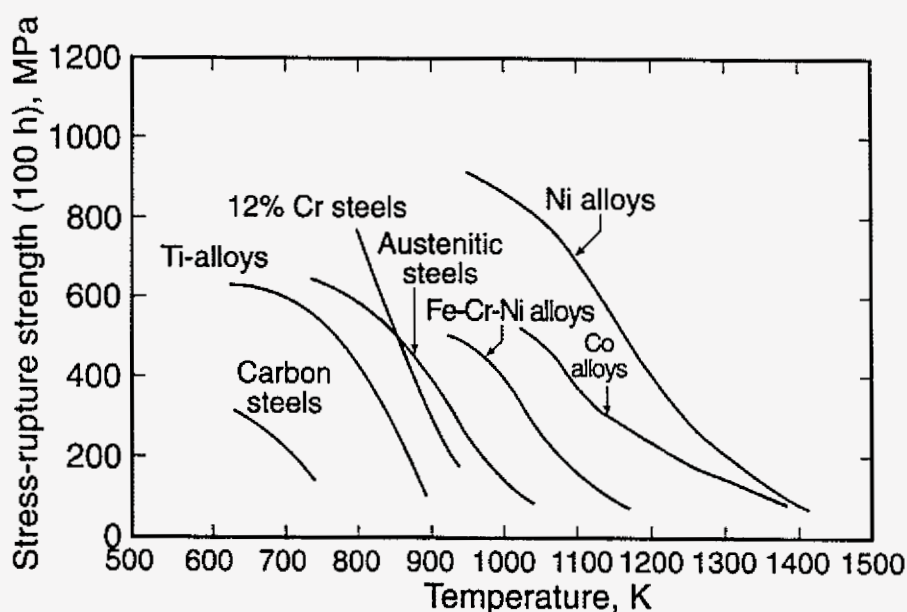
Figure 2.34. Stress to produce creep-rupture in 100h for various alloys.

Superalloys consist of the austenitic face-centered-cubic (FCC) matrix phase gamma (γ) plus a variety of secondary phases. The principal secondary phases are the carbides MC, $M_{23}C_6$, M_6C and M_7C_3 (rare) in all superalloy types and the gamma prime (γ') FCC ordered $Ni_3(Al,Ti)$ intermetallic compound in Ni- and Fe-Ni-base alloys. Table 2.5 gives a generalized list of alloying elements and their effects in superalloys [148].

Table 2.5. Main alloying elements and their effects in superalloys [148].

Element	Range (wt.%)	Effects
Ni	>30	Stabilizes austenite; forms hardening precipitates
Cr	5-25	Oxidation and corrosion resistance; carbides; solid solution hardening
Co	0-20	Affects amount of precipitates
Al	0-6	Precipitation hardening; oxidation resistance
Ti	0-6	Precipitation hardening; carbides
Mo, W	0-12	Carbides; solid solution hardening

In order to obtain optimal performance, such as mechanical properties and high-temperature corrosion resistance, one of characteristics of commercial superalloys is multiple alloying additions, such as Al, Mn, Ti, Si, Mo, B, and one or more rare-earth (RE) metals. The presence of multiple elements in the alloy complicates high-temperature oxidation behavior. The following section will discuss the composition of commercial superalloys and the oxidation behavior of these alloys.

2.3.2 Metallurgy of Commercial High-Temperature Alloys

Iron-base superalloys are nominally defined as those alloys that have iron as the major constituent and that are hardened by a carbide or intermetallic precipitate [150]. In general, iron-base alloys are used at the lower end of the temperature range of superalloy use because they rapidly decline in strength above about 650 °C [151]. Iron-base alloys are typically strengthened by precipitation hardening and have Fe, Ni, and Cr as the main elements, together with minor additions of Mo, Si, Ti, and Al. The most important class of Fe-base superalloys includes those alloys that are strengthened by intermetallic compound precipitation in the FCC matrix, such as V-57 (15Cr-27Ni-48Fe-3Ti-1Mo). Other Fe-base superalloys consist of modified stainless steels primarily strengthened by solid solution hardening, such as the 800 series of alloys (e.g., 21Cr-32Ni-46Ni-0.38Al-0.38Ti for the 800H alloy, in which Al and Ti yield some γ' precipitates).

Nickel-base alloys generally have greater high-temperature degradation than low-alloy steels and stainless steels. Nickel-base alloys contain 30-75 wt.% Ni and up to 30 wt.% Cr. Because of the high solubility of chromium in austenitic alloys, these commercial alloys have been developed without melting and processing difficulties. Excessive amount of chromium tends to promote embrittling intermetallic phases, such as sigma phase or even alpha-chromium ferrite. Iron contents range from a relatively small amount in most alloys to about 35 wt.% in an alloy such as Incoloy 901 [150]. Many Ni-base alloys contain small amounts of aluminum, titanium, niobium, molybdenum, and tungsten to enhance either strength or corrosion resistance. The combination of nickel and chromium gives these alloys outstanding oxidation resistance. Nickel-base alloys exceed stainless steels in mechanical strength,

especially at temperatures above 650 °C (Fig. 2.30). Thus, Ni-base alloys are widely used in high-temperature conditions requiring high strength or resistance to oxidation and corrosion.

Most Ni-base superalloys consist of two major phases: the FCC γ- matrix and the $Ni_3(Al,Ti)$-based γ' precipitate phase [152]. Ni-base superalloys can be highly strengthened through the precipitation of γ'-$Ni_3(Al,Ti)$. This phase has an ordered, $L1_2$ crystal structure (*i.e.*, FCC with Ni occupying the face-centered positions and Al and/or Ti the corner positions) and exhibits increase in strength with increase in temperature up to about 800-900 °C, depending on composition [153]. The γ' precipitates, which are stable typically at temperatures below about 930-1040 °C, are generally cuboidal in morphology as a consequence of being either coherent or semicoherent with the γ matrix [1]. About 5-20% cobalt is often added to increase the solvus temperature at which γ' starts to dissolve on heating. Further, the chromium content is reduced to 5-15% in order to increase the Al+Ti solubility in the γ-Ni matrix at the solutionizing heat-treating temperature.

As the superalloys become highly alloyed with refractory elements (W, Re, Mo, and Ru) to achieve better strengths, so-called topological closed packed (TCP) phases often appear [152]. The TCP phases include sigma (σ), mu (μ), P, and Laves, which can be detrimental to mechanical properties. In superalloys containing a high concentration of Ti or Nb, either eta (η) or delta (δ) phases may form. Both η and δ can be detrimental to the properties of superalloys since they form at the expense of the γ' phase, and they can limit ductility. Sometimes, the formation of carbides (MC, $M_{23}C_6$, and M_6C) and/or borides (M_3B_2 and M_5B_3) are promoted to strengthen the grain boundaries of superalloys [154].

The phases in Ni-base superalloys can strongly depend upon their product form and thermal history as well as their chemistry [152]. Wrought superalloys generally have less γ' phase and undergo deformation processing such as forgoing or rolling to arrive at a final product. Wrought superalloys generally can start with either a cast or an extruded power metallurgy (P/M) billet. The P/M superalloys typically have a more uniform spatial distribution of phases, which results from their better composition homogeneity duo to their much faster solidification rates.

2.3.3 Oxidation of Commercial High-Temperature Alloys

As described above, commercial alloys have multiple alloying elements in order to obtain optimum mechanical properties. Those additions make the oxidation behavior of commercial alloys more complex. This increased complexity is usually reflected in complex reaction mechanisms, where mixtures of the features discussed for oxidation of pure metals and simpler binary alloys are observed.

2.3.3.1 Aspects of High-Temperature Oxidation of Commercial Superalloys

The oxidation resistance of a given superalloy is primarily obtained from the formation of an alumina or chromia scale. For chromia-forming superalloys, that contain additions of Al, Si, and Ti, internal oxides of Al, Si, and Ti may form when chromia scale is established. The sequence of those internal oxides from scale to matrix would be in SiO_2, TiO_2, and Al_2O_3 according to their thermodynamic stabilities and assuming $a_{Si} = a_{Ti} = a_{Al}$. Figure 2.35 shows the internal oxides in an 800HT alloy oxidized after 6 180-day cycles at 982 °C [109]. The cross-sectional SEM image shows that the alloy underwent a considerable amount of internal oxidation which was primarily intergranular in form. X-ray and EDS analyses showed that outer scale region consisted of $MnCr_2O_4$ and the scale was primarily Cr_2O_3. Near the alloy/scale interface, the precipitates were typically rich in titanium while, deeper into the alloy, they were rich in aluminum.
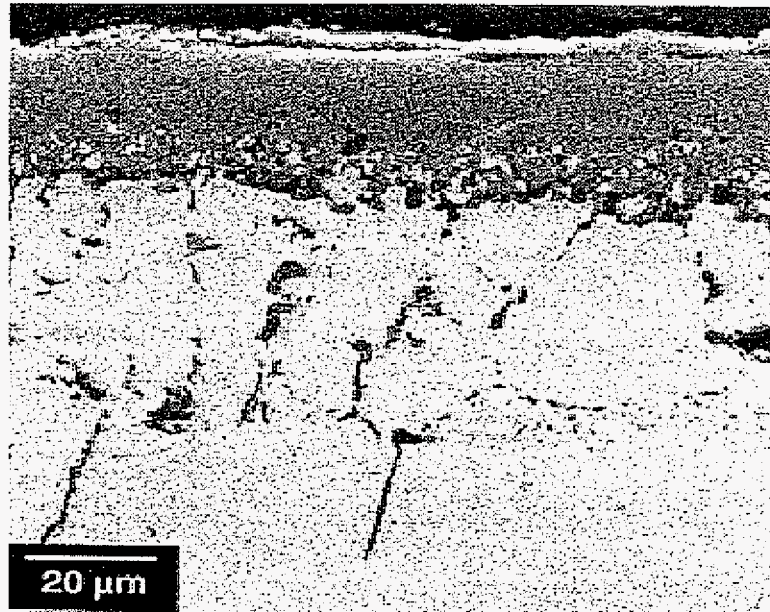
Figure 2.35. Cross-section SEM image of Incoloy 800HT alloy oxidized
after 6 180-day cycles at 982 °C.

Wlodek [155] studied the alloy Renè 41, which is a commercial nickel-base alloy. Rene-41 contains approximately 19 % Cr, 11% Co, 10% Mo, 3.1% Ti, 1.5% Al and 0.7% Fe, and minor additions of silicon, manganese, boron, carbon and sulphur. Figure 2.36 shows the main reaction products in oxidation of the alloy in air at 870-1150 °C. The phases shown in the numerators represent the scale constitutes, and those in the denominators represent the internal oxidation reaction products. It is seen that the oxidation products change with temperature and the elapsed time of reaction.
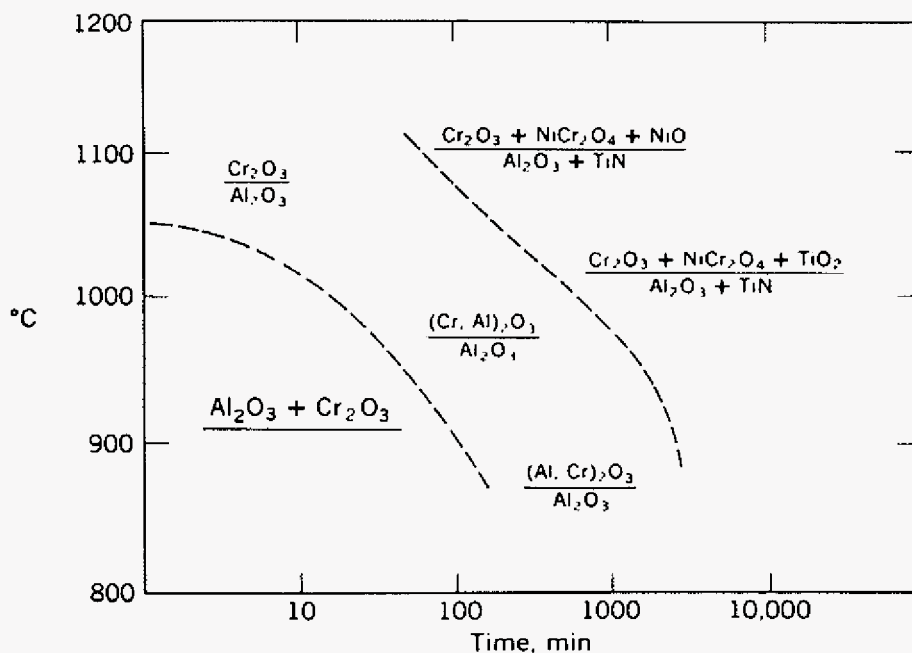
Figure 2.36. Schematic representation of the main reaction products

formed in air oxidation at 870-1100 °C of Renè 41.

Minor additions in the alloys not only develop oxidation products, but affect the diffusion behavior of chromium in alloys. Harper and Walker [156] studied chromium depletion for several commercial alloys oxidized in air at 1050 °C for 30 day. 800HT alloy contains 31.4% Ni, 45.5 % Fe, 20.1% Cr, 0.94% Mn, 0.12% Si, 0.4 Al, and 0.4 Ti, while DS alloy has 34.6% Ni, 42.8% Fe, 18.1% Cr, 1.08% Mn, and 2.515 Si. Figure 2.37 shows the resulting chromium depletion profiles in 800HT and DS alloys. According to the depletion profiles, the calculated average effective interdiffusion coefficient for Cr in 800HT and DS alloys are 2.2×10^{-11} and 1.6×10^{-10} cm²/s, respectively. Thus, DS alloy showed deeper Cr depletion profile and about one order larger interdiffusion coefficient than 800HT. This significant difference is apparently attributable to the relatively high silicon content in DS alloy.
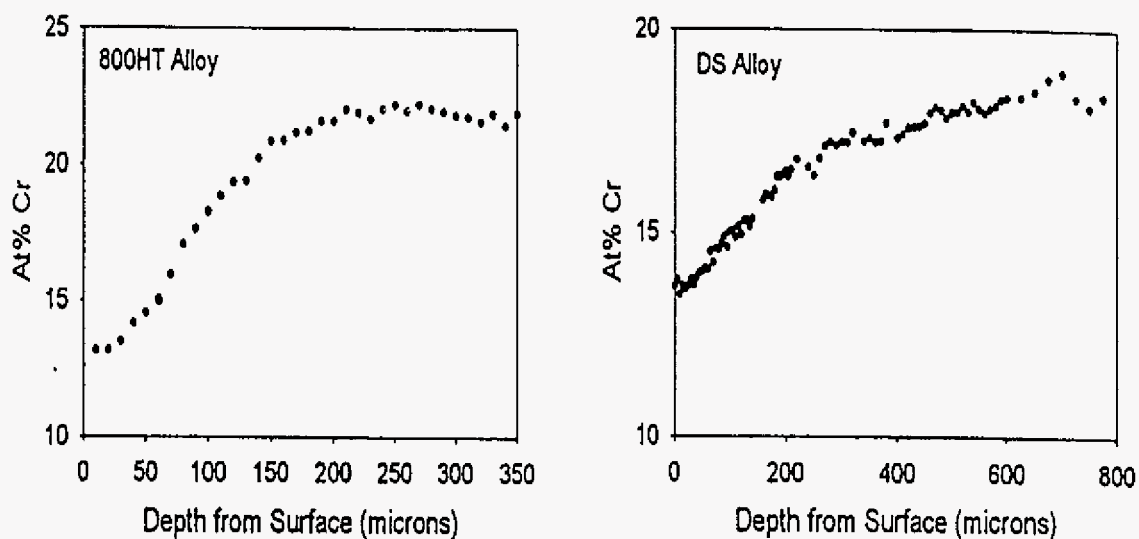
Figure 2.37. Cr concentration profiles for 800HT and DS alloys
after isothermal oxidation in air at 1050 °C for 720 hours.

2.3.3.2 Oxidation of Fe-Based Commercial Superalloys

The oxidation behavior of these alloys is relatable directly to that of ternary Fe-Ni-Cr
alloys [151]. Oxidation is generally parabolic to form Cr_2O_3 scales, with an outer layer of
iron and nickel oxides formed during the initial stages, in amounts depending on the
homogeneity of the alloy surface layer and the rapidity with which a complete Cr_2O_3 layer is
formed [157].

In Fe-Cr alloys, it appears that a minimum of approximately 18 wt.% chromium is needed
to develop a continuous Cr_2O_3 scale against further oxidation attack [158]. When the service
temperature is above 640 °C, nickel is added to Fe-Cr alloys to stabilize the FCC austenitic
structure and thus obtain higher creep strengths. Nickel improves the resistance of alloys to
cyclic oxidation [1]. Figure 2.38 illustrated that the scaling resistance of several high-Ni
alloys was better than that of austenitic stainless steels when cycled to 980 °C in air [159].
Brasunas *et al.* [160] studied the oxidation behavior of about 80 experimental Fe-Cr-Ni
alloys exposed to an air-H_2O mixture at 870 to 1200 °C for 100 and 1000 hours. They

observed that increases in Ni in excess of 10% in alloys containing 11 to 36% Cr improve the oxidation resistance of the alloys.
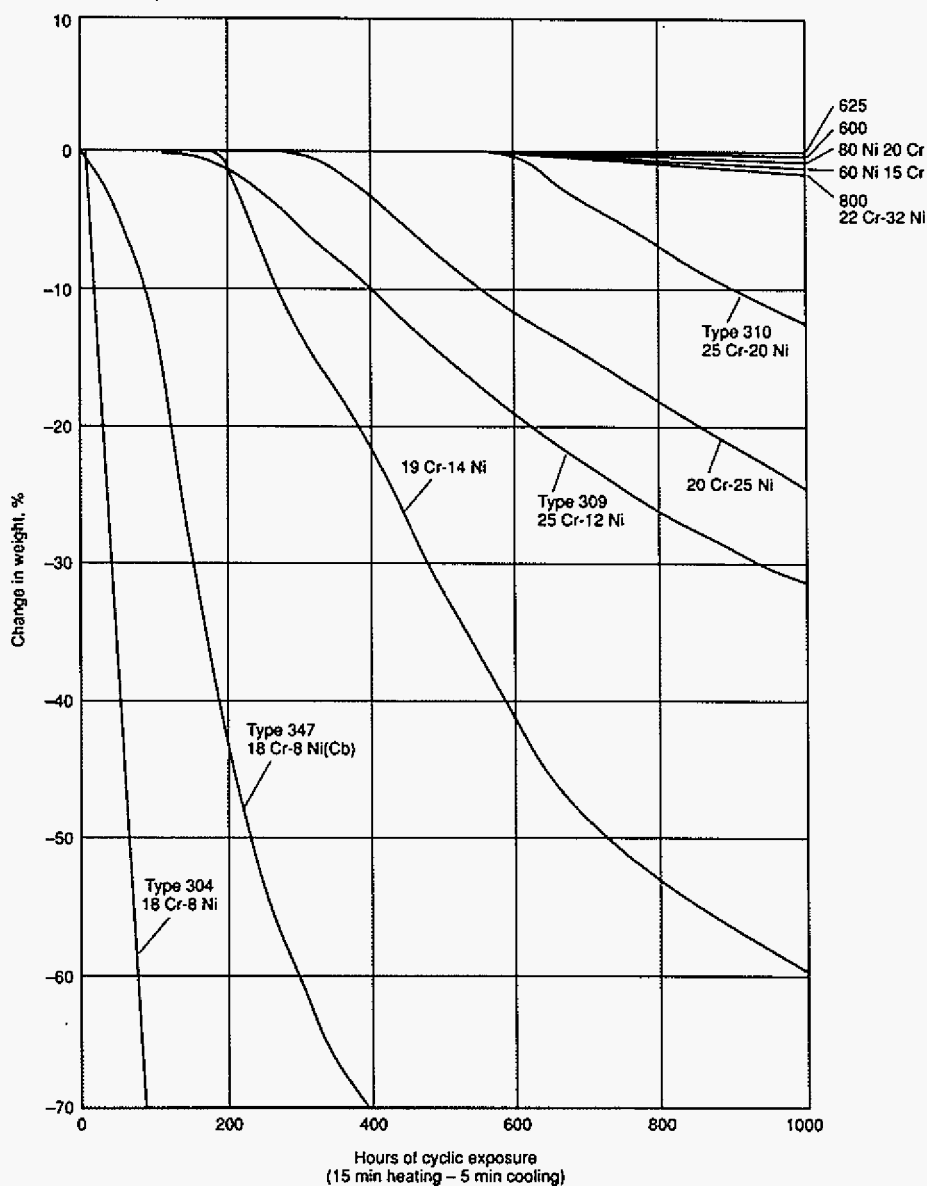
Figure 2.38. Cyclic oxidation resistance of several stainless steels and Ni-base alloys in air at 980 °C.

Aluminum and silicon are found to be beneficial to the spallation resistance of a chromia scale [115,141,142,161]. For instance, it was inferred that the 18SR stainless steel (18% Cr)

was as good as, and sometimes better than the Type 446 (27% Cr) stainless steel due to the presence of 2% Al and 1% Si in the former [162].

Haynes 556 alloy (Fe-22Cr-20Ni-18Co-3Mo-2.5W-0.6Ta-0.02La) has significantly better oxidation resistance than Multimet alloy N-155 (Fe-21Cr-20Ni-20Co-3Mo-2.5W-1.0(Cb+Ta)) even though these two alloys have similar chemical compositions [163]. Alloy 556 was developed by making small changes to minor alloying element contents in alloy N-155. Specifically, the improved oxidation resistance resulted from replacement of niobium with tantalum, as well as the controlled addition of reactive elements, such as lanthanum and aluminum. Irving *et al.* [164] also found that tantalum is beneficial and niobium is detrimental to the oxidation resistance of a Co-20Cr-base alloy.

For Fe-Cr alloys with chromium contents below 18 wt.%, a protective Cr_2O_3 layer will initially be able to form, but will relatively shortly undergo "break-away" oxidation, with the production of alternate layers of iron-rich and chromium-rich scales [5,67,151]. Figure 2.39 shows the oxidation kinetics associated with break-away behavior. After an initial period of protective behavior (region OW), rapid break-away oxidation (WX) occurs, which may continue until the specimen is consumed (XY), or healing takes place (XZ). Breakaway oxidation occurs after scale breakdown, where bare, chromium-depleted metal underneath the scale is exposed to the oxidizing environment, causing an immediate increase in oxidation rate.
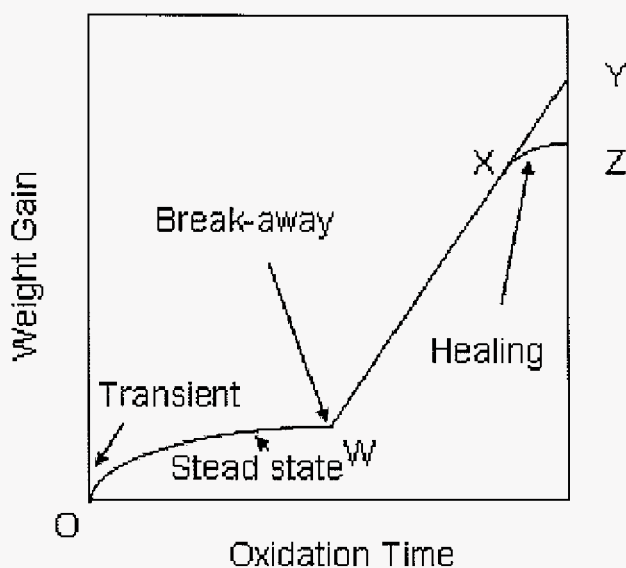
Figure 2.39. Schematic oxidation rate curve showing breakaway behavior.

2.3.3.3 Oxidation of Ni-Based Commercial Superalloys

As the nickel content in the Fe-Ni-Cr system increases from austenitic stainless steels to Fe-base supperalloys, and finally to Ni-base alloys, the alloys become more stable in terms of metallurgical structure, and more resistant to creep deformation as well. The alloys also become more resistance to scaling as nickel content increases. Though not clearly established, the beneficial effects of nickel may involve in beneficially influencing scale adhesion and mechanical properties, reducing the rate of chromium diffusion in the Cr_2O_3 scale, and retarding the breakthrough transformation, Cr_2O_3 to $FeCr_2O_4 + Fe_2O_3$ [165,166].

In general the oxidation behavior of Ni-base alloys is analogous to that of the equivalent Ni-Cr binary alloys, with 20 to 25 percent chromium content required in order for a Cr_2O_3 healing layer to be able to form [151]. Some reduction in chromium content may be possible when elements known to promote Cr_2O_3 formation are present, such as aluminum and silicon, but in some cases any such benefits would be negated by alloy in-homogeneity at the surface. Reduced grain size and/or the presence of a small amount of reactive elements in the alloys tends to promote Cr_2O_3 scale formation, although other oxides may also be present

[167,168]. The reactive element and grain boundaries may act as finely dispersed nucleation sites and thus particles of Cr_2O_3 are uniformly nucleated across the surface. These nuclei then rapidly coalesce to form a continuous layer [168].

It has been reported that the oxidation of Ni-20Cr generally leads to the formation of a steady-state oxide scale consisting of an NiO outer layer, an inner layer of NiO containing particles of Cr_2O_3, and a basal layer of either $NiCr_2O_4$ or Cr_2O_3 [65,169,170]. These steady-state scales are reported to form following several transient stages. Initially nuclei of all the possible oxides, NiO, Cr_2O_3, and possibly $NiCr_2O_4$, form on the alloy surface. Chromia is reported to form mainly where the metal grain boundaries intersect the surface, while NiO is more prominent elsewhere. It is thought that NiO then overgrows the other oxides producing an external NiO layer that incorporates Cr_2O_3 particles. The formation of chromia where the metal grain boundaries intersect the surface is thought to be due to the more rapid grain-boundary diffusion of Cr atoms [171,172]. At longer oxidation times, oxygen partial pressure at the alloy/scale interface decreases and the growth of NiO slows. Thus, a continuous chromia layer would be established along the scale-alloy interface as the Cr_2O_3 particles coalesce.

Aluminum and silicon also affect the nature and morphology of the oxide scales [137]. Aluminum is very effective in improving alloy oxidation resistance [2]. As temperature increases, the amount of aluminum needed in the alloy to resist cyclic oxidation also increases. With only about 1.4 % Al, alloy 601 (Ni-23Cr-14.4Fe-1.4Al-0.1C) forms a Cr_2O_3 scale when heated to elevated temperatures [2]. The Cr_2O_3 oxide begins to convert to volatile CrO_3 as the temperature exceeds about 1000 C, thus losing its protective capability against oxidation attack [173]. Alloy 214 (Ni-16Cr-4.5Al-3Fe-0.1Y), with about 4.5% Al, on the other hand, forms an Al_2O_3 scale that is significantly more protective.

The silicon content in high-temperature alloys is usually limited to less than 3% because of mechanical, weldability, and thermal-stability constraints. For most wrought alloys, the silicon content is kept below about 1.0% [165]. Low silicon contents less than 1% may or may not be sufficient to form a continuous SiO_2 layer at the alloy/scale interface, but are sufficient to have a beneficial effect on oxidation kinetics, especially by facilitating exclusive Cr_2O_3 scale formation [100,114,174]. Ahmad and Fox [175] studied the transient oxidation

behavior of a Ni-20Cr alloy and suggested that the beneficial effect of silicon (and aluminum) is established at room temperature by the formation of a thin passive oxide film rich in silicon and aluminum (3 nm). It is possible that upon initial heating, the presence of the thin passive oxide layer causes the outward flux of chromium to be significantly greater than the inward flux of oxygen to the extent that the initial nucleation of Cr_2O_3 occurs primarily at the alloy surface, thus helping to facilitate Cr_2O_3-scale formation [165].

CHAPTER 3 EXPERIMENTAL PROCEDURES

3.1 Alloys Studied and Sample Preparation

The alloys studied were supplied by three commercial companies – Special Metals Corporation, Haynes International and Krupp VDM GmbH. All of the alloys were wrought and in plate form. Table 3.1 gives the density and coefficient of thermal expansion (CTE) of the alloys studied, together with their as-received thickness. The measured chemical compositions of the alloys were provided by the alloy producers and are summarized in Table 3.2.

Table 3. 1. Properties and as-received thickness of the alloys studied.

Alloys	UNS	Thickness (mm)	Density (g/cm^3)	CTE (10^{-6}/°C)	Producer
Incoloy 800 (800)[a]	N08800	1.0	7.95	18.4 (RT-871 °C)	Special Metals
Incoloy 800HT (800HT)[a]	N08811	3.0	7.95	18.4 (RT-871 °C)	Special Metals
Inconel 601 (601)[a]	N06601	2.0	8.1	14.6 (20-300 °C)	Special Metals
Inconel 617 (617)[a]	N06617	3.0	8.2	13.4 (20-300 °C)	Special Metals
Hastelloy X (X)[a]	N06002	1.5	8.22	16.6 (RT-1000 °C)	Haynes
Haynes HR-160 (HR-160)*	N12160	1.5	8.8	17.1 (RT-982°C)	Haynes
Haynes D-205 (D-205)[a]		0.8	8.03	16.6 (RT-982 °C)	Haynes
Haynes 230 (230)[a]	N06230	1.5	8.97	16.1 (RT-1000 °C)	Haynes
Haynes 214 (214)[a]	N07214	1.5	8.05	18.6 (RT-1000 °C)	Haynes
Nicrofer 3220H (VDM800)[a]	N08800	5.0	8.0	15.8 (20-300 °C)	Krupp VDM
Nicrofer 3220HT (VDM800HT)[a]	N08811	5.0	8.0	15.8 (20-300 °C)	Krupp VDM
Nicrofer 45TM (45TM)[a]	N06045	2.0	8.0	14.9 (20-300 °C)	Krupp VDM
Nicrofer 4722Co (4722Co)[a]	N06002	3.0	8.3	14.3 (20-300 °C)	Krupp VDM
VDM 6025HT (602CA)[a]	N06025	3.0	7.9	17.5 (20-1000 °C)	Krupp VDM

Note: [a] alloy abbreviation that will be used in this thesis.

Table 3.2. Measured chemical composition of the alloys studied

Alloys	Composition (wt.%)															Others	
	C	Mn	Si	S	P	Cr	Ni	Mo	Fe	Ti	Al	Co	W	Cu	B		
601 (Inconel 601)	0.03	0.26	0.19	< 0.001	0.007	21.86	60.73	0.37	15.49	0.41	1.32	0.06		0.12	0.002	Mg:<0.01 Ta:<0.01	Zr:<0.1 Nb:0.18
617 (Inconel 617)	0.08	0.06	0.09	< 0.001	0.003	21.73	53.16	9.79	1.09	0.35	1.11	12.5		0.04	0.003	Ta< 0.01	Nb 0.09
X (Hastelloy X)	0.1	0.5	0.35			22.0	46.5	9.0	18.8		0.12	1.5	0.6		0.005		
HR-160	0.05	0.59	2.75			28.8	38.5	<1	0.4	0.5	0.03	28	<1			Nb 1	
230	0.1	0.6	0.45			22.5	63.0	2	1.7		0.35	<5	14		< 0.015	La 0.02	
602CA	0.179			0.003	0.008	25.3	62		9.65	0.18	2.13					Y 0.07	Zr 0.08
214	0.043	0.18	0.04			16.22	74.5		3.68	0.39	4.79					Y 0.006	Zr 0.016
D-205	< 0.03	0.18	5.3			19.5	64.0	2.5	6.6		0.13			2			
800HT (Incoloy 800HT)	0.07	0.79	0.15	< 0.001	0.015	19.96	33.59	0.27	44.19	0.55	0.46	0.06		0.24		Nb 0.05	
800 (Incoloy 800)	0.02	0.78	0.13	0.002	0.014	20.05	33.64	0.26	44.46	0.41	0.30	0.06		0.21		Nb 0.01	
VDM 800HT (Nicrofer 3220HT)	0.075	0.70	0.37	0.002	0.012	20.20	30.35		46.80	0.49	0.58			0.16			
VDM 800 (Nicrofer 3220H)	0.061	0.70	0.38	0.002		20.50	30.30		47.15	0.32	0.25			0.07			
45TM (Nicrofer 45TM)	0.080	0.36	2.66	0.002	0.014	27.40	46.35		22.65					0.05		Se 0.07	
4722Co (Nicrofer 4722Co)	0.062	0.52	0.5	0.002	0.013	21.95	47.4	9.16	18.30			0.99	0.65				

Oxidation coupons were cut from the alloy plates using a water-cooled abrasive cut-off wheel, to a size of approximately 20 x 15 mm. The thickness of a given sample coupon was not controlled, but was instead in the as-received state of between 0.8-4 mm (depending on the alloy). The coupons were then abraded down to a 600-grit finish using silicon carbide grit paper. After surface preparation, the coupons' weight and dimensions were measured. The accuracies were ±0.01mm for the dimension measurements and ±0.1 mg for the weight measurement. Just prior to oxidation testing, the coupon samples were degreased and then cleaned in acetone and alcohol.

3.2 Oxidation Procedures

3.2.1 Kinetics Calculation

The oxidation kinetics will be presented as weight gain (mg/cm^2) as a function of exposure time. The calculation of weight gain, ΔW, is

$$\Delta W = \frac{W_t - W_i}{A_i} \tag{3.1}$$

where W_t is the weight (mg) of sample after oxidation for some time t, W_i is the initial sample weight (mg), *i.e.*, before oxidation testing, and A_i is the sample surface area (cm^2) before oxidation testing.

3.2.2 Isothermal and Cyclic Oxidation

Cyclic-oxidation testing involved exposing the alloys to still air at 1000 and 1100 °C (within ±3 °C) for 1-day and 7-day periods in a box furnace followed by ambient-air cooling to room temperature. Isothermal oxidation for 1 and 7 days at 1000 °C and 1100 °C were conducted to analyze the phase constitution of the scales and the steady-state chromium profile in the alloys' subsurface. For long-term cyclic oxidation tests, the samples were tested for up to 18 or 125 thermal cycles for 7-days or 1-day cycling, respectively (3000h at temperature). The heating and cooling rates during cyclic oxidation testing were larger than 100 °C/min. The samples for both types of oxidation testing were kept in individual alumina

crucibles (about Φ25×20 mm) during the oxidation process in order to retain any spalled scale and to keep the samples isolated (Figure 3.1). The samples were weighed using an analytical balance and then placed back into the box furnace typically within one hour of cooling.
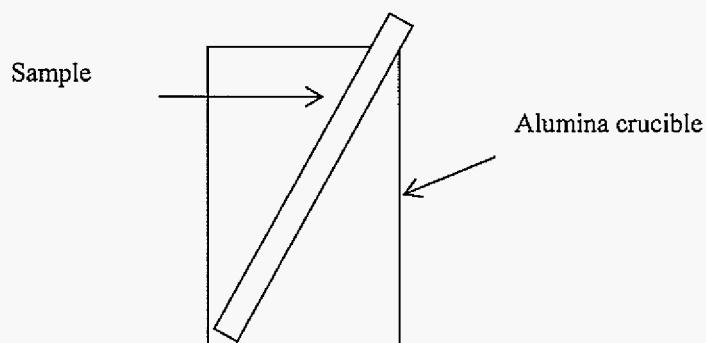
Figure 3.1. Schematic of sample placement for oxidation test.

3.2.3 Thermo-Gravimetric Analysis

Thermo-gravimetric analysis (TGA) was also conducted for all alloys at 1000 °C in air in order to measure the dynamic weight-change behavior during isothermal exposure. Figure 3.2 shows the TGA apparatus (CAHN-131) employed in this study. The TGA unit used has a sensitivity of ±0.001mg and a capacity of 100 g. The coupons are put in a quartz crucible. The apparatus was interfaced to a computer which allowed for continuous weight change measurements to be recorded via a data collecting software. The heating rate was about 100 °C/min and the cooling rate was about -40 °C/min.
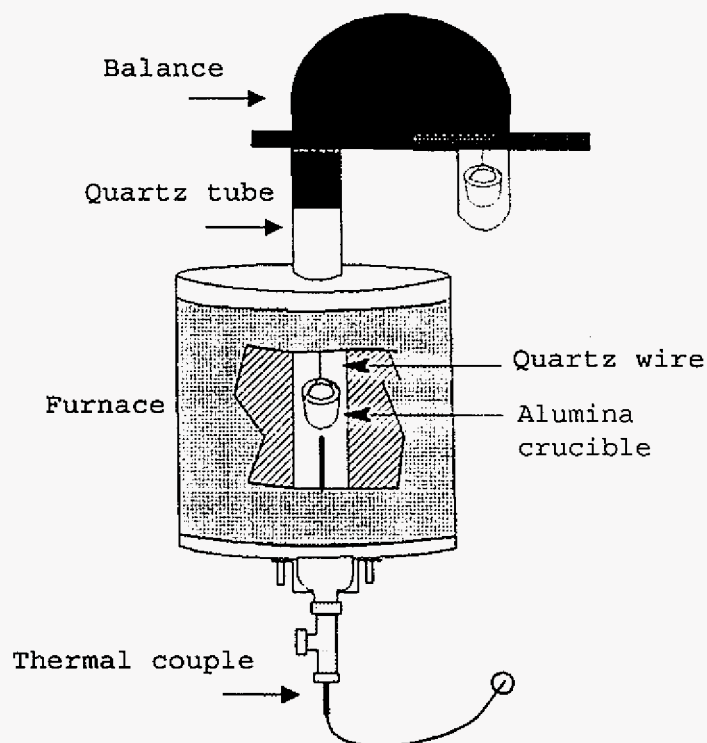
Figure 3.2. Schematic of the CAHN-131 thermo-gravimetric analysis unit used in this study.

3.3 Sample Analyses

At the completion of a given oxidation experiment, the samples were weighed and then stored in a desiccator until further analysis.

Copper K_α X-ray diffraction (XRD) was used as an initial analysis to ascertain the phase constitution of the scales. The samples were typically then mounted and polished using standard metallographic techniques. Optical microscopy and scanning electron microscopy (SEM) with energy dispersive spectrometry (EDS) were used to obtain the cross-sectional images and to help identify the phase constitution of scale and internal oxides. Electron probe microanalysis (EPMA) was used to obtain chromium depletion profiles and the chromium content at the alloy/scale interface.

3.3.1 Mounting, Grinding, and Polishing Procedures of Oxidized Samples

The samples were mounted on their longitudinal axis in cold-setting epoxy resin, which has excellent edge retention and abrasion resistance. The mounts were allowed to set for 12 hours, and then subjected to metallographic grinding and polishing procedures. The mounted samples were ground from 60- to 1200- grit on SiC paper, and then polished with 6 and then 1 μm diamond suspension on Leco Red Felt polishing cloths. The samples were water-washed and turned 90° for each change of grit size. The final polishing used a vibratory machine with a colloidal silica suspension for one hour. The vibratory polishing procedure was not used for samples requiring silicon analysis.

In order to remove and polish residue, samples were ultrasonically cleaned in acetone for 30 seconds and then cleaned in alcohol and dried.

3.3.2 Etching Techniques for Alloy Microstructure Characterization

Different etchants were used to identify the microstructures of the alloys studied. Three common etchants and the procedures used are given below [176].

Etchant 1 (used for the iron-base, 45TM, and D-205 alloys)
1. Immerse and slightly swirl (do not swab) sample in straight HCl acid for about 10 seconds.
2. Removed sample from HCl acid and then immerse and swirl in methanol for about 10 seconds (do not rinse with water between the HCl and methanol).
3. Immerse and swirl in a methanol + 1% Br solution until surface discoloration starts to occur. Exact time will vary depending on alloy, but typically ranges from 5 to 20 seconds.
4. Rinse with water, then methanol, dry with hot air.

Etchant 2 (used for HR-160 alloy)
5 ml HNO_3, 200 ml HCl, and 65 g $FeCl_3$
1. Immerse and swirl samples in alcohol.

   2. Immerse and swirl samples in etchant for 20-30 seconds.

   3. Rinse with water and alcohol, dry with hot air.

Etchant 3 (used for the X, 601,617, 230, 4722C0, 602CA, 214 alloys)

   50 ml H_2O, 150 ml HCl, and 25 g CrO_3

   1. Immerse and swirl samples in alcohol.

   2. Immerse and swirl samples in etchant until surface discoloration starts to occur. The typical time necessary is 10-30 seconds.

   3. Rinse with water and alcohol, dry with hot air.

3.3.3 Optical Microscope Examination

Optical microscopy was used to analyze cross-sectional microstructures of the as-received alloys and the surface regions of the oxidized alloys. A digital camera attached to the microscope was used to obtain digital images. This also allowed for certain quantitative analyses, such as for grain size and internal oxidation depth.

3.3.4 SEM/EDS Analyses

Scanning electron microscopy (SEM) with energy dispersive spectrometry (EDS) was used for the semi-qualitative analysis of the scales and internal oxidation zones. The SEM can take a higher magnification image than an optical microscope and the former provides details of small precipitates and voids. EDS was used to semi-quantitatively analyze internal oxides and oxide scale phases, and to obtain cross-sectional X-ray dot maps. Pure element standards for Ni and Cr were used for semi-quantitative EDS analysis.

3.3.5 EPMA Analyses

Electron probe microanalysis (EPMA) was used to obtain the concentration profiles across the oxidation-affected regions of selected samples. EPMA was also useful in identifying the internal precipitates. Before analysis, the unetched, metallographically

prepared samples were coated with carbon to reduce charging and, hence, increase the accuracy of EPMA. Three alloy/scale interfacial points were selected to obtain the average interfacial chromium content. A spatially long scan with 5 or 10 μm steps, depending upon the extent of oxidation, and two short scans with 1 μm steps were conducted to obtain the chromium depletion profiles from the alloy surface to the matrix.

3.4 Calculation of Effective Interdiffusion Coefficients

The chromium depletion profiles obtained by EPMA were typically not smooth, and any variation or roughness in the Cr profile would increase the error in the calculation of the average effective interdiffusion coefficient of chromium. Thus, the experimental profiles often needed to be fit to polynomial curve, which was obtained by treating Cr contents in some small distance interval (Δx). A C++ program was written to calculate the average effective interdiffusion coefficients (section 2.2.6.1). The input parameters were subsurface composition profile, scan step for Cr profile (Δx) by EPMA, and oxidation time (t). Then, the effective interdiffusion coefficients were determined. Figure 3.3 shows the flow chart for the C++ program, which itself is given in Appendix A. The Cr depletion profile is formatted with Cr contents in distance sequence in a data text file. When running, the program first inquires the Cr profile name and input parameters, t and Δx, and then reads the profile data. If needed, the program will fit the Cr profile to polynomial curve. The program calculates the average interdiffusion coefficient of Cr using equations 2.58, 2.59, and 2.67(b).
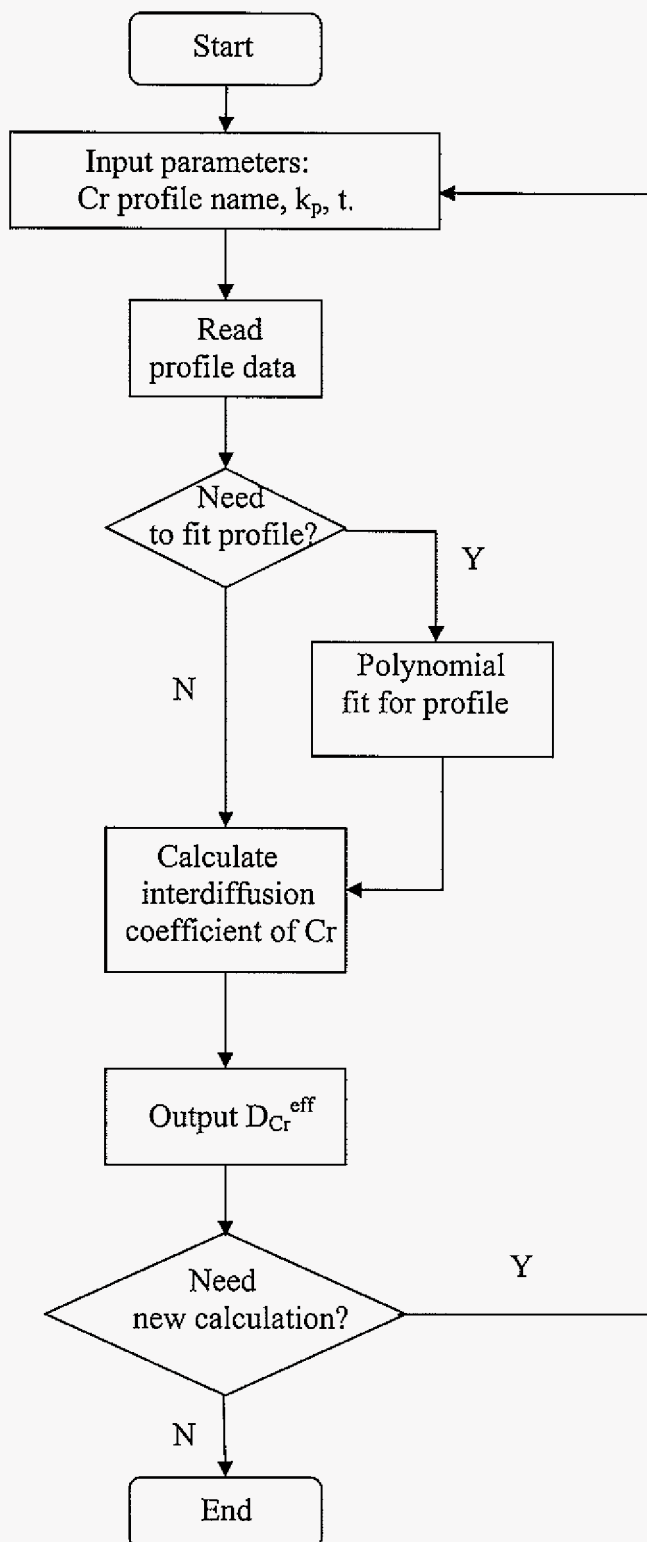
Figure 3.3. Flow chart for the program calculating average effective

interdiffusion coefficient of Cr.

CHAPTER 4 CYCLIC OXIDATION BEHAVIOR OF COMMERCIAL HIGH-TEMPERATURE ALLOYS

4.1 Introduction

As discussed in the previous sections of this thesis, high-temperature alloys need to form a protective external scale to resist high-temperature oxidation. The properties of the external scale determine the extent to which protection can be provided. Ideally, the scale should exhibit a slow growth rate, good adherence to the alloy substrate, a high stability, and be continuous and free of defects such as microcracks or large voids [177]. Typically the scale to meet these requirements for high-temperature oxidation resistance is based on either chromia or alumina, with chromia-forming alloys being extensively used in high-temperature industrial applications [148,178-181]. A scale can exhibit less protective behavior under thermal cycling conditions due to scale cracking and even spallation caused by thermal stresses induced during a thermal cycle. This occurs on account of the scale having a lower coefficient of thermal expansion than the alloy subsurface on which it forms [1].

The oxidation performance of commercial alloys is highly variable and, accordingly, cannot be simply generalized. Oxidation resistance can vary dramatically with, for instance, alloy composition and structure, scale phase constitution, and oxidation conditions (such as temperature, environment, thermal cycling schedule). Thus, it is necessary to examine the behavior of a large number of commercial alloys to obtain a better understanding of the variables affecting oxidation resistance. This chapter analyzes the oxidation behavior of 14 commercial wrought Fe- and Ni-base alloys having different levels of alloying elements. The results will allow for the comparison of base alloying elements such as Cr, Ni, and Fe, and an indication of the oxidative effects of minor alloying elements such as Al, Si, Ti, Mn, and reactive elements.

The commercial wrought alloys studied were chromia- and alumina-formers. 602CA (2.13 wt.% Al) and 214 (4.79 wt.% Al) are considered alumina-forming alloys because their high Al contents ensure formation of a continuous Al_2O_3 scale. All of the other alloys studied are considered chromia-formers because the primary oxide scale formed is Cr_2O_3.

4.2 Experimental Results

4.2.1 Cyclic Oxidation Kinetics

Each of the commercial alloys studied was oxidized in air for 1-day and 7-day cycles at 1000 and 1100 °C. Plots showing the cyclic oxidation kinetics are shown in Figs 4.1-4.6.

Figures 4.1 and 4.2 show the 1-day cyclic oxidation kinetics of the alloys studied up to 125 cycles (about 3000 hours) at 1000 °C. Some alloys, such as 214, 45TM, 602CA, and 230, exhibited small weight change during the test, and consequently can not be easily discerned in the large weight-change scale in the plot in Fig. 4.1. Figure 4.2 re-plots the data in Fig. 4.1, but over a smaller range of weight-change values. From Fig. 4.1, the 800HT alloy is seen to show the most weight-loss, up to around -400 mg/cm^2 after 125 1-day cycles, while from Fig. 4.2 it is seen that 214 and 602CA showed the smallest positive weight change. The latter is indicative of protective and adherent scale formation, while the former is indicative of extensive scale spallation. The only chromia-former to show positive weight-change behavior over the entire testing duration was 45TM. It is seen that the 800 series alloys (800, 800HT, VDM800, and VDM800HT), HR-160, and D-205 exhibited larger weight loss than the other alloys. The 800 series alloys are Fe-based (about 45 wt.% Fe), while HR-160 and D-205 are Ni-based (less than 20 wt.% Fe) but with relatively high silicon contents (about 2.7 and 5.3 wt.%, respectively). Thus, the Fe-based alloys generally showed worse oxidation behavior compared to the Ni-based alloys. The high silicon contents in the alloys D-205 and HR-160 may have played an important role in decreasing their oxidation resistance compared to the other Ni-base alloys.

The Special Metals (SM) 800HT alloy showed breakdown behavior after around 18 1-day cycles during oxidation at 1000 °C, while the VDM800HT alloy showed a similar breakdown behavior after around 95 1-day cycles (Fig. 4.1). The alloys 800HT and VDM800HT have similar compositions, however, the different oxidation resistance of the two alloys indicates that the small differences in the minor-alloying-element contents have a large affect on oxidation behavior. For instance, VDM800HT alloy has a higher Si content (0.37 wt.%) than
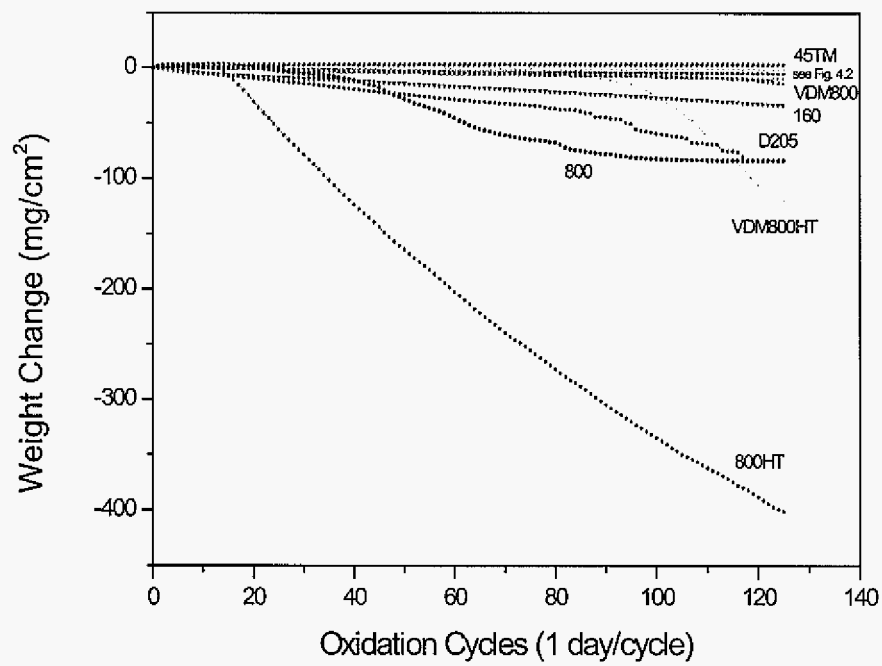
Figure 4.1. 1-day cyclic oxidation kinetics of studied alloys at 1000 °C.
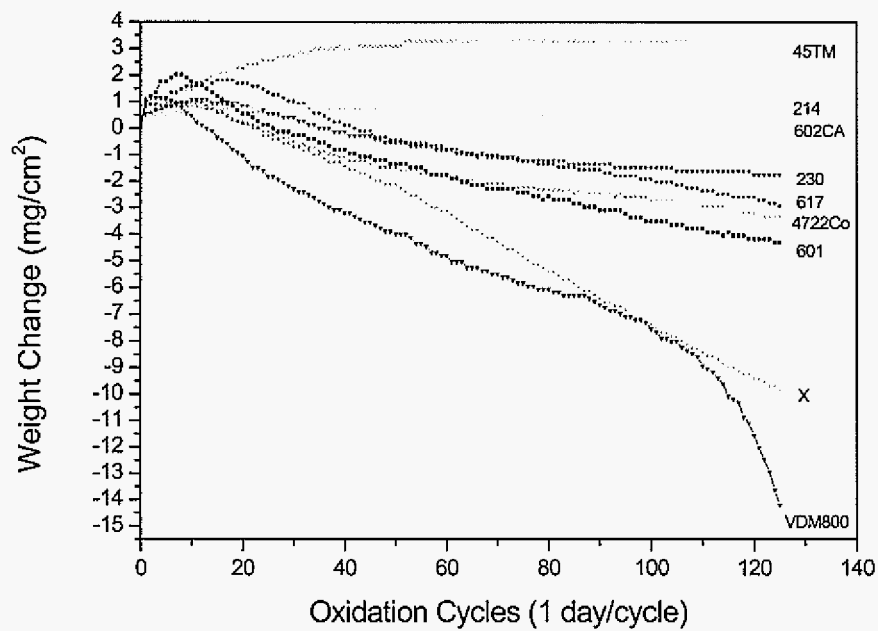
Figure 4.2. More detailed scale showing the lower oxidation kinetics in Figure 4.1.
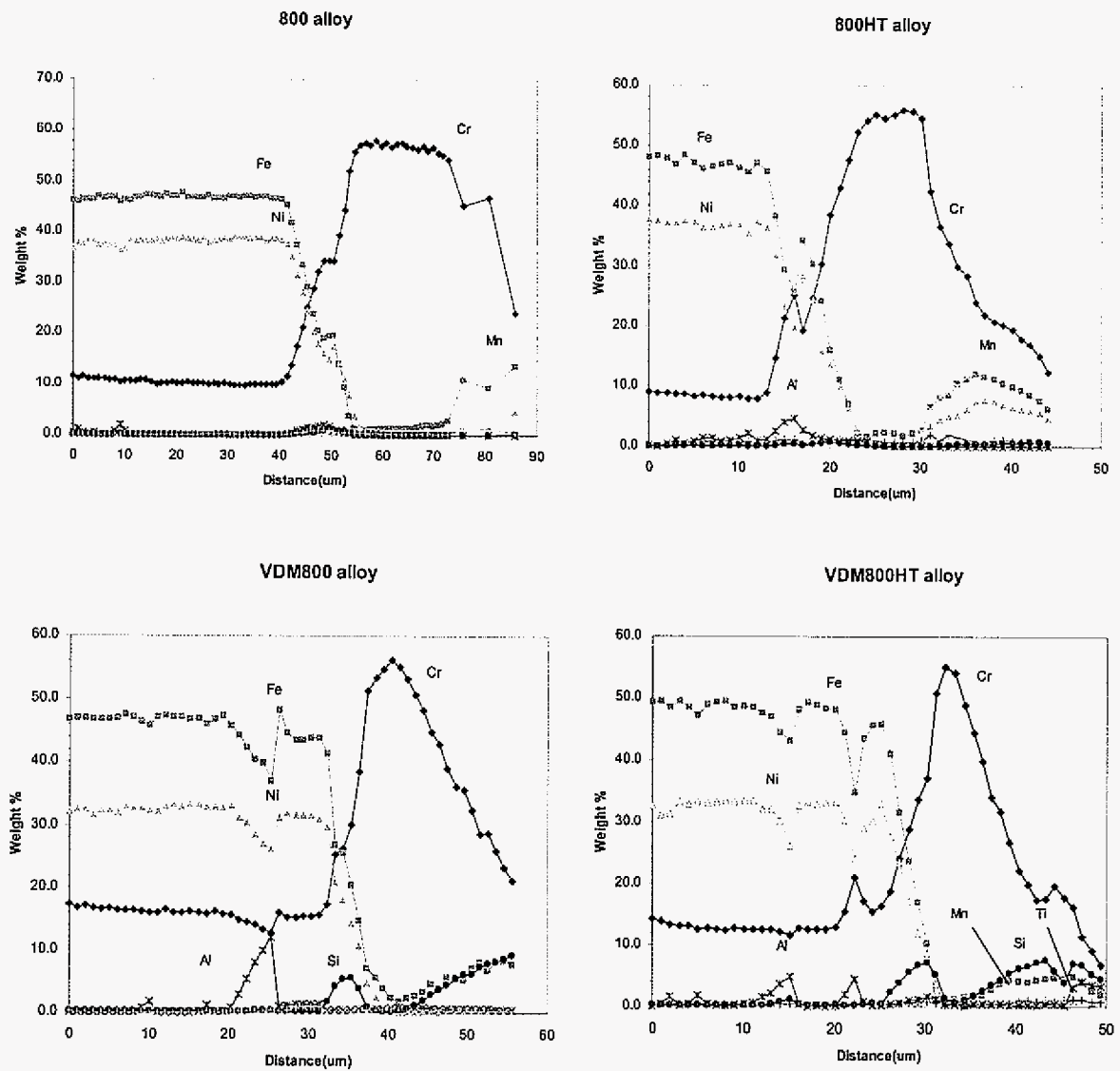
Figure 5.14. Concentration profiles in the four alloys studied after 18 1-day oxidation cycles at 1000 °C. Distance is measured from within the alloy (still within the depletion zone) to the scale surface.
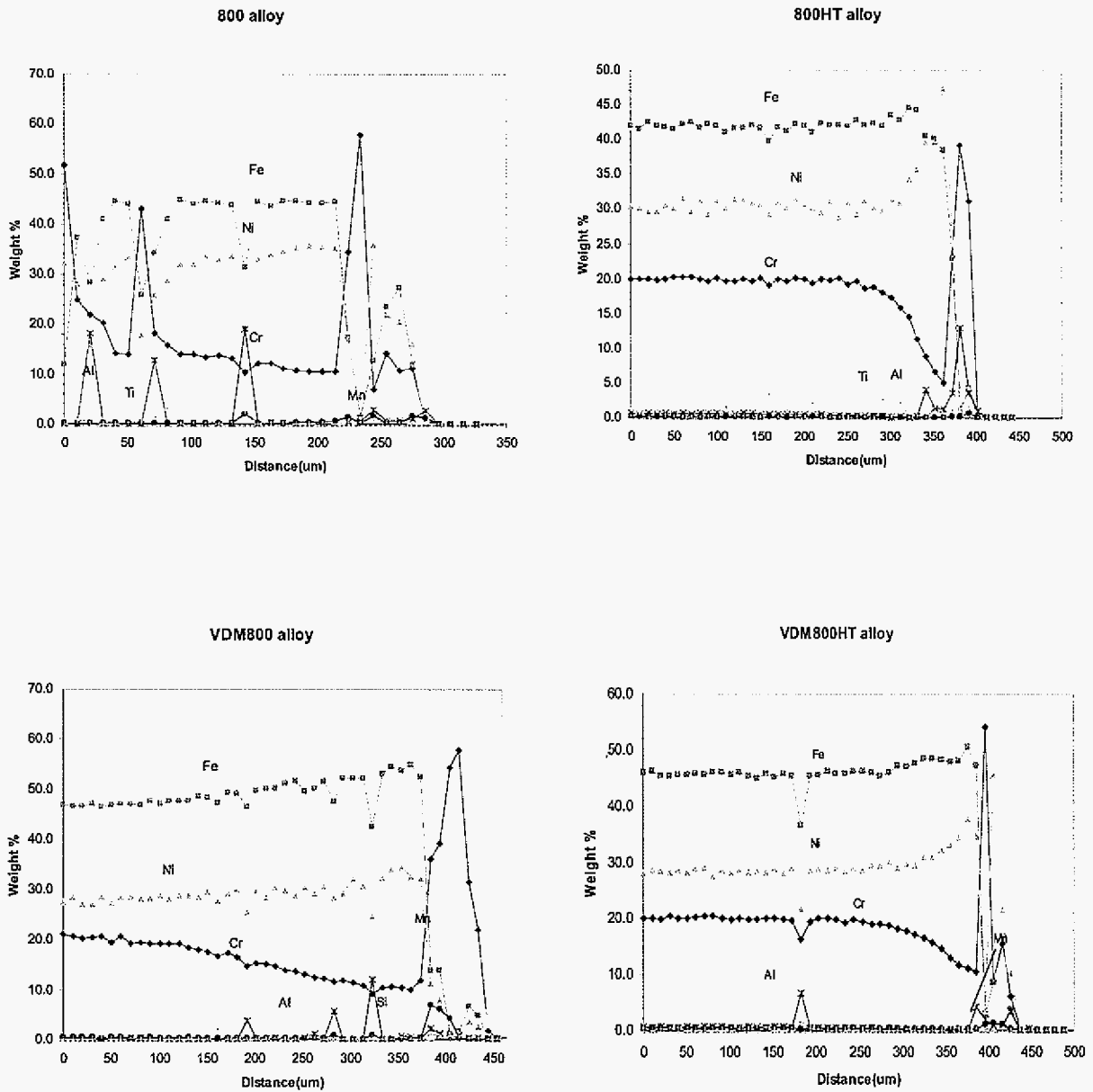
Figure 5.15. Concentration profiles in the four alloys studied after 125 1-day oxidation cycles at 1000 °C. Distance is measured from within the alloy to the scale surface.

alloy/scale interface for 800HT is consistent with its breakdown after 18 1-day oxidation cycles.

A relatively high silicon content was measured in the scales on VDM800 and VDM800HT at the alloy/scale interface after both 18 and 125 cycles, corresponding to the Si-rich oxide being present as an inner layer in the scale. The interfacial enrichment of silicon could not be detected in 800 and 800HT, which is in agreement with the SEM/EDS results. It is also seen in Fig. 5.14 that there was a relatively high aluminum content in the scale at the alloy/scale interface in VDM800, whereas no similar type of enrichment could be found in 800. In the case of VDM800, the Al enrichment is believed to correspond to the Al_2O_3 particles at the alloy/scale interface. It is seen that a relatively large amount of manganese (more than 15 wt. %) was detected in the outer scale formed on 800 and 800HT when compared to the outer scale formed on VDM800 and VDM800HT.

The chromium content at the alloy/scale interface in 800HT dropped to about 5 wt. % after 125 oxidation cycles (Fig. 5.15), while the other three alloys sustained an N_{Cr}^i of about 10 wt.%. After 125 cycles, the alloys 800HT and VDM800HT showed steeper chromium concentration profiles and a relatively shallow depth of Cr depletion (100-150μm). By contrast, the 800 and VDM800 alloys exhibited less steep but deeper (~ 300μm) chromium concentration profiles in the subsurface. The large concentration changes in the profiles for the 800 alloy are due to the presence of numerous internal oxide particle associated with the through-oxidation of the alloy. The chromium gradient (dCr/dx) in 800HT at the alloy/scale interface was about 0.22 wt.%/μm, and in VDM800HT it was about 0.1 wt.%/μm. In the case of the 800 and VDM800 alloys, the chromium gradients were about 0.03 and 0.02 wt.%/μm, respectively. Compared to the interfacial chromium gradients measured after 18 cycles, there was an increase for the 800HT and VDM800HT alloy, but a decrease for the 800 and VDM800 alloys after 125 cycles. About 5 and 20 wt. % manganese was detected in the outer scale formed on VDM800HT and VDM800, respectively, after 125 cycles. It is recalled that no manganese was detected in the outer scale of these alloys after 18 oxidation cycles; whereas, manganese was detected after 18 cycles in the case of 800 and 800HT. For the 800HT and VDM800HT alloys, there was an apparent enrichment of nickel (about 10-15

wt.%) at the alloy/scale interface after 125 cycles. The concentration of iron at the alloy/scale interface also increased to some extent in these alloys, but not as significant as that for nickel.

5.3 Discussion

5.3.1 Oxidation Behavior

The measured weight gain of the four initial alloys studied after 7-day isothermal oxidation at 1000°C was found to rank from the smallest to the largest VDM800HT < VDM800 < 800HT < 800. In accordance with the weight-gain results, the measured scale thickness followed the same ranking order. The weight gain and thickness measurement are the result of oxide growth and any spallation that may have occurred during the oxidation process. The extent of spallation can be approximated by calculating the difference between the weight gain predicted based on the measured parabolic rate constants (Table 4.1) and the measured weight gain. This difference will be referred to as *Spall*, *i.e.*

$$Spall = \frac{(W_c - W_m)}{W_c} \qquad (5.1)$$

where W_c is calculated weight gain and W_m is measured weight gain. This Spall parameter can range from one (complete spallation) to zero (no spallation). Moreover, the Spall parameter is directly related to the fraction of total scale spalled. Thus, a given *Spall* value presents primarily the extent of spallation during the cooling period after isothermal oxidation. The values of *Spall* for each of the four alloys are listed in Table 5.6. It is seen in this table that the largest spallation was from the 800 alloy while the smallest was from the VDM800 alloy. Many studies [195-197] have shown that the relative amount of scale spallation increases with scale thickness. Thus, in accordance with the measured parabolic rate constants, 800 should have large spallation if the same oxide structures exist for the four alloys, which was proven by XRD and SEM/EDS analyses (Table 4.2 and Fig. 4.12) to essentially be the case. In addition, the smallest spallation should be from VDM800, which has the smallest parabolic rate constant. The *Spall* values show that the extent of spallation should be larger for VDM800HT (0.16) than for 800HT (0.12); however, VDM800HT

showed better oxidation resistance. Spallation is affected by many other factors, such as transient oxidation behavior, cooling rate, and surface preparation. As a result, the parabolic rate constants for 800HT and VDM800HT do not solely determine the spallation extent of the two alloys.

Table 5.6. Measured and calculated weight gain of the alloys studied after 7 days isothermal oxidation at 1000 °C, together with corresponding Spall values.

Alloys	Measured weight gain (mg/cm^2)	Calculated weight gain (mg/cm^2)	Spall
800	1.79	2.5	0.28
800HT	1.77	2.0	0.12
VDM800	1.58	1.7	0.07
VDM800HT	1.50	1.8	0.16

The SM alloys were found to perform poorer than the VDM alloys during long-term 1-day-cyclic oxidation testing in still air at 1000°C. The ranking of the alloys from best to worst was in the order: VDM800 > VDM800HT > 800 > 800HT. All of the alloys exhibited spallation within the scale as opposed to spallation at the alloy/scale interface (Fig. 5.6). The 800HT alloys showed poorer oxidation resistance than the 800 alloys from the same supplier. The 800HT alloy exhibited the greatest amount of spallation, undergoing breakdown mass-loss kinetics after about 18 cycles. By contrast, the VDM800HT alloy did not undergo breakdown until about 95 cycles. Table 5.2 shows that the alloys 800HT and VDM800HT exhibited similar spallation rates (-4.5 to –5.0 mg/cm^2·day$^{1/2}$) after breakdown oxidation, which indicates that the two alloys formed similar less-protective oxides after breakdown. The decreased spallation trend of the 800 alloy after about 70 cycles was due to its through oxidation. The observed difference in cyclic oxidation behaviors can be partly ascribed to differences in scale spallation behavior which, in turn, can be related to differences in both scale properties and alloy compositions [110].

As discussed in section 2.2.7, the spallation of oxide scale generally involves the separation of cracked scale either by de-cohesion at the alloy/scale interface or by fracture on

planes within the scale itself [142,143]. Equation (2.87) shows that thicker oxide scale, larger temperature drop, and weaker scale adhesion can result in a larger extent of oxide scale spallation. It was found that the SM alloys formed thicker scales than the VDM alloys during oxidation at 1000 °C (Table 5.2 and Fig. 5.6). Thus, the semi-quantitative prediction from Equation (2.87) that the extent of scale spallation should increase with an increase in scale thickness is in agreement with the present results. The superior performance of the VDM alloys in comparison to the SM alloys can therefore be partly ascribed to the lower scaling kinetics on the former alloys. It is believed that the lower kinetics can, in turn, be partly ascribed to the formation of a discontinuous inner scale layer of Si- and Al-rich oxides at the scale/alloy interface in the VDM alloys. Such a layer would partially block the outward migration of chromium and also change the boundary conditions for the Cr_2O_3 scale layer growth. Both of these factors would have contributed to decreasing the overall rate of scale growth.

Thermal cycling tends to promote scale spallation, and spallation accelerates chromium depletion and consequently lowers interfacial chromium content. When the interfacial chromium content decreases below the critical value for chromia formation, a non-protective scale grows instead and this marks the start of breakdown oxidation. For the 800 series alloys, the less-protective oxides that formed were found to be primarily $(Fe,Ni)_3O_4$, $NiFe_2O_4$, and NiO. The VDM800 alloy maintained a primary chromia scale, which was consistent with its good long-term cyclic oxidation resistance.

In the cross-sectional SEM images (Fig. 5.8), the partially spalled oxides from the 800, 800HT, and VDM800HT alloys were detected as $(Fe,Ni)_3O_4$ and/or $NiFe_2O_4$. Some regions in the SEM images showed that complete spallation had occurred, thus the alloy would have been exposed to the atmosphere. Thus, at least two possible modes of oxide growth must have taken place after breakdown oxidation. In the event of complete spallation, non-protective oxides such as NiO, $(Fe,Ni)_3O_4$, and $NiFe_2O_4$ grew because the interfacial chromium content was too low to form a chromia scale. With continuous oxidation, chromia may have formed under the non-protective oxides owing to the higher stability of chromia. However, the inner chromia layer that may form would not likely act as a protective layer because it is typically thin and uneven, which would make it easy to crack and spall during

cooling. In the event that the spallation was not complete, the other possible mode of non-protective oxide growth is that a large amount of Ni^{2+}, Fe^{2+}, and/or Fe^{3+} diffused through the thin inner chromia layer, which likely contained cracks, and formed non-protective oxides as an outer layer. Based on this latter possibility, the inner chromia layer would not be dense and would instead contain a large amount of defects in the form of microcracks. Such a chromia layer would not provide much in the way of oxidation resistance and could even have poor adhesion with the alloy.

The VDM800 alloy (Fig. 5.8) maintained a primarily chromia scale during long-term cyclic oxidation; however, it formed a large amount of internal oxides. The chromia scale ostensibly provided the good oxidation resistance, while the large amount of internal oxides would be detrimental and significantly affect the service life of the alloy. The comparatively lower amount of internal oxidation in the 800, 800HT, and VDM800HT alloys is very likely associated with their breakdown oxidation, which resulted in greater metal recession and possibly also significant depletion of minor elements, such as Ti, Si, and Al, in the subsurface region.

5.3.2 Interactive Effect of Minor Alloying Elements

The 800 series alloys contain various minor alloying elements and showed significantly different oxidation behavior. Lobb *et al.* [117] reported that silicon can increase the extent of scale spallation when its content in the alloy is above about 0.6 wt. %. Stott *et al.* [101] showed that scale spallation is particularly facilitated under cyclic oxidation conditions if the inner silica scale layer is continuous. The silicon content in the currently studied alloys was less than 0.6 wt.% and no continuous inner silica layer was observed. The VDM alloys with higher Si contents (about 0.37 wt.%) formed discontinuous silica particles at the scale/alloy interface, which may have contributed to their better oxidation resistance than the SM alloys having lower Si contents (about 0.15 wt.%). It can be inferred from the present results that a discontinuous distribution of silica precipitates at the alloy/scale interface is much less detrimental from the standpoint of scale spallation than if the silica were continuous. This is because scale spallation was always observed to occur from a location within the scale rather than at the alloy/scale interface. The VDM alloys showed shallower depth of internal

oxidation, which is quite possibly associated with the presence of silica particles along the scale/alloy interface. Specially, the silica particles may act as a barrier to the inward diffusion of oxygen. The low Al+Ti content in VDM800 contributed to this alloy exhibiting the least internal attack, and thus the best cyclic oxidation resistance.

Barrett [181] reported that the likelihood and extent of scale spallation is related to alloy composition and, in particular, the apparent interaction between alloy elements. The present results suggest that there is an interplay between the minor elements Al, Si and Ti in effecting scale spallation. It was found that the alloy/scale interface in the SM alloys contained a greater amount of small protrusions into alloy at the alloy/scale interface (Fig. 5.6). EDS analysis indicated that the protrusions were Cr- and Ti-rich oxide. Titanium is known to be detrimental to the scale-spallation resistance of chromia formers [118-122,161,198]. Litz et $al.$ [199] reported that oxygen diffusion through TiO_2 is very fast to the extent that the inner TiO_2 layer would be expected to grow inwards at the TiO_2/metal interface. Although the titanium contents in the present alloys were not enough to form a continuous TiO_2 layer at the alloy/scale interface, the TiO_2 that did form would have promoted the development of a non-planar interface. The non-planar interface could develop large stresses which would promote spallation during cyclic oxidation. Fig. 5.11 shows cross-sectional images of three modified 800HT alloys after 18 1-day cycling oxidation.

The modified 800HT alloys showed only marginal, yet systematic, improvement in cyclic oxidation resistance with increasing silicon contents from 0.17 to 0.49 wt.% (Fig. 5.5). It is found that higher silicon content alloy (0.49 wt.%) formed a large amount of oxide protrusion into the alloy at the scale/alloy interface, together with more extensive internal oxidation. It is possible that Si promoted the formation of Ti- and Cr-rich oxide protrusions at the scale/alloy interface, which in turn led to the development of stresses and detrimental cyclic oxidation resistance. 800HT-2 (0.27 wt.% Si) formed silica particles at the scale/alloy interface. It is believed that the silica particles contributed to the better oxidation resistance of 800HT-2. The higher silicon content (0.49 wt.%) in 800HT-3 resulted in the formation of a discontinuous silica layer at the front of oxide protrusions at the scale/alloy interface (Fig. 5.12). The protrusions combined with the silica layer were apparently detrimental to the cyclic oxidation resistance of the 800HT-3 alloy. Comparing the oxidation kinetics of the

alloys from the same supplier, which have similar Si contents, the 800HT alloys showed poor cyclic oxidation resistance than the 800 alloys. The alloys studied contained low Al contents (<0.6 wt.%) and consequently did not form an Al_2O_3 scale layer. However, considering the effect of Al, the higher Al contents in the 800HT alloys (0.46 wt.% for 800HT and 0.58 wt.% for VDM800HT) did not result in better oxidation resistance. Thus, it is believed that the amount of Al addition in the 800 series alloys was not sufficient to provide beneficial effect on the oxidation resistance. Further, high Al content (<1 wt.%) may increase the extent of internal oxidation, which may in turn be detrimental to oxidation resistance. The VDM800 alloy exhibited the best cyclic oxidation resistance, which is believed to be due to its optimal silicon content (0.38 wt.%) and the small Al and Ti contents (0.25 and 0.32 wt.% respectively) minimizing the amount of internal oxidation of Ti-rich protrusions into the alloy at the scale/alloy interface.

The manganese in the 800 series alloys is also known to affect the scale composition and properties, due to the formation of an outer scale layer of the less-protective $MnCr_2O_4$ spinel. According to Caplan *et al.* [114] the presence of manganese in a chromia-forming alloy promotes scale blistering and cracking. During oxidation, a layer of $MnCr_2O_4$ becomes established on the outer surface and thickens with time. The greater amount of manganese-containing oxide in the outer part of a scale would result in faster scaling kinetics which, in turn, would increase the extent of scale spallation. From EPMA results, the SM alloys contained about 12 wt.% Mn in the outer layer after 18 cycles, while the VDM alloys contained a much lower amount of Mn after the same number of cycles (Fig. 5.13). Although the reason for this result is not readily apparent, it may be that the discontinuous Al- and Si-rich inner layer in the VDM alloys also acted to partially block the outward migration of Mn, similar to what was proposed for Cr.

5.3.3 Effect of Alloy Microstructure

The most significant microstructural difference (before oxidation) between the two sets of alloys studied is that the SM alloys contained a large amount of twinning. It is possible that the twins played a role in promoting scale spallation; however, it is not entirely clear what that role would be. Figure 5.9 shows internal oxidation along twins in the 800HT alloy after

125 oxidation cycles. After 125 oxidation cycles, the Cr content at the alloy/scale interface in 800HT decreased to about 5 wt.% and the scale was more discontinuous and apparently less protective. The less-protective oxide scale together with the consequently higher oxygen pressure, would have increased the tendency for internal oxidation and, as seen in Fig. 5.9, the twins were preferred sites for the internal oxidation. Kiyoshi *et al.* [200] also found that the intergranular oxides fomed along twin boundaries in a 40.72Fe-38.70Ni-13.53Co-4.70Nb-1.54Ti-0.36Si-0.04Cr-0.04Mn alloy oxidized at 827-1027 °C for 5-100 hours. The added preferential oxidation along twin boundaries may have contributed to increasing the extent of scale spallation, and, hence, decreasing the time to breakdown.

The 800 alloy was superior to the 800HT alloy within a given set of supplied alloys. The 800HT alloys contained a higher volume fraction of carbides than the 800 alloys. The higher carbide content confers higher strength to the 800HT alloys. However, the carbides are also prone to oxidation. Litz *et al.* [199] studied the oxidation of chromia-forming nickel-base alloys containing large blocky MC carbides and found that the MC carbides oxidize much faster than the matrix, with the corrosion product being more voluminous than the carbide. Similar results for the oxidation of carbides were reported by Chen *et al.* [198]. Those authors studied chromia-forming commercial nickel-base superalloys under cyclic conditions at 1000°C and reported that the difference in oxidation rates between the carbides and the matrix can result in high shear strains which may induce cracking at the interface or in the oxidized carbides, leading to further internal oxidation around the oxidized carbides. It is therefore believed that a larger amount of grain-boundary carbides in the 800HT alloy contributed to its poorer performance compared to the 800 alloy from the same supplier.

5.3.4 Analysis of Subsurface Depletion Behavior

The four 800 series alloys showed different subsurface Cr depletion behaviors. Generally, Cr depletion comes from chormia scale growth and is accelerated by the spallation and reformation of the chormia scale. Thus, a larger oxide growth rate and a greater extent of spallation would result in larger amount of Cr depletion. The depletion of Cr is supplied from the alloy matrix, which makes reformation of chromia scale possible. Thus, the diffusion

behavior of Cr in the alloy would affect the supply of Cr to reform a chromia scale, and further affect the oxidation behavior. A larger average effective interdiffusion coefficient of chromium supply of chromium to the alloy/scale interface can improve the oxidation resistance of the alloy. The better oxidation resistance of the VDM alloys could be partly attributed to their larger average effective interdiffusion coefficient of chromium. The reason for the larger average effective interdiffusion coefficient of chromium in the VDM alloys is not clear. Minor elements, especially silicon, may be contributing factors.

From the EPMA results, the 800 series alloys were found to exhibit different subsurface depletion profiles of chromium. For the chromium depletion profiles after 7-day isothermal oxidation in Fig. 5.13, the VDM alloys showed flatter and deeper profiles than the SM alloys, which is consistent with the larger D_{Cr}^{eff} values in the VDM alloys. Under thermal cycling conditions, the 800HT and VDM800HT alloys showed steeper Cr depletion profiles within the vicinity of the scale/alloy interface. A steeper subsurface Cr depletion profile corresponded to large chromium depletion, which could not be effectively replenished by chromium diffusion from the bulk, and correspondingly to a relatively low chromium content at the scale/alloy interface. When the interfacial Cr content is lower than the critical interfacial Cr content to form chromia scale, breakdown oxidation occurs.

After 18 1-day oxidation cycles, the 800HT alloy contained a subsurface chromium profile in which the interfacial chromium content dropped to 8 wt. %, which is apparently below the critical content for continuous Cr_2O_3 formation. Thus, the alloy was incapable of scale rehealing after only 18 cycles. After 125 cycles, the chromium profiles in the two 800HT alloys were steeper, indicating extensive chromium subsurface depletion in the vicinity of the alloy/scale interface due to significant spallation. By contrast, the profiles in the two 800 alloys indicated less extensive chromium depletion. However, the through-oxidation of the 800 alloy before 125 1-day oxidation cycles would have affected the chromium depletion profile. The subsurface Cr gradient in VDM800 after 125 1-day cycles decreased compared to after 18 cycles, indicating that the Cr interdiffusion behavior should vary upon composition. Specially, a D_{Cr}^{eff} that increased with increasing Cr content would result in a relatively flat and deep depletion profile, as was observed in VDM800.

As indicated above, the continual subsurface depletion of chromium eventually caused the alloy to be incapable of re-forming a continuous protective chromia scale. What resulted instead was the oxidation of the iron and nickel. This is confirmed in Fig. 5.8, which shows that the 800HT alloys contained nickel and iron oxides in the outer scale. As shown by Harper and Gleeson [110], a possible oxidation product of iron and nickel is $(Fe,Ni)_3O_4$, which is non-protective from the standpoint of spallation resistance. The current study showed that more complex non-protective scales formed on the 800 series alloys, containing $NiFe_2O_4$, and NiO, together with $(Fe,Ni)_3O_4$. Formation of the non-protective oxides apparently decreased the extent of subsurface depletion of chromium due very likely to an increase in the recession rate of the alloy/scale interface. It was found that chromium content at the scale/alloy interface in the 800HT alloy decreased from about 20 wt.% to 8 wt. % after 18 1-day oxidation cycles (breakdown), while the interfacial Cr content only dropped to about 5 wt.% after 125 1-day cycles. The less extent of drop for the interfacial Cr content after 18 cycles for 800HT was consistent with its breakdown, which contributed to a faster recession rate.

5.4 Conclusions

The 800 series alloys from Special Metals exhibited poorer cyclic oxidation resistance at 1000°C in comparison to those from Krupp VDM. The alloys studied formed under isothermal oxidation condition essentially a duplex scale structure consisting of a Cr_2O_3 inner layer and a thin $MnCr_2O_4$ outer layer. The 800HT alloy exhibited the worst oxidation performance and also exhibited the greatest extent of subsurface chromium depletion. Only the VDM800 alloy did not exhibit breakdown weight-loss kinetics for up to the maximum duration studied of 125 1-day oxidation cycles. Variations in minor constituent contents are believed to have contributed to the different oxidation behaviors observed. A Si content of about 0.3-0.4 wt % in combination with a low Ti+Al content (*i.e.*, below about 0.6 wt. %) provided the best spallation resistance for the 800 series alloys studied. A high concentration of Ti is detrimental because it forms internal oxidation products and it may increase the tendency towards the development of a non-planar alloy/scale interface.

A discontinuous inner scale layer of Si- and Al-rich oxides contributed to decreasing the rate of scale growth on the VDM alloys. The discontinuous layer acted to partially block the outward migration of chromium and also to change the boundary conditions for the Cr_2O_3 scale growth. Both of these effects caused a decrease in the overall rate of scale growth. The lowering of the scaling kinetics had the beneficial effect of decreasing the extent of scale spallation for a given number of cycles. Silicon played a more important effect than aluminum to improve cycling oxidation resistance. A high Al content (*i.e.*, < 1 wt.%) results in more extensive internal oxidation, which is detrimental to oxidation resistance. The low Ti and Al contents in the VDM800 alloy resulted in the least internal attack, which is beneficial for cycling oxidation resistance. The greater amount of manganese-containing oxide in the outer part of the scale formed on the SM alloys resulted in faster scaling kinetics which, in turn, increased the extent of scale spallation. The discontinuous Si- and Al-rich inner layer in the VDM alloys also acted to partially block the outward migration of Mn, hence decreasing the formation of a less-protective outer layer.

The internal oxidation of titanium promoted the development of Ti-rich and Cr-rich oxide protrusions into the alloy at the scale/alloy interface. The protrusions may act to decrease the adhesion of the scale and introduce stresses, and hence can be detrimental to cyclic oxidation resistance. Scale spallation is related to alloy composition and, in particular, the apparent interaction between alloy elements. A high amount of Si addition would increase the formation of Ti- and Cr-rich protrusions at the scale/alloy interface, especially in alloys having a high Ti content. A high silicon content (0.49 wt.%) results in the formation of a silica layer at the protrusion front, which is detrimental to the cyclic oxidation resistance of the alloy. Optimum silicon content is about 0.3-0.4 wt.%, which results in the formation of discontinuous silica particles and the least amount of Cr- and Ti-rich oxide protrusions at the scale/alloy interface if the Ti content is low (about 0.3 wt.%).

The 800HT alloys contained a higher volume fraction of carbides than the 800 alloys. The difference in oxidation rates between the carbides and the matrix can lead to further internal oxidation and contributed to poorer performance of the 800HT alloy compared to the 800 alloy from the same supplier.

The SM alloys contained a great amount of twinning. The added preferential oxidation along twin boundaries may have contributed to increasing the extent of scale spallation, and hence decreasing the time to breakdown.

The 800HT alloys exhibited relatively rapid chromium depletion under the alloy/scale interface and eventually underwent breakdown oxidation, in which the iron and nickel oxidized to form a less protective scale. The VDM alloys showed flatter and shallower chromium depletion profiles than the SM alloys after relatively short-term oxidation. Diffusion analysis of the subsurface Cr depletion profiles after isothermal oxidation found that the VDM alloys have higher average effective interdiffusion coefficients of chromium than the SM alloys. A high D_{Cr}^{eff} is beneficial to sustaining relatively high interfacial Cr content and the healing or reformation of chromia-scale. The higher silicon contents in the VDM alloys may have contributed to the larger D_{Cr}^{eff} values.

CHAPTER 6 EFFECTS OF SILICON ON CYCLIC OXIDATION BEHAVIOR OF CHROMIA-FORMING ALLOYS

6.1 Introduction

As discussed in Chapter 5, the chromia-forming 800 series Fe-base wrought alloys show significant variation in oxidation resistance with in the chemical composition specifications. This variation was attributed to the variation (from alloy to alloy) of the minor alloying elements, such as Al, Si, Ti, and Mn, in the alloys. Among the minor additions, silicon was believed to be one of the most significant effects, as it can improve oxidation resistance significantly if present at an optimum content. It was inferred in the previous chapter that the optimum silicon content is about 0.3-0.4 wt.% for the 800 series alloys. Many commercial alloys contain higher silicon content (up to 5 wt.%), thus it is necessary to determine the effect of silicon on cyclic oxidation behavior within a wide range of silicon content.

A large amount of literature [101,114,115,116,143] shows that the high-temperature oxidation behavior of chromia-forming alloys is significantly influenced by the presence of silicon additions, particularly under thermal cycling condition. Silica is thermodynamically more stable than chromia and will consequently tend to form beneath or at the alloy/Cr_2O_3-scale interface. The formation of a continuous inner silica layer, which acts as a diffusion barrier, tends to improve isothermal oxidation resistance by suppressing cation transport through the Cr_2O_3 scale and thus reduces the rate of Cr_2O_3-scale growth; however, an inner SiO_2 layer can also greatly worsen the extent of scale spallation. Some studies [201,202,203] reported that the silica layer formed at the chromia/alloy interface is vitreous. Two features of vitreous silica are low defect concentration and the lack of grain boundaries, both of which would contribute to low rates of diffusion. As a result, vitreous silica could act as an excellent diffusion barrier. Previous studies [72,88,115,143,204] have also shown that silicon facilitates the formation of a chroma scale. For example, Kumar and Douglass [102] studied the oxidation behavior of an austenitic Fe-14Cr-14Ni steel that contained up to 4 wt.% Si over the temperature range 900-1100 °C in air. The alloy without Si addition formed a scale comprised of Fe- and Ni-rich oxides and internal precipitates of spinel oxides, while a

continuous chromia layer formed above a silica layer for the alloy with 4 wt.% Si, which showed good resistance to cracking and spallation. However, evidence in the literature [101,116,205,206] indicates that the presence of a continuous silica layer can lead to scale spallation. According to Stott *et al.* [101], the formation of silica precipitates during the early stages of oxidation facilitates the development of a Cr_2O_3 scale on an Fe-14Cr-10Si alloy oxidized at 1000 °C. The continuous inner scale layer of silica that eventually developed on this alloy improved isothermal oxidation resistance compared to Fe-26Cr-1Si and Fe-14Cr-3Si alloys, but did result in more extensive scale spallation on cooling.

The aim of this chapter is to determine the effect of silicon on the cyclic oxidation behavior of the chromia-forming alloys at 1000 °C. Not only will the oxide characteristics be analyzed, but the subsurface changes and the interdiffusion behavior of Cr in the alloys will also be addressed.

6.2 Results

The alloys studied in this chapter are divided into two groups: low-Si (Si < 1 wt.%) Fe-base alloys and high-Si (Si > 2 wt.%) Ni-base alloys. For low-Si (<1 wt%) 800 series alloys, Chapter 5 showed that the modified 800HT alloys with higher Si levels (up to 0.49 wt.%) did not form a continuous Si-rich scale, and also did not show any marked improvement in cyclic oxidation resistance compared with the other modified 800HT alloys with lower Si contents. It was inferred that the high Ti content in the 800HT alloys (0.50-0.55 wt.%) resulted in the formation of Ti- and Cr-rich oxide protrusions at the alloy/scale interface, which were detrimental to cyclic oxidation resistance. A higher Si content in 800HT promoted more formation of oxide protrusions, thus countering any beneficial Si effect. As discussed in Chapter 5, the SM 800 alloy showed poorer oxidation resistance than the VDM alloys, even though the former has a lower Ti content (0.41 wt.%) than the 800HT alloy. In order to better identify the Si effect, which may be offset by the presence of Ti, two modified 800 alloys (800-1 and 800-2) with different Si levels were supplied by Special Metals in plate form about 3 mm thick. Table 6.1 lists the measured chemical composition of the SM 800 alloys. It is seen that the Si content ranges from 0.13 wt.% to 0.77 wt.% in the alloys. The amount of

other minor elements, such as Ti, Al, and Mn, were kept close to the same for the three SM 800 alloys. Compared with the 800HT alloy (Table 5.4), the Ti content in the modified 800 alloys is lower by about 0.1-0.14 wt.%. As a comparison, the composition of the VDM800 alloy is also shown in Table 6.1. This alloy had the lowest Ti content (0.32 wt.%). The summed Ti+Al content of each alloy is also summarized in Table 6.1. The VDM800 alloy contained a lower Ti+Al content than the SM 800 alloys. And the SM alloys contained a higher Cu content than the VDM800 alloy.

Table 6.1. Measured composition of the SM 800 alloys with different Si contents (wt.%).

Alloys	C	Mn	Si	Cr	Ni	Fe	Ti	Al	Cu	Ti+Al
VDM800	0.061	0.70	**0.38**	20.50	30.30	47.15	0.32	0.25	0.07	0.57
800	0.02	0.78	**0.13**	20.05	33.64	43.64	0.41	0.30	0.21	0.71
800-1	0.024	0.75	**0.39**	19.90	33.5	44.2	0.42	0.39	0.19	0.81
800-2	0.031	0.76	**0.77**	19.90	33.6	43.7	0.42	0.39	0.19	0.81

The commercial wrought Ni-base alloys 45TM, HR-160 and D-205, grouped as high-Si alloys, were received in plate form of thickness 2.0, 1.6, and 0.8 mm, respectively. The measured compositions of these Ni-base alloys are listed in Table 6.2.

Table 6.2. Measured chemical composition (wt.%) of the high-Si Ni-base alloys studied.

Alloys	C	Mn	Si	Cr	Ni	Fe	Ti	Al	Others	
45TM	0.08	0.36	2.66	27.40	46.35	22.65	0.41	0.06	0.07Ce	0.05Cu
HR-160	0.05	0.59	2.75	28.8	38.5	0.4	0.5	0.03	28Co	1Nb
D-205	0.03	0.18	5.3	18.6	64	6.6	-	0.03	2.5Mo	2Cu

The 45TM and HR-160 alloys have very similar silicon contents, but are significantly different in base metal contents with 22.65 wt.% Fe in 45TM and 28 wt.% Co in HR-160. In

order to reveal the effect of Fe and Co on the oxidation behavior of 45TM and HR-160, six model Ni-Cr alloys based on the composition of 45TM and HR-160 were designed and cast. The cast Ni-Cr alloys were homogenized for 24 hours in Ar at 1050 °C before oxidation testing. The nominal compositions of the six cast Ni-Cr alloys are listed in Table 6.3.

Table 6.3. Nominal chemical compositions (wt.%) of the model cast Ni-Cr alloys.

Alloys	Ni	Cr	Fe	Co	Si
NiCr	72	28	-	-	-
NiCrFe	50	28	22	-	-
NiCrCo	44	28	-	28	-
NiCrSi	69.3	28	-	-	2.7
NiCrFeSi	47.3	28	22	-	2.7
NiCrCoSi	41.3	28	-	28	2.7

6.2.1 Oxidation Kinetics

Table 6.4 summarizes the parabolic rate constant of steady-state oxidation and the transient-state oxidation time of the alloys studied. These values were obtained from TGA tests at 1000 °C. TGA plots of the wrought alloys studied were shown in Figure 4.9, and Figure 6.1 shows the TGA plots of the cast Ni-Cr alloys. For the wrought alloys, the HR-160 and 800 alloys exhibited the largest parabolic rate constants, followed by the modified 800 alloys, D-205, and then 45TM. The parabolic rate constants for HR-160 and 45TM were very different, with an ratio of about 4.4, even though the Cr and Si contents are very similar in these two alloys (i.e., ~28 wt% Cr and ~2.7 wt% Si). Closer analysis of the TGA results showed that 45TM, D-205 and HR-160 underwent relatively fast oxide growth (transient oxidation) during the first 1-3h of oxidation followed by slower steady-state oxidation kinetics, while the 800 series alloys showed a transient duration of about 3~5 hours.

Table 6.4. Parabolic rate constants (k_p) and transient-stage duration for the alloys oxidized isothermally in air at 1000 °C.

Alloys	k_p (g^{2}cm^{-4}s^{-1}) (steady-state stage)	Transient-stage duration (hours)
VDM800	4.8×10^{-12}	~5
800	1.3×10^{-11}	~5
800-1	6.8×10^{-12}	~3
800-2	7.8×10^{-12}	~3
45TM	2.7×10^{-12}	~3
D-205	3.1×10^{-12}	~1
HR-160	1.2×10^{-11}	~1
NiCrFeSi	2.6×10^{-12}	~11
NiCrSi	2.9×10^{-12}	~17
NiCoCoSi	3.2×10^{-12}	~17
NiCr	9.0×10^{-12}	~3
NiCrFe	1.1×10^{-11}	~1
NiCrCo	1.9×10^{-11}	~22

The oxidation kinetics of the cast Ni-Cr alloys compared to the commercial wrought alloys 45TM and HR-160, may be expected to be quite different because of the difference in the way they were processed (*i.e.*, cast vs. wrought). Thus, the cast Ni-Cr alloys were analyzed separately. From the TGA plots in Fig. 6.1, the cast Ni-Cr alloys with silicon addition showed that the transient oxidation consisted of two growth stages: a very fast and short initial oxidation stage (about 40 minutes), followed by a relatively slow and long intermediate stage (about 15 hours). Of the cast Ni-Cr alloys, the NiCrCo alloy showed the largest steady-sate rate constant (1.9×10^{-11} g^{2}cm^{-4}s^{-1}), while the NiCrFeSi alloy showed the lowest (2.6×10^{-12} g^{2}cm^{-4}s^{-1}). The parabolic rate constants of the cast Ni-Cr alloys varied by a factor of about ten. The parabolic rate constants of the cast Ni-Cr alloys are compared graphically in Figure 6.2. It is seen that three Ni-Cr alloys with silicon addition showed much
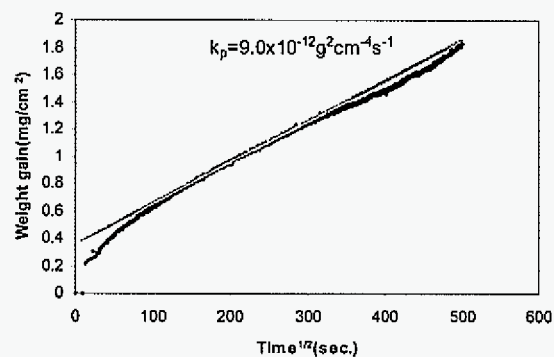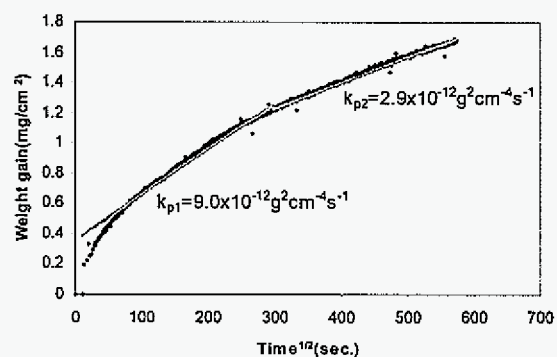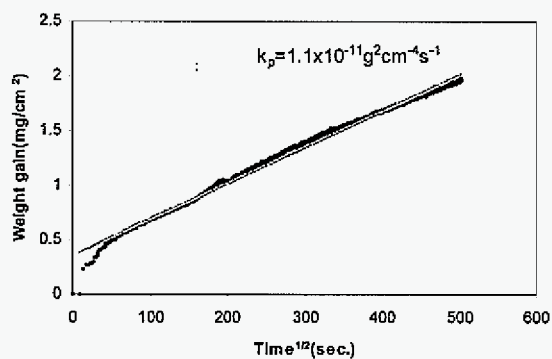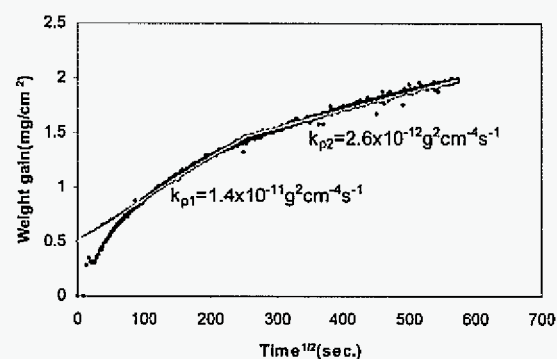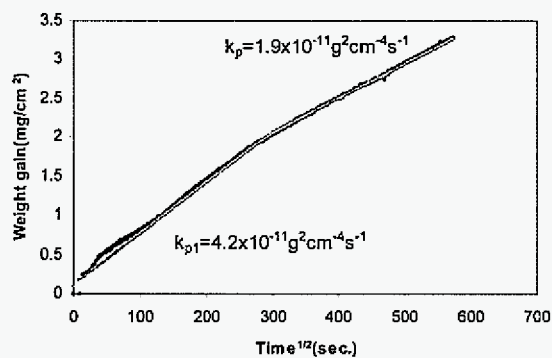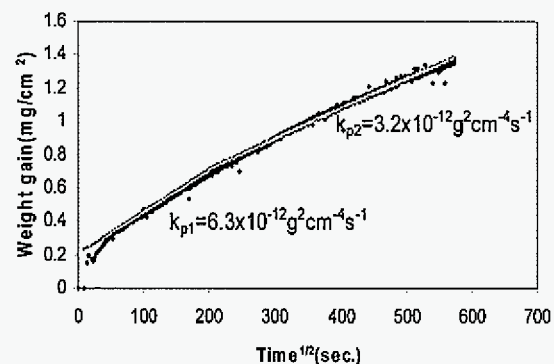
Figure 6.1. TGA results of NiCr-based alloys at 1000 °C.

smaller parabolic rate constants than the Ni-Cr alloys without silicon addition. The addition of Co to the Ni-Cr alloy apparently increased the parabolic rate constants, while Fe only marginally increased the parabolic rate constant of the NiCr alloy. However, silicon addition marginalized the effect of Co and Fe on parabolic rate constant in the Ni-Cr alloys.
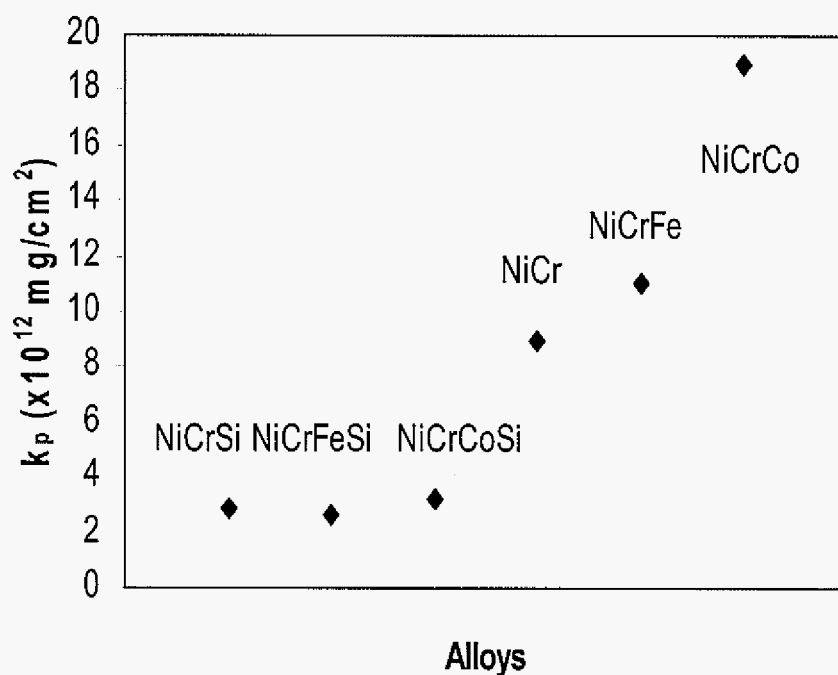
Figure 6.2. Comparison of parabolic rate constants of NiCr-based alloys at 1000 °C in air.

Figure 6.3 shows the weight-change behavior of the 800 alloys studied as a function of of the number of oxidation cycle over the entire testing duration of 125 1-day cycles at 1000 °C. It is seen that the 800-2 alloy (0.77 wt.% Si) exhibited better oxidation resistance than 800-1 (0.39 wt.% Si), while the 800 alloy (0.13 wt.% Si) showed the worst oxidation resistance. Thus, increasing Si addition improved the cyclic oxidation resistance of the SM 800 alloys. The significant reduction in the rate of weight loss for the 800 alloy after about 70 cycles was due to through-oxidation. The VDM800 alloy showed the best oxidation behavior, even though its silicon content was not the highest of the four alloys studied. The 800 and 800-1 alloys showed rapid weight-loss kinetics after about 40 and 70 cycles, respectively, of

relatively protective oxidation, while the 800-2 and VDM800 alloys did not undergo breakdown behavior over the entire test duration.
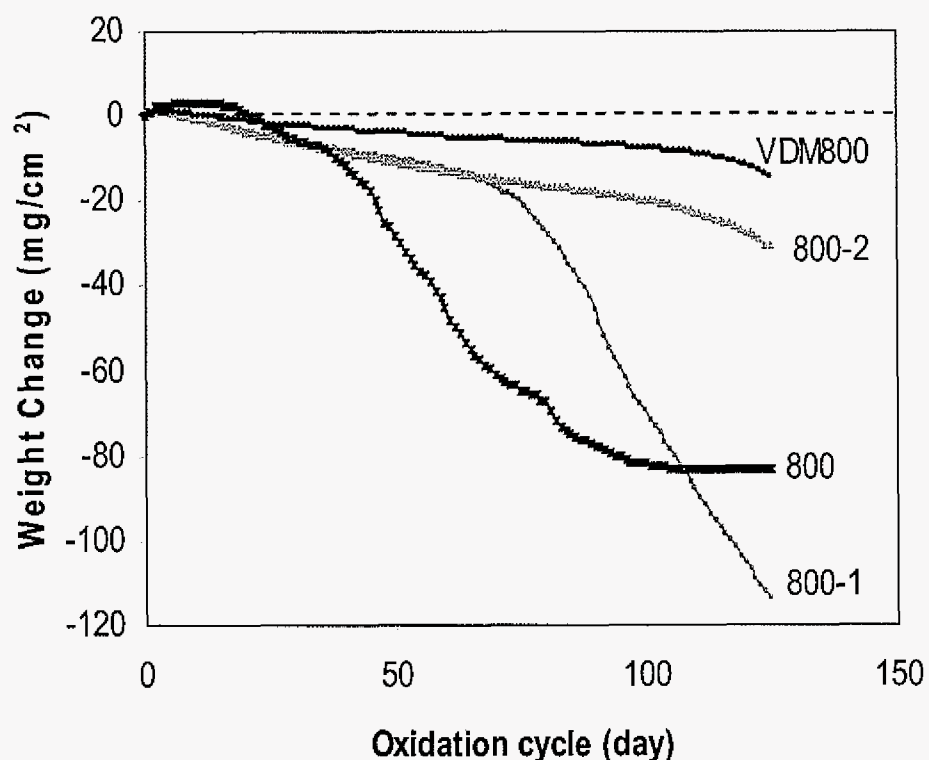
Figure 6.3. Cyclic oxidation behavior of the 800 alloys exposed to 1-day cycles at 1000 °C in air.

The 1-day cyclic oxidation behavior of the three high-Si commercial Ni-base alloys at 1000 °C is shown in Figure 6.4. It is seen that the D-205 alloy exhibited the worst oxidation resistance and the 45TM alloy the best, with HR-160 being intermediate. The HR-160 alloy underwent a relatively steady rate of weight-loss over the entire testing duration, indicating that a similar scale spallation and reformation process occurred during and after each thermal cycle. The D-205 alloy also exhibited a relatively steady rate of weight loss for about the first 90 cycles, but then underwent an increasing rate of weight loss. The accelerated weight-loss kinetics of D-205 alloy after 90 cycles coincided with the formation of a less protective oxide

scale. The 45TM alloy showed very good oxidation resistance compared to the other two alloys.
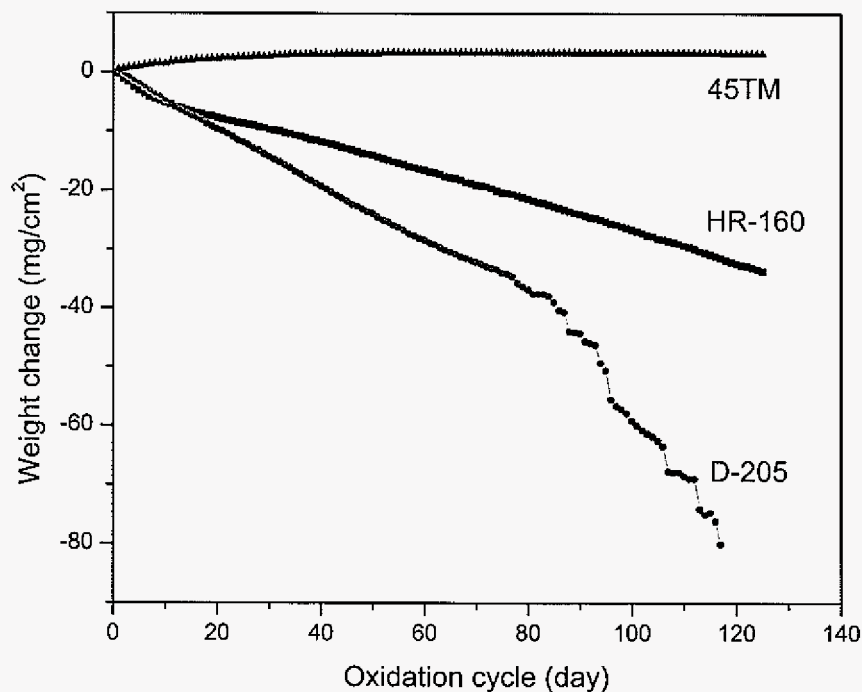
Figure 6.4. 1-day cyclic oxidation kinetics of the high-Si alloys at 1000 °C.

As shown in Figure 6.5, the cast NiCr-base alloys showed significantly different 1-day cyclic oxidation behavior at 1000 °C. It is seen that the NiCr alloys without silicon addition exhibited poorer oxidation resistance than those with Si. The binary NiCr alloy showed rapid weight loss after about 25 1-day cycles, while rapid weight loss occurred for the NiCrFe alloy after about 15 cycles. The NiCrCo alloy showed the poorer oxidation resistance, exhibiting rapid weight loss after only about 5 cycles. The cyclic oxidation resistance of the three cast NiCr-based alloys improved significantly with silicon addition with no rapid weight loss occurring over the entire test duration of 100 cycles. The NiCr alloys with Si addition showed similar oxidation kinetics, which indicated that Si addition eliminated the apparently detrimental effect of Co and Fe on oxidation resistance of the cast NiCr-based alloys.
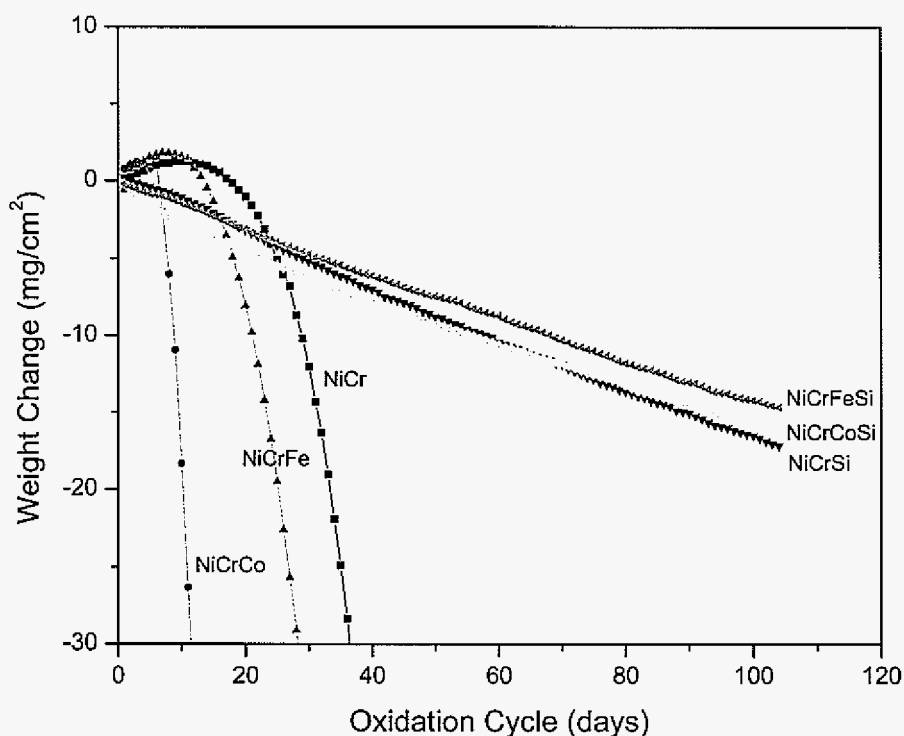
Figure 6.5. 1-day cyclic oxidation kinetics of the cast NiCr-based alloys at 1000 °C.

6.2.2 XRD Analysis of Oxide Scales

The phases present in the scales formed on the alloys after 90h isothermal oxidation at 1000 °C were determined using XRD, and the results are summarized in Table 6.5. It was found that the primary scale product was Cr_2O_3 for all alloys studied. These results are in agreement with those reported by others [110,112,114,189,191]. It is seen in Table 6.5 that all of the commercial wrought alloys formed $MnCr_2O_4$ spinel. SiO_2 peaks were detected in the high-Si alloys 45TM and D-205. The cast NiCr-based alloys also formed Cr_2O_3 as the primary phase, while $NiCr_2O_4$ and $CoCr_2O_4$ spinels were also detected on the NiCrCo alloy.

Table 6.5. Summary of oxide phased detected form XRD analysis of the scales formed on the alloys after isothermal oxidation in air at 1000 °C.

Alloys	Phases identified
VDM800	Cr_2O_3, $MnCr_2O_4$
800	Cr_2O_3, $MnCr_2O_4$
800-1	Cr_2O_3, $MnCr_2O_4$
800-2	Cr_2O_3, $MnCr_2O_4$
45TM	Cr_2O_3, $MnCr_2O_4$, SiO_2
HR-160	Cr_2O_3, $MnCr_2O_4$
D-205	Cr_2O_3, $MnCr_2O_4$, SiO_2
NiCr	Cr_2O_3
NiCrFe	Cr_2O_3
NiCrCo	Cr_2O_3, $NiCr_2O_4$, $CoCr_2O_4$
NiCrSi	Cr_2O_3
NiCrFeSi	Cr_2O_3
NiCrCoSi	Cr_2O_3

6.2.3 Microstructural Characterizations

Cross-sectional SEM images of the four 800 alloys after 18 1-day oxidation cycles at 1000 °C are shown in Figure 6.6. The 800 alloy showed the thickest scale (~15 μm), which is consistent with its largest parabolic rate constant, while the VDM800 alloy formed the thinnest scale (~5 μm). The 800 alloy formed the least amount of Si-rich oxide particles at the alloy/scale interface, and its alloy/scale interface was more planar than the other three alloys. The three alloys with higher Si contents, VDM800, 800-1, and 800-2, formed non-planar alloy/scale interfaces with oxide protrusions and internal oxide particles. The 800-2 alloy formed the largest amount of oxide protrusions and particles along the alloy/scale interface, followed by 800-1, and then VDM800. More metal inclusions were present in the

800(0.13Si)

VDM800(0.38Si)

800-1(0.39Si)

800-2(0.77Si)
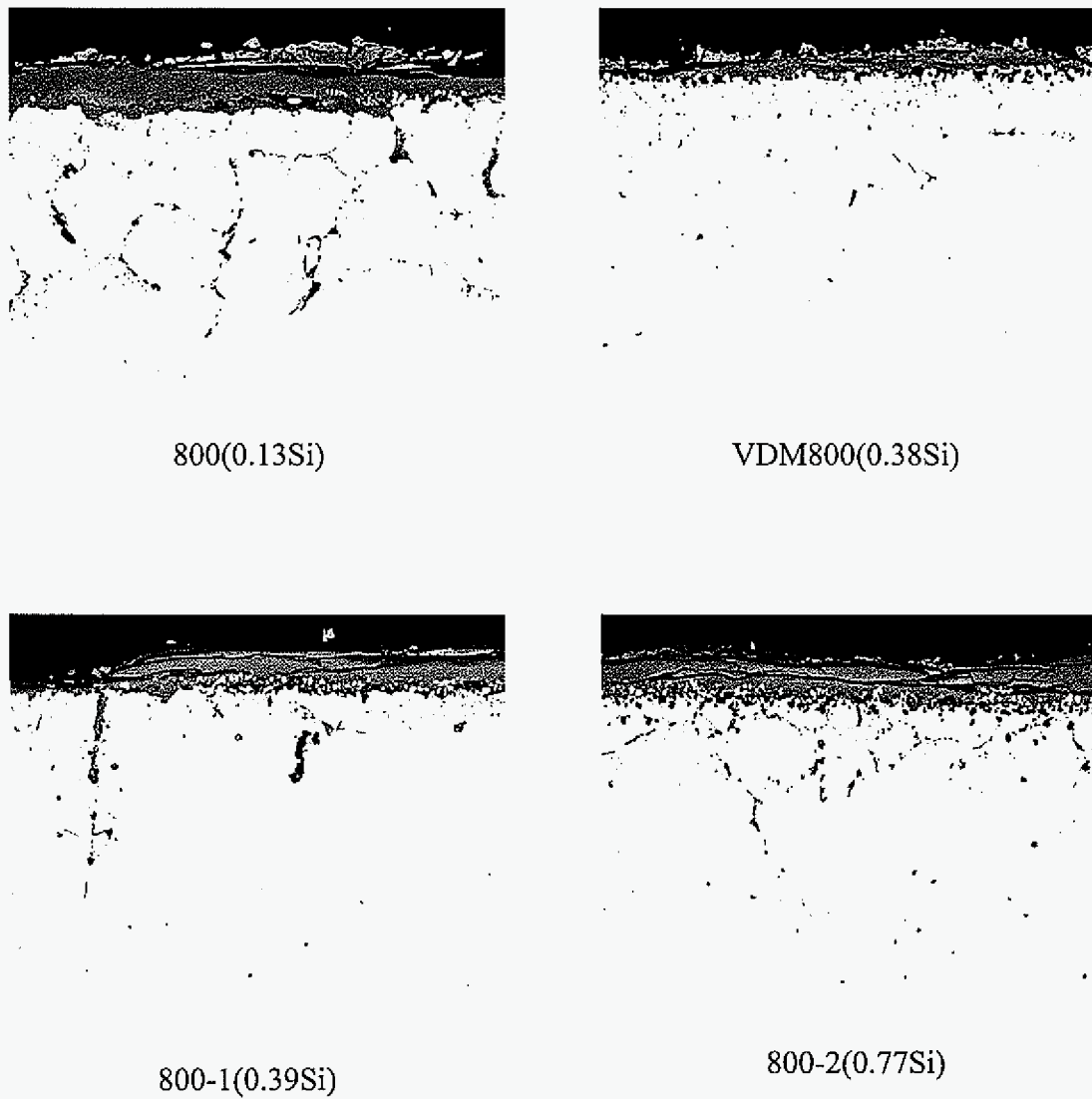
Figure 6.6. Cross-sectional SEM images of the 800 alloys after
18 1-day oxidation cycles at 1000 °C.

oxide scale near the alloy/scale interface for the alloys with more oxide protrusions. EDS analysis showed that the oxide protrusions consisted of Cr- and Ti-rich oxides, while the internal oxide particles at the alloy/scale interface were Si- and Al-rich oxides. It is seen that the 800-2 alloy formed the greatest amount of Si-rich internal oxide precipitates. As discussed in Chapter 5, the Si- and Al-rich oxides are believed to be SiO_2 and Al_2O_3, respectively. The metal inclusions in the chromia scale were detected by EDS to be Ni- and Fe-rich. For the three 800 alloys with higher Si contents, the VDM800 alloy showed the least amount of internal oxidation. The scales formed on the 800-1 and 800-2 alloys exhibited more cracking than the scale formed on VDM800. The cracks in the scales were typically parallel to the alloy/scale interface. The origin of the cracks was often found to be the metal inclusions in the scales or the roots of oxide protrusions at the alloy/scale interface. This is shown schematically in Figure 6.7.
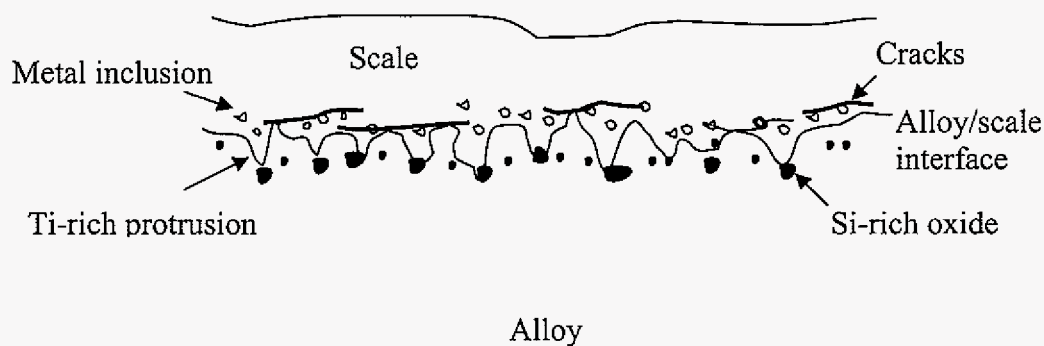
Figure 6.7. Schematic showing the origin of cracks in the scale of on alloys forming Ti- and Si-rich oxide at the alloy/scale interface.

Figure 6.8 shows cross-sectional SEM images of the 45TM, HR-160, and D-205 alloys after 18 1-day oxidation cycles at 1000 °C. All three alloys exhibited internal oxidation, but the characteristics of the internal oxidation were very different. The 45TM and D-205 alloys exhibited internal oxidation to a depth of about 50μm, whereas the HR-160 alloy oxidized internally to a depth of about 100 μm. There was a predominance of intergranular attack in all three alloys. The 45TM alloy appeared to have formed a dispersed distribution of internal oxide. EDS analysis identified the internal oxide in 45TM to be Si-rich, which very likely corresponds to the SiO_2 that was detected on this alloy by XRD. The 45TM alloy showed some voids near the scale/alloy interface within the zone of Si-rich internal oxides. The D-205 alloy showed the least amount of internal oxidation, and the dispersed phase in the matrix of D-205 was Mo-rich.

Figure 6.9 compares cross-sectional SEM images of 45TM after cyclic and isothermal oxidation testing. It is seen that the amount of internal (silicon) oxide significantly decreased with increasing isothermal oxidation time. In fact, after 28 days of isothermal oxidation, the internal oxide in 45TM was found to be mainly alumina. Thus, it can be inferred that cyclic oxidation promoted the formation of inner silica precipitates and that prolonged isothermal oxidation resulted in the dissolution of the silica precipitates. The exact reasoning for this is not yet fully understood.

Inspection of Figure 6.10 reveals that HR-160 formed an apparently continuous silicon-rich layer under the oxide scale after 18 1-day oxidation cycles. Numerous cracks parallel to the scale/alloy interface were located within the oxide protrusions. It is believed that these cracks developed through the scale and greatly facilitated scale spallation during thermal cyclic oxidation.

The D-205 alloy showed completely different oxidation characteristics compared to the other Ni-base alloys (Figure 6.11). The internal oxides were Al-rich, and silicon existed in the form of $MoSi_2$. It is very interesting that molybdenum tended to diffuse and segregate along the scale/alloy interface. There was also silicon enrichment near the scale/alloy interface (see Si X-ray map in Fig. 6.11). The D-205 alloy developed the most irregular scale compared to the other Ni-base alloys (Fig. 6.8). Many macro-cracks developed in the scale
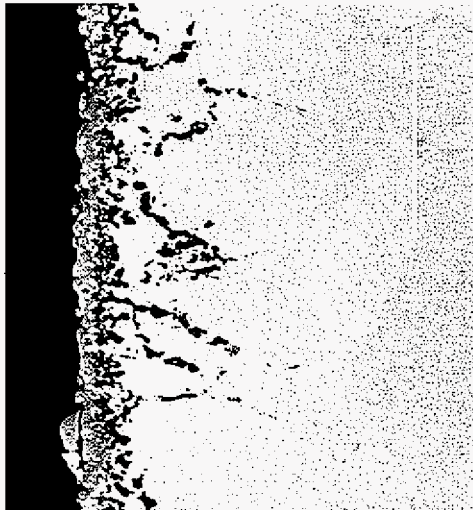
45TM (Ni-27Cr-23Fe-2.7Si)   HR-160 (Ni-28Cr-28Co-2.8Si)   D-205 (Ni-20Cr-6.6Fe-5.3Si)
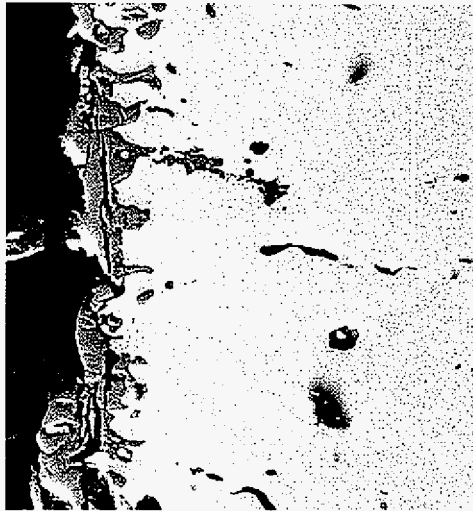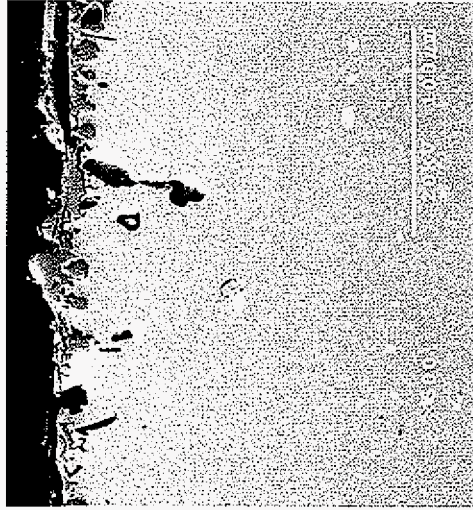
Figure 6.8. Cross-sectional SEM images of the alloys 45TM, HR-160, and D-205 after 18 1-day oxidation cycles at 1000 °C.
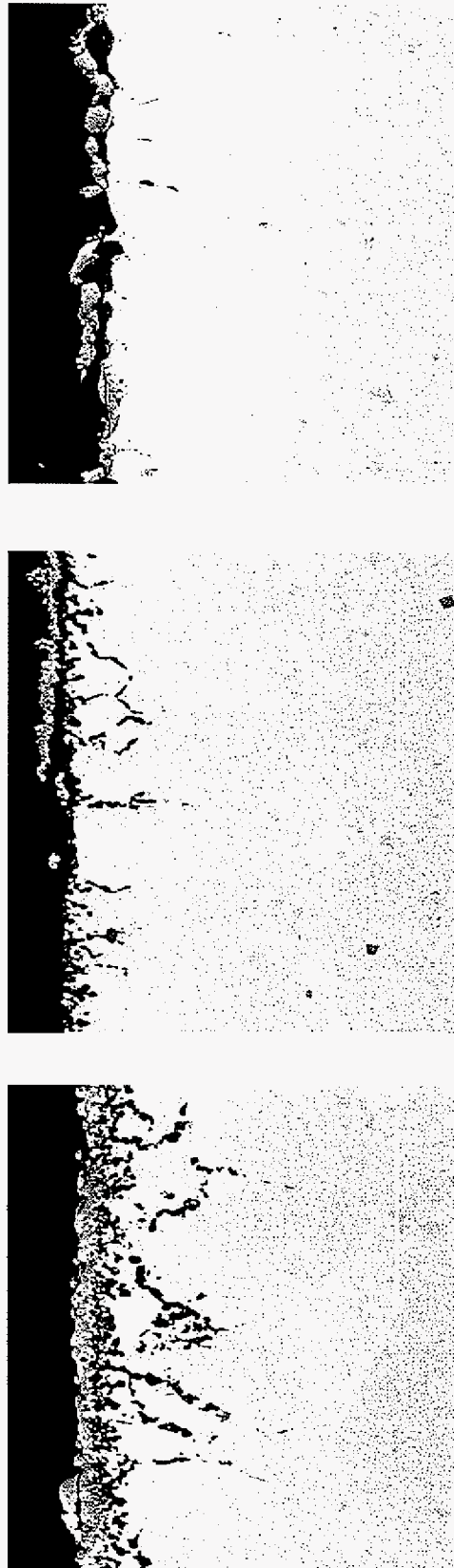
18 1-day cycles

Isothermal 7days

Isothermal 28days

Figure 6.9. Cross-sectional SEM image of the 45TM alloy after different cyclic and isothermal oxidation tests at 1000°C.
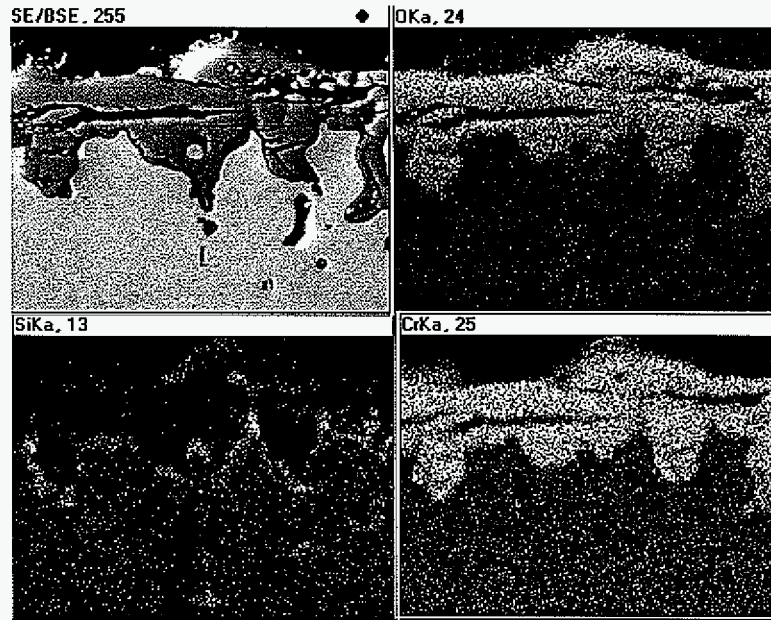
Figure 6.10. Cross-sectional SEM image and corresponding X-ray maps
of the HR-160 alloy after 18 1-day cycles at 1000°C.
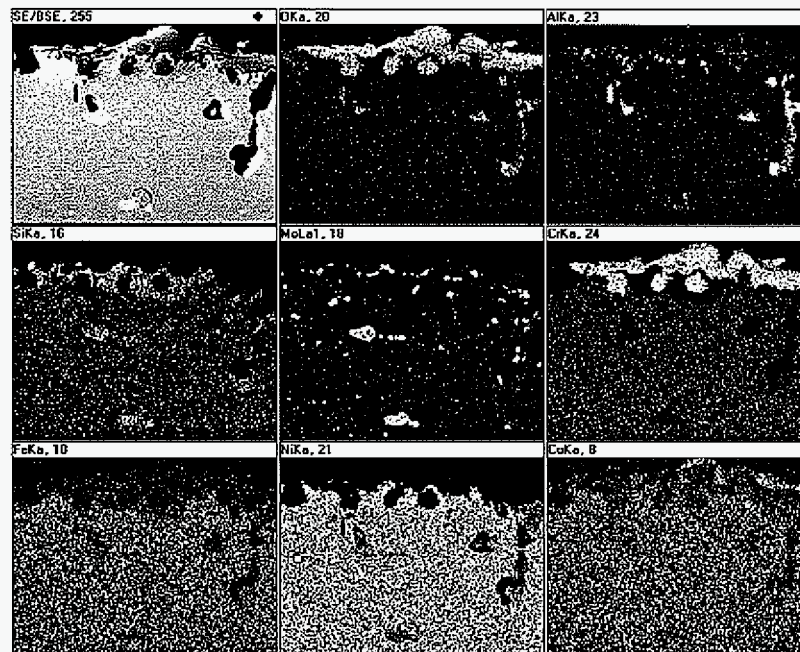
Figure 6.11. Cross-sectional SEM image and corresponding X-ray maps of
the D-205 alloy after 18 1-day oxidation cycles at 1000°C.
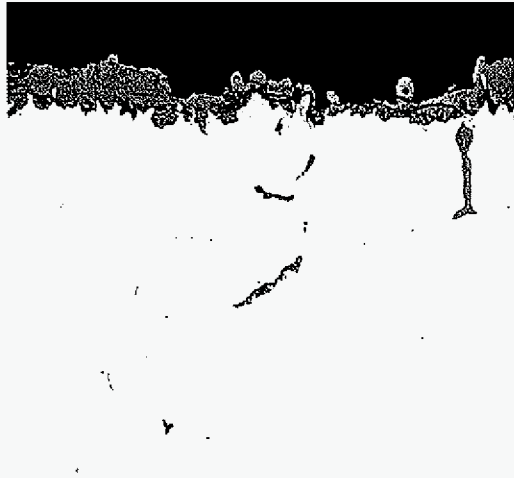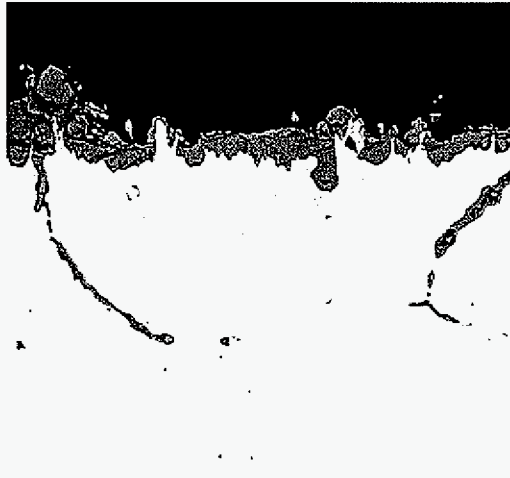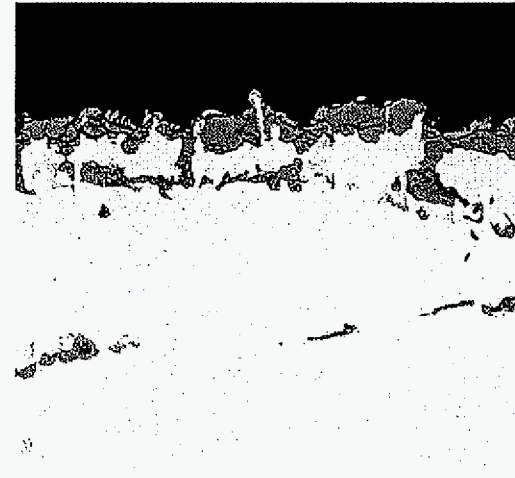
NiCrSi   NiCrFeSi   NiCrCoSi

Figure 6.12. Cross-sectional SEM image of the cast alloys NiCrSi, NiCrFeSi, and NiCrCoSi after different 18 1-day cyclic oxidation tests at 1000°C.

NiCrCoSi alloys after 18 1-day oxidation cycles at 1000 °C. Each of those cast alloys formed a non-planar alloy/scale interface, with the NiCrSi alloy being the least non-planar. It was found that the scale spallation occurred primarily at the metal protrusion front in the oxide scale. As a consequence, the remaining scale was highly variable in thickness. No apparent Si-rich oxide formed in the three Si-containing NiCr-based alloys. Inspection of the NiCrSi alloy surface after 104 1-day oxidation cycles revealed the presence of Si-rich oxide associated with exposed regions of the alloy matrix (Figure 6.13). Although not shown, the other Si-containing cast NiCr-based alloys also showed the presence of Si-rich oxide after 104 1-day oxidation cycles.
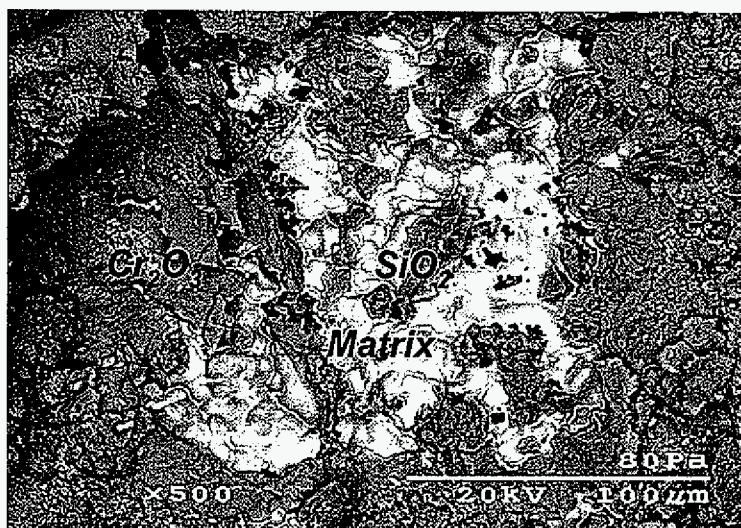
Figure 6.13. SEM surface SEM image of the cast NiCrSi alloy after 104 1-day oxidation cycles at 1000°C.

6.2.4 EPMA Measurement of Composition Profiles in the Oxidized Samples

The oxide scale and subsurface regions of the 45TM, HR-160, and D-205 alloys oxidized isothermally for 7 days at 1000 °C were analyzed using EPMA. The results are shown in Figure 6.14. As would be expected from the differences in scaling rate constants for those
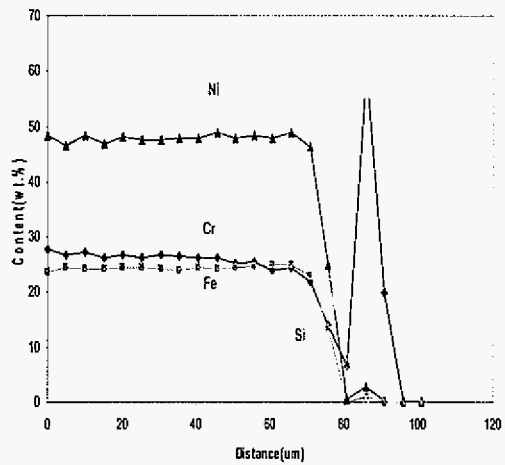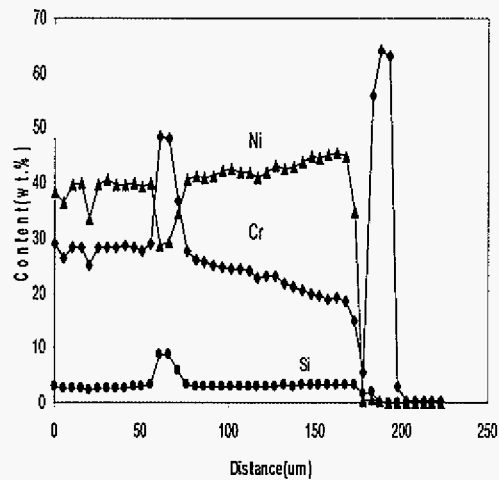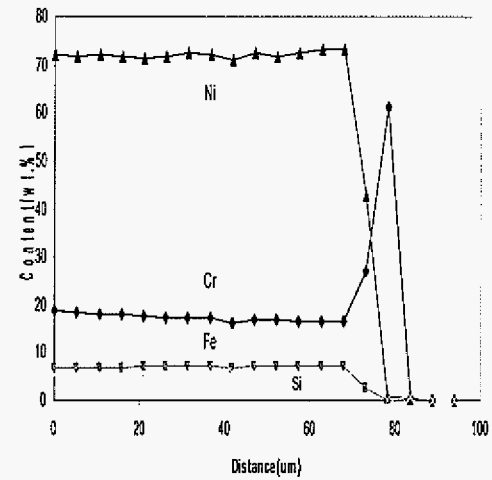
45TM   **HR-160**   **D-205**

Figure 6.14. Concentration profiles in the 45TM, HR-160, and D-205 alloys studied after seven days isothermal oxidation at 1000 °C. Distance is measured from within the alloy to the scale surface.

alloys, there were differences in the composition profiles. After 7 days oxidation, N_{Cr}^{i} was about 5 wt.% for the 45TM and HR-160 alloys, and the chromium profiles were very steep near the scale/alloy interface, i.e., about 8 wt.%/μm. The rate of Cr depletion at the alloy/scale interface was smallest for the D-205 alloy, with N_{Cr}^{i} almost 16 wt. %. It is also seen in Fig. 6.14 that the scale thickness was the largest for the HR-160 alloy (about 25 μm), while for the other two alloys the scales were about 15 μm thick. These results are in agreement with the HR-160 alloy having a larger parabolic rate constant than D-205 and 45TM (Table 6.4). The 45TM alloy developed a Si-rich subsurface region beneath the scale/alloy interface and within the steep Cr depletion region, which is consistent with the SEM and EDS results (Fig. 6.9). It is possible that the interfacial enrichment of silicon could not be detected in D-205 and HR-160 because these Si-rich regions were too thin to be resolvable by EPMA.

Table 6.6 gives the average effective interdiffusion coefficients of chromium, $\tilde{D}_{Cr}^{eff}$, using the measured chromium profiles after 7-day isothermal oxidation and Dayananda's model (Eq. 2.58). It can be seen that 45TM had the smallest $\tilde{D}_{Cr}^{eff}$ (1.9×10^{-12} cm^{2}s^{-1}), while HR-160 had the largest $\tilde{D}_{Cr}^{eff}$ (1.6×10^{-11} cm^{2}s^{-1}), followed by D-205 (1.2×10^{-11} cm^{2}s^{-1}).

Table 6.6. The average effective interdiffusion coefficient of Cr ($\tilde{D}_{Cr}^{eff}$) determined from the alloys isothermally oxidized after 7 days in air at 1000 °C.

Alloys	$\tilde{D}_{Cr}^{eff}$ (cm^{2}s^{-1})
45TM	1.9×10^{-12}
HR-160	1.6×10^{-11}
D-205	1.2×10^{-11}

The subsurface chromium concentration profiles in the cast NiCr-based alloys were analyzed using EDS, and the profiles after 7-day isothermal oxidation at 1000 °C are shown in Figure 6.15. The NiCr-based alloys without silicon addition showed lower interfacial Cr
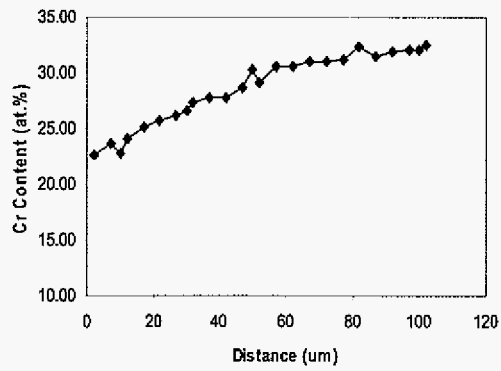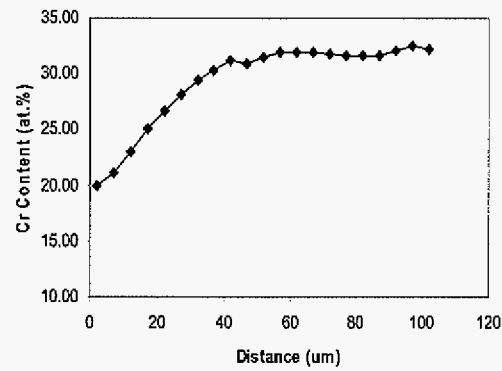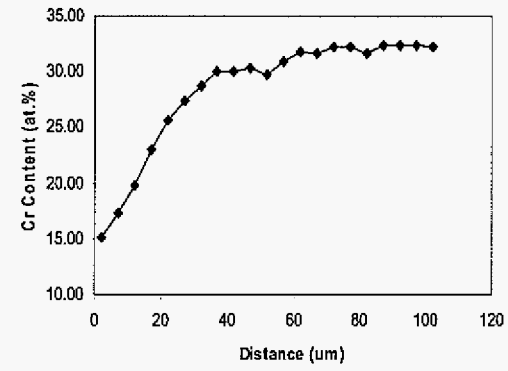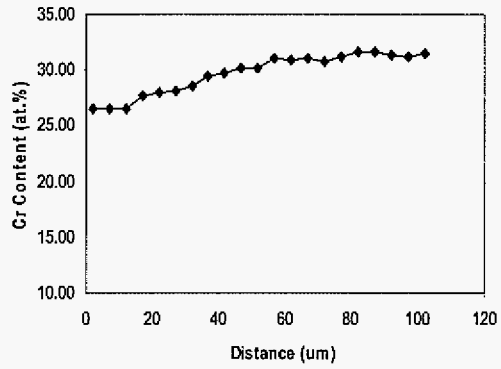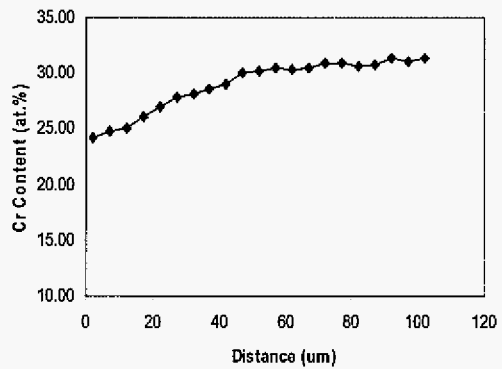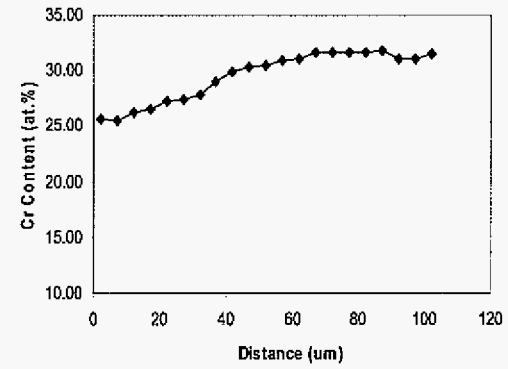
Figure 6.15. Subsurface Cr profiles of the cast NiCr-based alloys
after 7 days isothermal oxidation in air at 1000 °C.

contents than those measured in the NiCr-based alloys with silicon addition. The NiCrCo alloy showed the lowest interfacial Cr content (about 13.5 at.%). A higher interfacial Cr content (about 19 at.%) was detected in the NiCrFe alloy, while the NiCr alloy had an interfacial Cr content of about 22.5 at.%. The results of interfacial Cr content in the NiCr-based alloys without Si addition were consistent with their oxidation behaviors, with the lower interfacial Cr content corresponding to the alloy with the poorest oxidation resistance. The Cr depletion depth in each of the three Si-containing alloys was similar, at about 100 μm. The NiCrCo alloy showed the steepest Cr depletion profile within the alloy in the vicinity of the scale/alloy interface, while the NiCr alloy showed the shallowest. Addition of silicon significantly increased the interfacial Cr content to about 24-26 at.% in the NiCrSi, NiCrFeSi, and NiCrCoSi alloys. Applying the Dayananda's model (Equation 2.58), the average effective interdiffusion coefficient of chromium, $\tilde{D}_{Cr}^{eff}$, was determined for each of the cast NiCr-based alloys (Table 6.7). Fig. 6.16 compares the $\tilde{D}_{Cr}^{eff}$ values. It is clearly seen

Table 6.7. The average effective interdiffusion coefficient of Cr ($\tilde{D}_{Cr}^{eff}$) for the cast NiCr-based alloys determined from subsurface depletion profiles resulting from 7 days isothermal oxidation in air at 1000 °C.

Alloys	$\tilde{D}_{Cr}^{eff}$ (cm^{2}s^{-1})
NiCr	1.5×10^{-11}
NiCrFe	1.3×10^{-11}
NiCrCo	7.0×10^{-12}
NiCrSi	2.6×10^{-11}
NiCrFeSi	2.1×10^{-11}
NiCrCoSi	1.1×10^{-11}

in this figure that Si addition increases the average effective interdiffusion coefficient of chromium, while Fe and Co decreased $\tilde{D}_{Cr}^{eff}$, with more decrease by Co than by Fe. The calculated $\tilde{D}_{Cr}^{eff}$ results are consistent with the results in Chapter 5, in which the VDM alloys with higher silicon contents had larger $\tilde{D}_{Cr}^{eff}$ values than the SM alloys containing lower silicon contents.
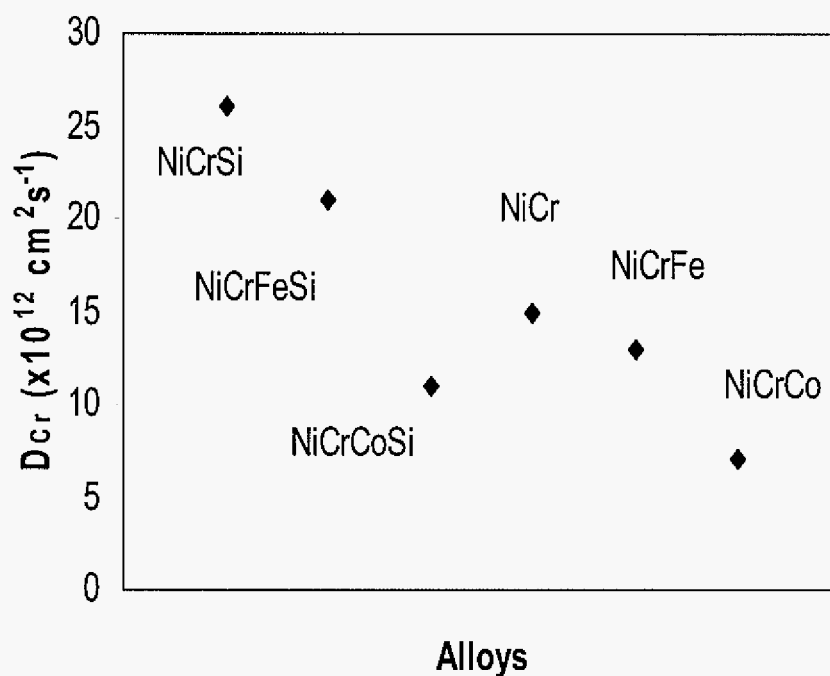
Figure 6.16. Comparison of average effective interdiffusion coefficient of Cr in the NiCr-based alloys at 1000 °C.

6.3 Discussion

The experimental results showed that Si addition measurably influences the oxidation resistance of the low-Si Fe-base and high-Si Ni-base alloys. The low-Si Fe-base alloys did not form a resolvable (by SEM) continuous SiO_2 layer during oxidation, and the distribution of internal SiO_2 particles at the alloy/scale interface in these alloys appeared to have significantly affected oxidation behavior. A continuous SiO_2 layer may have formed in the high-Si alloys; however, the relatively dense dispersion of SiO_2 particles within the subsurface region of the 45TM alloy may have been sufficient to provide its good oxidation resistance during 1-day cyclic oxidation at 1000 °C. The following sections will discuss the effect of Si addition according to two alloy groups studied: low-Si Fe-base and high-Si Ni-base alloys.

6.3.1 Low-Si Fe-Based Alloys

The 800 series alloys belong to this group, as they contain a low silicon content (<1 wt.%) and a high Fe content (> 40 wt.%). With increasing Si content, the SM 800 alloys showed better cyclic oxidation resistance at 1000 °C. The results conclusively demonstrated the beneficial effect of Si on the cyclic oxidation resistance of the 800 alloys. However, the VDM800 alloy, which had a lower Si content (0.38 wt.% Si) than 800-2 (0.77 wt.% Si), showed the best oxidation resistance of the alloys studied (800, 800-1, 800-2, VDM800). Thus, other minor elements, such as Ti, Al, and Mn, which are apt to form external and/or internal oxides, also play a role in affecting oxidation behavior.

The four 800 series alloys showed different steady-state parabolic rate constants (Table 6.4) even though they formed the same scale phases (primarily a Cr_2O_3 layer with a thin outer $MnCr_2O_4$ layer) during isothermal oxidation (Table 6.5). The largest oxidation rate of the 800 alloy was consistent with the thickest observed scale, which was prone to spallation during cyclic oxidation. As a result, the 800 alloy showed the poorest oxidation resistance of the four alloys studied (Fig. 6.3). The VDM800 alloy had the smallest parabolic rate constant, which apparently contributed to it exhibiting the best oxidation behavior (Fig. 6.6).

The four 800 series alloys showed a similar initial transient oxidation duration (3-5 hours), which suggests that silicon content only marginally affected transient oxidation kinetics. It may be inferred that the small amount of Si (< 1 wt.%) was insufficient to form a large amount of Si-rich oxide to affect the transient oxidation.

The oxides of Ti, Si, and Al, are thermodynamically more stable than chromia and therefore these elements can internally oxidize in chromia-forming alloys, which is generally detrimental to oxidation resistance. The Ti+Si+Al content was least in the VDM800 alloy (about 0.83 wt.%) and, accordingly, this alloy showed the least amount of internal oxidation. Notwithstanding, the silicon content in the VDM800 alloy (0.38 wt.%) was apparently sufficient to form Si-rich oxide particles along the alloy/scale interface. These oxide particles may have acted to impede oxygen diffusion inward and chromium diffusion outward, which would have contributed to the VDM800 alloy exhibiting the least amount of internal oxidation and forming the thinnest scale.

The 800 alloy formed the least amount of Si-rich oxide particles at the alloy/scale interface, which is in accordance with this alloy having the lowest Si content (0.13 wt.%). As shown by other studies [74,88,115,143,202], silicon facilitates chromium scale formation. The low silicon content in the 800 alloy may be not have been enough to establish sufficient chromia-scale formation. Thus, the 800 alloy formed faster-growing oxides during the transient oxidation stage, as evidenced by its largest transient scaling kinetics (Fig. 4.9). Since the 800 alloy also did not form sufficient SiO_2 particles at the alloy/scale interface to suppress the diffusion of chromium and oxygen, the steady-state oxidation of this alloy resulted in its forming the thickest oxide scale and a large amount of internal oxide. Both of these factors contributed to the 800 alloy exhibiting the poorest oxidation resistance of the four alloys studied.

The higher Si contents in the 800-1 and 800-2 alloys contributed to their better oxidation resistance compared to the 800 alloy. The 800-1 and 800-2 alloys formed Si-rich oxide particles (SiO_2) at the alloy/scale interface, and the 800-2 alloy further formed Si-rich oxide within the vicinity of subsurface region of the alloy. As in the case of the VDM800 alloy, the SiO_2 formed at the alloy/scale interface in 800-1 and 800-2 would have acted to impede to

some extent the diffusion of Cr outward and oxygen inward, thus resulting in a slower oxide growth rate and less internal oxidation compared to the 800 alloy.

It was found that the amount of oxide protrusions into the alloy along the alloy/scale interface increased with increasing of silicon content, with the most being in 800-2 and the least in 800 (Fig. 6.6). The 800-1 alloy also showed a larger amount of oxide protrusions than the VDM800 alloy, even though the two alloys had a similar silicon content (0.39 and 0.38 wt.% for 800-1 and VDM800, respectively). It is believed that the different Ti contents in the two latter alloys result in their difference in amount of oxide protrusions: the 800-1 alloy had a higher Ti content (0.42 wt.%) than the VDM800 alloy (0.32 wt.%). Titanium oxide (TiO_2) is thermodynamically more stable than chromia. Thus, TiO_2 could nucleate at the front of chromia scale, and EDS detected Ti-rich oxide combined with Cr-rich oxide at the front of oxide protrusion. Litz *et al.* [198] reported that TiO_2 provides a fast oxygen diffusion path, which promotes further internal oxidation and decreases the overall oxidation resistance of the alloy. It is postulated here that the Ti-rich oxide alloy boundary can offer fast short-circuit diffusion path for oxygen and chromium, which would facilitate the formation of chromia around the Ti-rich oxide. This is shown schematically in Fig. 6.17. Thus, it is inferred that the presence of Ti in the alloy contributed to the formation of oxide protrusions so that more oxide protrusions developed in 800-1 than in VDM800. With the growth of oxide protrusions into alloy matrix at the alloy/scale interface into alloy matrix, metal between the protrusions became incorporated as inclusions in the oxide scale. As discussed in Chapter 5, the large amount of oxide protrusions and metal inclusions at the alloy/scale interface in the 800-2 alloy contributed to it having poorer oxidation resistance than the VDM800 alloy.

The 800-2 alloy also showed a larger extent of internal oxidation than the VDM800 and 800-1 alloys. It is believed that higher Ti+Si+Al in 800-2 (1.58 wt.%) resulted in its large extent of internal oxidation. The larger extent of internal oxidation must have, in turn, detrimentally affected the oxidation behavior of the 800-2 alloy compared to the VDM800 alloy.

O₂ → O_2
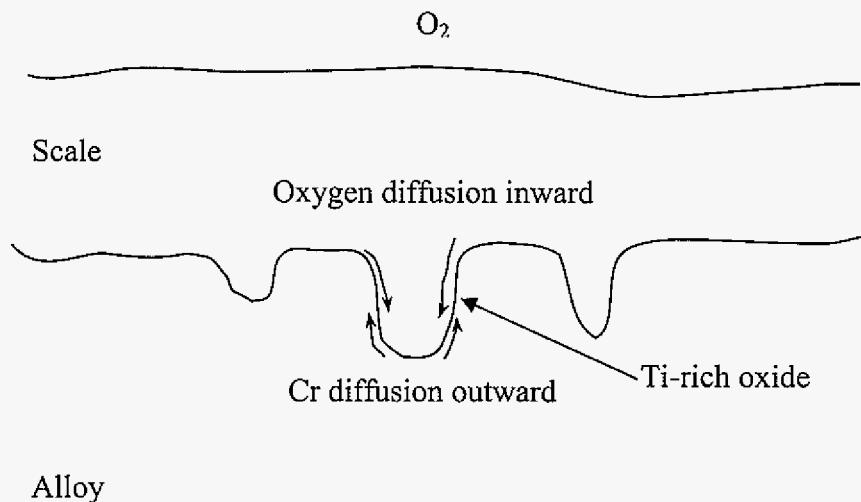
Figure 6.17. Schematic indicating the short-circuit phase-boundary diffusion paths provided by the Ti-rich oxide protrusions.

Cracks developed in the oxide scales of the 800-1 and 800-2 alloys that appeared to have originated from the roots of oxide protrusions (Fig. 6.6). It is believed that the oxide protrusions were crack initiation sited due, in part, to larger state of stress in the vicinity of the protrusion. Table 6.8 lists the molar volume and CTE of the 800 alloy matrix, and the

Table 6.8. Equivalent molar volume and CTE values of oxides and the alloy studied [50,51,207].

Alloy and oxides	Molecular molar volume	CTE $(x10^6\,K^{-1})$
Alloy 800	7.0	15.8 (20-300 °C)
Cr_2O_3	5.8	7.3 (100-1000 °C)
TiO_2	6.3	7.2-10.6 (20-277 °C)

oxides Cr_2O_3 and TiO_2. The difference of the CTE values is seen to be greatest between the 800 alloy and the two oxides. This difference would result in thermal stresses during temperature change. Finite element simulations by Rosler *et al.* [208] showed that cracks would develop in a thermal barrier coating (TBC) system at the peak of a thermally grown oxide (TGO) if stresses are controlled by CTE-misfit (Figure 6.18). The 800 alloy had a similar structure at the alloy/scale interface to that considered in the model of Rosler *et al.*. In the context of this study, cracks developed at the "peaks" of the alloy protrusions. Thus, a large amount of oxide (and therefore alloy) protrusions at the alloy/scale interface would promote cracking within the oxide scale during thermal cycling.
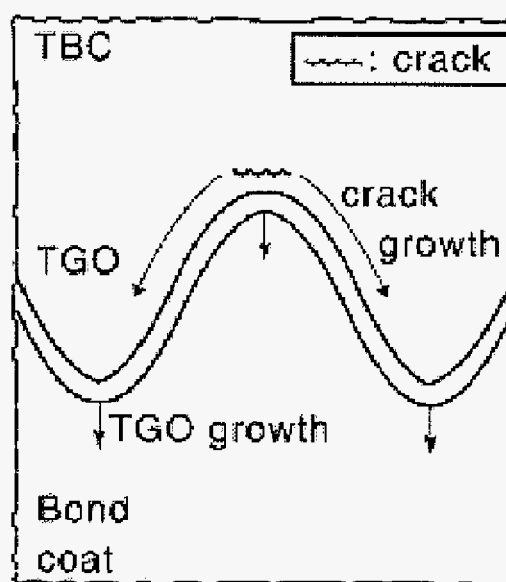
Figure 6.18. Stress state and failure mechanisms of thermal barrier coating.

Based on the above analysis, the VDM800 alloy showed the best oxidation resistance in the four low-Si alloys studied because it has an optimum content of minor elements. A low amount of Ti+Al minimized its internal oxidation, while 0.38 wt.% Si was sufficient to form SiO_2 particles at the alloy/scale interface, which beneficially impeded diffusion of oxygen inward and chromium outward. Too high a Si content in the 800 series alloys promoted the

formation of oxide protrusions, which promoted cracking in the scale during thermal cycling. Thus, the intermediate level of silicon content coupled with a relatively small amount of Ti content in the VDM800 alloy limited the development of oxide protrusions along the alloy/scale interface, which significantly contributed to this alloy exhibiting the best oxidation resistance. The further effect of silicon on the subsurface depletion and diffusion behavior will be discussed in greater detail in following section.

6.3.2 High-Si Ni-Based Alloys

The 45TM, HR-160, and D-205 alloys exhibited different oxidation behaviors during long-term, 1-day cyclic oxidation in still air at 1000 °C. The ranking of the alloys from best to worst was in the order: 45TM > HR-160 > D-205. The 45TM exhibited good oxidation resistance, while HR-160 and D-205 experienced different extents of spallation. In general, however, it is believed that silicon was beneficial to the oxidation resistance of the D-205, HR-160 and 45TM alloys. This beneficial effect could not be explicitly identified due to the interplay of many factors.

In the high-Si alloys studied, 45TM and HR-160 had close Si contents (about 2.7 wt.%), but showed significantly different oxidation behavior. The 45TM alloy did not experience apparent spallation during long-term 1-day cyclic oxidation at 1000 °C, while HR-160 showed large spallation from the initial one or two cycles. The observed difference in the cyclic oxidation behavior of 45TM and HR-160 can be partly ascribed to a difference in scale spallation behavior which, in turn, can be related to differences in both scale properties and alloy compositions. The 45TM alloy has a high Fe content (*i.e.*, ~22 wt%), while HR-160 has a high Co content (*i.e.*, ~28 wt%). It is well established that the growth rate of a Cr_2O_3 scale can vary over several orders of magnitude at a given temperature when the subsurface composition varies [191]. Somewhat related, Frederick and Cornet [209] found that more than 11% cobalt caused a rapid increase in the rate of nickel oxidation in air at temperatures ranging from 800-1400 °C. In the present study, it was found that the HR-160 alloy with a relatively high cobalt content formed a Cr_2O_3 scale at the highest growth rate (Table 6.4). The reason for this apparent cobalt effect is not yet understood. The high rate of scale growth on HR-160 may be partly related to the adjustment of the boundary conditions at the

alloy/scale interface, as influenced by the high cobalt content, causing increased rates of diffusion in Cr_2O_3 scale layer.

There was a large amount of what were inferred to be finely distributed SiO_2 precipitates within the alloy at the scale/alloy interface in the 45TM alloy, whereas HR-160 formed an apparently continuous SiO_2 layer at the scale/alloy interface (Fig. 6.8 and Fig. 6.10). The results indicate that a SiO_2 precipitate distribution is much less detrimental from the standpoint of scale spallation than if the SiO_2 was continuous. A sufficient amount of finely distributed subsurface SiO_2 precipitates in 45TM could also act to impede the diffusion of oxygen inward and chromium outward. This blocking effect contributed to the 45TM alloy showing the smallest parabolic rate constant for the three commercial Ni-based alloys studied. 45TM developed voids at the alloy/scale interface that were often associated with SiO_2 particles. Voids at the alloy/scale interface may be expected to worsen cyclic oxidation resistance. However, the good cyclic oxidation behavior of 45TM suggested that the presence of voids at the alloy/scale interface did not decrease cyclic oxidation resistance to any significant extent. What is apparently more important is the SiO_2 distribution beneath the chromia scale. In the case of HR-160, a thin continuous silica layer (about 0.8 μm) developed at the nonplanar scale/alloy interface (Fig. 6.10). The difference in the manner in which the SiO_2 formed in 45TM and HR-160 may be indicative of the diffusivity of silicon being higher in HR-160 than in 45TM. It is important to realize, however, that another possible factor that would contribute to the formation of a continuous SiO_2 layer is a lower oxygen permeability in HR-160 compared to 45TM. Sufficient data are not available to develop this line of analysis any further.

The silicon in the D-205 alloy behaved much differently by reacting with molybdenum to form $MoSi_2$ at the alloy/scale interface. $MoSi_2$ is known to undergo catastrophic "pesting" oxidation at 500 to 700 °C [210,211]. The mechanism of "pesting" is associated with stresses from a voluminous oxidation product of an inward-growing microfilament mixture of SiO_2 and MoO_x. It is possible that the eventual dissolution of $MoSi_2$ contributed the formation of a silicon-rich inner layer on D-205, which may have then suppressed oxygen diffusion inward, and hence decreased the extent of internal oxidation. The exact composition of the silicon-rich inner layer could not be determined. It could possibly be nickel silicide or silicon nitride.

The EPMA results for D-205 (Fig. 6.14) showed almost no subsurface depletion of Cr, Fe and Si, which may be due to the silicon-rich inner layer acting as a barrier and thereby allowing for the homogenization of these elements in the subsurface region of the alloy. However, this barrier apparently also hindered healing or re-formation of the protective scale. Thus D-205 exhibited poorer oxidation resistance than 45TM and HR-160 despite its higher Si content. The Si- and Mo-rich inner layer would also bring about a volume change at the scale/alloy interface to the extent that it may have possibly weakened the scale/alloy interface strength.

From the EPMA results, the three alloys were found to exhibit different Cr subsurface depletion profiles after isothermal oxidation. The 45TM and HR-160 alloys developed subsurface chromium profiles in which the interfacial chromium concentrations dropped below 5 wt%. Even so, the 45TM and HR-160 alloys showed significantly different oxidation behavior, as there was almost no scale spallation from 45TM, but there was large spallation from HR-160. As discussed above, this can be ascribed in part to the influence of minor elements on oxidation behavior, silicon in particular.

The interfacial chromium content in the HR-160 alloy dropped steeply within just 10 μm beneath the scale/alloy interface. This is true even though a relatively large average effective interdiffusion coefficient of chromium was detrimental for HR-160. Harper and Walker [156] studied the oxidation and corresponding subsurface depletion behavior in several chromia-forming alloys at 1050 °C. They found that $\tilde{D}_{Cr}^{\textit{eff}}$ in DS alloy, which has relatively high silicon content (2.51 wt%), was the highest of the alloys studied. In the present study, there was also found to be an influence of silicon on $\tilde{D}_{Cr}^{\textit{eff}}$; however, the trend was not clear. The 45TM alloy with ~2.7 wt% silicon showed the lowest $\tilde{D}_{Cr}^{\textit{eff}}$, while $\tilde{D}_{Cr}^{\textit{eff}}$ in the D-205 alloy with ~5 wt% silicon showed a larger $\tilde{D}_{Cr}^{\textit{eff}}$, being one order magnitude larger than in 45TM. The HR-160 had the largest $\tilde{D}_{Cr}^{\textit{eff}}$ although its Si content is less than that in D-205. The Si-effect on $\tilde{D}_{Cr}^{\textit{eff}}$ may be affected by oxide distribution and other elements, Co, Fe, and RE. Compared with the effect of silica distribution, the effect of $\tilde{D}_{Cr}^{\textit{eff}}$ on oxidation resistance was less apparent in the three alloys studied.

The NiCr-based alloys with Si addition showed a short transient stage of about 40 minutes, followed by an intermediate stage of about 15 hours, and then eventually to a steady-state oxidation behavior (Fig. 6.1). It is believed that a silica layer formed during the early stages of oxidation (as early as 40 minutes) because the growth rate of the NiCr-based alloys with Si additions showed a significant decrease in the scaling kinetics after about 40 minutes. Thus, the intermediate stage (about 15 hours before the steady-state oxidation) is postulated to be due to the development of a thin inner silica layer. The early establishment of an inner SiO_2 layer is supported by the results of Ahmad and Fox [175], who studied the transient oxidation of a Ni-20Cr-1.29Si-0.42Mn-0.20Al-0.46Fe alloy at 950 °C, and found that a very thin and continuous silica layer (~3nm) formed after about 25 minutes. The addition of Si to the NiCrCo and NiCrFe also significantly reduced the effect of Co and Fe on increasing the scaling kinetics. This can be attributed to the formation of a continuous silica layer on the Si-containing alloys.

The NiCr-based alloys with Si addition were similar in cross-section after 18 1-day oxidation cycles: spalled chromia scale, non-planar alloy/scale interface, and interdendritic internal oxidation (Fig. 6.12). The morphology results are consistent with the similar oxidation kinetics of these alloys. The Si-containing alloys were also found to have a higher interfacial Cr content, large $\widetilde{D}_{Cr}^{\it eff}$, significantly smaller k_p, but similar Cr depletion depth (about 100 μm), compared to the NiCr-based alloys without Si addition. The results show that the subsurface depletion profile of a selectively oxidized element is dependent upon both k_p and $\widetilde{D}_{Cr}^{\it eff}$. Specifically, the larger $\widetilde{D}_{Cr}^{\it eff}$ and small k_p for the Si-containing alloys combined to result in relatively high interfacial Cr contents, which is beneficial from the standpoint of chromia-scale reformation after spallation. The similar k_p and $\widetilde{D}_{Cr}^{\it eff}$ values found for the Si-containing NiCr-based alloys resulted in their similar interfacial Cr contents after steady-state, isothermal oxidation (Fig. 6.16).

Addition of Fe and Co to the NiCr alloy caused an increase in the scale growth rate, but an apparent decrease in $\widetilde{D}_{Cr}^{\it eff}$. The combination of these two effects resulted in poorer oxidation performance. The detrimental effect of Fe on oxidation behavior was discussed in Chapter 4. From the current study, Co is also found to detrimentally affect the oxidation behavior of

NiCr-based alloys. NiO and CoO have the same crystal structure (NaCl type structure) and almost the same lattice parameter (4.17 Å for NiO and 4.25 Å for CoO). The activation energy for oxidation of Co at high temperature is only slightly lower than that for Ni, but Co oxidizes about 25 times faster than Ni [13,209]. The addition of cobalt to chromia should decrease the number of cation vacancies ($V_{Cr}^{'}$) according, for example, to the reaction:

$$2CoO + 2V_{Cr}^{'} + \frac{1}{2}O_2 = 2Co_{Cr}^{'} + 3O_O \qquad (6.1)$$
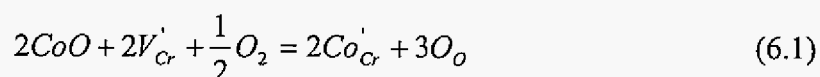
This would have the effect of decreasing the diffusive flux of chromium in Cr_2O_3, which in turn would decrease the scaling kinetics [13,212,213]. XRD analysis showed that $CoCr_2O_4$ formed with Cr_2O_3 and $NiCr_2O_4$ on the NiCrCo alloy. Thus, the increased scaling kinetics on this alloy must be largely attributed to cobalt oxidation and to the change in the boundary conditions at the alloy/scale interface for scale growth. These effects outweighed any beneficial doping effect of Co in Cr_2O_3.

Fe and Co apparently decreased $\tilde{D}_{Cr}^{eff}$ in the NiCr-based alloys. The diffusion process involves the movement of atoms in an alloy, and movement of atoms requires the breaking of bonds, which exists between the metal atoms. Strong metallic bonding will restrict the movement of an atom and thus result in a low diffusion coefficient. The melting point of a solid indicates the temperature to which the material must be subjected to provide sufficient thermal energy to break its bonds [214]. Thus, metals having high melting points suggest strong bonds between the atoms. Table 6.9 summarizes the equilibrium temperature for onset of liquid-phase formation during heating of different Ni-based alloys. It is seen that Ni-based alloys with Fe or Co addition have higher the equilibrium temperature of liquid phase formation. It is therefore concluded that Fe or Co addition increases the metallic bond strength in the NiCr-based alloys, thus hindering atom movement and consequently decreasing $\tilde{D}_{Cr}^{eff}$.

Table 6.9. Equilibrium temperature for liquid phase formation in Ni-based alloys [215-217].

Alloys (wt.%)	Temperature for onset of liquid phase (°C)
72Ni28Cr	1401.0
78Ni22Fe	1448.9
72Ni28Co	1461.1
50Ni28Cr22Fe	1402.8
44Ni28Cr28Co	1406.3

The wrought HR-160 alloy and the compositionally similar cast NiCrCoSi alloy had comparable oxidation kinetics ($\sim$ -25 mg/cm^2 and $\sim$ -17 mg/cm^2 after 100 cycles, respectively) and Cr interdiffusion coefficients (1.6×10^{-11} cm^2/s and 1.1×10^{-11} cm^2/s, respectively). The slightly higher scaling rate constant on HR-160 than NiCrCoSi is quite possibly due to the present of Mn ($\sim$0.59 wt.%) in HR-160, which oxidized to form MnCr$_2$O$_4$ during the early stages of oxidation (Table 6.5). By contrast, the wrought 45TM and cast NiCrFeSi alloys were similar in composition, but the two alloys showed significantly different oxidation kinetics, subsurface oxide formation, and Cr interdiffusion behavior. Dispersed SiO$_2$ particles formed in the subsurface region of 45TM contributed to its good cyclic oxidation resistance. However, no similar types of SiO$_2$ particle dispersion formed within the subsurface region in the NiCrFeSi alloy. The significant difference in oxidation behavior of the wrought 45TM alloy and the cast NiCrFeSi alloy is believed to be related to their chemical compositions rather than, for instance, their microstructure. One apparent difference is that 45TM contains a reactive element, Ce, which is generally found to be beneficial to oxidation resistance [115]. The addition of Ce in the 45TM alloy may have aided in promoting the dispersive formation of SiO$_2$ particles in the subsurface, the mechanism of which is beyond the scope of this thesis.

The steep subsurface Cr depletion profile near the alloy/scale interface in 45TM coincided with a Si enrichment profile (Fig. 6.14), which may have affected the calculation of $\tilde{D}_{Cr}^{eff}$.

Adjusting for no Si-enriched region in 45TM, the interfacial Cr content would go up and the interdiffusion coefficient of chromium in matrix should increase due to a consequential decrease in the Cr gradient at the alloy/scale interface, , as seen from the following equation,

$$\widetilde{J}_{Cr} = \widetilde{D}_{Cr} \frac{\partial N_{Cr}}{\partial x} \tag{6.2}$$

After adjusting for the presence of Si enrichment near the alloy/scale interface, the average effective interdiffusion coefficient of chromium in 45TM after 7-day isothermal oxidation at 1000 °C is calculated to be 5×10^{-12} cm^2/s, which is still the smallest of the three alloys studied. Thus, there should be other factors attributing to the small $\widetilde{D}_{Cr}^{\textit{eff}}$ in 45TM. Addition of Ce may affect the interdiffusion coefficient of Cr in 45TM; however, there are insufficient data to support this point.

6.4 Conclusions

The alloys with different silicon contents exhibited a large variation in resistance to cyclic oxidation at 1000°C in air. Increasing the Si content in the SM alloys (<1 wt.%) resulted in improved oxidation resistance. Formation of Si-rich oxide particles at the alloy/scale interface is believed to aid by impeding the diffusion of oxygen and chromium, thus decreasing oxidation kinetics of the 800 alloys. A higher silicon content facilitates the formation of oxide protrusion, such as Cr_2O_3 and TiO_2, at the alloy/scale interface of the Ti-containing alloys, which can result in larger stresses and poorer spallation resistance. Ti can oxidize at the alloy/scale interface, which induces complex stresses and initiates the formation of cracks along the alloy/scale interface. Higher minor alloying element content of Ti or Al also increases the extent of internal oxidation, which could offset the beneficial effect of silicon. Thus, the VDM800 alloy shows an optimum composition, proper Si content and low Ti+Al content, which provided the best oxidation behavior in the 800 series alloys.

The high-Si (>2 wt.%) Ni-base alloys in the current study showed different oxidation behavior. Silicon oxidized and formed what was inferred to be a continuous SiO_2 layer at the alloy/scale interface or a dispersion of SiO_2 particles in the subsurface region of the alloys. The formation of a disperse distribution of SiO_2 particle in the vicinity of the scale/alloy

interface in the 45TM alloy apparently caused a decrease in the growth rate of the Cr_2O_3 scale. The fast diffusion of silicon in 160-HR promoted the formation of a continuous SiO_2 layer, which partially blocked oxygen diffusion inward and resulted in less internal oxidation attack. The development of a continuous silica layer initiated the formation of cracks within the scale and a general weakening of scale strength during cyclic oxidation.

Molybdenum in the D-205 alloy reacted with silicon to form $MoSi_2$, which aggregated along the scale/alloy interface and affected the silicon distribution. The eventual development of silicon-rich and molybdenum-rich layer beneath the scale/alloy interface blocked oxygen diffusion inward and depletion of chromium from the subsurface, thus resulting in less internal oxidation, but also caused less healing of protective oxide and a weakening of the scale adhesion.

Addition of Fe and Co to a NiCr-based alloy increased oxidation growth rate and resulted in poorer cyclic oxidation resistance, while addition of Si decreased oxide growth rate, and thus improved cyclic oxidation resistance.

It was found that $\tilde{D}_{Cr}^{eff}$ is very sensitive to the alloy compositions. Higher Si content may increase the value of $\tilde{D}_{Cr}^{eff}$. Larger $\tilde{D}_{Cr}^{eff}$ could supply sufficient chromium to compensate the chromium consumption due to the formation of chromia scale, and thus facilitates the re-formation of chromia scale and improve oxidation resistance. Addition of Fe and Co in NiCr alloy decreases the interdiffusion coefficient of chromium and increases the scaling kinetics, thus resulting in poorer oxidation behavior.

CHAPTER 7 PREDICTION OF CYCLIC OXIDATION RESISTANCE FOR CHROMIA-FORMING ALLOYS

7.1 Introduction

The formation of a chromia scale on an alloy results in the development of a subsurface depletion profile of chromium. As was shown in Fig. 2.25, the chromium concentration in the alloy at the alloy/scale interface lowers to a value given as, N_{Cr}^i, after some period of selective chromia formation. In order to sustain oxidation resistance, chromia formers require sufficient diffusion of chromium from the alloy bulk to the alloy/scale interface to maintain $N_{Cr}^i > N_{Cr}^*$. The ability to predict the subsurface depletion profile of chromium as a function of oxidation schedule would be required for any lifetime prediction model of chromia-forming alloys.

The prediction of subsurface depletion requires a holistic characterization of the oxidation process. A typical weight-change behavior during the cyclic oxidation of a chromia-forming alloy is illustrated in Figure 7.1. Initially a weight gain is usually observed from the oxygen uptake associated with the scale growth (o → a in the Fig. 7.1). After reaching a certain scale thickness (or, conversely, after a certain number of thermal cycles), weight loss occurs due to partial scale spallation. The rate of this weight loss is determined by the combined extents of scale spallation and scale formation. Continued spallation eventuates in a negative weight change (a → b → c in Fig. 7.1). As indicated above, protective-scale breakdown will occur (point c in Fig. 7.1) if the chromium content at the alloy/scale interface is decreased beneath some critical level N_{Cr}^*. The kinetics of the oxidation process will therefore be determined by a number of factors, including:

- Chemical and mechanical properties of the alloy and oxide scale;
- Growth rate of the oxide scale;
- Spallation behavior of oxide scale;
- Diffusion behavior of chromium in the alloy to the alloy/scale interface.
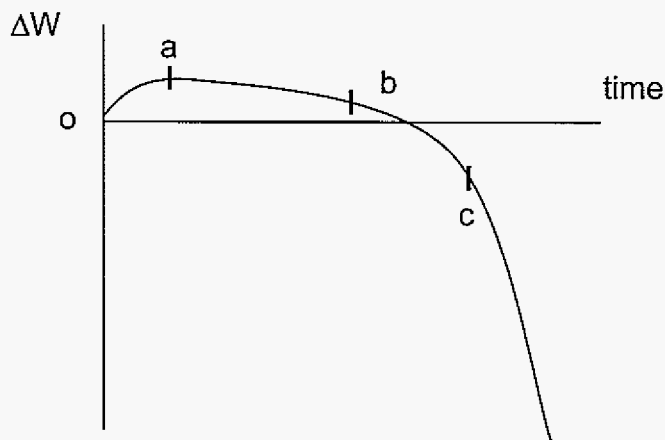
Figure 7.1. Typical long-term cyclic oxidation behavior of a chromia-forming alloy.

The first three of these factors can be obtained by chemical and microstructural analyses, gravimetrical analysis (TGA), and cyclic oxidation testing. Diffusion behavior may be approximated by the utilization of an average effective interdiffusion coefficient. The following section will briefly describe alternative methods to calculate an average effective interdiffusion coefficient, and the model to predict the extent of subsurface Cr depletion and the time to breakdown of the protective scale. It is noted that oxidation is a dynamic process, especially for cyclic oxidation, thus the effects of the principle variables used in the prediction of the subsurface depletion behavior will also be discussed.

7.2 Modeling Subsurface Chromium Depletion and Lifetime Prediction During a Selective Oxidation Process

As discussion in section 2.2.6, the diffusion process in the alloy subsurface during selective isothermal oxidation can been simulated using different types of models [64,68,132-140]. This section will briefly review models which can be used to predict subsurface chromium depletion and time to breakdown of chromia-forming alloys during cyclic oxidation.

7.2.1 Methods to Approximate Average Effective Interdiffusion Coefficient of Chromium

The resulting subsurface chromium profile after a given period of oxidation is the result of interdiffusion and the profile can therefore be used to calculate the interdiffusion coefficient. An average effective interdiffusion coefficient of chromium, $\tilde{D}_{Cr}^{eff}$, averages out cross-term effects and greatly simplifies any diffusion calculation. Dayananda [135,136] developed a method to calculate an average effective interdiffusion coefficient over the concentration profile range in a diffusion couple. For an oxidation depletion profile, the following equation based on Dayananda's method can be used to calculate $\tilde{D}_{Cr}^{eff}$,

$$\tilde{D}_{Cr}^{eff} = \frac{1}{2t} \frac{\int_{N_{Cr}^{i}}^{N_{Cr}^{o}} (x - x_o)^2 dN_{Cr}}{(N_{Cr}^{o} - N_{Cr}^{i})} \qquad (7.1)$$

where N_{Cr}^{i} and N_{Cr}^{o} are the chromium contents at the alloy/scale interface and matrix, x_o is the location of the alloy/scale interface, x is the depth into the alloy from the alloy/scale interface, and t is time.

Dayananda's method neglects any strong composition dependence of the interdiffusion coefficient. In an attempt to account for a composition dependence in the local interdiffusion coefficient of Cr, two models are developed in the current study: average-D model and average-slope model.

The local interdiffusion coefficient of Cr at some composition, N_{Cr}^{n}, can be obtained as

$$\tilde{D}_{N_{Cr}^{n}} = -\frac{1}{2t(dN_{Cr}^{n} / dx)} \int_{N_{Cr}^{o}}^{N_{Cr}^{n}} (x - x_o) dN_{Cr}^{n} \qquad (7.2)$$

The average effective interdiffusion coefficient of Cr, $\tilde{D}_{N_{Cr}^{n}}^{avd}$, is thus obtained by averaging all the local interdiffusion coefficients of Cr:

$$\tilde{D}_{Cr}^{avd} = \frac{\sum_{n=1}^{n_t} \tilde{D}_{N_{Cr}^{n}}}{n_t} \qquad (7.3)$$

where n is the number of measurements along the depletion profile (from 1 to n_i). This model shall be called the average-D model.

For the average-slope model, it is proposed that the average effective interdiffusion coefficient of Cr, $\tilde{D}_{N_{Cr}^n}^{avg}$, is obtained as

$$\tilde{D}_{Cr}^{avs} = -\frac{\tilde{J}_{Cr}}{dN_{Cr}/dx} = -\frac{\int_{N_{Cr}^o}^{N_{Cr}^i}(x-x_o)dN_{Cr}}{2t} \cdot \frac{1}{dN_{Cr}/dx} \tag{7.4}$$

where dN_{Cr}/dx represents the average slope over the chromium depletion profile, and is given by

$$\frac{dN_{Cr}}{dx} = \frac{\int_{x_o}^{x_m} \dot{N}_{Cr} \, dx}{x_m - x_o} \tag{7.5}$$

where x_m is the position of the depletion front into matrix, as shown in Fig. 2.25.

7.2.2 Subsurface Depletion Models

Wagner [68] analyzed binary alloy oxidation by assuming that the process was diffusion controlled. The expression for the subsurface depletion profile was determined from this analysis to be given by,

$$N_{Cr}(x,t) = N_{Cr}^i + (N_{Cr}^o - N_{Cr}^i)\frac{erf[\frac{x}{2(\tilde{D}_{Cr}t)^{1/2}}] - erf[\frac{k_c}{2\tilde{D}_{Cr}}]^{1/2}}{1 - erf[\frac{k_c}{2\tilde{D}_{Cr}}]^{1/2}} \tag{7.6}$$

where $\tilde{D}_{Cr}$ is the interdiffusion coefficient of chromium in the binary alloy and k_c is the corrosion constant that is related to the parabolic rate constant, k_p, by,

$$k_c = \left(\frac{V_m}{v \cdot M_o}\right)^2 \cdot k_p \tag{7.7}$$

where V_m is the molar volume of the alloy and M_o is the atomic weight of oxygen.

Equation (7.6) was determined assuming steady-state diffusion-controlled growth of a scale that grows in an ideal manner and, hence, does not undergo cracking or spalling. Thus, Wagner's theory is limited primarily to isothermal oxidation. Under cycling condition

conditions, scale cracking and spallation occurs during cooling and the scale growth can depart significantly from ideal behavior. Another limitation of equation (7.6) in practical application is that its solution requires the value of the chromium content at the alloy/scale interface. In any lifetime prediction model of a chromia-forming alloy, it is necessary to predict $N_{Cr}{}^{i}$.

Subsurface depletion during cyclic oxidation can be simulated by utilizing a numerical model that was is developed by Nesbitt [137,138] to predict the subsurface depletion profile during selective oxidation of a ternary alloy. Here, a finite-difference technique is used to calculate the concentration change in a given small time interval Δt by considering the weight gain in terms of k_p, weight loss in terms of a spallation constant, Q_o, and interdiffusion coefficient of Cr ($\widetilde{D}_{Cr}$) to predict the rate of Cr consumption associated with partial scale spallation. The numerical model to predict the depletion profile is called OxDiff (Oxidation and Diffusion), which is written in FORTRAN. For a given alloy system, several main parameters are required to predict the depletion profile: the molar volume of the alloy, phase constitution of the oxide scale, oxide growth rate (k_p), oxide spallation constant (Q_o), and interdiffusion coefficient of the species in the alloy being oxidized ($e.g., \widetilde{D}_{Cr}^{eff}$).

The spallation parameter is determined using the Cyclic Oxidation Spallation Program (COSP), which tracks weight change associated with scale growth and spallation during each cycle. If t is the duration of one thermal cycle, then the final specific weight change of the sample after the first cycle is given by:

$$\Delta W = (k_p t)^{1/2} - Q_o (W_f)^2 \qquad (7.8)$$

where k_p is parabolic rate constant, and W_f is the specific weight of total scale present before cooling.

An output of the numerical model is the depletion profile of Cr after any period of oxidation. In turn, the time to breakdown can be predicted if the critical Cr content at the alloy/scale interface, $N_{Cr}{}^{*}$, is known. It should be noted that the value of $N_{Cr}{}^{*}$ will usually be lower than the critical compositions predicted from Wagner's analysis (Equation 2.72) [1]. This is because in practice scales undergo partial, as opposed to complete, scale spallation.

Thus, use of Wagner's analysis that predicts the critical concentration for the transition from internal to external oxidation would represent an upper limiting value for N_{Cr}^{*}.

COSP does not consider the effect of transient oxidation which may play important role in the oxidation kinetics, and, more important, in the subsurface depletion behavior. A new C++ program, called as Cyclic Oxidation Spallation Program with Transient Stage (COSP-TS), was developed in this study to simulate cyclic oxidation kinetics with consideration of the transient oxidation stage (Appendix B provides the program code). A spallation parameter, Q, is defined in the COSP-TS program as,

$$(Q / Q_{to}) = (W_f / k_p t)^m \tag{7.9}$$

where Q_{to} is a characteristic spallation constant for a specific oxide scale and m is a positive constant which also depends on the oxide scale [144]. It is seen that spallation parameter, Q, will vary with scale thickness. A brittle oxide scale would have a larger m value than ductile scale, with the value of m typically being in the range of 1 to 4. For a chromia scale, the value of m is found to be between 1~2 [139,218].

Thus, the final specific weight change of the sample after a given cycle is given by:

$$\Delta W = W_f [1 - Q_{to} (W_f / k_p t)^m] \tag{7.10}$$

In COSP-TS program, the scale growth rate and time of the transient oxidation stage are embedded to calculate the weight gain of the transient stage. By comparing Eq. 7.10 with experimental oxidation kinetics, the spallation constant, Q_{to}, can be determined. The k_p is taken here to be a constant, yet only valid over a specific period. Accordingly, a k_p is specified for both the transient and the steady-state periods of oxidation.

The current modeling will use the three approaches (Dayananda's, average-D, and average-slope model) for calculating the average effective interdiffusion coefficient of Cr in the commercial alloys studied, and then applies both Wagner's and numerical models to simulate subsurface chromium depletion profile under isothermal condition. The Cr depletion prediction during cyclic oxidation is obtained by the numerical model. The oxidation-resistant lifetime of the alloy will then be assessed in terms of time to chromia-scale breakdown. The sensitivity of oxide growth rate, interdiffusion coefficient of Cr, and spallation constant will also be discussed in this chapter.

The two Fe-base alloys, 800HT and VDM800HT, were selected for the prediction of subsurface Cr depletion and lifetime because these two alloys showed breakdown behavior with a relatively short period of time.

7.3 Experimental Results

Figure 7.2 shows the weight-change behavior of the 800HT and VDM800HT alloys as a function of time over the testing duration of 125 1-day cycles at 1000 °C. It is seen that 800HT exhibited rapid weight-loss kinetics after about 18 cycles of relatively protective oxidation, while VDM800HT showed breakdown after about 95 cycles. It is recalled that this time to protective-scale breakdown was found to be quite reproducible for the particular alloy studied as shown for the case of 800HT in Fig. 5.3.
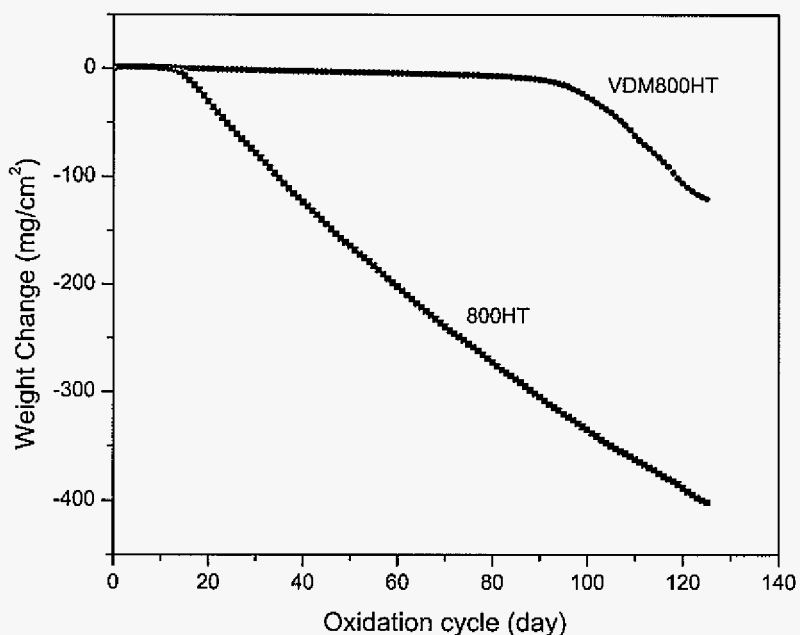

Figure 7.2. Weight change vs. number of 1-day oxidation cycles at 1000°C.

Figure 7.3 shows the TGA results for the 800HT and VDM800HT alloys oxidized in still air at 1000 °C. Both of the alloys showed a transient stage of relatively fast oxidation kinetics (7.2×10^{-11} $g^2cm^4s^{-1}$ and 6.4×10^{-11} $g^2cm^4s^{-1}$ for 800HT and VDM800HT, respectively) with a

duration of 5 hours for 800HT and 4 hours for VDM800HT, followed by slower steady-state kinetics. The steady-state parabolic rate constants were measured to be 6.3×10^{-12} $g^2cm^4s^{-1}$ and 5.4×10^{-12} $g^2cm^4s^{-1}$ for 800HT and VDM800HT, respectively. The determination of the parabolic rate constant provided a basic parameter for the COSP and OxDiff programs.

800HT   VDM800HT
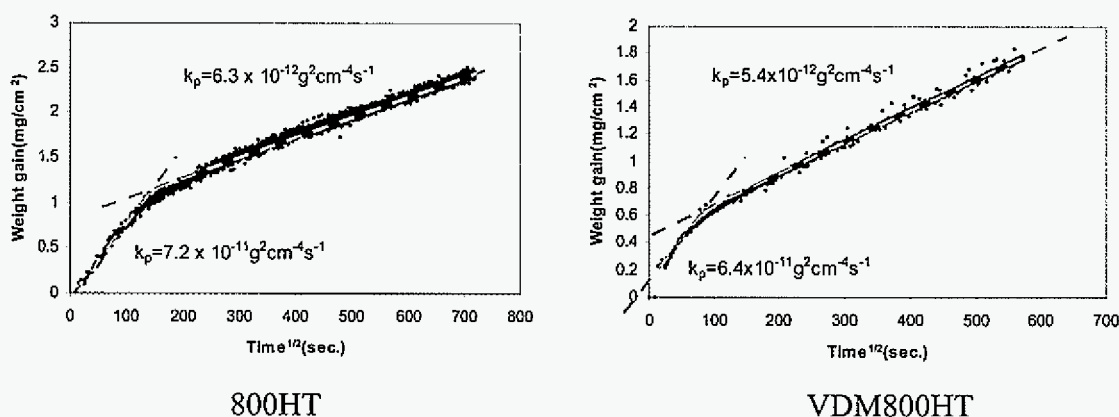
Figure 7.3. Parabolic plots showing TGA results for isothermal oxidation in air at 1000°C.

Cross-sectional SEM images of the two alloys after the TGA testing are shown in Figure 7.4. Combining the EDS and XRD analysis results, the scales were found to consist primarily of two oxide layers: an inner layer (about 10 μm) of Cr_2O_3 and an outer layer, $Cr_2O_3+NiFe_2O_4$ (about 7 μm) for 800HT and $Cr_2O_3+MnCr_2O_4$ (less than 1 μm) VDM800HT. VDM800HT formed a thinner oxide scale than 800HT, which was consistent with their parabolic rate constants. A large amount of less-protective $NiFe_2O_4$ formed on 800HT which must have been detrimental to the oxidation resistance of this alloy. For the purpose of modeling, it is important to quantify the phase constitution of the scale. Based on the cross-sectional SEM image of 800HT, the inner Cr_2O_3 layer constituted approximately 60% of the oxide scale thickness. Considering the outer layer to be $Cr_2O_3+NiFe_2O_4$, chromia in the oxide scale was assumed to constitute 80% (volume percent). In the case of VDM800HT, which formed a small amount of $MnCr_2O_4$, chromia was assumed to constitute 90% (volume percent) of the scale.

<div align="center">800HT   VDM800HT</div>

Figure 7.4. Cross-sectional SEM image of alloy 800HT and VDM800HT
isothermally oxidized at 1000 °C for 90h.

The oxidized alloys underwent intergranular internal oxidation. The compositions of the
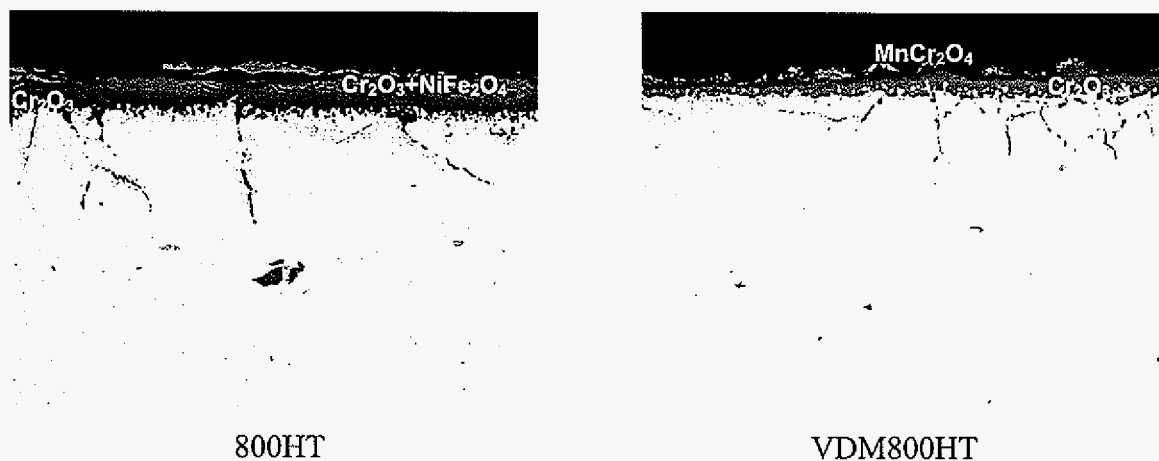internal oxides depended upon depth into the alloy. Deep into the alloy at the intergranular
oxidation front, the oxides were always found to be aluminum-rich. At a shallower depth the
internal oxide was rich in titanium. Further EDS analysis showed that silicon-rich oxide co-
existed with aluminum-rich oxide in the vicinity of the alloy/scale interface. Based on the
analyses in chapter 5, the Al-rich, Si-rich and Ti-rich oxides are believed to be Al_2O_3, SiO_2,
and TiO_2, respectively. Internal oxidation should affect growth rate of oxidation and
subsurface diffusion behavior. However, internal oxidation was neglected in the prediction in
the current model because the internal oxide quantity and distribution were considered
sufficiently low to only marginally affect the calculation of oxidation kinetics and
interdiffusion of chromium.

The subsurface chromium content in the alloys isothermally oxidized for 7 days and those
thermally cycled for 3, 10, 18, and 125 1-day cycles at 1000 °C were analyzed using EPMA.
The results are shown in Figures 7.5-7.7. After 7 days of isothermal exposure (Fig. 7.5), the
chromium content in the alloys at the alloy/scale interface, N_{Cr}^i, was lower than the bulk
chromium content, which is clearly a consequence of the selective oxidation of chromium.
800HT had an N_{Cr}^i of only about 8.5 at.% and a depletion-zone width of about 60 μm after 7
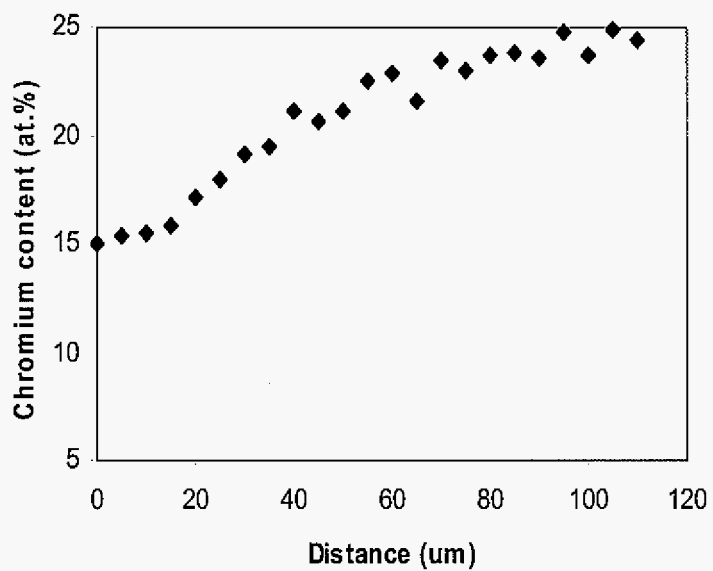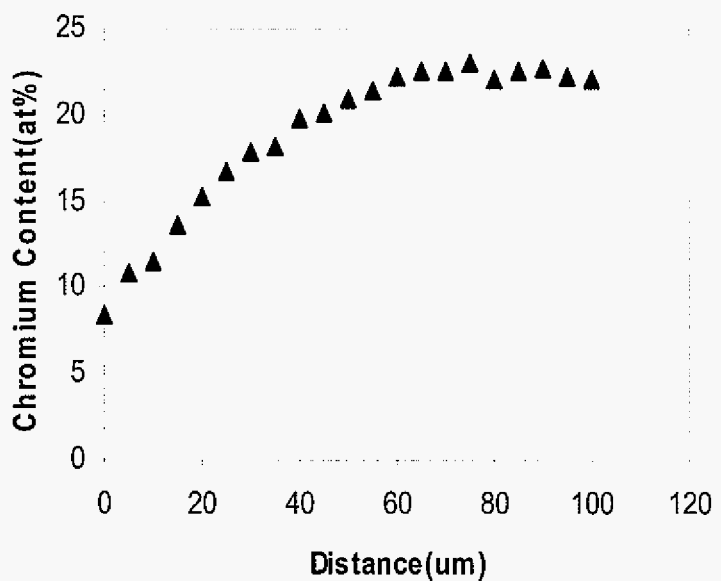
Figure 7.5. Subsurface depletion profile of chromium after 7-days isothermal oxidation at 1000 °C.
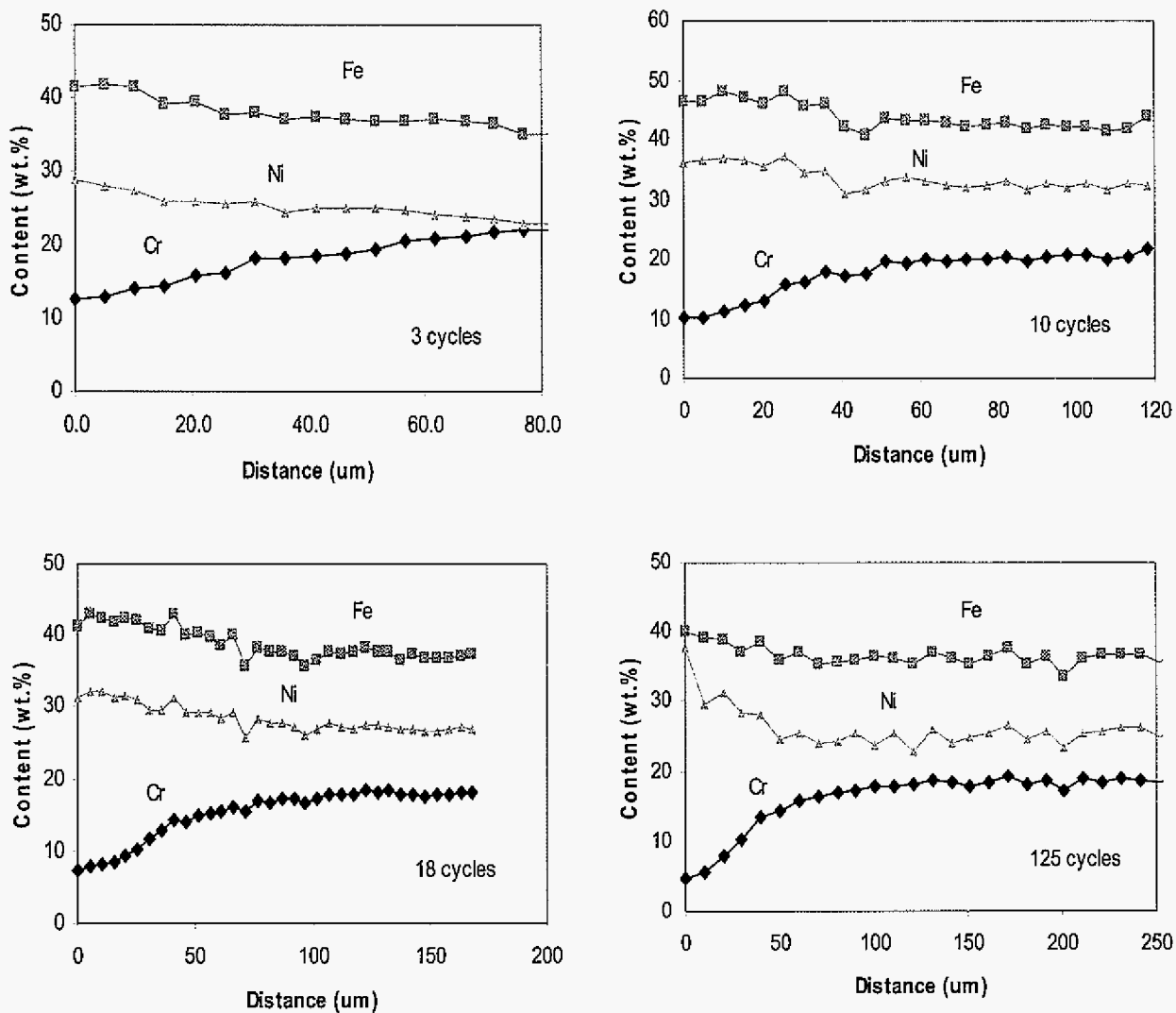
Figure 7.6. Subsurface depletion profiles of Cr, Fe, Ni in the 800HT alloy after various durations of 1-day cyclic oxidation exposures at 1000 °C.
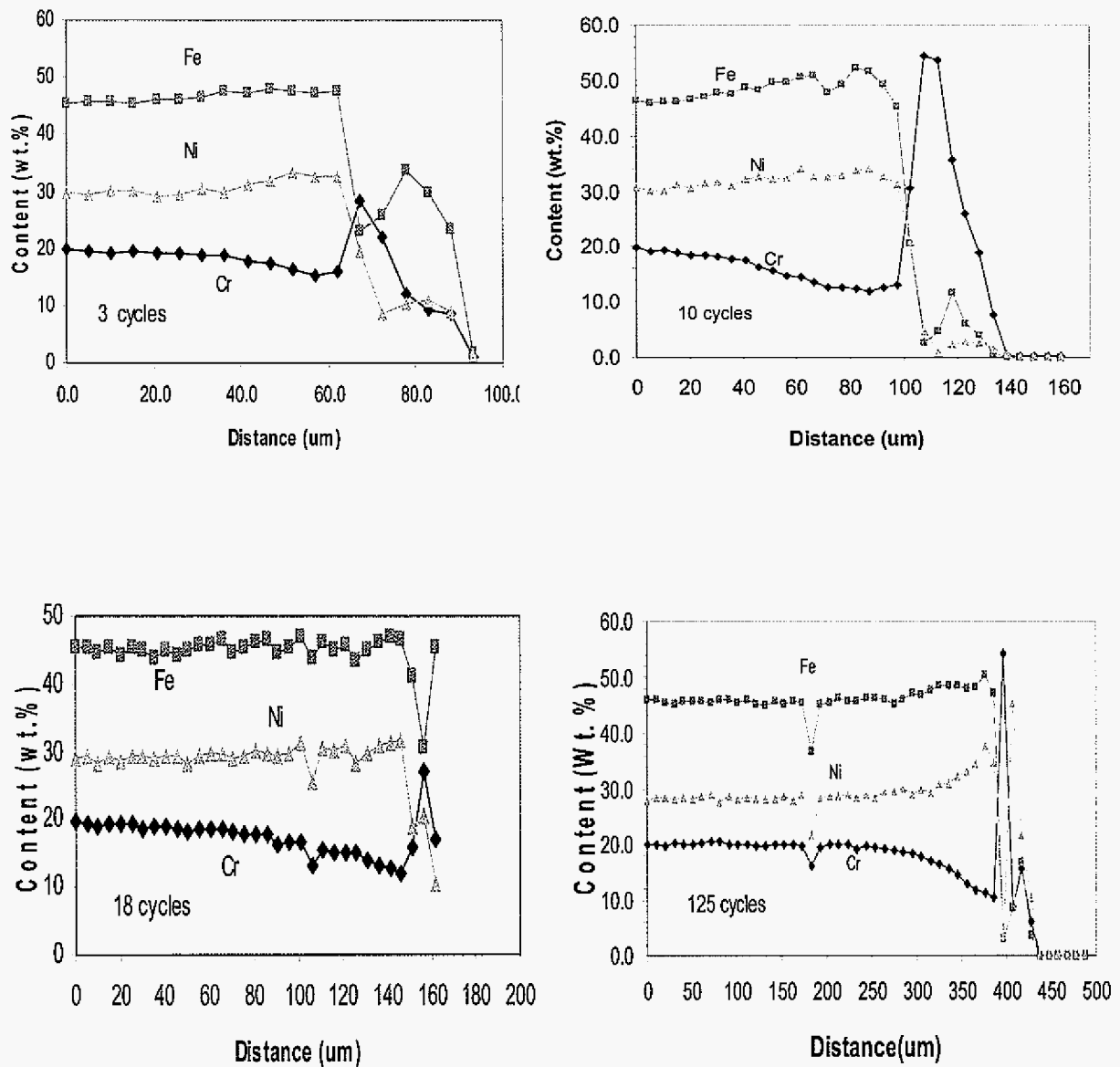
Figure 7.7. Subsurface depletion profiles of Cr, Fe, Ni in the VDM800HT alloy after various durations of 1-day cyclic oxidation exposures at 1000 °C.
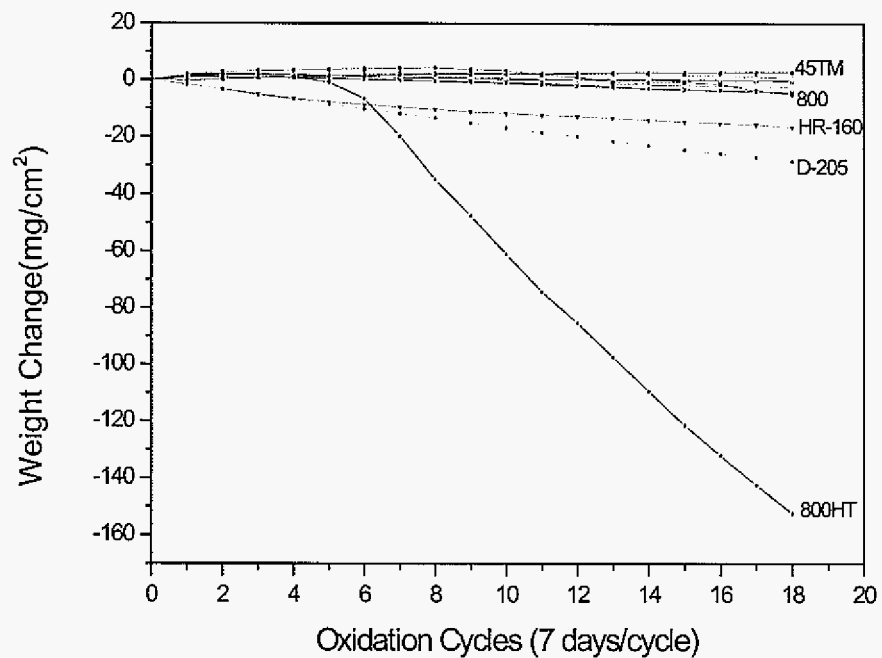
Figure 4.3. 7-day cyclic oxidation kinetics of alloys studied at 1000 °C.
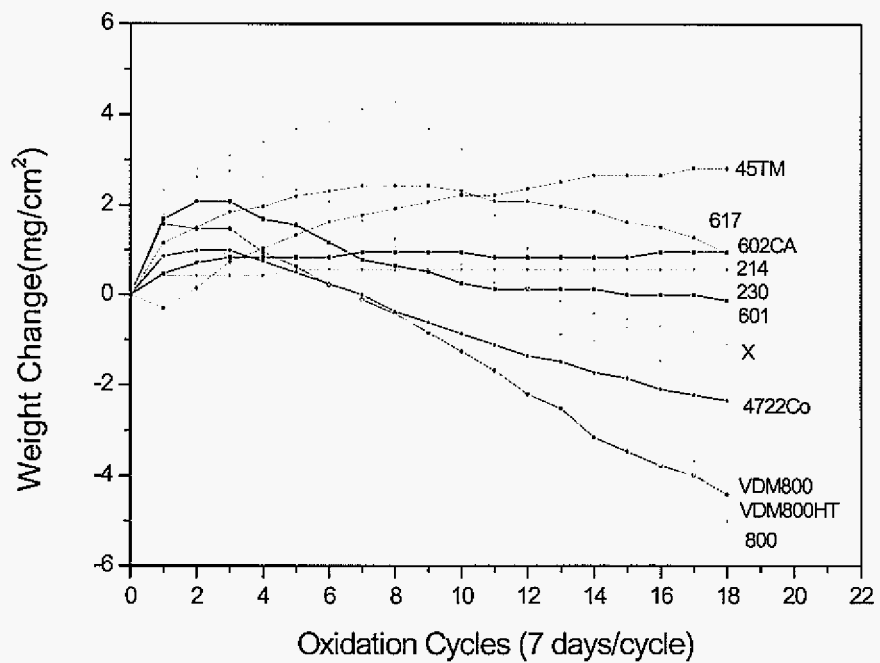
Figure 4.4. More detailed scale showing the lower oxidation kinetics in Figure 4.3.
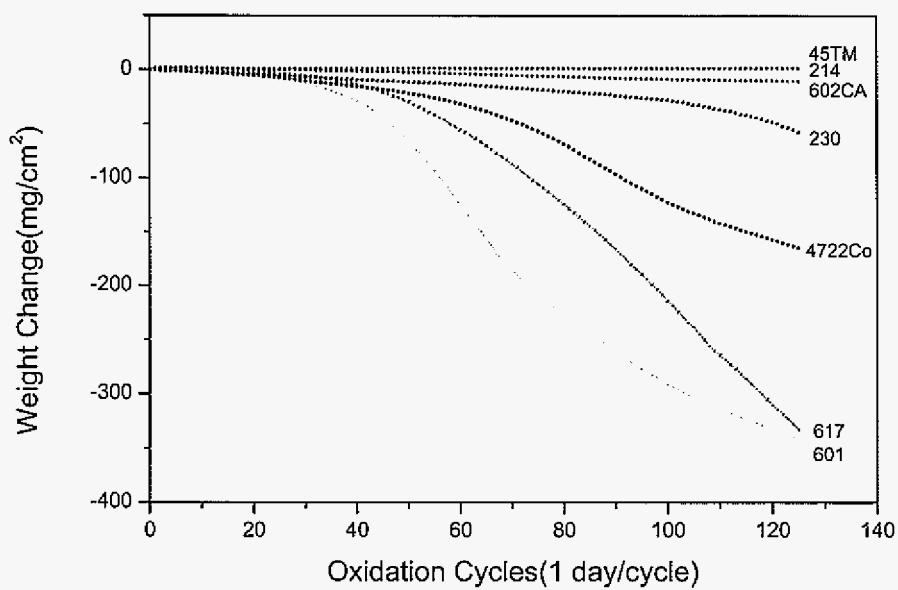
Figure 4.5. 1-day cyclic oxidation kinetics of alloys studied at 1100 °C.
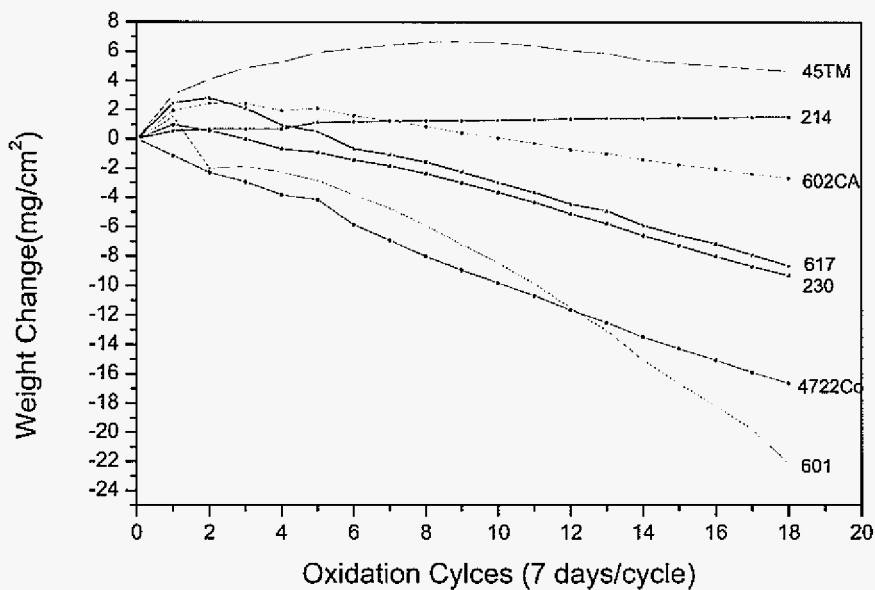
Figure 4.6. 7-day cyclic oxidation kinetics of alloys studied at 1100 °C.

the 800HT alloy (0.15 wt.% Si). As discussed in section 2.2.5.3.2, silicon can have a significant effect on oxidation behavior. Thus, the difference of Si contents in two alloys could contribute to their difference in oxidation resistance.

Figure 4.2 shows that 214 and 602CA have excellent oxidation resistance (the least weight gain and loss) weight change being within 1 mg/cm^2 during the long-term 1-day cyclic oxidation at 1000 °C. The 45TM alloy showed the largest weight gain over the oxidation period (125 1-day cycles), exhibiting very stable oxidation resistance (almost no weight gain and spallation) after about 50 cycles. Based on the weight-change kinetics shown in Fig. 4.2, the oxidation resistance of other chromia-forming Ni-base alloys can be ranked in the following order: 230>617>4722Co>601>X; however, apart from alloy X, the differences were not significant. This ranking is of course specific to the testing conditions used and may not be applicable to other conditions. The 601 alloy showed the largest weight gain in the early stage of oxidation, at about 10 cycles.

Figures 4.3 and 4.4 show the 7-day cyclic oxidation kinetics of the alloys studied up to 18 cycles (about 3000 hours) at 1000 °C. Compared to the 1-day cyclic oxidation, 7-day cyclic oxidation was generally less severe, with the weight-loss for 7-day cycles being about one-third that of 1-day cycles for the alloys 800HT, HR-160, and D-205. The 800 series, D-205, and HR-160 alloys still showed the poorest oxidation resistance of the alloys studied. 800HT also exhibited breakdown behavior after 5 cycles (around 35 days). Different from the 1-day cycles, the 800 alloy showed the largest weight gain (about 4 mg/cm^2 after 9 cycles). The close weight changes (within 3 mg/cm^2 range) for the alloys 214, 602CA, 617, 601, 230 show that they have excellent oxidation resistance (very small spallation) for up to 18 7-day cycles at 1000 °C.

Most of the Ni-base alloys studied showed good oxidation resistance at 1000 °C, so to further explore their oxidation behavior, the alloys 45TM, 214, 602CA, 230, 617, 601, and 4722Co, were cyclically oxidized at 1100 °C (Figs. 4.5 and 4.6). The 45TM alloy showed weight gain for most of the testing duration under both 1-day and 7-day thermal cycling at 1100 °C, as was also the case at 1000 °C. The 214 alloy showed the smallest weight gain and spallation during the thermal cycling oxidation tests at 1100 °C. The alloys 601 and 617 showed the worse oxidation resistance of the Ni-base alloys oxidized at 1100 °C under 1-day

thermal cycling. Less cycling (18 7-day compared to 125 1-day) for the same oxidation time resulted in improving oxidation resistance for the 601 alloy in terms of weight loss by over a factor of 15 (about 350 mg/cm^2 for 1-day cycling compared to 20 mg/cm^2 for 7-day cycling). The alloys 601, 617, 4722Co, and 230 experienced breakdown at around 40, 50, 70, and 110 1-day cycles, respectively, at 1100 °C. The alloys 617 and 4722Co ranked differently for the two cycle durations studied. The 617 alloy was better than 4722Co for 7-day cycling, but the opposite was the case for 1-day cycles.

It is seen from the results presented that most alloys exposed to thermal cycling conditions undergo an initial mass gain to a maximum value, then a change to a negative rate mass change due to continuous weight loss owing to scale spallation. The time to cross zero mass change may be taken as an initial indicator of cyclic oxidation resistance. A longer time to cross zero mass change indicates less spallation and hence better oxidation resistance [145]. Figure 4.7 shows the time to cross zero mass change for some of the alloys studied as a function of nickel content for 1-day and 7-day cyclic oxidation at 1000 °C. It is seen that the time to cross zero mass change generally increases with increasing nickel content in the alloy for the two cycle durations studied.

(a) 1-day cycles

(b) 7-day cycles
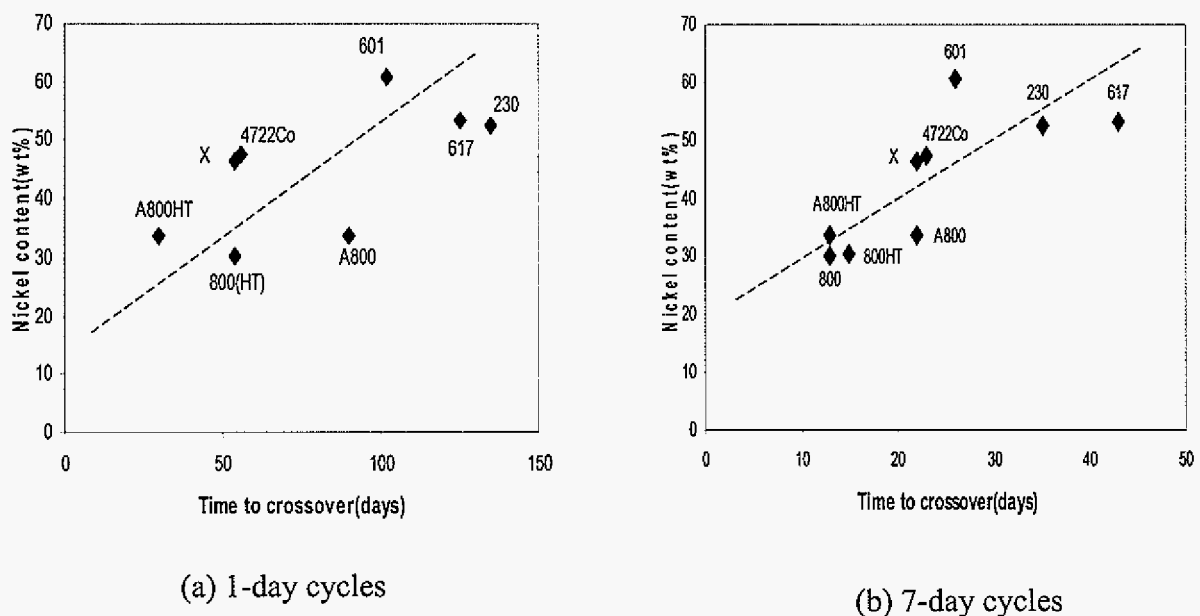
Figure 4.7. Effect of nickel content on the time to cross zero mass change at 1000 °C.

Figure 4.8 shows the dependence of cycle duration on the time to cross zero mass change at 1000 °C. As the cycle duration (Δt) is increased, the number of days to cross zero mass change is also increased. The dependency is about as $\Delta t^{(2/3)}$ for the number of days to cross zero mass. The observed $\Delta t^{(2/3)}$ dependency is in agreement with the cyclic oxidation spallation model (COSM) developed by Smialek *et al.* [139,145].
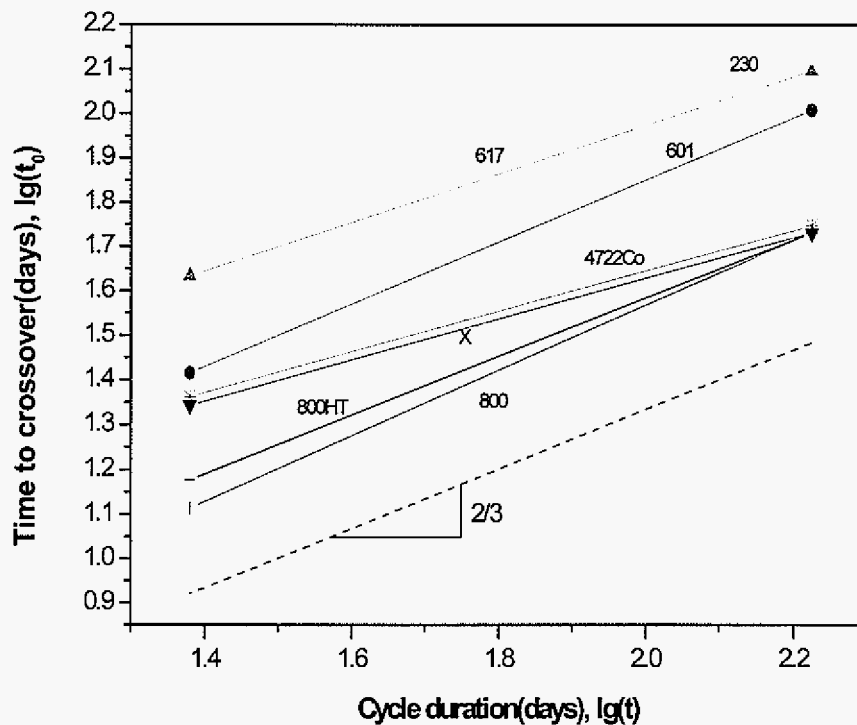
Figure 4.8. Dependence of cycle duration on time to cross zero mass at 1000 °C.

4.2.2 Isothermal Oxide Growth

Figure 4.9 shows the TGA results for 14 alloys oxidized at 1000 °C in air. Plots (a) in Fig. 4.9 are weight gain (mg/cm^2) as a function of time (second) and plots (b) in Fig. 4.9 are weight gain as a function of the square-root of time. Thus, plots (b) are parabolic plots and the data fit should be linear if the scale growth is a diffusion-controlled process. A more detailed analysis of the oxidation kinetics using log (weight) vs. log(time) plots revealed that the kinetics were often sub-parabolic.

From Fig. 4.9 (b), all alloys studied showed parabolic oxide growth kinetics after an initial transient stage in which the weight-change kinetics were more rapid. The transient and steady-state growth rate constants and the duration of the faster transient stage are summarized in Table 4.1. For many of the alloys, the transient stage kinetics were not clearly parabolic and in some cases were closer to linear. This reflects the complexity of the initial transient stage of oxidation and the transient stage k_p values listed in Table 4.1 should be used more for comparison than for any sort of analysis or interpretation. The faster transient stage for most of the alloys was under 5 hours. The 617, 4722Co, X, and 214 alloys showed the longest transient stage of about 9-15 hours, while HR-160, D-205, and 601 showed the shortest transient stage of about 1 hour. The chromia-forming alloys showed a spread in the steady-state parabolic rate constants from 6.4×10^{-13} (4722Co) to 1.2×10^{-11} $g^2/cm^4 \cdot s$ (HR-160). The alloys 214, 4722Co, and 230 showed the lowest steady-state parabolic rate constants ($<10^{-12}$ $g^2 cm^{-4} s^{-1}$), while HR-160 and 601 showed the highest parabolic rate constants ($>10^{-12}$ $g^2 cm^{-4} s^{-1}$). The parabolic scale-growth rates during the transient stage were about a factor of 10 larger than the steady-state rates for most of the alloys, while for the alloys 230, 617, D-205, VDM800, and HR-160, it was about a factor of 5 times high.
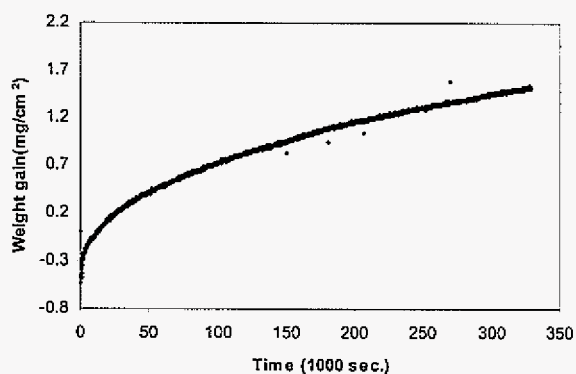
(a) weight gain vs. time
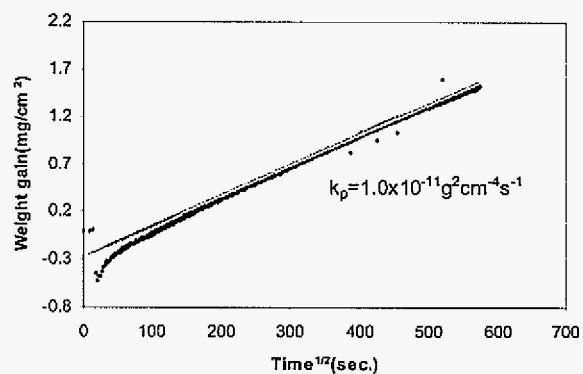
(b) Weight gain vs. (time)$^{1/2}$

800
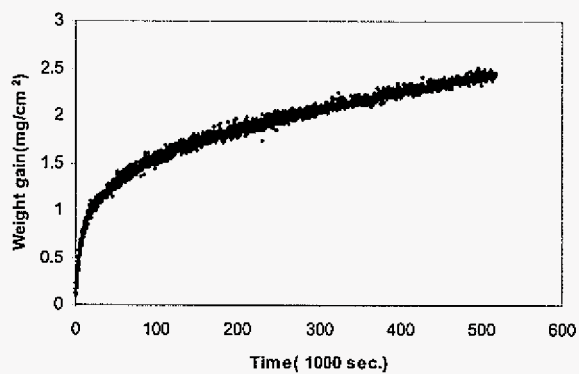
(a) weight gain vs. time
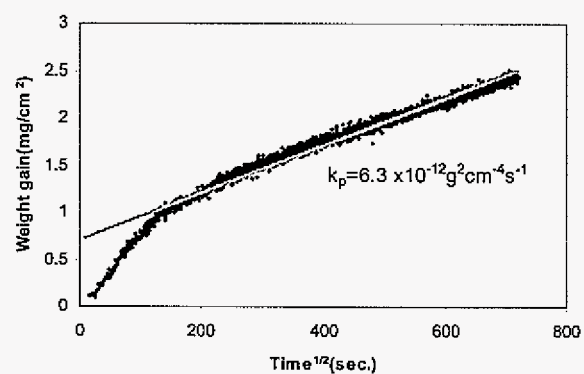
(b) Weight gain vs. (time)$^{1/2}$

800HT
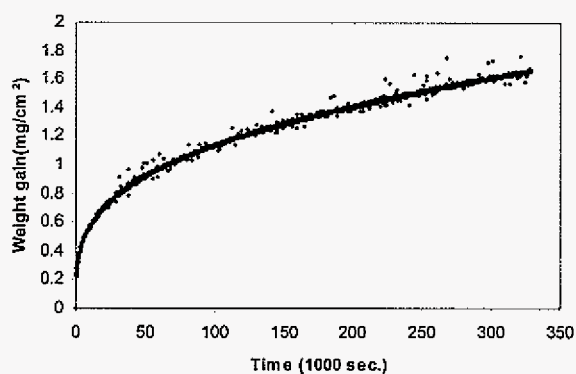
(a) weight gain vs. time
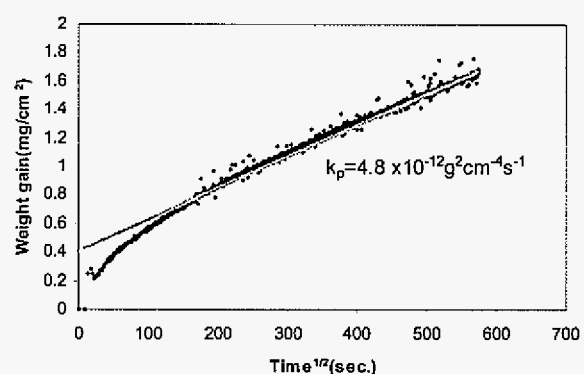
(b) Weight gain vs. (time)$^{1/2}$

VDM800

Figure 4.9. TGA results for oxidation in air at 1000 °C. Plots in (a)
Are linear while corresponding plots in (b) are parabolic.
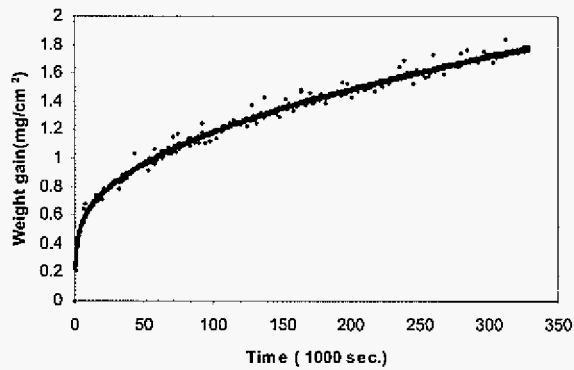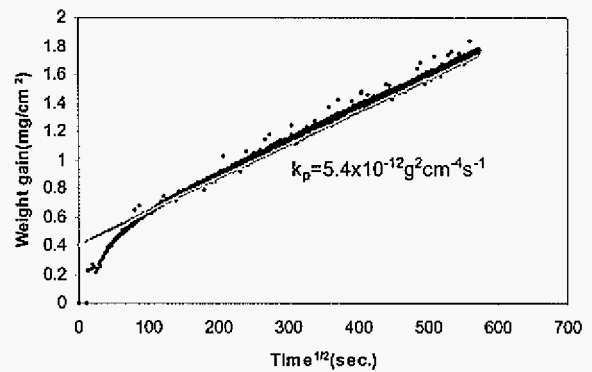
(a) weight gain vs. time   (b) Weight gain vs. $(time)^{1/2}$

VDM800HT

$k_p=5.4 \times 10^{-12} g^2 cm^{-4} s^{-1}$
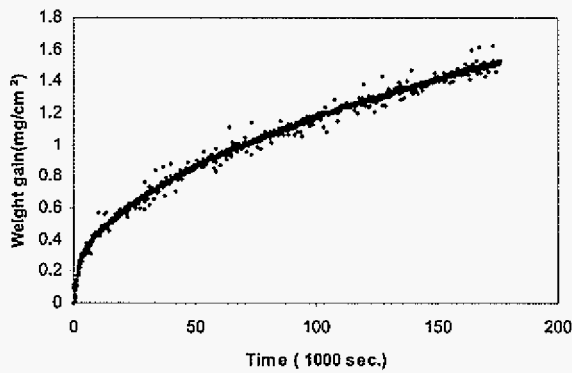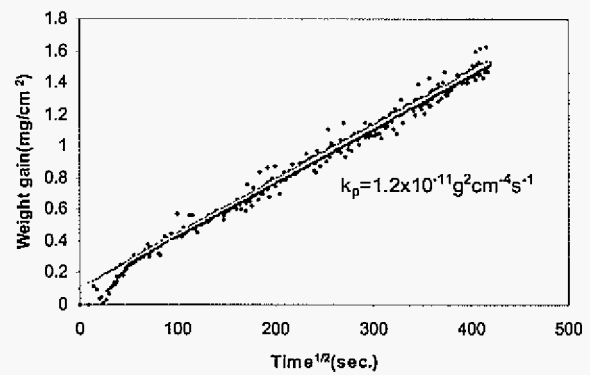
(a) weight gain vs. time   (b) Weight gain vs. $(time)^{1/2}$

HR-160

$k_p=1.2 \times 10^{-11} g^2 cm^{-4} s^{-1}$
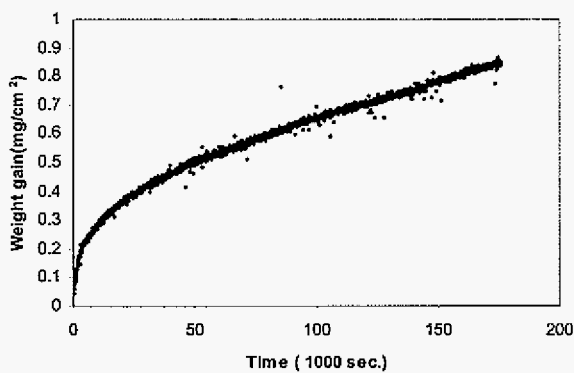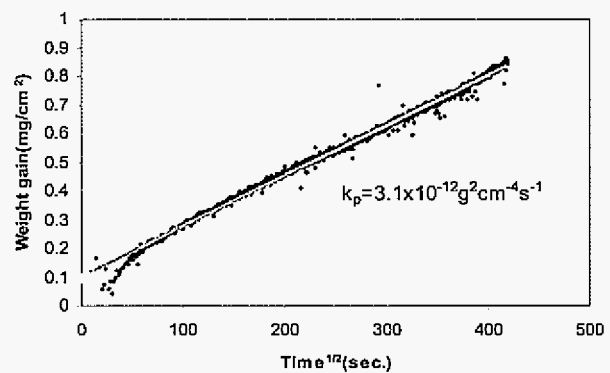
(a) weight gain vs. time   (b) Weight gain vs. $(time)^{1/2}$

D-205

$k_p=3.1 \times 10^{-12} g^2 cm^{-4} s^{-1}$

Figure 4.9. (continued)
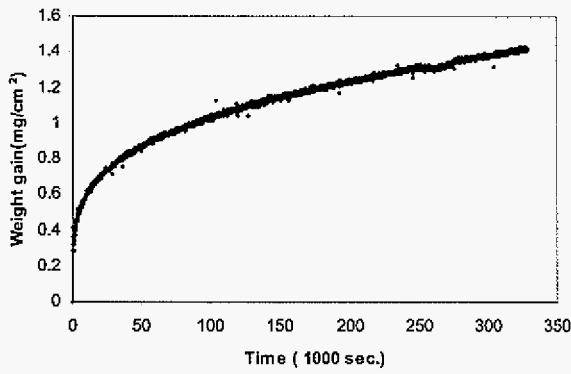
(a) weight gain vs. time
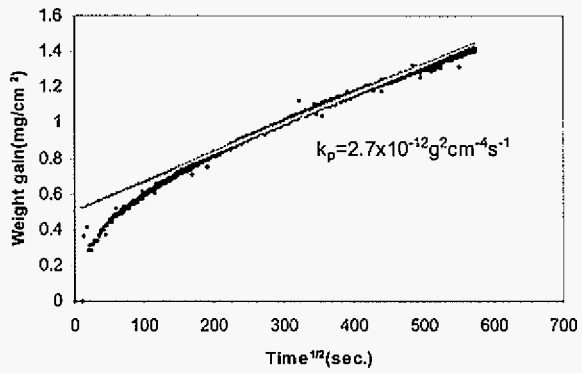
(b) Weight gain vs. (time)$^{1/2}$

X
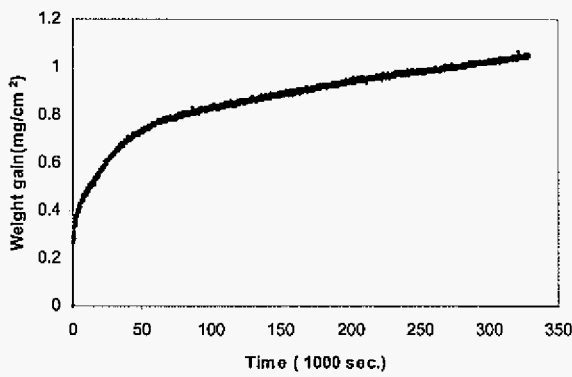
(a) weight gain vs. time
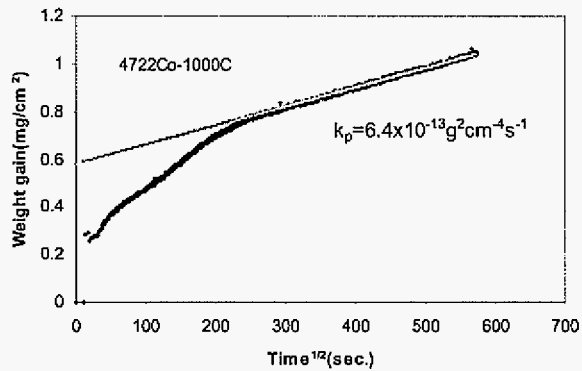
(b) Weight gain vs. (time)$^{1/2}$

4722Co
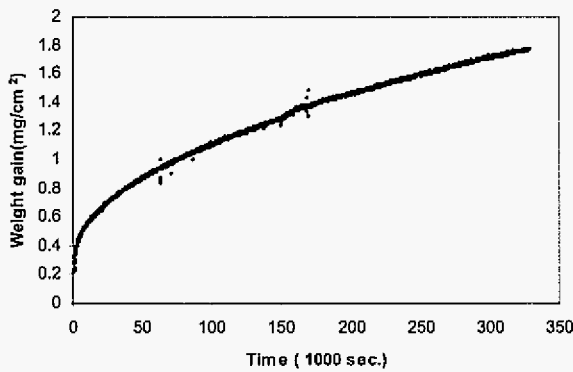
(a) weight gain vs. time
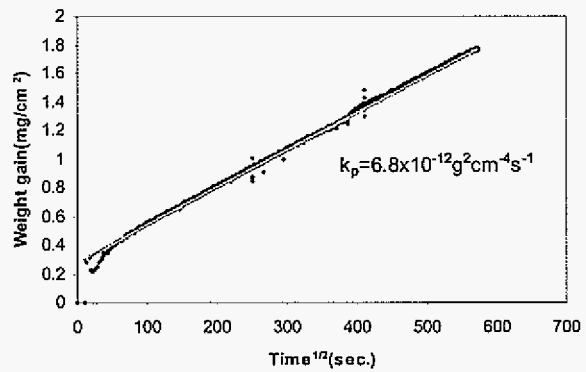
(b) Weight gain vs. (time)$^{1/2}$

601

Figure 4.9. (continued)
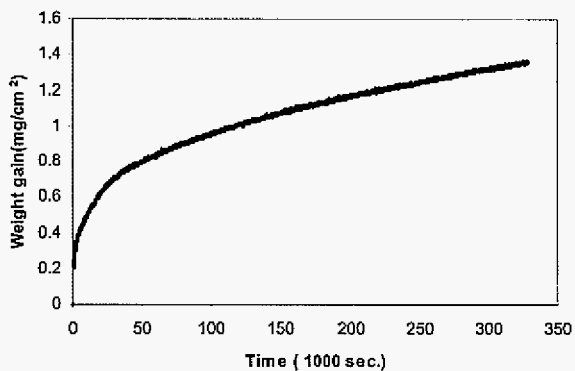
(a) weight gain vs. time
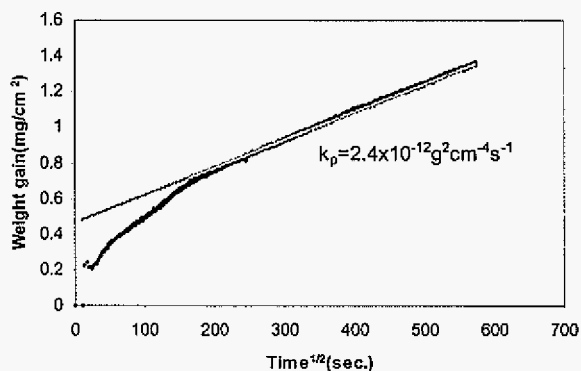
(b) Weight gain vs. $(time)^{1/2}$

617
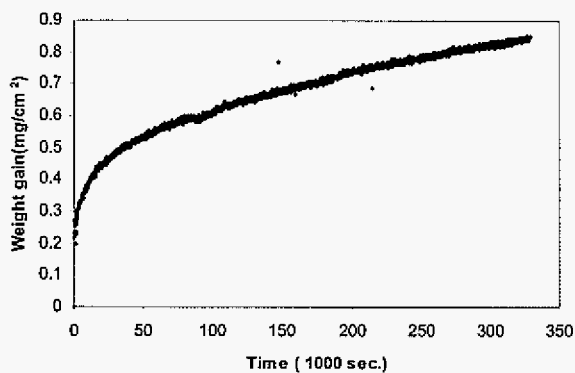
(a) weight gain vs. time
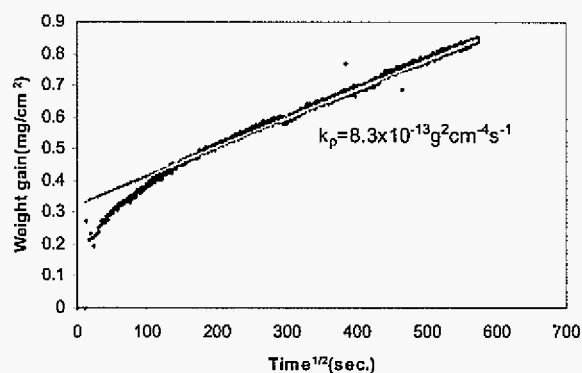
(b) Weight gain vs. $(time)^{1/2}$

230
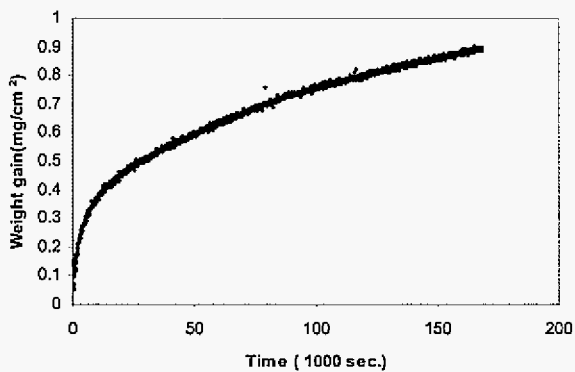
(a) weight gain vs. time
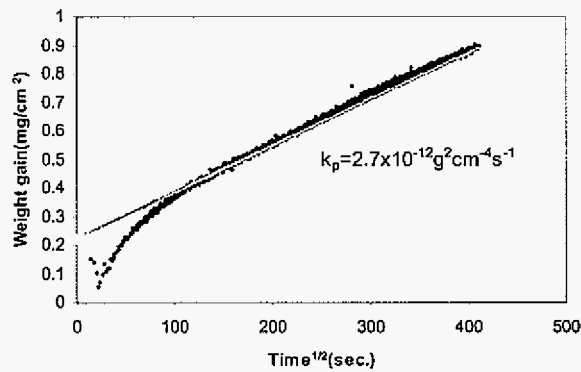
(b) Weight gain vs. $(time)^{1/2}$

45TM

Figure 4.9. (continued)
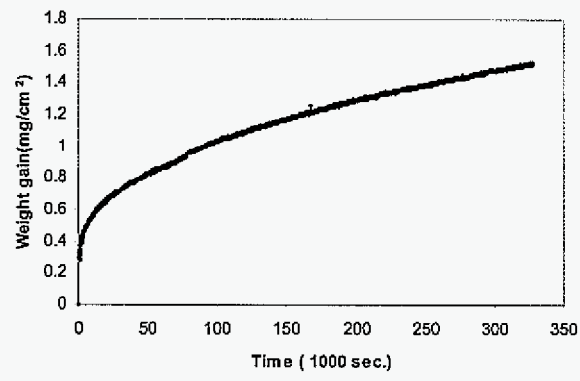
(a) weight gain vs. time
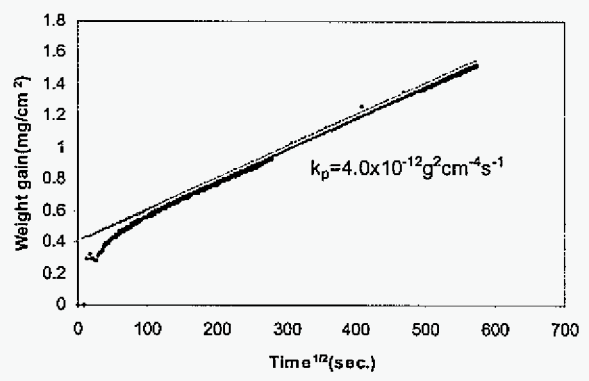
(b) Weight gain vs. (time)$^{1/2}$

602CA
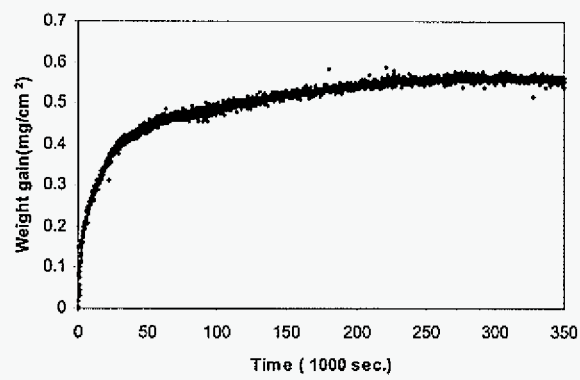
(a) weight gain vs. time
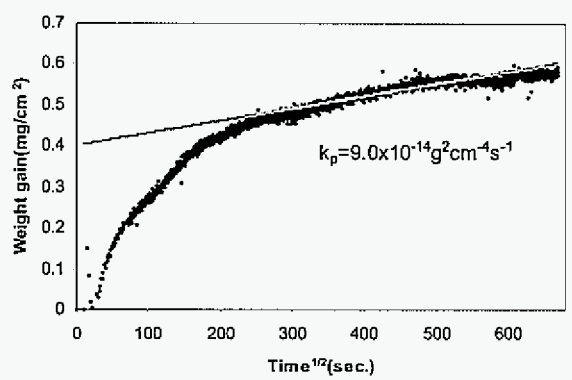
(b) Weight gain vs. (time)$^{1/2}$

214

Figure 4.9. (continued)

Table 4.1. Measured rate constant (k_p) for alloys isothermally oxidized in air at 1000 °C.

Alloys	Transient stage		Steady-state stage
	Duration (hour)	k_p (g^{2}cm^{-4}s^{-1})	k_p (g^{2}cm^{-4}s^{-1})
214	~12	4.0×10^{-12}	9.0×10^{-14}
4722Co	~15	6.3×10^{-12}	6.4×10^{-13}
230	~5	4.4×10^{-12}	8.3×10^{-13}
617	~9	1.0×10^{-11}	2.4×10^{-12}
45TM	~3	2.5×10^{-11}	2.7×10^{-12}
X	~10	2.5×10^{-11}	2.7×10^{-12}
D-205	~1	1.6×10^{-11}	3.1×10^{-12}
602CA	~4	3.0×10^{-11}	4.0×10^{-12}
VDM800	~5	1.6×10^{-11}	4.8×10^{-12}
VDM800HT	~4	6.4×10^{-11}	5.4×10^{-12}
800HT	~5	7.2×10^{-11}	6.3×10^{-12}
601	~1	4.9×10^{-11}	6.8×10^{-12}
800	~5	1.4×10^{-10}	1.0×10^{-11}
HR-160	~1	5.6×10^{-11}	1.2×10^{-11}

Figure 4.10 plots the transient stage k_p versus the duration of the transient stage for the various alloys studied. It is seen that a long transient duration was always associated with a small transient k_p, while a large transient k_p generally resulted in a short transient duration. The alloys 214 and 4722Co showed the longest initial oxidation stage with the lowest initial oxide growth rate, while alloys 800HT, VDM800HT, HR-160, and 601 with large transient growth rates showed comparatively short transient durations.
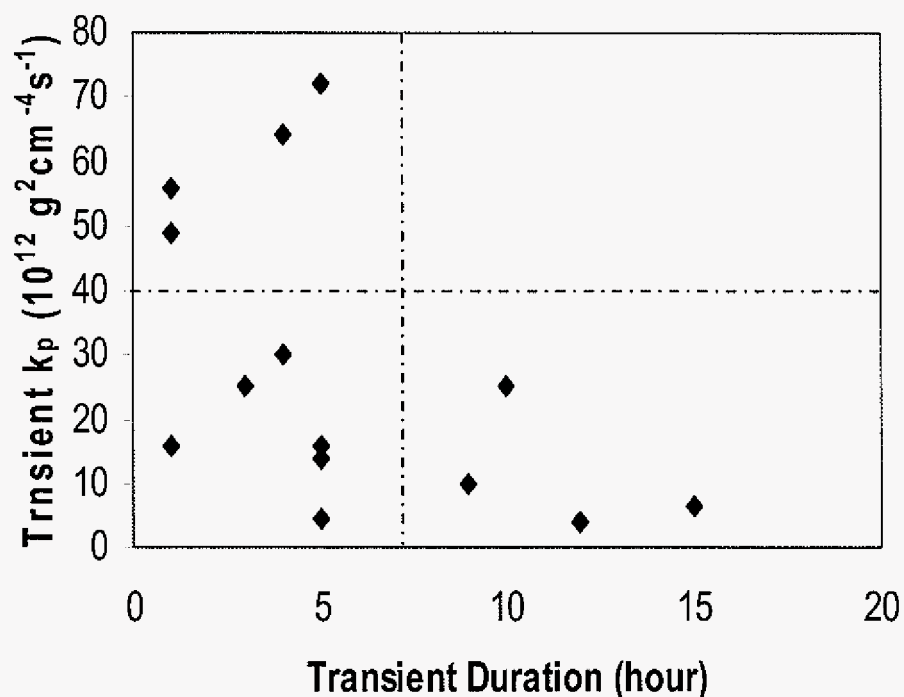
Figure 4.10. Transient oxidation growth rate as a function of transient growth time

oxidized in air at 1000 °C.

Figure 4.11 shows the reproducibility of TGA test for the 800 alloy oxidized at 1000 °C in air. Both alloys showed a similar transient stage duration of about 1 hour. The parabolic rate constants for the two TGA tests were virtually the same at 1.0×10^{-12} $g^2/$ $cm^4 \cdot s$. The agreement of two TGA results ensured the accuracy of TGA test for the alloys studied.

$k_p = 1.0 \times 10^{-11} g^2 cm^{-4} s^{-1}$
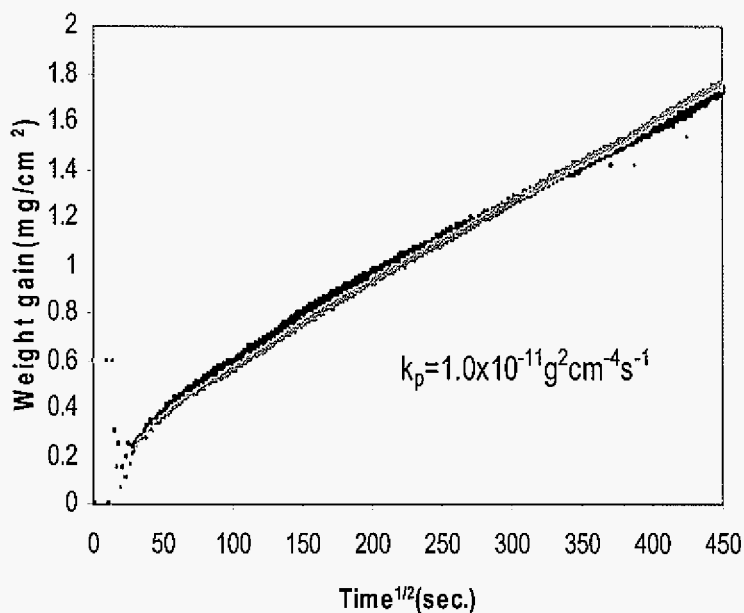
Figure 4.11. Reproducibility of TGA test for the 800 alloys oxidized in air at 1000 °C.

4.2.3 XRD Analysis of the Oxidized Alloys

At the completion of the TGA tests, the alloys were analyzed using XRD to identify the surface oxide phases. Figure 4.12 shows the XRD patterns for the alloys studied. The oxide phases are summarized in Table 4.2. A Cr_2O_3 scale formed on all alloys except for 214, which formed an Al_2O_3 scale. The XRD pattern from the other alumina-forming alloy, 602CA, did not show distinct Al_2O_3 peaks. It is possible that the lower Al content in 602CA and the relatively short TGA time (90 hours) were insufficient for a detectable alumina layer to form. The spinel $MnCr_2O_4$ was detected on most of the alloys, except on 617, 602CA, and 214. The alloys D-205 and 45TM showed peaks for quartz SiO_2, while the spinels $FeCr_2O_4$ and $NiCr_2O_4$ were detected on 602CA and 214, respectively.
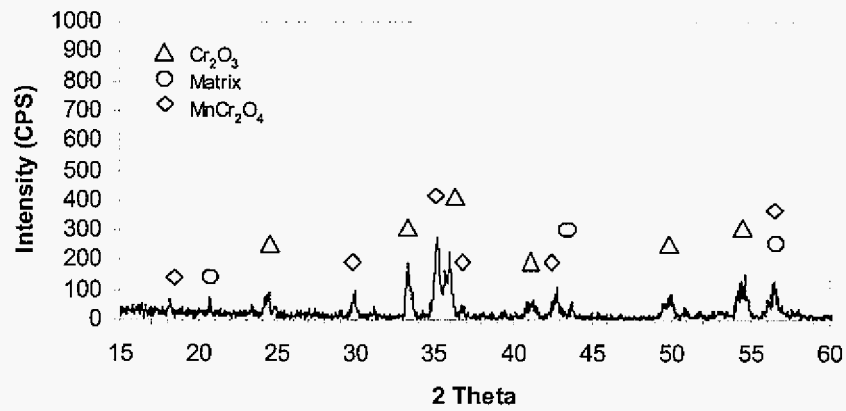
(a) Alloy 800
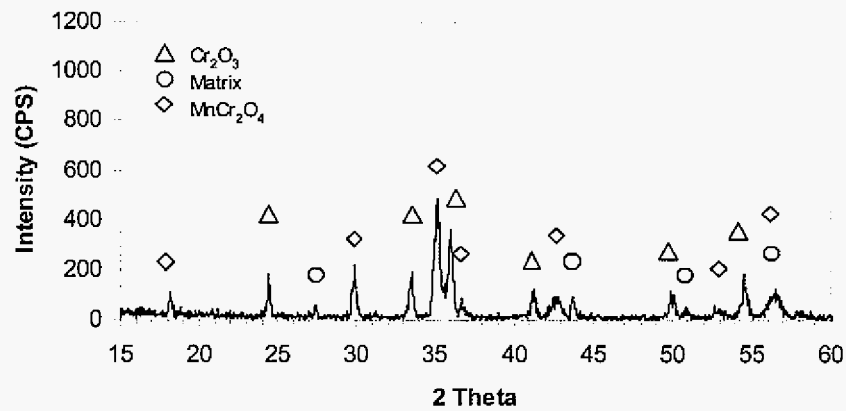
(b) Alloy 800HT
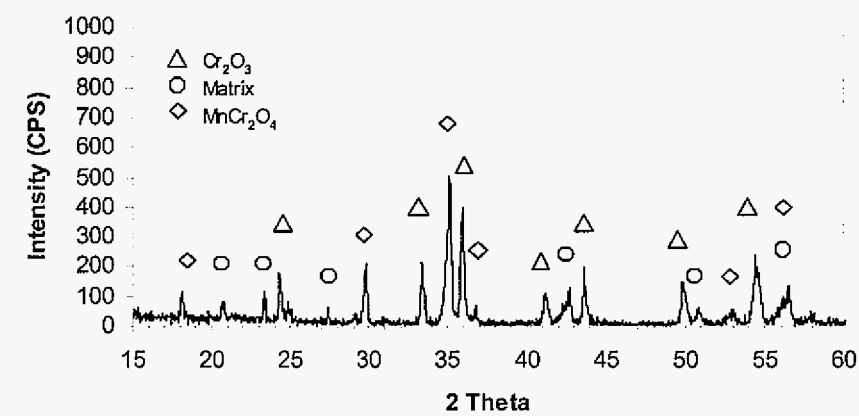
(c) Alloy VDM800

Figure 4.12. XRD patterns for the alloys studied after TGA
oxidation in air at 1000 °C.
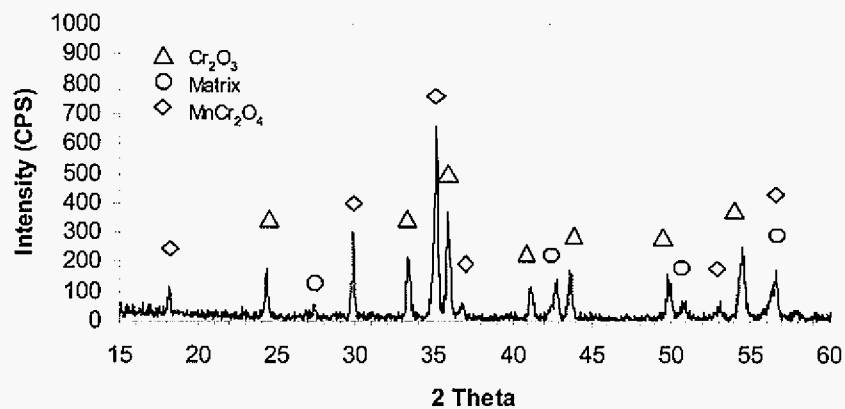
(d) Alloy VDM800HT
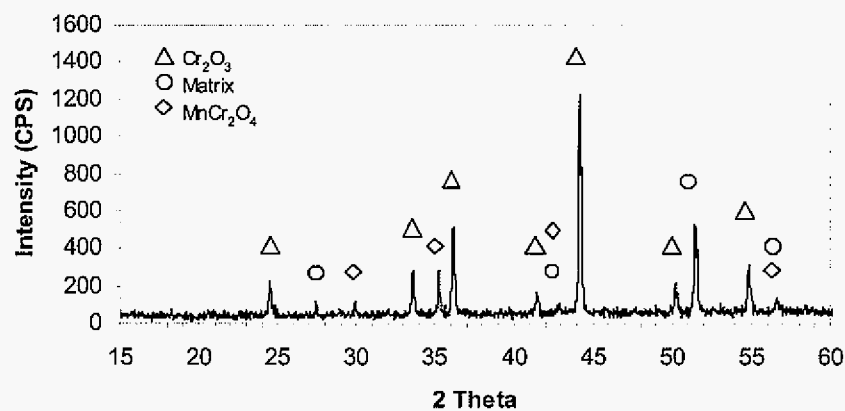
(e) Alloy HR-160
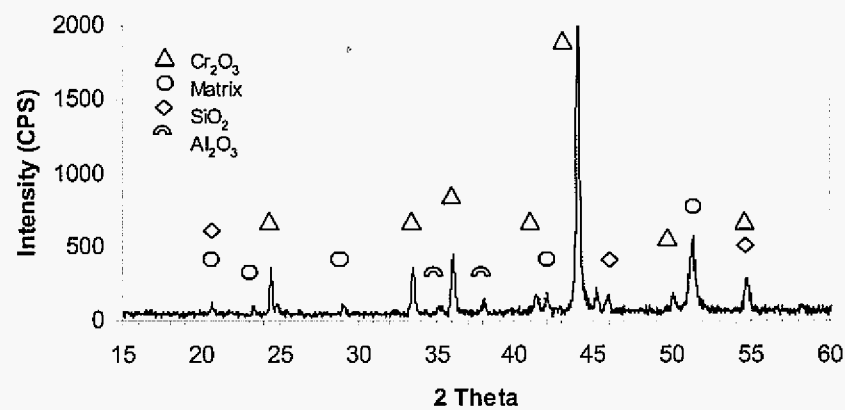
(f) Alloy D-205

Figure 4.12. (continued)
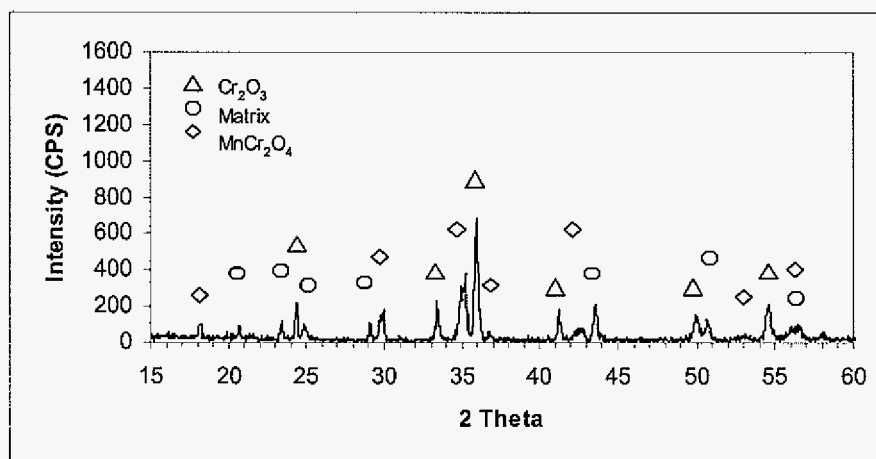
(g) Alloy X
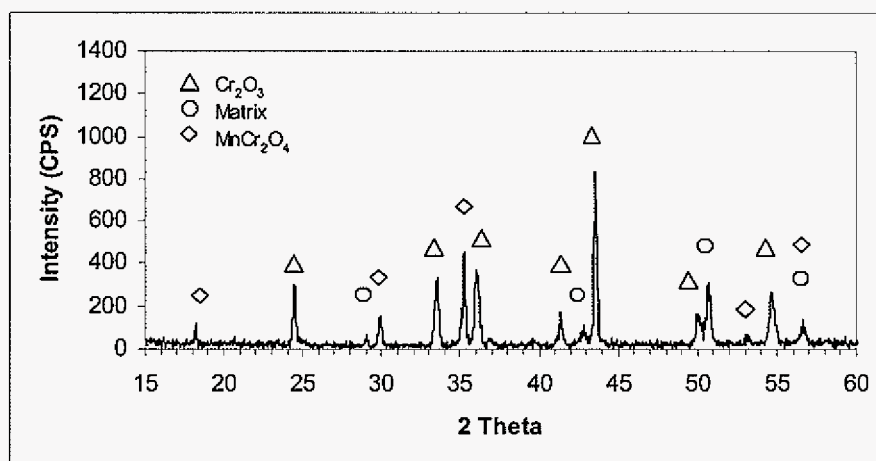
(h) Alloy 4722Co
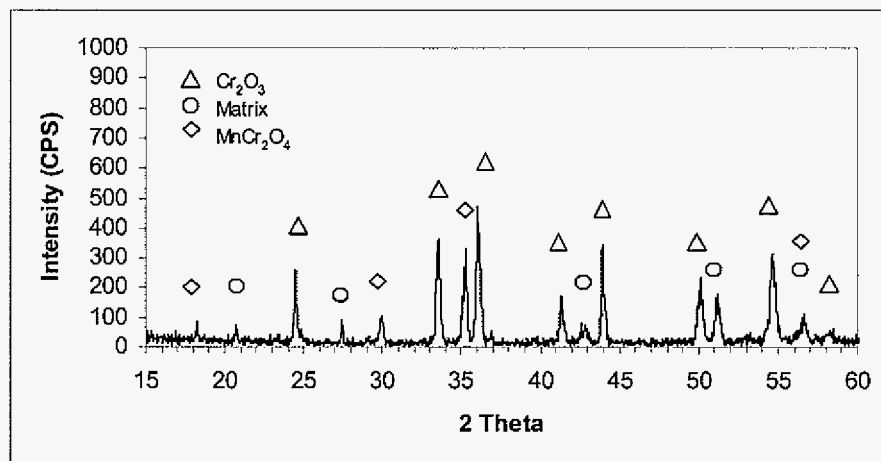
(i) Alloy 601

Figure 4.12. (continued)
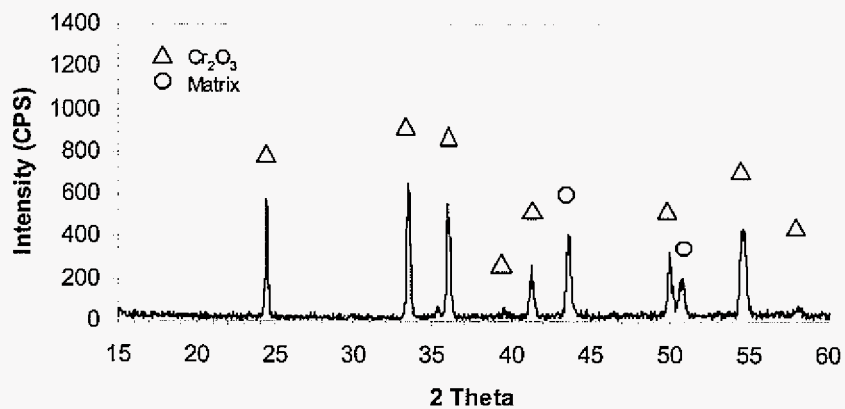
(j) Alloy 617
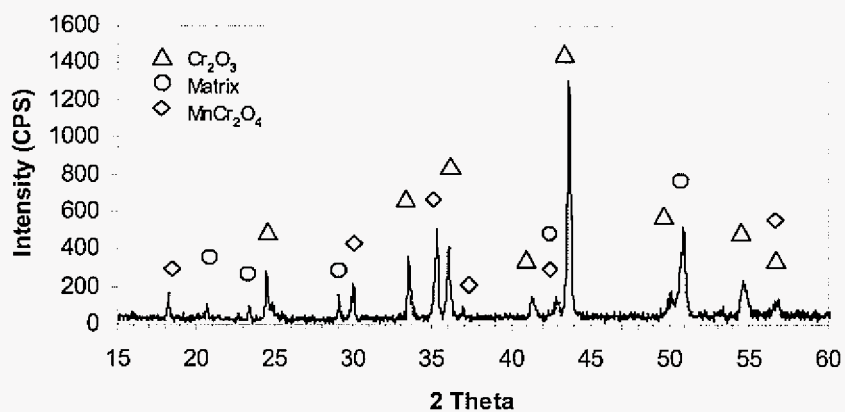
(k) Alloy 230
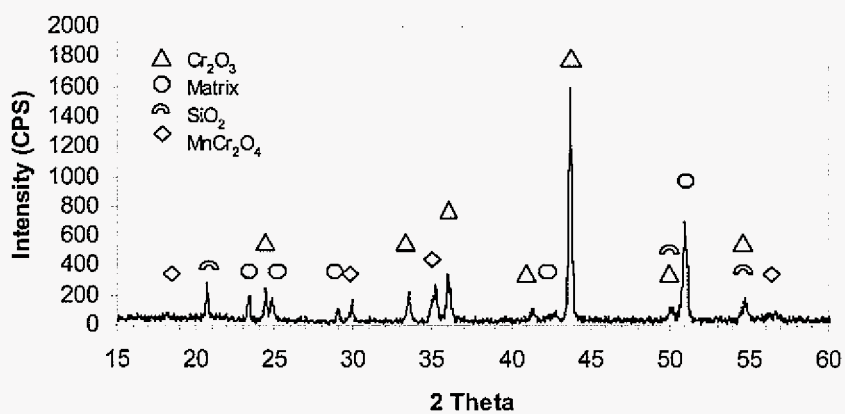
(l) Alloy 45TM

Figure 4.12. (continued)
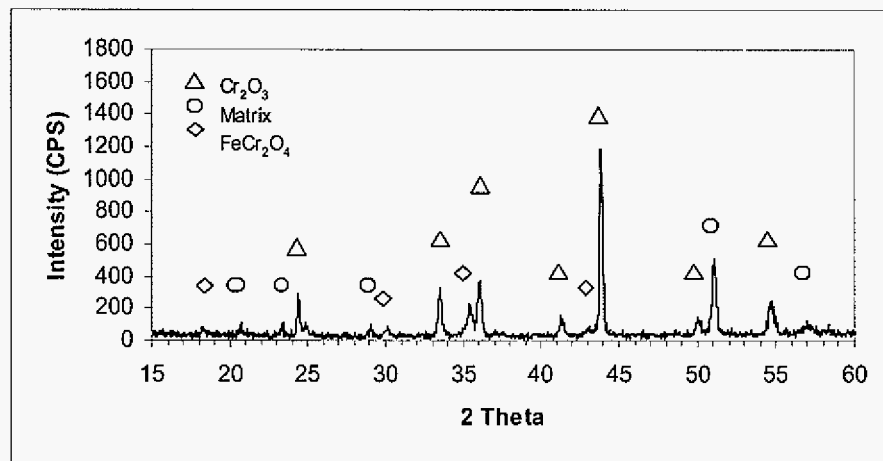
(m) Alloy 602CA
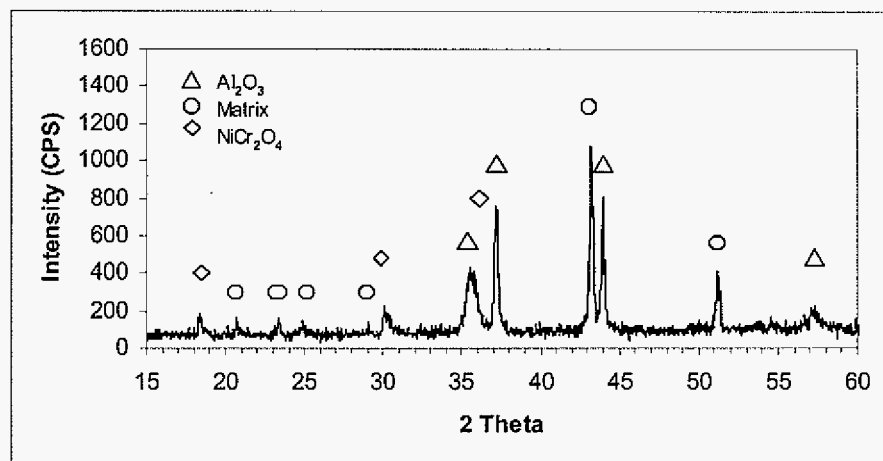
(n) Alloy 214

Figure 4.12. (continued)

After breakdown oxidation occurred for some alloys, non-protective oxides formed as an external oxide scale. XRD analysis showed that the Fe-base alloys studied formed $(Fe,Ni)_3O_4$ and the Ni-base alloys studied formed NiO and $NiCr_2O_4$ oxides after breakdown oxidation.

Table 4.2. XRD analysis on the surface oxides of alloys studied isothermally oxidized in air at 1000 °C.

Alloys	Phases identified
214	Al_2O_3, $NiCr_2O_4$
4722Co	Cr_2O_3, $MnCr_2O_4$
230	Cr_2O_3, $MnCr_2O_4$
617	Cr_2O_3
45TM	Cr_2O_3, $MnCr_2O_4$, SiO_2
X	Cr_2O_3, $MnCr_2O_4$
D-205	Cr_2O_3, Al_2O_3, SiO2
602CA	Cr_2O_3, $FeCr_2O_4$
VDM800	Cr_2O_3, $MnCr_2O_4$
VDM800HT	Cr_2O_3, $MnCr_2O_4$
800HT	Cr_2O_3, $MnCr_2O_4$
601	Cr_2O_3, $MnCr_2O_4$
HR-160	Cr_2O_3, $MnCr_2O_4$
800	Cr_2O_3, $MnCr_2O_4$

4.2.4 Microstructural Characterizations

Figure 4.13 shows cross-sectional SEM images of the alloys studied after 18 1-day oxidation cycles at 1000 °C. The alloys 601, 617, 45TM, 230, 602CA, and 214 showed good resistance at 1000 °C. Thus, they were selected to be oxidized at 1100 °C and their microstructural characteristics were analyzed using SEM after 40 1-day cycles at 1100°C (Figure 4.14). It is recalled that the 800HT alloy showed breakdown after 18 1-day cycles at

(a) 800

(b) 800HT

(c) VDM800

(d) VDM800HT

(e) HR-160

(f) D-205

(g) 4722Co

(h) X
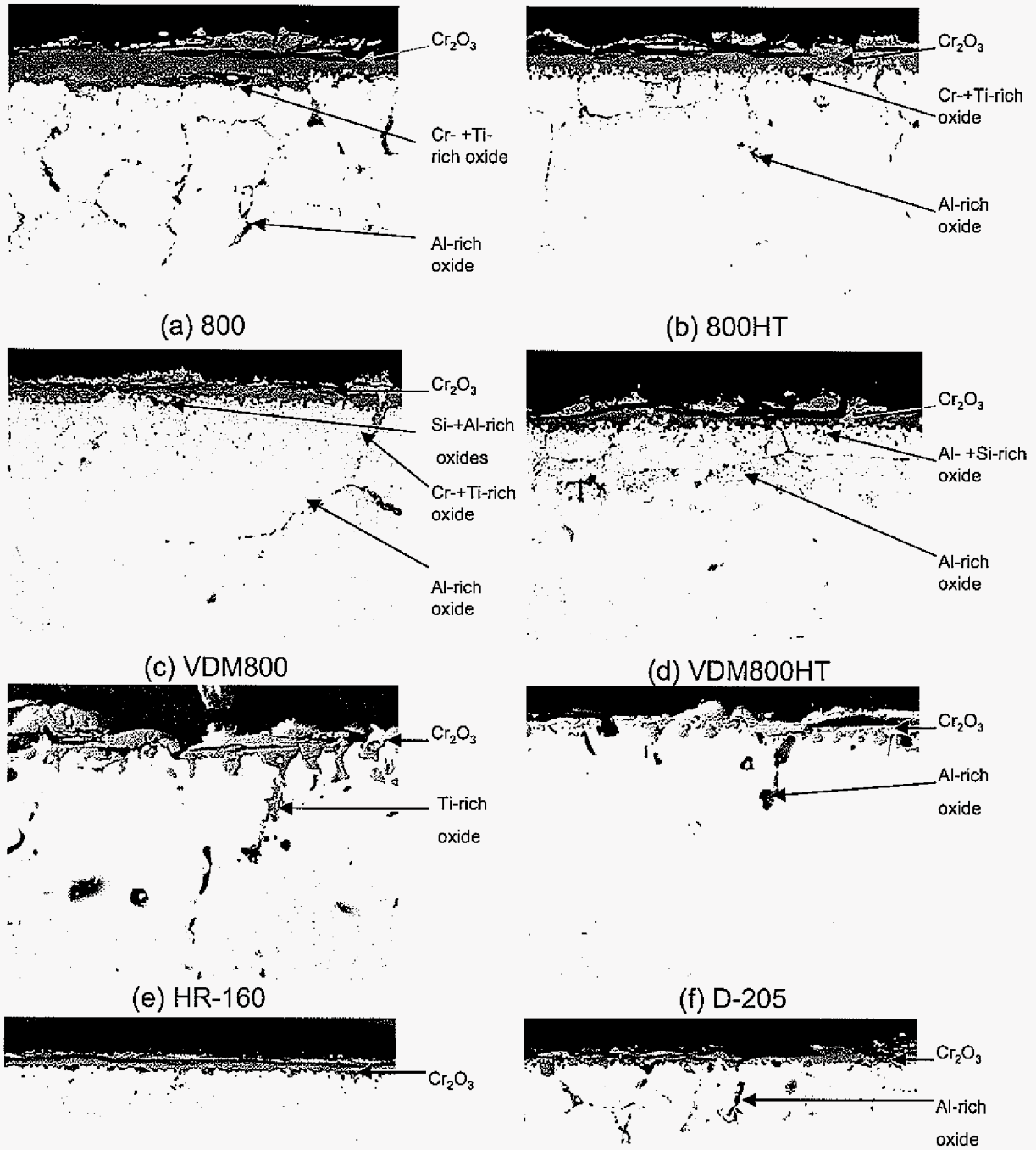
Figure 4.13 Cross-sectional SEM images of the alloys oxidized
after 18 1-day cycles at 1000 °C.

(i) 601

(j) 617

(k) 45TM

(l) 230

(m) 602CA

(n) 214

Figure 4.13. (continued)

(a) 601

(b) 617

(c) 45TM

(d) 230

(e) 602CA

(f) 214
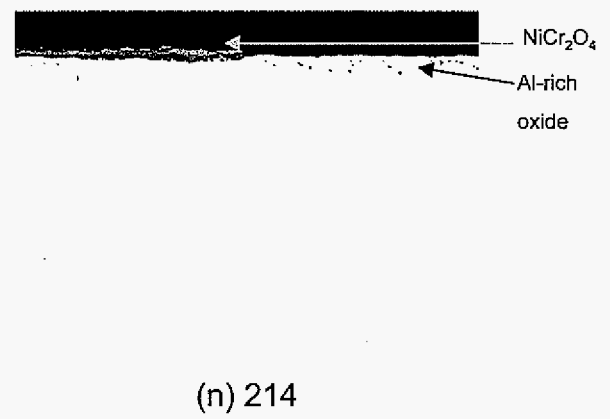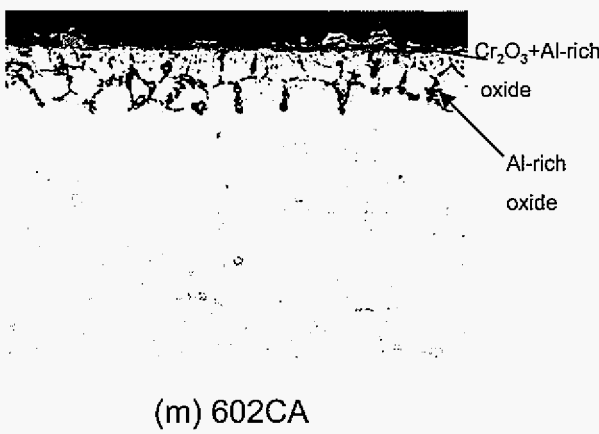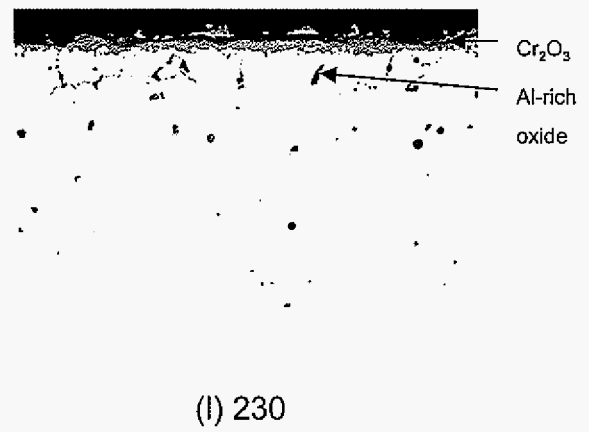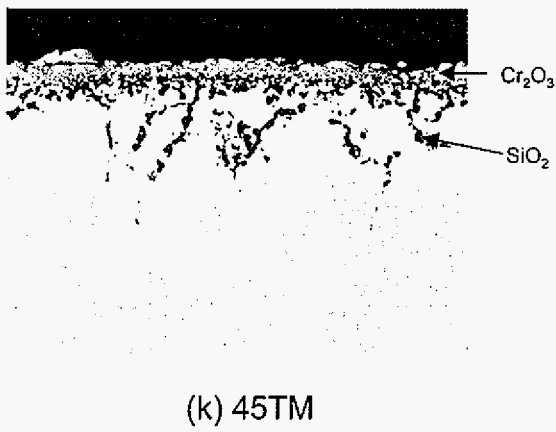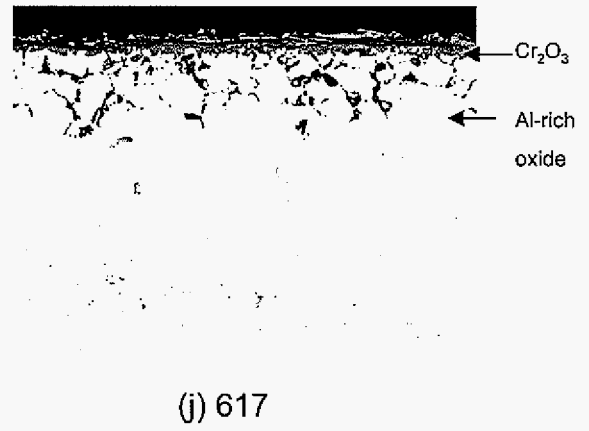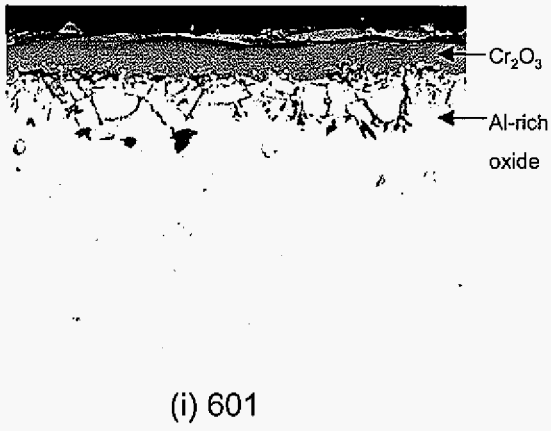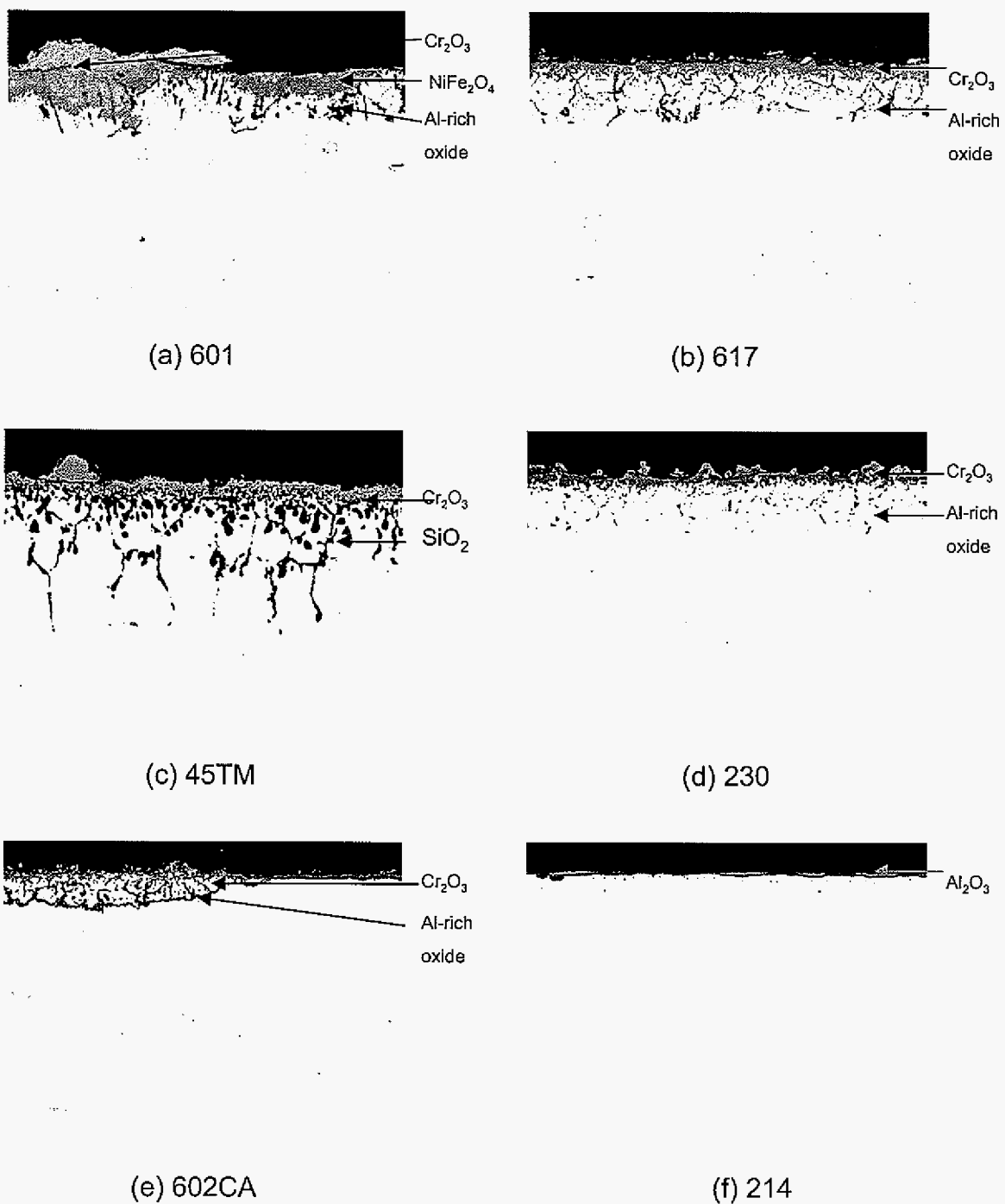
Figure 4.14. Cross-sectional SEM images of the alloys oxidized
after 40 1-day cycles at 1100 °C.

1000 °C and the 601 alloy showed breakdown after 40 1-day cycles at 1100 °C. The oxides were also analyzed using EDS, and so the oxide phases could be inferred by considering the XRD and EDS results.

From Figs. 4.13 and 4.14, all alloys showed external oxide scale and internal oxidation attack after cyclic oxidation. The primary external oxide scale was Cr_2O_3 except for 214, which formed an Al_2O_3 scale. Most of the alloys developed a two-layered scale, with only remnants of the outside layer often remaining due to partial spallation. The morphology of and phases in the oxide scale varied among the alloys. The four 800 series, HR-160, and 601 alloys showed the larger scale thicknesses, which is consistent with their larger steady-state parabolic rate constants in Table 4.1. Similarly, 214, which exhibited excellent oxidation resistance, formed the thinnest scale and showed no evidence of internal oxides. Even though no alumina was detected via XRD of 602CA after the TGA test, its cross-sectional SEM image clearly showed that a continuous Al–rich oxide formed as an internal network or very thin inner layer. It is presumed that this is Al_2O_3. The 45TM alloy formed dispersed SiO_2 internal particles based on EDS and XRD results within the alloy subsurface region. The excellent oxidation resistance for 602CA and 214 (Fig. 4.1-4.6) is clearly attributable to the formation of continuous Al_2O_3 oxide layer, while dispersed internal SiO_2 particles may have contributed to the good oxidation resistance of 45TM. The alloys 601 and 617 have relatively high Al contents (about 1.2 wt.%), and formed extensive Al-rich oxide particles within subsurface region. Although not shown in images, a continuous Si-rich layer was detected under the chromia scale on HR-160 and D-205 by higher magnification cross-sectional SEM imaging after 18 1-day cycles. It is recalled that these alloys contain high Si contents (2.75 and 5.3 wt.%, respectively).

Figure 4.13 shows that the four Fe-base alloys had similar oxidation characteristics with the deep internal intergranular oxidation attack (about 50-100 μm) compared to the Ni-base alloys, which typically formed an internal oxidation zone less than 50 μm after 18 1-day oxidation cycles. The compositions of the intergranular oxides were dependent upon depth into the alloy. Deep into the alloy at the intergranular oxidation front, the oxides were always found to be Al-rich. Progressing towards the alloy surface, the intergranular oxides

transitioned from Al-rich to Ti-rich. Internal oxides rich in Al and Si were found at the alloy/scale interface in the alloys VDM800 and VDM800HT.

The alloys HR-160 and D-205 showed an extensively cracked and damaged oxide scale. The brittle and spalled scale agreed with their poor oxidation kinetics. The 4722Co and X alloys formed similar oxide scales, with an inner Cr_2O_3 layer and an outer $MnCr_2O_4$ layer; although, much of the outer $MnCr_2O_4$ layer on X had spalled and this alloy developed a deeper internal oxidation zone (about 50 μm Al-rich oxide). The 601 alloy formed a thicker Cr_2O_3 scale than the 617 alloy, but shallow internal oxidation attack (about 30 μm in 601 compared 50 μm in 617). The 45TM alloy formed an external Cr_2O_3 scale and SiO_2 precipitates within the alloy subsurface region. The 230 alloy developed an external Cr_2O_3 oxide scale and internal Al-rich precipitates. Compared with their cyclic oxidation behavior at 1000 °C, the alloys 601, 617, 45TM, 230, 602CA, and 214 showed similar oxidation characteristics under cyclic oxidation at 1100 °C (Fig. 4.14). As would be expected, the extent of degradation was greater at 1100 °C, with a thicker oxide scale and deeper internal oxidation formed at this temperature compared to 1000 °C. The 602CA alloy clearly showed a two-layered scale structure with an outer Cr_2O_3 and an inner Al_2O_3–rich layer oxidized cyclically at 1100 °C. However, the Al_2O_3 layer in alloy 602CA was not complete and a interconnected Al_2O_3 internal oxide network existed in some regions.

The 4722Co, X, D-205, and 230 alloys showed depletion of precipitates within their subsurface region after 18 1-day cycles at 1000 °C and 40 1-day cycles 1100 °C. EDS analysis detected that the precipitates in 4722Co, X, and D-205 are Mo- and Si-rich, and W-rich precipitate for 230. The precipitates in the alloys typically were less than 1 μm, and it was therefore very difficult to identify their phase structures.

4.3 Discussion

Almost all high-temperature alloys are Fe- or Ni-based. Fe-Cr alloys with more than about 20 wt.% Cr can form a primary Cr_2O_3 scale, but the alloys would have relatively low high-temperature strength. Multi-component superalloys are strengthened by solid-solution hardening and precipitate hardening. The Fe-base alloys can be strengthened the least and the

Ni-base alloys the most. The major advantage of Fe-base superalloys is low cost, which makes them the most used in commercial applications. Ni-base alloys have high strength at high temperature and can be used at higher temperatures than Fe-base alloys. Iron and nickel are also quite different in their inherent oxidation behavior, with nickel forming a much slower-growing oxide scale than iron. This difference ultimately contributes to the two types of superalloys exhibiting much different oxidation resistance. In addition, the various minor alloying element additions in commercial alloys not only improve fabrication and mechanical properties, but play a significant role in causing variations in oxidation behavior [165].

4.3.1 Oxidation Behavior of the Alloys Studied

Under the cyclic oxidation conditions studied, most of the alloys studied showed a weight change as a function of oxidation cycle that transitioned from positive to negative. The positive weight gain primarily comes from scale growth, and the weight loss is due to scale spallation during the cooling period in a thermal cycle. The amount and time of weight gain and weight loss were alloy-dependent.

Figure 4.15 [139] shows an idealized cyclic oxidation weight-change curve, which shows parabolic growth legs, punctuated by fractional spall events upon cooling. The weight change curve can be considered as a combination of two processes: each heating cycle is associated with a weight gain, and each cooling cycle produces a superimposed weight loss.
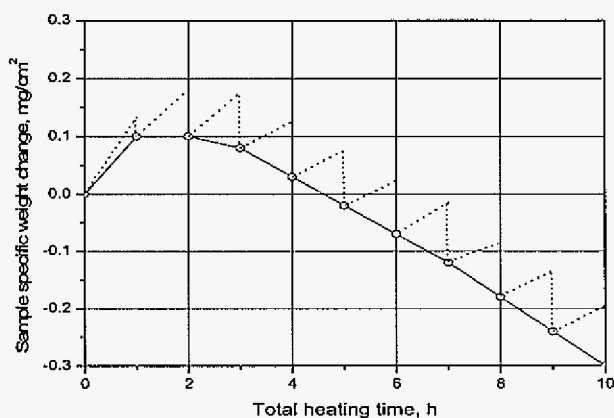
Figure 4.15. Idealized cyclic oxidation kinetics showing parabolic growth and spall events.

It was found from the isothermal oxidation tests that all of the alloys studied went through an initial transient oxidation stage followed by a steady-state oxidation stage. The transient oxidation stage has been shown in other studies to represents the concurrent oxidation of all the major alloying elements present on the alloy surface, even though one oxide is usually greatly favored from a thermodynamic standpoint [148]. This proceeds until the initial rapid kinetics have transitioned to a lower rate and the P_{O_2} at the oxide/alloy interface has been lowered, both of which favor the formation of a healing layer of the most stable oxide. The stable oxide layer − Cr_2O_3, Al_2O_3, or both, offers oxidation resistance during high-temperature process.

As discussed in section 2.3.3.3, an external NiO layer forms during the transient oxidation stage of Ni-Cr alloys containing 20 wt.% Cr. The NiO layer decreases the oxygen partial pressure at the alloy/scale interface, which promotes Cr_2O_3 growth along the alloy/scale interface. Wood and Whittle [182] showed that Cr_2O_3 and Fe_2O_3 form during the initial oxidation stage of Fe-Cr alloys containing 14-25 wt.% Cr. The transient oxidation behavior is complex and affected by many variables [65,167,168,172], such as alloy composition and structure, surface preparation, and duration and temperature of oxidation. Indeed, the establishment of steady-state scaling kinetics in many systems requires time and a considerable scale thickness. From Fig. 4.10, a high transient-stage growth rate apparently results in a short transient duration, while a low transient-stage growth rate generally results in a long transient duration.

The parabolic rate constant of chromia is reported to be in the range of 1~60 ×10^{-12} g^2/cm^4s^1 (Fig. 2.2). From the XRD results (Fig. 4.12), most of the alloys studied, except for the 214 alloy, formed a primarily Cr_2O_3 scale, and their steady-state parabolic rate constants are generally within this range (Table 4.1). However, for reasons that are not completely clear, the two chromia-forming alloys 230 and 4722Co showed smaller steady-state parabolic rate constants than the reported lower limit of 1 ×10^{-12} g^2/cm^4s^1. These two alloys also showed a slower rate of transient oxidation compared to other chromia-forming alloys. The transient oxide phases and/or the boundary conditions for the chromia-scale growth may have played a role in lowering the parabolic rate constants measured for these the two alloys. Compared to the parabolic rate constant of some chromia-forming alloys, the alumina-

forming alloy 602CA showed a relatively larger parabolic rate constant. The reason may be that the time of the TGA test was not enough to establish a continuous Al_2O_3 scale layer. There was no Al_2O_3 detected by XRD after the TGA test, while the results after long-term cyclic oxidation showed the existence of Al_2O_3 in 602CA (Fig. 4.13).

The oxide growth rate was apparently affected by the alloy composition. For Fe-Cr and Ni-Cr alloys containing a sufficiently high Cr content, the scale is primarily Cr_2O_3 containing a low level of iron or nickel [114, 182-184]. The doped Cr_2O_3 layer affects the scale plasticity and the ability of vacancies to penetrate to the subjacent alloy, which would affect scale growth rate. Both Ni-Cr and Fe-Cr systems display a minimum in the scaling rate at about 20% Cr. This could be due to critical doping of the supposedly metal-deficient, p-type Cr_2O_3 by Ni^{2+} and Fe^{2+} ions [175]. In addition, an alloy containing 20% Cr would have a lower chemical activity of chromium at the alloy/scale interface than alloys with higher Cr contents. The lower Cr activity at the alloy/scale interface results in a higher partial pressure of oxygen at the alloy/scale interface in comparison to a higher Cr activity. Thus, the gradients of Cr and O activity across chromia scale decreases with decreasing Cr activity. As a result, the growth rate of chromia should decrease. For commercial alloys, minor alloying elements such as Mn, Si, Ti, and Al, could also affect the structure of the oxide scale and the boundary condition of oxidations for the Cr_2O_3 scale growth, and hence result more complex of varied scaling rates.

The 601 alloy showed the largest weight gain during 1-day cyclic oxidation before the onset of a spalltion, while the 800 alloy showed the largest weight gain for 7-day cyclic oxidation at 1000 °C. Under isothermal oxidation at 1000 °C, the 601, 800, and HR-160 alloys showed the largest steady-state parabolic rate constants with sequence HR-160>800>601. A large parabolic rate constant promotes the kinetic establishment of chromia scale; however, cycling condition would affect spallation behavior, and hence affect weight gain during cyclic oxidation. The HR-160 alloy did not show weight gain during cyclic oxidation because of its large spallation behavior from the first cycle. The 800 alloy was prone to spall under 1-day cyclic oxidation compared to its less spallation behavior under 7-day cyclic oxidation at 1000 °C. This is clearly a consequence of the higher number of thermal cycles associated with the 1-day cyclic oxidation tests. The 601 alloy had small

spallation behavior oxidized under 1-day cycling condition and thus showed the largest weight gain at 1000 °C.

Isothermal oxidation did not show the breakdown behavior at 1000 and 1100 °C. The alloys 800HT and VDM800HT showed breakdown of about 18 and 95 1-day oxidation cycles, respectively, at 1000 °C, while the 601, 617, 4722Co, and 230 alloys showed breakdown after different 1-day cycles at 1100 °C. Scale spallation can occur because adherence between the scale and the underlying alloy is weakened, due for instance to vacancy coalescence at the alloy/oxide interface [184,185]. Cr_2O_3 scale cracking or spallation exposes the underlying Cr-depleted alloy to the atmosphere, Cr_2O_3 re-formation may not be possible and, instead, a less protective oxide containing iron or nickel forms. It is important to predict the interfacial chromium content which could determine when the breakdown oxidation happens. Practically, the critical chromium content to form Cr_2O_3 scale is dependent upon alloy composition and oxidation condition. Thus, this value is difficult to obtain. The kinetics results from this study showed that the Fe-base alloys cannot be used to resist long-term oxidation above 1000 °C. While many Ni-base alloys showed oxidation resistance at 1100 °C. It would be reasonable to infer that this difference is due to the fact that iron oxidized much more rapidly than nickel, e.g., $k_p(Fe)/k_p(Ni) \approx 940$ at 1100 °C. More discussion on the effects of Ni and Fe on oxidation behavior will be presented in section 4.3.2. Wood [67] reported that isothermal breakdown is rarer because scale adhesion is better, due to a more irregular and interlocked alloy-oxide interface. Another factor is less thermal stress developed under isothermal condition.

All of the chromia-forming alloys studied developed internal oxides at 1000 °C and 1100 °C (Fig. 4.13 and 4.14). Because Si, Ti, and Al are thermodynamically more stable than Cr, internal SiO_2, TiO_2, and/or Al_2O_3 could develop below the external chromia scale. The partial pressure of oxygen decreases from the scale/alloy interface into matrix of alloy, thus internal oxides generally form according to their thermodynamic stability, from SiO_2, TiO_2, and then Al_2O_3 to alloy matrix. All internal oxides formed in the current study obeyed such a sequence. From Fig. 4.13, the four Fe-base alloys showed internal SiO_2, TiO_2, and Al_2O_3, and their internal oxidation had a larger amount and penetration depth than in the Ni-base alloys. Most of the Ni-base alloys mainly showed internal Al_2O_3, except for the 214 alloy,

which showed no internal oxidation. The Ni-base alloys showed less spallation behavior, indicating that the scale was more adherent to the substrate. This, in turn, would minimize oxygen penetration to alloy matrix and therefore result in less internal oxidation. The internal oxides developed predominantly along grain boundaries, which act as short-circuit paths for oxygen diffusion inward. Internal oxidation, which may shorten the effective thickness of alloy and increase internal stress, is detrimental for oxidation resistance. From the standard point of internal oxidation, Fe-base alloys should provide worse oxidation resistance than Ni-base alloys.

Thermal cycling clearly played an important role on the oxidation resistance of the alloys studied. Scale spallation generally occurs during cooling period, during which thermal stresses develop and the oxide scale is less ductile than at higher oxidizing temperature. As discussion in section 2.2.7.2, a decrease in cycle frequency would decrease the induced thermal stresses, which is beneficial to spallation resistance; however, the decrease in cycle frequency prolongs the hold time at high temperature, which could increase scale thickness and develop defects, and then result in the larger amount of spallation. Comparing Fig. 4.1 to 4.6, 7-day cyclic oxidation was less aggressive than 1-day cyclic oxidation. This was more clearly shown in Fig. 4.8, in which the dependence is about as $\Delta t^{(2/3)}$ (cyclic duration) for the number of days to cross zero mass change. Thus, thermal stress was apparently a more important effect on spallation than growth stress oxidized for the conditions studied. However, the 617 and 4722Co alloys showed a different sequence of oxidation resistance under 1-day and 7-day cyclic oxidation at 1000 °C. Thus, dwell time (Δt) is not always a clear indicator of cyclic oxidation conditions.

After cyclic oxidation, the depletion of Mo- and W-rich precipitates within the subsurface region of the 4722Co, X, D-205, and 230 alloys showed that these precipitate phases became unstable due to either change in the local alloy chemistry or, more specifically, the presence of oxygen. The data is not enough to clearly show how the dissolution of these precipitates affected cyclic oxidation behavior. Elliot and Hampton [186] reported that addition of Mo and W promoted catastrophic scale spalling from Ni-10Cr alloys with 8 wt.% Mo or 14.3 wt.% W oxidized at 1000 °C, especially if the cycling frequency increased. The dissolution of

these Mo- or W-rich precipitates should decrease the high-temperature strength of the alloys within the depleted subsurface, and hence decrease the effective thickness of the alloys.

4.3.2 The Effects of Nickel and Iron Contents on Oxidation Behavior

Based on oxidation kinetics, the Fe-base alloys showed worse oxidation resistance than the Ni-base alloys in the current study (Figs. 4.1-4.6). The Fe-base alloys also showed severe internal oxidation as discussed in previous section. From Fig. 4.7, it is seen that the time to crossover (zero mass change) increases with increasing nickel content in the alloys, which shows that nickel content is beneficial for oxidation spallation. The explanations for the effect of Ni and Fe on oxidation behavior are not conclusive as discussed in section 2.3.3.3. Briefly, there are three possible reasons for the beneficial effect of Ni: reduces the rate of cation diffusion in Cr_2O_3 scale [120], influences the adhesion and mechanical properties of the scale [187], and retards the breakthrough transformation, Cr_2O_3 to $FeCr_2O_4$ + Fe_2O_3 [188].

Table 4.1 shows that the Ni-base alloys generally had lower parabolic rate constants than the Fe-base alloys when oxidized isothermally at 1000 °C. The smaller parabolic rate constant corresponds to slow oxide growth and, hence, thinner oxide scale. The cross-sectional SEM images (Fig. 4.13) also showed that the Cr_2O_3 scale on most of the Ni-base alloys were thinner than that on the Fe-base alloys after cyclic oxidation. A thinner oxide scale develops less stresses and would be expected to decrease spallation according to Equation 2.87. The Ni-base 601 alloy formed a thick oxide scale, but the integrity of the scale ensured its good oxidation resistance compared to Fe-base alloy. Moreover, less cracking or spallation at the scale/alloy interface was found for most Ni-base alloys compared to Fe-base alloys. Thus, Ni may promote the integrity of oxide scale and adherence of the scale/alloy interface [166,187]. However, the Cr_2O_3 scale formed on the Ni-base HR-160 and D-205 alloys was extensively damaged, which worse their cyclic oxidation resistance. The reason for these two alloys should be related to some high alloying element contents, such as Co or Si.

Hobby and Wood [187] studied austenitic Fe-Cr-Ni alloys in 1 atm oxygen at 800-1200 °C. They found that Ni reduced the steady oxidation rate, which was attributed to an more

effective "blocking" of cation vacancies in Cr_2O_3 by Ni^{2+} and Fe^{2+} and Fe^{3+} in optimum quantities conjointly than alone. Iron ions may produce the effect wither by Fe^{2+} blocking vacancies in Cr_2O_3 or by Fe^{3+} giving Cr_2O_3-Fe_2O_3 solid solution [184], where Ni^{2+} ions act entirely by the former mechanism, which could decrease the cation vacancy concentration in the chromia scale. And the following defect reaction also shows that the doping of Ni^{2+} chould decrease the cation vacancies concentration (assumed here to be singly effective negative charged, $V_{Cr}^{'}$):

$$2NiO + 2V_{Cr}^{'} + \frac{1}{2}O_2 = 2Ni_{Cr}^{'} + 3O_o \qquad (4.1)$$
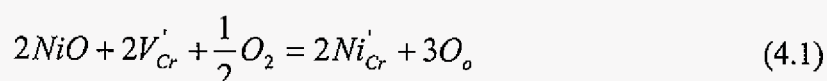
Another factor may be that Fe-Cr-Ni alloys are less effective at absorbing inwardly flowing cation vacancies than Fe-Cr alloys, so that the vacancy gradient across the scale is less. Most Ni-base alloys studied, except for HR-160 and D-205, showed relatively integrity for the oxide scale after 18 1-day cycles oxidized at 1000 °C.

With the depletion of chromium in the alloys, less-protective oxides can form on the Ni- and Fe-base alloys as nickel oxide or iron oxide, respectively. From XRD analysis, the Fe-base alloys studied formed $(Fe,Ni)_3O_4$ and the Ni-base alloys studied formed NiO and $NiCr_2O_4$ after breakdown. NiO is known to be more protective than FeO, Fe_3O_4, and Fe_2O_3. Thus, Ni-base alloys would show better resistance even after breakdown.

4.3.3 The Effects of Minor Alloying Elements

Nickel is beneficial to oxidation resistance, and its effect limits generalized interpretations of the oxidative effects of minority elements. However, the alloys studied with close Ni, Cr, and Fe levels showed different oxidation behaviors, which revealed the effects of minority elements. For example, 800HT (44Fe-20Cr-34Ni) and VDM800HT (47Fe-20.5Cr-30Ni) showed breakdown behavior during 1-day cyclic oxidation at 1000 °C, while VDM800 (47Fe-20Cr-30Ni) did not undergo breakdown under the same oxidation conditions. Further, the 800HT and VDM800HT alloys showed significantly different breakdown behaviors with the onset of breakdown after about 18 and 95 cycles, respectively. The four Fe-base 800 series alloys studied have very close Ni (~30-34 wt.%), Fe (~44-47 wt.%) and Cr (~20 wt.%)

contents, thus the difference of their oxidation behavior should be at least partly associated with the minority elements in the alloys, such as Mn, Si, Ti, and Al.

Manganese is added during the melt processing of an alloy for the purpose of deoxidizing and desulfurizing. Generally, an Fe-base alloy has a maximum Mn content of about 1.5-2.0 wt.%, and Mn content in Ni-base alloy is less than 0.5 wt.% [165]. In the current study, the four 800 series alloys had about 0.7 wt.% Mn, while Mn contents in Ni-base alloys varied from 0.06 wt.% (617) to 0.59 wt.% (HR-160). As discussed in section 2.2.5.3.1, manganese is detrimental to oxidation resistance because it diffuses relatively faster through a Cr_2O_3 scale and leads to external $MnCr_2O_4$ formation, which is less protective and more prone to spallation. XRD results (Fig. 4.12) showed that most of the chromia-forming alloys studied formed $MnCr_2O_4$ except for 617, D-205, and 214. The 617 and D-205 alloys have the lowest Mn contents (0.06 and 0.18 wt.%, respectively) which may have led to too small amount of $MnCr_2O_4$ formation to be detected by XRD. It should be noted that the existence of $MnCr_2O_4$ could not be detected using the SEM because of very close characteristics energies for Cr and Mn. Thus, it was hard to separate the Mn and Cr signals completely, which makes it difficult to detect Mn if combining with an invariably large amount of Cr. The 617 alloy showed good oxidation resistance against the chromia-forming alloys studied, which could be attributed to this alloy having the least amount of Mn. The 214 alloy formed an Al_2O_3 scale, which may inhibit the outward diffusion of Mn to the scale surface.

Silica is a thermodynamically more stable oxide than chromia and could form under a chromia scale during oxidation. From cross-sectional SEM images (Fig. 4.13), most of alloys studied with Si addition formed Si-rich oxides within their subsurface region after 18 1-day oxidation cycles. However, the morphology of the Si-rich oxides was alloy dependent. The four 800 series alloys (800, 800HT, VDM800, and VDM800HT) had a low Si content (less than 0.5 wt.%) with VDM800 and VDM800HT containing about 0.37 wt.% Si compared to about 0.15 wt.% Si in 800 and 800HT. The cross-sectional SEM images show that VDM800 and VDM800HT formed Si-rich oxide particles at the scale/alloy interface, while no Si-rich particles formed in the 800 and 800HT alloys. Some researches [100,115] concluded that the surface formation of Si-rich oxide particle helps to facilitate Cr_2O_3-scale formation and promotes oxidation resistance. The combination of Si-rich and Al-rich oxide particles at the

alloy/scale interface in VDM alloys may have reduced the diffusion of oxygen inward and chromium outward, thus lowering the scale growth rate. For the high-Si (>2 wt.%) alloys studied, a continuous Si-rich oxide layer was detected in HR-160 (2.75 wt.% Si) and D-205 (5.3 wt.% Si), while a large amount of SiO_2 precipitates formed within subsurface region in the 45TM alloy. It is reported that an inner SiO_2 layer can greatly worsen the extent of scale spallation [101,114,116]. Thus, it is believed that the continuous Si-rich oxide layer at the scale/alloy interface resulted in the worse oxidation resistance for the alloys HR-160 and D-205. But for the 45TM alloy (2.66 wt.% Si), with a large amount of SiO_2 particle within subsurface region, its excellent oxidation behavior should be partly attributed to the SiO_2 precipitates.

Titanium forms a more stable oxide than Cr_2O_3 and tends to oxidize at both the scale surface and the alloy/scale interface [116-122]. Titanium is detrimental for creep strength, toughness, and oxidation resistance, and thus is limited in alloying below about 0.6% [189]. The alloys with Ti addition were found to form internal particles of Ti-rich oxide. Of the four 800 series alloys, VDM800 had the lowest Ti content (0.31 wt.%) and showed the best oxidation resistance, indicating that keeping the Ti content low could improve cyclic oxidation resistance.

Alumina is thermodynamically more stable than SiO_2 and TiO_2. A slow-growing, dense, and adherent Al_2O_3 layer confers excellent oxidation resistance for alumina-forming alloys. In the current study, only the 214 alloy with the highest aluminum content (4.79 wt.%) in the alloys studied formed a continuous Al_2O_3 scale and showed excellent oxidation behavior. The 602CA alloy (2.13 wt.% Al) formed a continuous internal Al_2O_3 network or very thin layer with an outer Cr_2O_3 and $FeCr_2O_4$ layer during cyclic oxidation at 1000 and 1100 °C. The good oxidation resistance of 602CA apparently came from this continuous internal Al_2O_3 network, which could have reduced the diffusion of oxygen inward and chromium outward, thus decreasing of depletion of Cr within subsurface region. Further, the continuous Al_2O_3 could also act as barrier for further oxidation attack after spallation of the chromia scale, and even help the re-formation of chromia scale. The same effect may work for the 601 and 617 alloys, which have 1.32 and 1.11 wt.% Al, respectively. These two alloys formed extensive internal Al-rich oxide during cyclic oxidation. The 601 alloy showed worse

oxidation resistance compared to 617. The 601 alloy had a higher Fe content (15.49 wt.%) than 617 (1.09 wt.% Fe). The higher Fe content in 601 may be partly the reason for its larger parabolic rate constant and thicker chromia oxide thickness.

Low aluminum content (<1 wt.%) could have also affected the oxidation behavior of the four 800 series alloys studied. As discussed above, VDM800 and VDM800HT had better oxidation resistance than 800 and 800HT due to Si-rich and Al-rich oxide particles formed at the scale/alloy interface in the VDM alloys. The higher Al content (0.46 wt.%) in the 800HT alloy may have resulted in worse oxidation behavior than the 800 alloy (0.30 wt.% Al) during 1-day cyclic oxidation at 1000 °C. A similar effect is found in the VDM800 alloy (0.25 wt.% Al), which had better cyclic oxidation resistance than VDM800HT (0.58 wt.% Al). The reasons for these observations may be associated with an increased extent of internal oxidation at these Al contents.

A small amount (0.005-0.3%) of reactive element (RE) can improve the spallation resistance of a scale [123]. It is believe that addition of Ce (0.007 wt.%) in 45TM, and Y in 602CA (0.07 wt.% Y) and 214 (0.006 wt.% Y) improved their oxidation resistance. However, it was not possible to trace the small amount RE in these alloys for the characterization techniques used.

It should be mentioned that the effect of minority elements may be more complex on oxidation behavior than discussion above. For example, interactive effect of minority elements should happen during oxidation, and the interactive effect may vary with element content and oxidation condition. The interactive effects of minority elements will be studied further in later chapters.

4.4 Conclusions

The commercial wrought alloys studied showed highly variable oxidation resistance, which depends upon alloy composition, structure, oxide phase, and oxidation condition. The Fe-base alloys generally showed poorer oxidation resistance with a large amount of spallation than the Ni-base alloys during cyclic oxidation. The 800HT alloy exhibited breakdown oxidation after only 18 1-day cycles at 1000 °C, while breakdown occurred at

about 95 1-day cycles for VDM800HT alloy. The Ni-base alloys also showed dramatic variability in their oxidation behavior, from negative weight change (large spallation) to stable positive weight gain (small spallation) during cyclic oxidation. The variation in oxidation behavior is mainly attributed to the alloying elements in the alloys. The alumina-forming alloys, 214 and 602CA, showed excellent oxidation resistance during cyclic oxidation at 1000 and 1100 °C, in which an Al_2O_3 scale conferred to their excellent spallation resistance. The chromia-forming alloy 45TM also showed excellent oxidation resistance which is attributed to the beneficial effect of SiO_2 particles within subsurface region formed during cyclic oxidation and to the presence of a minor amount of reactive element (*i.e.*, Ce). By contrast, the relatively continuous Si-rich oxide layer that developed in the HR-160 and D-205 alloys resulted in extensive scale spallation during cyclic oxidation.

From isothermal oxidation, all alloys showed a fast-growing transient oxidation stage, followed by steady-state oxidation obeying parabolic growth rate, which corresponds to diffusion-controlled kinetics. Generally, the Fe-base chromia-forming alloys had larger parabolic rate constants than the Ni-base chromia-forming alloys. A large parabolic rate constant would help to establish the chromia scale, but would also result in a thicker chromia scale, which could develop large stresses and be prone to spallation during cyclic oxidation. The 214 alloy formed an exclusive alumina scale and showed the lowest parabolic rate constant.

Nickel is more beneficial for oxidation resistance than iron. The following reasons may contribute to the beneficial effect of Ni: (1) Ni^{2+} doping in Cr_2O_3 decreases the cation vacancies concentration, and thus reduces the oxidation rate; (2) Ni may decrease the absorption of inwardly flowing cation vacancies and decrease the vacancy gradient across the scale; (3) Ni-base alloys may have better adhesion between oxide scale and subsurface alloy; and (4) Ni oxidizes more slowly than Fe and therefore it is kinetically easier for the Cr2O3 scale to establish itself on a Ni-base alloy.

Most of the alloys studied showed weight loss after some number of 1-day oxidation cycles at 1000 and 1100 °C. Two Fe-base alloys, 800HT and VDM800HT, showed breakdown oxidation at 1000 °C and 1100 °C, while the 601, 617, 4722Co, and 230 alloys showed breakdown behavior only at 1100 °C. The breakdown oxidation was due to

chromium depletion within subsurface region of the chromia-forming alloy to a point that Cr_2O_3 re-formation or healing could not occur in the event of scale cracking or spallation. Less-protective oxides, such as iron oxide or nickel oxide, would form if the interfacial Cr lowers to a critical level. The formation of less-protective oxide corresponds to faster spallation (breakdown), which marks the end of the alloy life.

The chromia-forming alloys underwent internal oxidation because the oxides of minority alloying elements, Si, Ti, and Al, are thermodynamically more stable than chromia. Thus, SiO_2, TiO_2, and/or Al_2O_3 could form as internal oxides under chromia scale. All internal oxidation in the alloys studied happened primarily along grain boundaries, which provide fast diffusion path and preferred sites for nucleation. The Fe-base alloys showed more severe internal attack than the Ni-base alloys: deeper internal oxidation and more internal oxides. The Ni-base alloys showed less internal oxidation in part because the scale minimized oxygen penetration to alloy matrix, which in turn would minimize the extent of internal oxidation.

Cycle duration was found to affect oxidation resistance. Generally, low cycle frequency could decrease induced thermal stress, thus be beneficial to spallation resistance. Under the cyclic oxidation conditions in current study, the dependence was about as $\Delta t^{(2/3)}$ (cyclic duration) for the number of days to cross zero mass change.

Minor alloying elements play significant role on cyclic oxidation behavior. Manganese is generally detrimental for oxidation resistance. Most alloys with Mn addition larger than 0.2 wt.% formed an $MnCr_2O_4$ outer oxide layer, which is less-protective and prone to spall. Silicon has different possible effects on oxidation resistance depending on its content. In generally, silicon can facilitate the formation of Cr_2O_3 scale. A continuous SiO_2 layer at the alloy/scale interface makes the scale prone to spallation during cyclic oxidation. Titanium is generally detrimental for oxidation resistance. It trends to oxidize at the scale surface and the alloy/scale interface, and intergranularly in the subsurface region of the alloy. Aluminum is generally beneficial for oxidation resistance if an Al_2O_3 scale forms. An internal continuous alumina network within the subsurface region of the alloy can reduce the diffusion of oxygen inward and alloying cation outward, which decreases the scale growth rate and the depletion of Cr within the subsurface region. Al-rich oxide particles combined with Si-rich oxide

particles at the alloy/scale interface are also beneficial for oxidation resistance. However, internal alumina oxidation should be a problem to decrease the mechanical properties of alloy.

CHAPTER 5 CYCLIC OXIDATION BEHAVIOR OF FE-BASED 800 SERIES ALLOYS

5.1 Introduction

As shown in chapter 4, the chromia-forming 800 series alloys can show significant variation in oxidation resistance during 1-day cyclic oxidition at 1000 °C. Although the alloys tested were of similar chemical composition (*i.e.*, within specifications), their variations in microstructures and minor alloying element contents were apparently sufficient to cause the marked differences in oxidation behavior. A more detailed study of the cyclic oxidation behavior of the 800 series alloys is presented in this chapter. The effect of minority elements on oxidation behavior will be discussed in particular, with focus on characterizing the alloy/scale interface and subsurface microstructural and compositional changes that occur during the oxidation process.

5.2 Experimental Results

The measured compositions of the wrought 800 series alloys studied are presented in Table 5.1. The 800 and 800HT alloys were supplied by Special Metals (SM alloys), and the VDM800 and VDM800HT alloys were supplied by Krupp VDM GmbH (VDM alloys). The SM alloys were 0.8 mm thick for the 800 alloy and 3 mm thick for the 800HT alloy; whereas the two VDM alloys (VDM800 and VDM800HT) were 4.8 mm thick.

Table 5.1. Measured composition (wt.%) of the 800 series alloys studied.

Alloys	C	Mn	Si	Cr	Ni	Fe	Ti	Al	Cu
800	0.02	0.78	0.13	20.05	33.64	44.46	0.41	0.30	0.21
800HT	0.07	0.79	0.15	19.96	33.59	44.19	0.55	0.46	0.24
VDM800	0.061	0.70	0.38	20.50	30.30	47.15	0.32	0.25	0.07
VDM800HT	0.075	0.70	0.37	20.20	30.35	46.80	0.49	0.58	0.16

Figure 5.1 shows the as-received mirostructures of the 800 series alloys listed in Table 5.1. The microstructures are seen to depend on the supplier. The SM alloys (800 and 800HT) are

800

800HT

20 μm
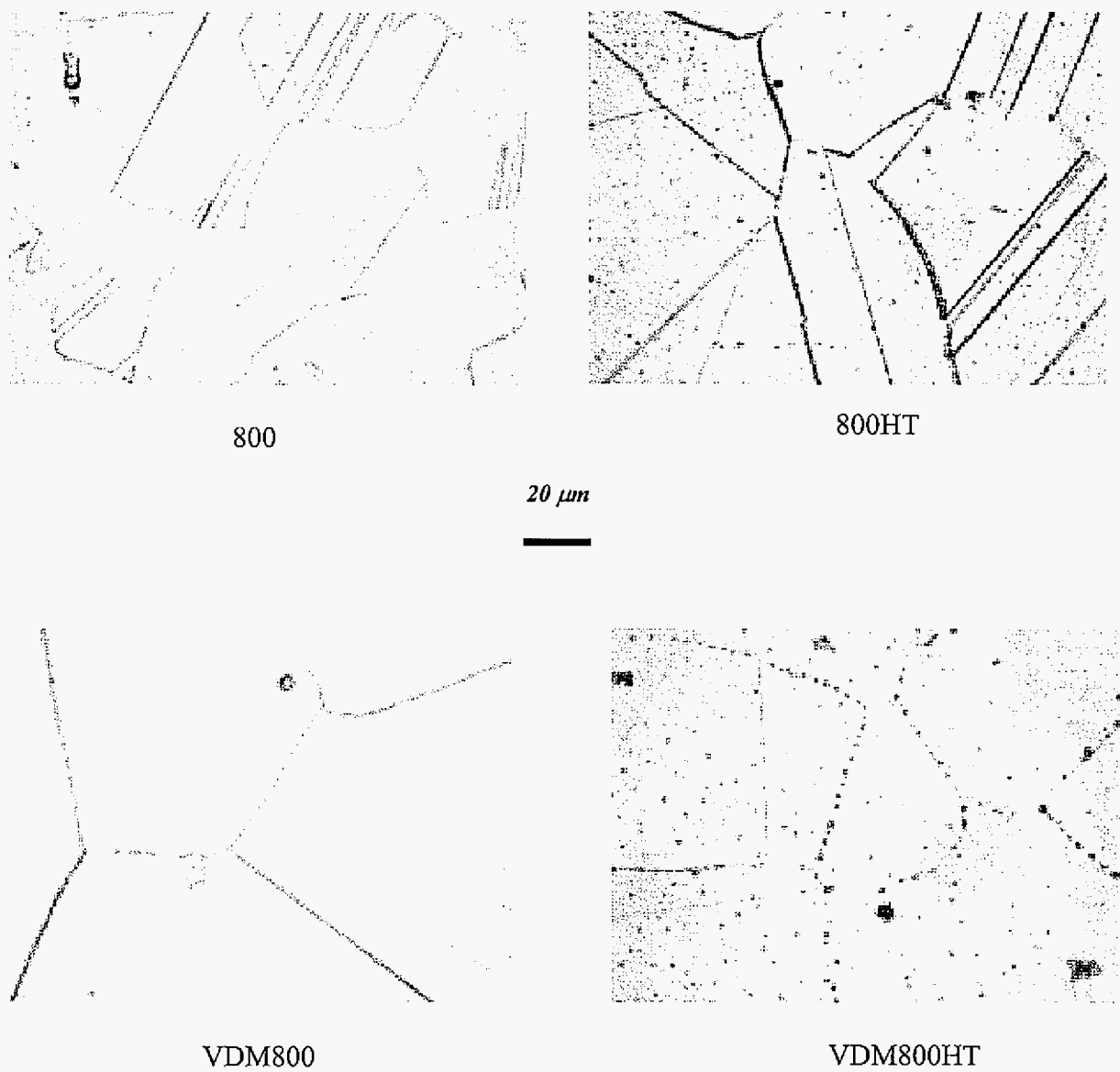
VDM800

VDM800HT

Figure 5.1. Optical micrographs of the as-received alloys.

seen to contain a significantly greater amount of twinning than the VDM alloys (VDM800 and VDM800HT). Another difference was the nature of the grain-boundary carbides in HT alloys. In VDM800HT the carbides were discrete, while in 800HT they were continuous along grain boundaries. It is possible that the continuous nature of the carbides in 800HT facilitated intergranular oxidant penetration; this, however, could not be conclusively verified.

5.2.1 Oxidation Kinetics

Figure 5.2 compares the weight change of the four 800 series alloys studied after isothermal exposure at 1000 °C for seven days. It is seen that VDM800 and VDM800HT exhibited less mass gains (about 1.58 and 1.50 mg/cm^2, respectively) than 800 and 800HT (about 1.79 and 1.77 mg/cm^2, respectively). Although not shown, the scale thicknesses
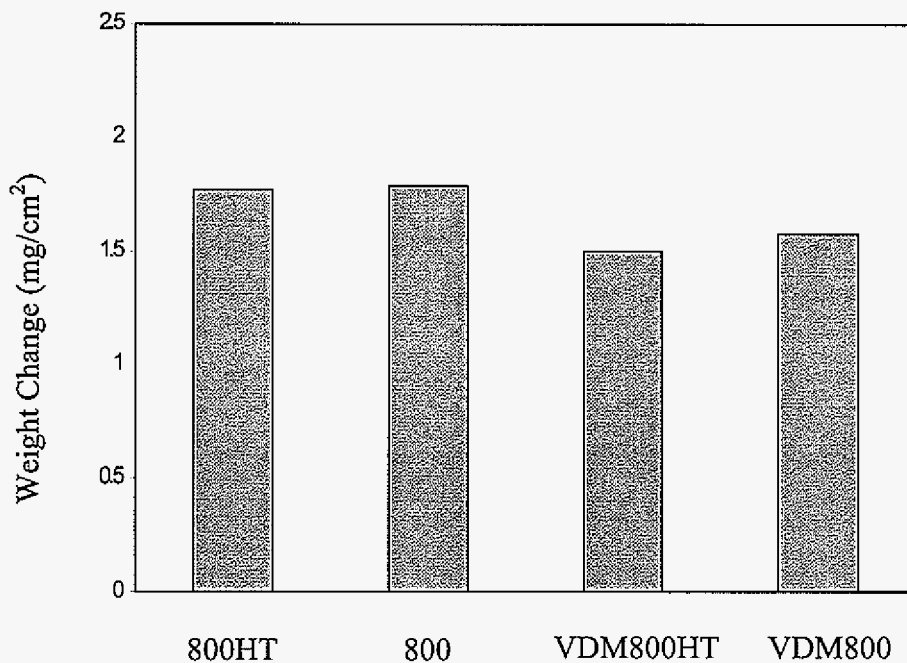
Figure 5.2. Mass gain for a 7-day isothermal oxidation at 1000°C.

followed the same trend as the weight-changes, with the VDM alloys forming the thinner scales than the SM alloys. The parabolic rate constants for steady-state oxide growth of the four alloys were presented in Table 4.1. The 800 alloy showed the largest parabolic rate constant (1.0×10^{-11} $g^2cm^{-4}s^{-1}$), followed by 800HT (6.3×10^{-12} $g^2cm^{-4}s^{-1}$) and VDM800HT (5.4×10^{-12} $g^2cm^{-4}s^{-1}$), and VDM800 showed the smallest (4.8×10^{-12} $g^2cm^{-4}s^{-1}$). As reported by Hindam and Whittle [190], the value of k_p for chromia scale growth van vary up to almost two orders of magnitude, depending on temperature and alloy composition. It is seen that the small variation of alloying composition in the 800 series alloys resulted in about two orders larger k_p of 800 than VDM800.

The mass-change behavior of the four 800 series alloys as a function of number of 1-day oxidation cycles is shown in Figure 5.3. Although not readily apparent in this figure, the 800
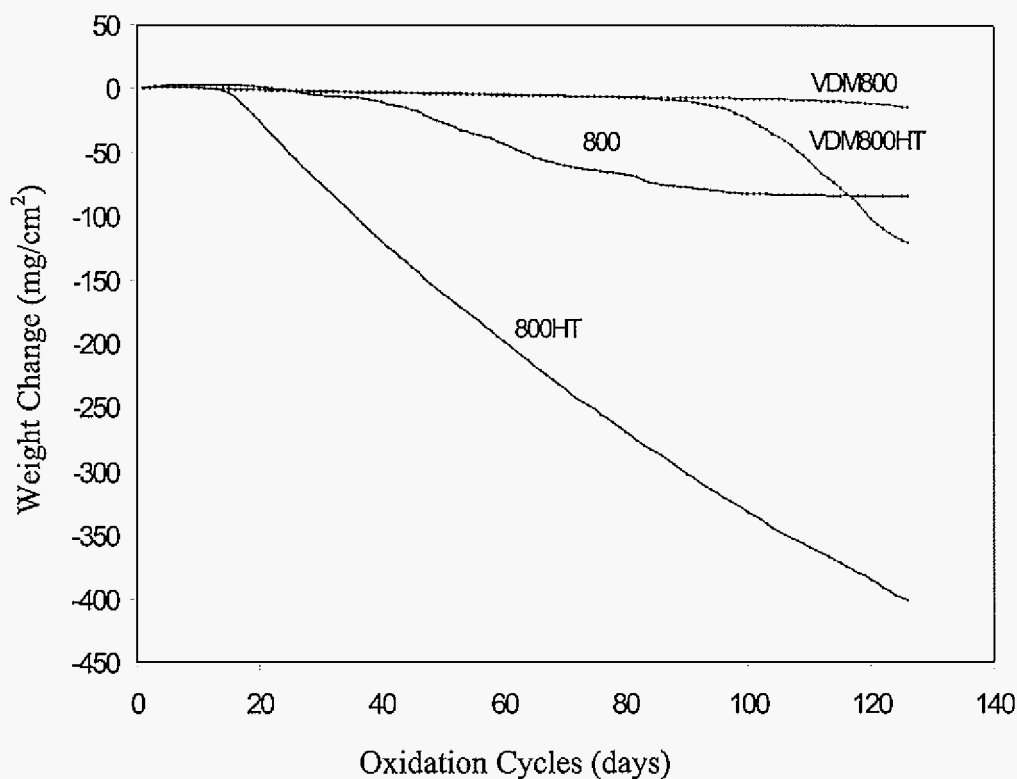
Figure 5.3. Weight change vs. time curves for 1-day cycling at 1000°C.

alloy exhibited the greatest mass gain (about 1.5 mg/cm^2•day$^{1/2}$) during the initial stages of oxidation, *i.e.*, within the first 10 cycles, while the other three alloys showed similar weight gain within first 6 cycles (about 0.8 mg/cm^2•day$^{1/2}$). The results are reasonably consistent with the measured parabolic rate constants. After about 18 1-day oxidation cycles, the four alloys exhibited different rates of mass loss. The VDM800 and VDM800HT alloys showed relatively low and constant rates of mass loss, with their rates being very similar up to about 95 cycles. The 800 alloy showed a higher mass-loss rate than the alloys VDM800 and VDM800HT; although, after about 80 cycles, the mass-loss rate decreased considerably for the 800 alloy. The amount of weight loss for the 800 alloy leveled out at about − 83 mg/cm^2 after approximately 95 cycles. This limiting weight loss corresponded to through-oxidation of the 800 alloy in which internal oxide and nitride precipitates had developed across the sample's thickness, as will be described later. The 800HT alloy performed the worst, undergoing rapid weight-loss kinetics after about 18 cycles of relatively protective oxidation. The VDM800HT alloy also underwent rapid weight-loss kinetics, but not until after 95 cycles. Table 5.2 gives the oxidation kinetics of each of the four alloys during the different stages of weight-change. It is seen in both Figure 5.3 and Table 5.2 that the weight change kinetics for the VDM800HT alloy after 95 oxidation cycles (-4.5 mg/cm^2•day) were similar to those for the 800HT alloy after 18 oxidation cycles (-5.0 mg/cm^2•day).

Table 5.2. Rates of weight change for the alloys studied.

Rate[a]	800	800HT	VDM800	VDM800HT
(mg/cm^2•day)	+1.5 (1-15)	+0.8 (1-6)	+0.8 (1-6)	+0.6 (1-7)
or	-0.3 (20-36)	-5.0 (20-40)	-0.11 (10-100)	-0.11 (10-80)
(mg/cm^2•day$^{1/2}$)	-1.5 (40-70)	-3.6 (40-100)	-0.3 (110-126)	-4.5 (95-120)

[a] Numbers in parentheses represent the cycle numbers for which given rate applies

Positive rates are parabolic (mg/cm^2•day$^{1/2}$) and negative rates are linear (mg/cm^2•day)

Cyclic oxidation tests were repeated to ensure the reproducibility of the results. Figure 5.4 shows the excellent reproducibility of the 800HT alloy under 1-day cyclic oxidation at 1000 °C. Breakdown oxidation occurred at around 18 1-day cycles for the three repeated tests.
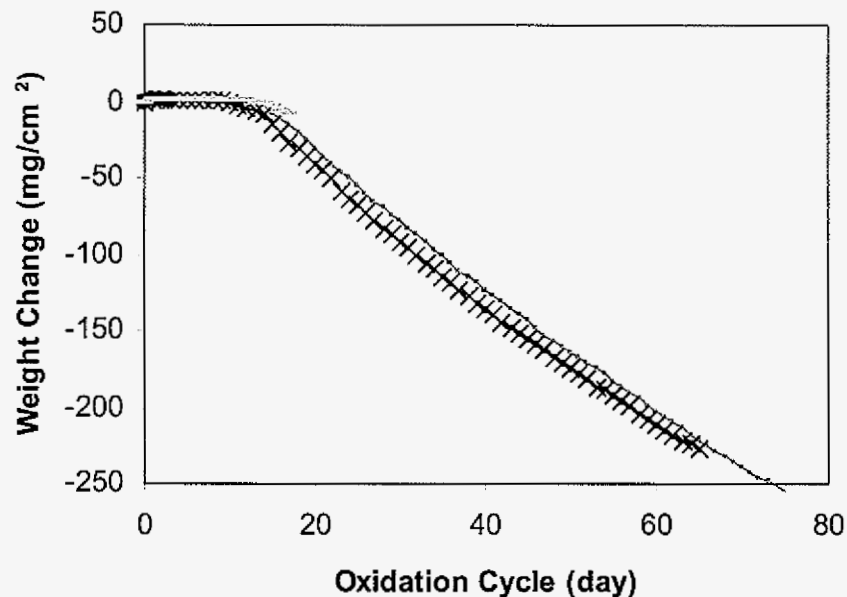
Figure 5.4. Reproducibly cyclic oxidation behavior of 800HT alloy
after 1-day cycles at 1000 °C.

The four 800 series alloys have very close chemical compositions. Thus, the slight variations in the minor element contents are believed to have played an important role in causing the significantly different cyclic oxidation behaviors of these alloys (Fig. 5.3). Table 5.3 summaries the variation of minor elements and ratio of Si to Ti and Si+Al to Ti content in

Table 5.3. Variation of minor elements in the four alloys studied (wt.%).

Alloys	Si	Al	Ti	Si/Ti	Si+Al/Ti
800	0.13	0.30	0.41	0.32	1.05
800HT	0.15	0.46	0.55	0.27	1.11
VDM800	0.38	0.25	0.32	1.19	1.97
VDM800HT	0.37	0.58	0.49	0.76	1.94

the four alloys. It is seen that (Si/Ti) and (Si+Al/Ti) ratios are almost a factor of two greater for the VDM alloys than the SM alloys. The poorer oxidation behavior of the 800HT alloy corresponds to its lowest value of Si/Ti (0.27), while the VDM800 alloy having the highest Si/Ti value (0.19) had the best oxidation resistance.

The VDM alloys contain a higher Si content (about 0.37 wt.%) than the SM alloys (about 0.15 wt.% Si), and showed better oxidation resistance. However, the Ti and Al contents do not show consistent variation within the two set alloys. In order to further determine the effect of Si addition on the cyclic oxidation behavior of the SM alloys, three additional 800HT alloys having different silicon contents were provided by Special Metals. The compositions of these alloys are listed in Table 5.4, and the corresponding weight-change kinetics is presented in Figure 5.5. The Si/Ti and Si+Al/Ti ratios for the modified 800HT
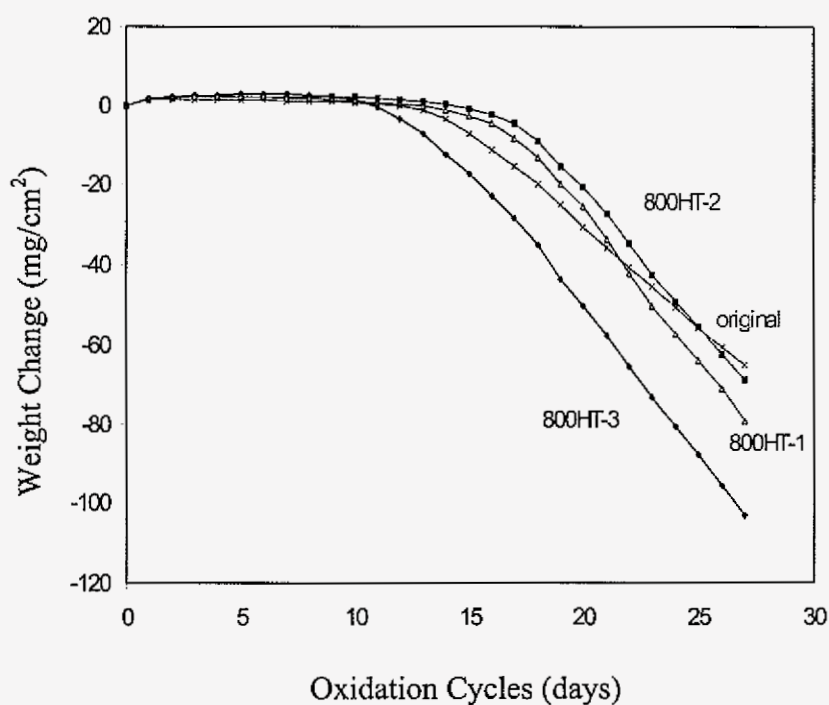
Figure 5.5. Cyclic oxidation kinetics at 1000 °C for the 800HT alloys having different Si contents .

alloys change from 1.29 to 1.77 and 0.31 to 0.92, respectively, with the higher values being close to those for the VDM800HT alloy (1.94 and 0.76). It is seen in Fig. 5.5 that the 800HT-

2 alloy, having a silicon content of 0.27 wt.%, maximized the time to breakdown oxidation. Increasing the Si content to 0.49 wt.% (800HT-3) decreased the time to breakdown oxidation; however, the extent of this detrimental effect was only marginally significant. The ranking form best to worst of the there modified alloys is seen to be 800HT-2>800HT-1>800HT-3. Moreover, it can be inferred from the results that the difference in silicon content between the alloys 800HT and VDM800HT was not the sole reason for the difference in weight-change behaviors shown in Fig. 5.3.

Table 5.4. The 800HT alloy compositions with 4 different Si contents (wt.%).

Alloys	C	Mn	Si	Cr	Ni	Fe	Ti	Al	Cu	Si/Ti	Si+Al/Ti
800HT-1	0.07	0.78	**0.17**	19.57	31.21	46.63	0.55	0.54	0.44	0.31	1.29
800HT-2	0.07	0.79	**0.27**	19.69	33.56	44.18	0.52	0.41	0.51	0.52	1.31
800HT-3	0.07	0.78	**0.49**	19.74	33.05	44.71	0.53	0.45	0.18	0.92	1.77
Original	0.07	0.79	**0.15**	19.96	33.59	44.19	0.55	0.46	0.24	0.27	1.11

5.2.2 Microstructural Characterizations

The cross-sectional SEM images of the 800 series alloys after 18 1-day oxidation cycles at 1000 °C are shown in Figure 5.6. Each alloy appeared to have formed a two-layered scale, with only remnants of the outside layer often remaining due to partial spallation. The thickness of the scales formed on the 800 and 800HT alloys were about 10 μm, while the scales on the VDM800 and VDM800HT alloys were consistently thinner at about 5 μm. The alloy/scale interface was most non-planar in the 800HT alloy. Qualitative chemical analysis using EDS indicated that the protrusion into the alloy at the alloy/scale interface in the 800HT and 800 alloys consisted of Cr- and Ti-rich oxides. All four alloys exhibited intergranular internal oxidation. The internal oxidation depths are about 100 μm for the 800 alloy and about 50 μm for the other three alloys, although the VDM800 alloy showed the least internal attack. The compositions of the internal oxides were dependent upon depth into the alloy. Deep into the alloy at the intergranular oxidation front, the oxides were always found to be Al-rich. Intergranular oxides rich in silicon and titanium were detected in addition to the Al-rich oxides in the VDM alloys at shallower depths. In the case of the 800
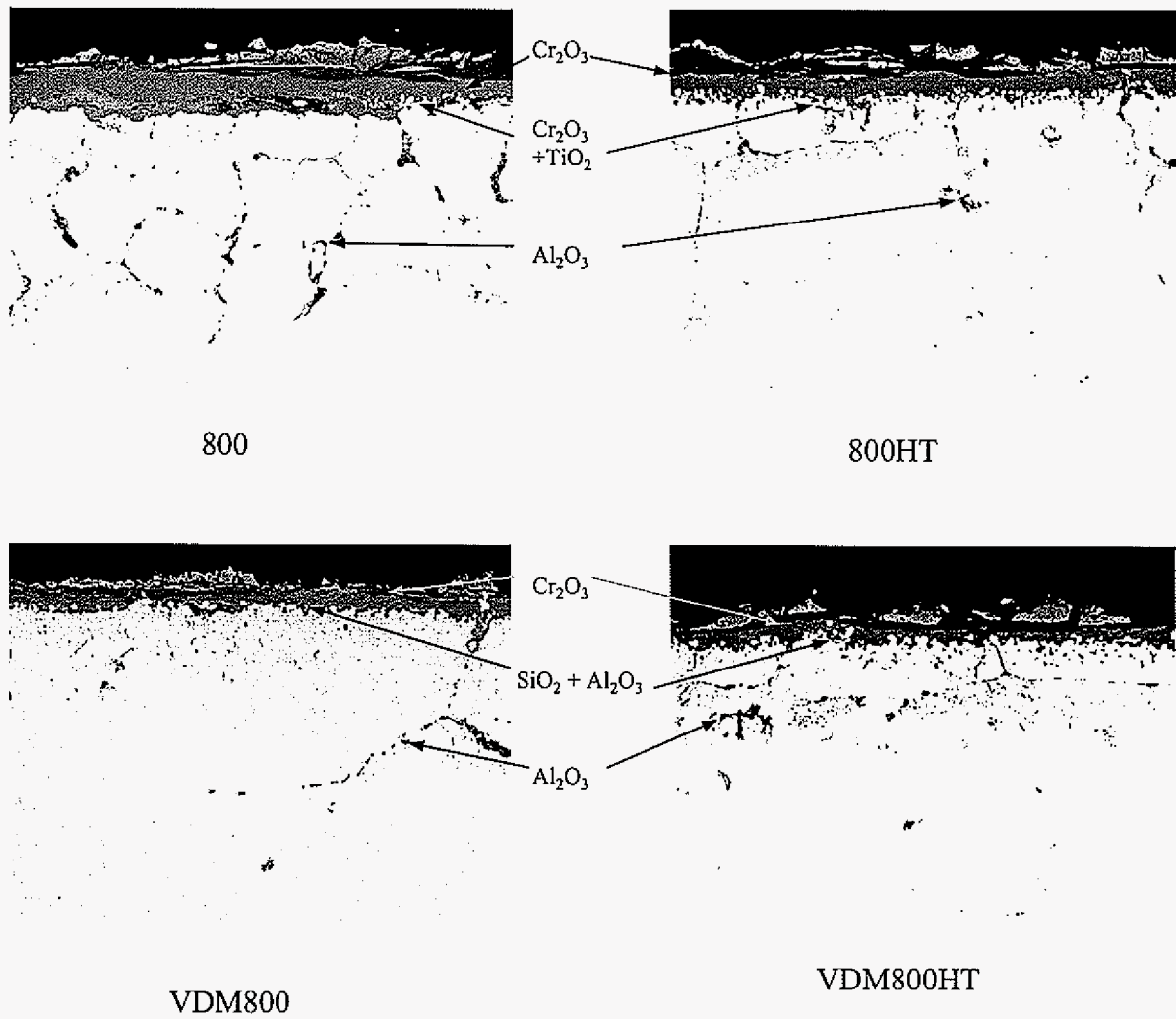
Figure 5.6. Cross-sectional SEM images of the four alloys
after 18 1-day oxidation cycles at 1000 °C.

and 800HT alloys, Al- and Ti-rich oxides were detected at shallower depths, followed by Cr- and Ti-rich oxides in the vicinity of the alloy/scale interface. The VDM alloys formed a discontinuous layer of Si-rich oxide at the alloy/scale interface with some Al-rich oxide. Such a layer was not observed in the SM alloys. Based on previous reports [100,161,192] and the thermodynamics of the system, the Al-, Si-, and Ti-rich oxides are believed to be Al_2O_3, SiO_2, and TiO_2, respectively.

The structure and composition of the external oxides formed on the initial four 800 series alloys during isothermal oxidation were analyzed initially using XRD (Fig. 4.12). The results were similar for all of the alloys, and confirmed that the scales were two-layered, consisting of an inner layer of Cr_2O_3 and an outer layer of $MnCr_2O_4$ spinel. These results are in agreement with those reported by others [110,112,114,188,191,192]. Yearian *et al.* [188] detected enrichments of manganese in the outer regions of a scale formed on commercial iron-chromium-base alloys and inferred that these regions contained the spinel $MnCr_2O_4$. Figure 5.7 shows the XRD patterns from the four alloys after 18 1-day cycles at 1000 °C. No $MnCr_2O_4$ was detected. Instead, the less-protective spinel oxides $FeCr_2O_4$ and/or $NiCr_2O_4$ were detected, together with Cr_2O_3. $FeCr_2O_4$ was detected for the 800, VDM800, and VDM800HT alloys, while $NiFe_2O_4$ peaks were found for the 800HT alloy. For the alloys VDM800 and VDM800HT, two $NiFe_2O_4$ peaks also were detected in the scale, and it is believed that $NiFe_2O_4$ was just a small amount in the scale of the VDM alloys. $NiFe_2O_4$ is less-protective than $FeCr_2O_4$, which is in agreement with the 800HT alloy showing breakdown behavior after only 18 1-day cycles at 1000 °C.

Figure 5.8 shows the cross-sectional SEM images of the four alloys after long-term 1-day cyclic oxidation at 1000 °C. The 800HT, VDM800, and VDM800HT alloys were analyzed after 125 1-day cycles, while the 800 alloy after 48 1-day cycles. The sample thickness of the 800 alloy was too thin to resist 125 1-day oxidation cycles. From the cyclic oxidation kinetics (Fig. 5.3), the 800 alloy is interpreted to have underwent large spallation after 40 cycles. Thus, 48 1-day cycles was selected as long-term to analyze the cross-sectional characteristics of the 800 alloy. From Fig. 5.8, it is seen that all four alloys underwent scale cracking and even scale spallation. Based on XRD and EDS analysis, only VDM800 retained a primary chromia scale. The scales on the other three alloys were complex, consisting of an inner
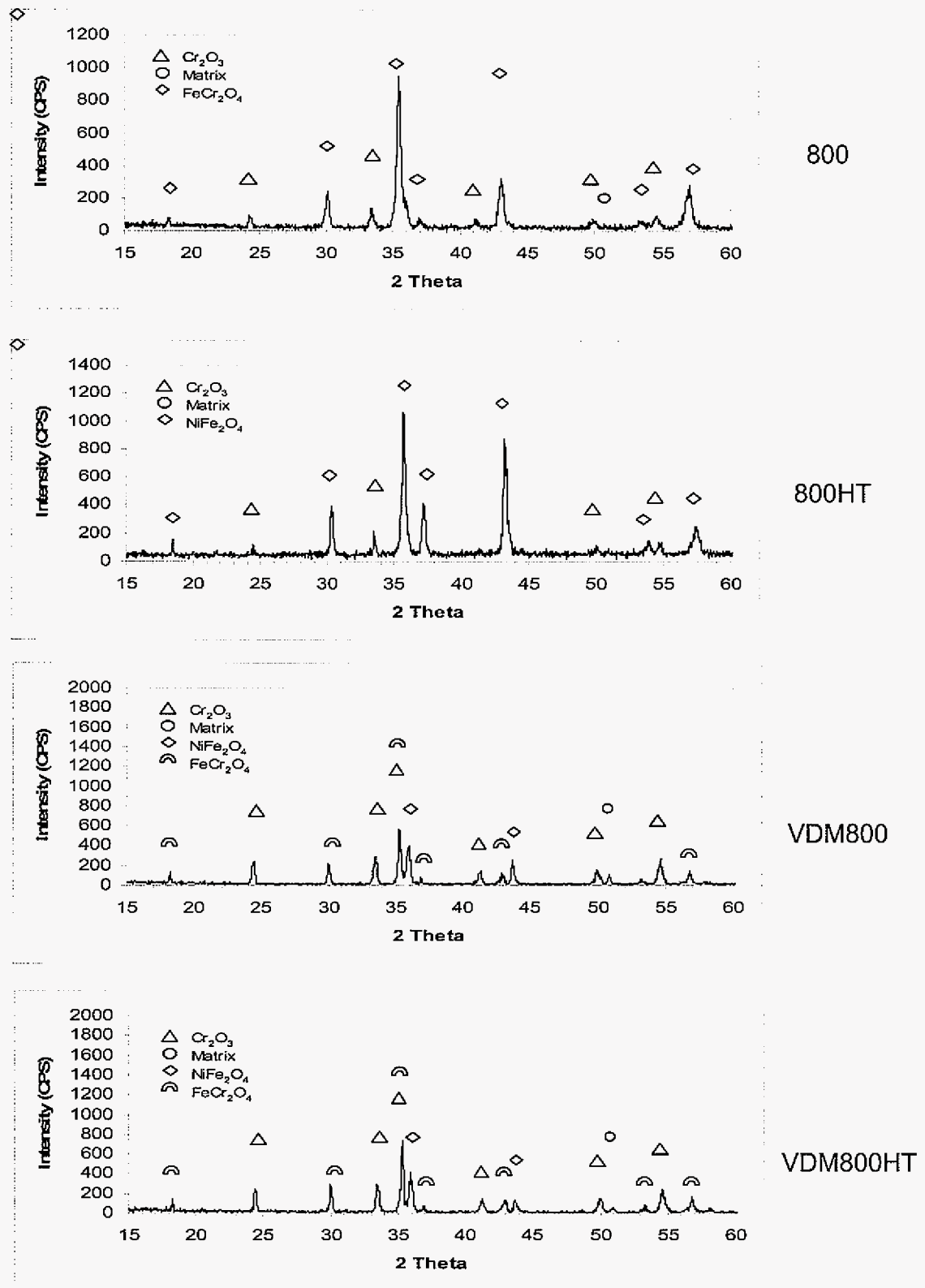
Figure 5.7. XRD patterns of the four alloys after 18 1-day oxidation cycles at 1000 °C.

800 (48 cycles)

800HT (125 cycles)

VDM800 (125 cycles)

VDM800HT (125 cycles)
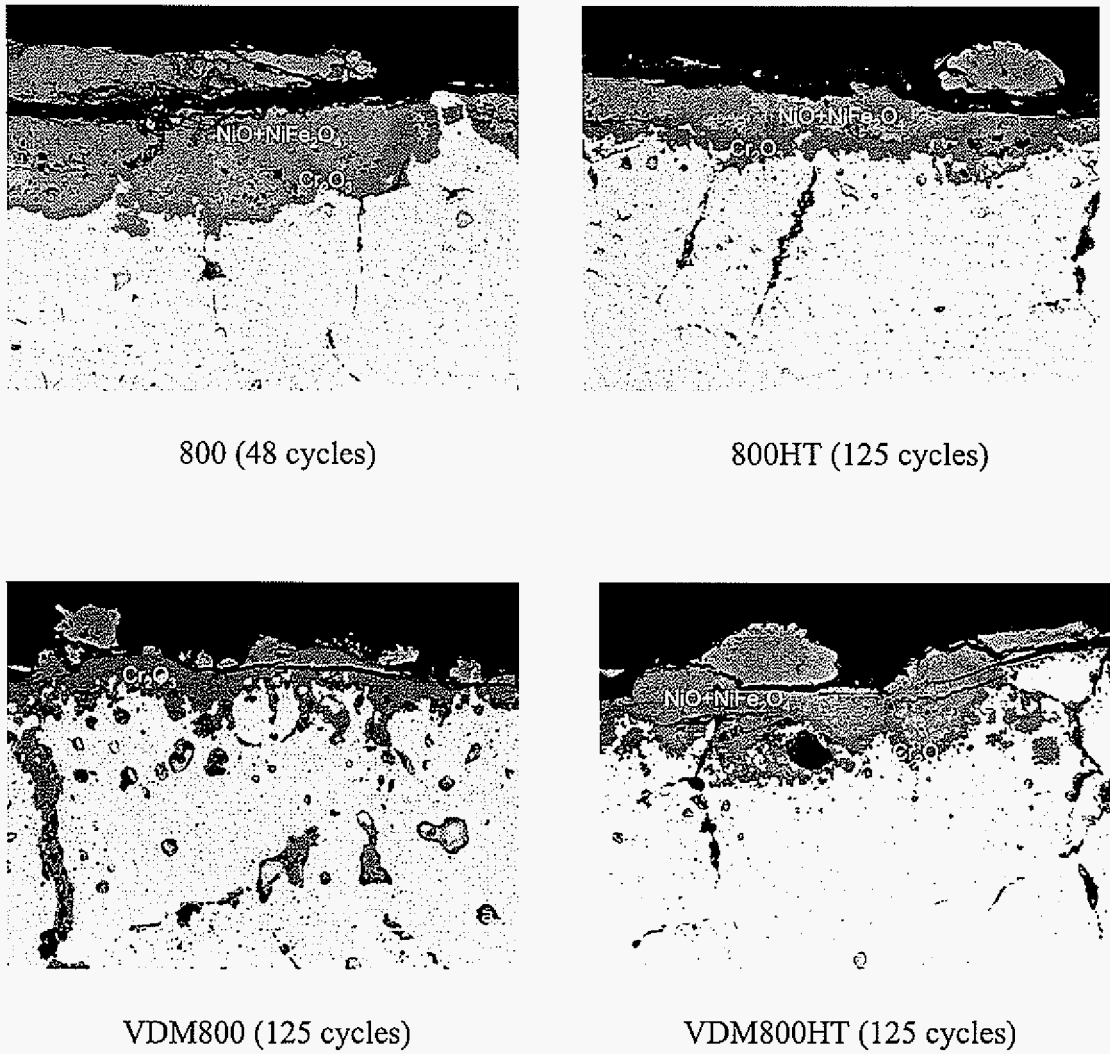
Figure 5.8. Cross-sectional SEM images of the four alloys
after long-term 1-day cycling oxidation at 1000 °C.

chromia layer and an external layer comprised of NiO, $NiFe_2O_4$, and/or $(Fe,Ni)_3O_4$ phases. The inner chromia layer in the three alloys was rather discontinuous and non-planar in nature. The VDM800 alloy apparently formed Si-rich oxide particles at the alloy/scale interface, which is similar to what observed after 18 1-day oxidation cycles. The four cross-sectional images in Fig. 5.8 also show extensive intergranular internal oxidation. The internal oxides formed according to their thermodynamic stability, from SiO_2, TiO_2, and then Al_2O_3 when progressing from the scale/alloy interface into matrix. Figure 5.9 shows the through-oxidation of the 800 alloy after 125 1-day cycles (the top of the image is approximately at the center of the oxidized sample). Nitride formed in the matrix in addition to the oxides. Based on EDS analysis, the nitride is believed to be Cr_2N, TiN, and AlN [193,194]. The other three alloys were thick enough to prevent through-oxidation after 125 1-day oxidation cycles. Figure 5.10 shows that the 800HT alloy exhibited internal oxide formation along twin boundaries in the structure after 125 1-day cycles.
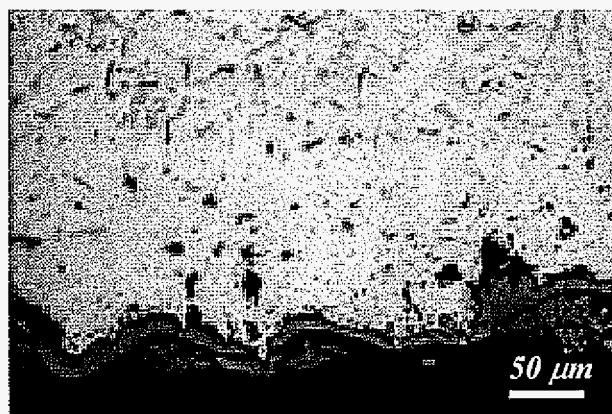
Figure 5.9. Optical micrograph of the 800 alloy oxidized

after 125-cycles at 1000°C.
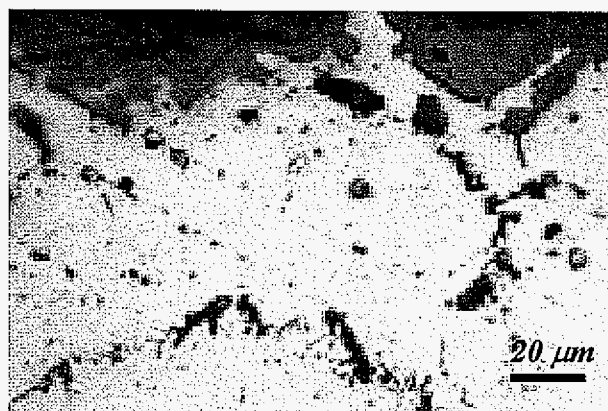
Figure 5.10. Internal oxidation along twinning of the 800HT alloy
oxidized after 125 1-day cycles at 1000°C.

Figure 5.11 shows the cross-sectional SEM images of the modified 800HT alloys with different silicon levels after 18 1-day oxidation cycles at 1000 °C. It is seen that two oxide layers formed, an inner Cr_2O_3 layer and an outer $NiFe_2O_4+FeCr_2O_4$ layer that is locally cracked, separated, or partially spalled. Internal oxidation was primarily intergranular, similar to what was found in the 800 series alloys (in Table 5.1) oxidized after 18 1-day oxidation cycles at 1000 °C. Al_2O_3 formed deepest into alloy matrix, while Ti-rich oxide combined with Cr-rich oxide as protrusions into the alloy at the alloy/scale interface. The two lower silicon content alloys (800HT-1 and 800HT-2) did not appear to form silica particles along the scale/alloy interface, while the 800HT-3 alloy with 0.49 wt.% Si formed a great amount of silica at the front of oxide protrusions along the scale/alloy interface. From Figure 5.12, which is a high magnification of the 800HT-3 alloy in Fig. 5.11, a thin silica layer can be seen on the front of oxide protrusions. Comparing the images in Fig. 5.11, more internal oxidation and oxide protrusions at the scale/alloy interface formed with increasing of silicon content in the alloy. When the oxide protrusions extended to some significant extent into the alloy, the result is entrapment of metallic "islands" in the oxide scale. The metallic "islands" mainly consist of Ni and Fe with the chromium, titanium, aluminum, and silicon contents being depleted in comparison to the bulk alloy. The oxygen activity in the vicinity of the metallic "islands" must not have been enough to oxidize the more noble Ni and Fe
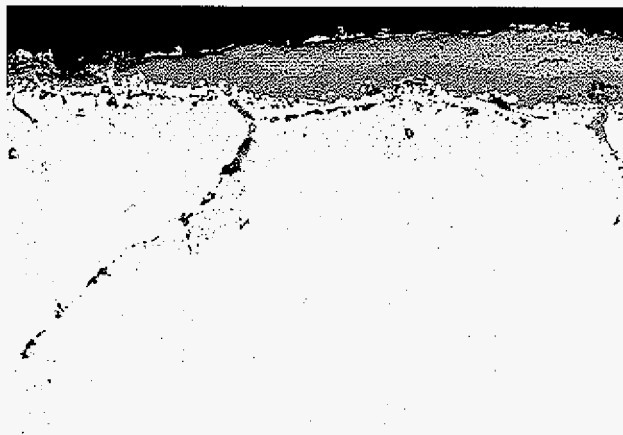
800HT-1 (0.17 wt.% Si)
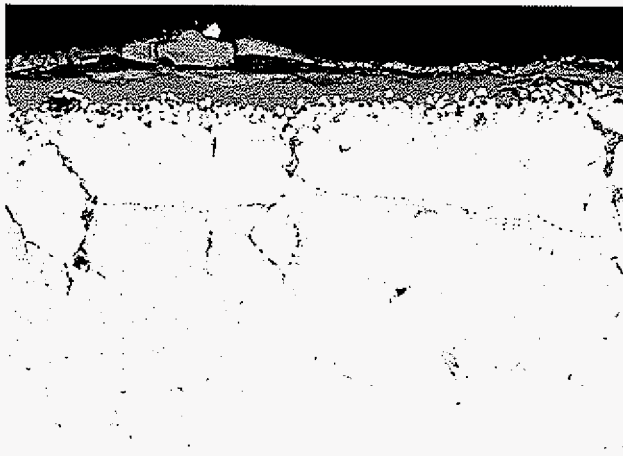
800HT-2 (0.27 wt.% Si)
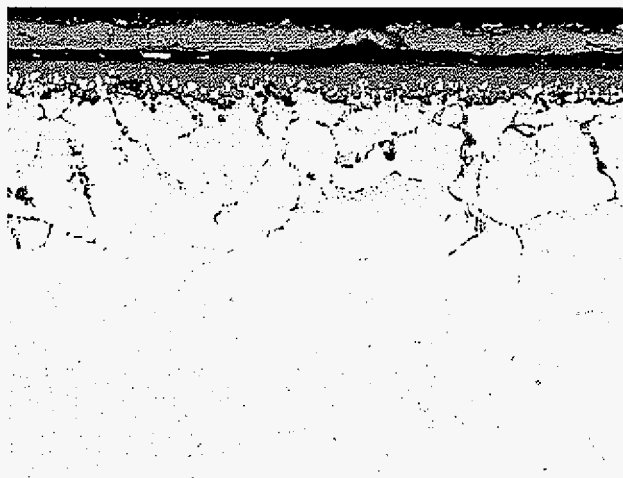
800HT-3 (0.49 wt.% Si)

Figure 5.11. Cross-sectional SEM images of the modified
800HT alloys after 18 1-day oxidation cycles at 1000 °C.
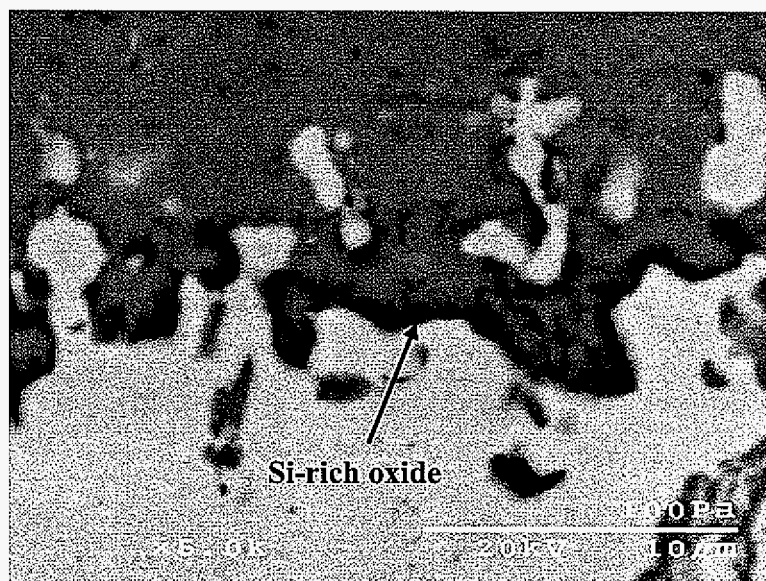
Figure 5.12. Cross-sectional SEM images of the modified 800HT-3 alloy (0.49 wt.% Si) after 18 1-day oxidation cycles at 1000 °C (Si-rich layer at the front of oxide intrusion).

(Ellingham diagram in Fig. 2.1). The metallic "islands" can act to destroy the continuity of chromia scale, and can thus be detrimental to oxidation resistance.

5.2.3 EPMA Measurement of Composition Profiles in Oxidized Samples

The oxidized samples were analyzed by EPMA to obtain the chromium depletion profiles within the subsurface. Figure 5.13 shows chromium depletion profiles from the four 800 series alloys studied after 7 days isothermal oxidation at 1000 °C. The VDM alloys showed a greater depth of chromium depletion (about 110 μm) with flatter profiles, while the SM alloys had a comparatively smaller depth of chromium depletion (about 70 μm) with steep chromium profiles within the vicinity of the scale/alloy interface. The chromium interfacial contents were about 10.5, 9.5, 14, and 15.5 at.% for 800, 800HT, VDM800, and VDM800HT, respectively. Thus, the SM alloys showed about 5 at.% lower interfacial chromium contents than the VDM alloys, which is consistent with the earlier breakdown of these alloys (Fig. 5.3). Based on the measured chromium depletion profiles, the average
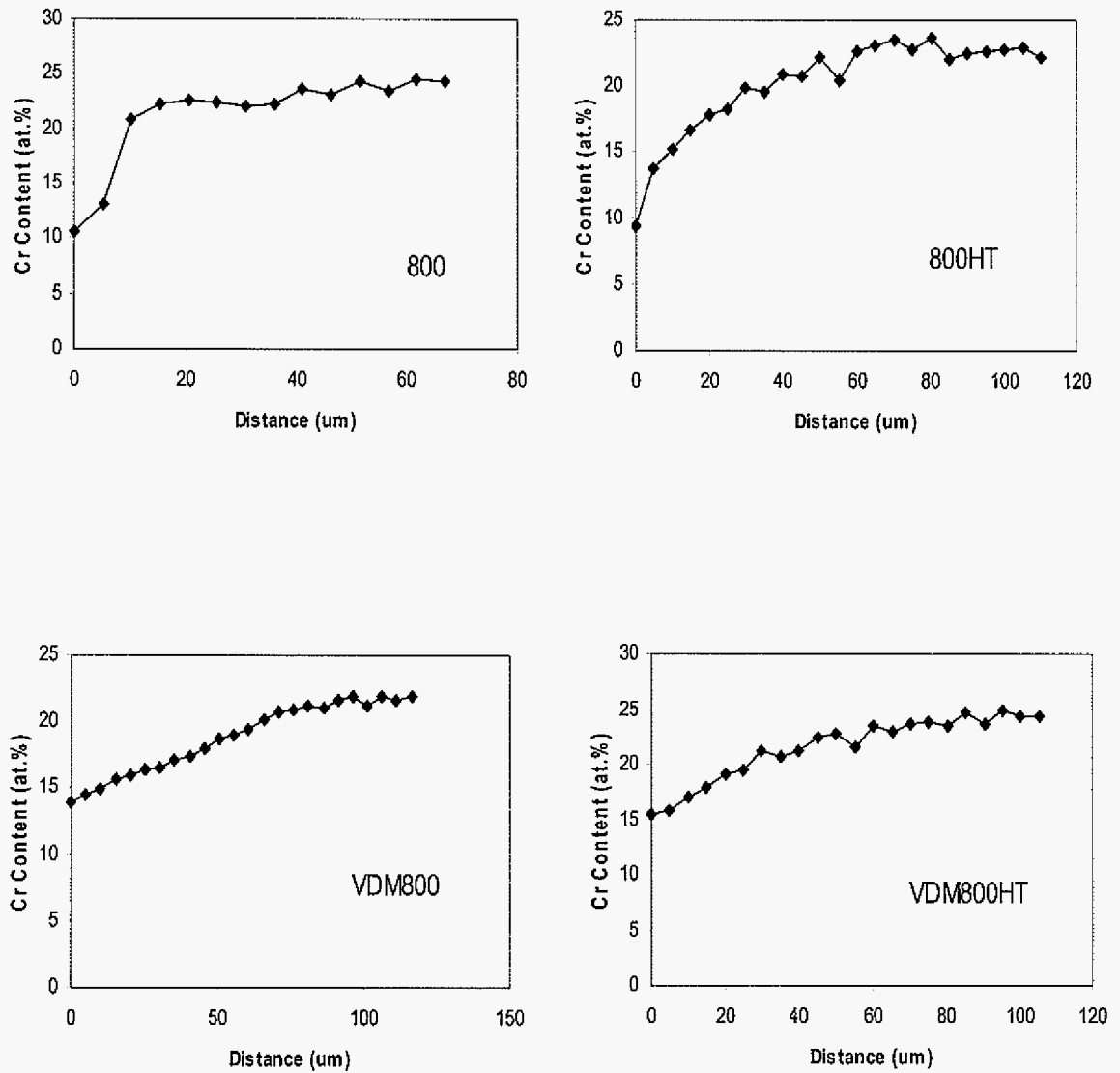
Figure 5.13. Chromium concentration profiles in the four alloys studied after 7 days isothermal oxidation at 1000 °C. Distance is measured from the scale/alloy interface to matrix.

effective interdiffusion coefficient of chromium, D_{Cr}^{eff}, could be obtained by using Dayananda's model (section 2.2.6.1). The results are listed in Table 5.5. The VDM alloys show a significantly larger D_{Cr}^{eff} (1.9×10^{-11} cm^2/s) than the SM alloys. The D_{Cr}^{eff} values were similar for the two VDM alloys, while a large variation of 2.2×10^{-12} and 7.4×10^{-12} cm^2/s was determined for 800 and 800HT, respectively.

Table 5.5. Average effective interdiffusion coefficient of chromium of the alloys studied after 7-day isothermal oxidation at 1000 °C.

Alloys	D_{Cr}^{eff} ($\times 10^{12}$ cm^2/s)
800	2.2
800HT	7.4
VDM800	19
VDM800HT	18

The subsurface alloying element profiles and oxide scale in each of the alloys oxidized for 18 and 125 cycles at 1000 °C were analyzed using EPMA. The results are shown in Figs. 5.14 and 5.15. As would be expected from the weight-change measurements in Fig. 5.2, the composition profiles were different for each of the alloys. After 18 1-day cycles (Fig. 5.14), the chromium content at the alloy/scale interface, N_{Cr}^{i}, was lower than the chromium content in the bulk for each alloy, which is clearly a consequence of the selective oxidation of chromium. The 800HT alloy had an N_{Cr}^{i} of only about 8 wt.% after 18 cylces, which was the lowest of the four alloys. For the 800 alloy, N_{Cr}^{i} was about 10 wt.% after 18 cycles, while for the alloys VDM800 and VDM800HT alloys N_{Cr}^{i} was over 12 wt. %. It is recalled that the 800HT alloy underwent breakdown after about 18 cycles (Fig. 5.3), thus 8 wt.%, which is equal to 7.3 at.%, can be inferred to be approximately the critical interfacial Cr content for chromia formation in 800HT. The chromium concentration gradients under the alloy/scale interface provide further information that aids in assessing the observed oxidation behaviors. The chromium concentration gradient (dCr/dx) in the 800HT alloy within in the vicinity of the alloy/scale interface was about 0.15 wt.%/µm after 18 cycles, while in the other three alloys it was about 0.05 wt.% µm. The consequently greater rate of Cr depletion at the

days isothermal exposure, while for VDM800HT N_{Cr}^{i} was about 15 at.% and the depletion-zone width was about 40 μm.

For the 800HT alloy, 7 days of isothermal oxidation at 1000 °C resulted in a shallow subsurface depletion-zone width in comparison to the depletion-zone with after 3 and 10 1-day oxidation cycles (Fig. 7.7), which showed depletion-zones of about 80 and 110 μm, respectively. After 18 and 125 1-day oxidation cycles, 800HT showed deeper depletion-zone widths of about 150 and 250 μm, respectively, than that developed after 3 and 10 1-day cycles. The chromium content at the alloy/scale interface in 800HT decreased from about 12.5 wt% after 3 cycles to about 7.3 wt.% after 18 cycles. Recalling that 800HT experienced breakdown after about 18 cycles, it is inferred that the critical Cr content, N_{Cr}^{*}, for 800HT during 1-day cyclic oxidation at 1000 °C is approximately 7.3 wt.%. After 125 cycles, the interfacial chromium content reduced to around 4.5 wt.%. The scale present after 125 cycles was primarily a mixture of iron and nickel oxides (Fig. 5.8), thus less Cr consumption and a large amount of metal recession prevented the occurrence of a large drop in the interfacial Cr content after 18 cycles. It is seen that the chromium depletion profiles after different oxidation cycles were relatively flat in nature within the vicinity of the alloy/scale interface. Fig. 7.6 also shows the enrichment of Ni and Fe near the alloy/scale interface within the subsurface of the alloy, which was due to the selective depletion of chromium in this region.

VDM800HT showed a similar trend in depletion behavior in the subsurface region (Fig. 7.7) to 800HT. However, VDM800HT showed a higher interfacial Cr content after different oxidation cycles, which was consistent with its better oxidation resistance. The interfacial Cr content in VDM800HT lowered to about 10.5 wt. % after 125 1-day cycles, and the alloy showed breakdown behavior after about 95 1-day cycles (Fig. 7.2). Considering that the interfacial Cr content in 800HT was about 7.3 wt.% for 800HT at the point of breakdown, it is clear that the critical interfacial Cr content for chormia formation varies significantly with alloy composition, thus making the prediction of the critical interfacial Cr content very difficult. It is noted that the intermittent abrupt drops in Cr, Ni, and Fe contents in Fig. 7.7 is attributed to the EPMA scan intersecting with internal oxides.

7.4 Calculation Results

The chromium depletion profiles measured in the 800HT and VDM800HT alloys after isothermal oxidized for 7 days at 1000 °C were used to calculate the average effective interdiffusion coefficient of Cr. The results for each of the three models (Equation 7.1, 7.2 and 7.4), for $\tilde{D}_{Cr}^{eff}$, are summarized in Table 7.1. It is seen that the average-slope model gave the largest $\tilde{D}_{Cr}$, while Dayananda's model gave the smallest. The $\tilde{D}_{Cr}$ values obtained using the three models were within a factor of two of one another.

Table 7.1. Average effective interdiffusion coefficients of chromium at 1000 °C calculated using the three models presented in Section 7.2.

Alloys	$\tilde{D}_{Cr}$ ($\times 10^{12}$ cm^2/s)		
	Dayananda's model (Eq. 7.1)	Average-D model (Eq. 7.2)	Average-slope model (Eq. 7.4)
800HT	7.4	9.9	12
VDM800HT	18	19	30

As discussed previously, the ratio of the inner Cr_2O_3 layer to the outer $NiFe_2O_4$ layer on 800HT was approximated to be 8:2, while for VDM800HT the Cr_2O_3/$MnCr_2O_4$ layer ratio was about 9:1. The ratio impacts the extent of chromium consumption and therefore needs to be accounted for in the prediction of Cr depletion. In Wagner's model (Equation 7.6), the chromium depletion profiles were obtained by inputting k_p, $\tilde{D}_{Cr}^{eff}$, N_{Cr}^i, V_m, v, and t. The numerical model required the additional parameter Q_o (zero for isothermal oxidation) to simulate Cr depletion profile, but did not required N_{Cr}^i.

Plots of the calculated chromium depletion profiles after 7-day isothermal oxidation at 1000 °C using the different $\tilde{D}_{Cr}^{eff}$ values are shown in Figure 7.8. The measured chromium depletion profiles are included in these plots for comparison. It is seen that Wagner's model generally shows a good match with the measured profiles for the two alloys. Comparing the
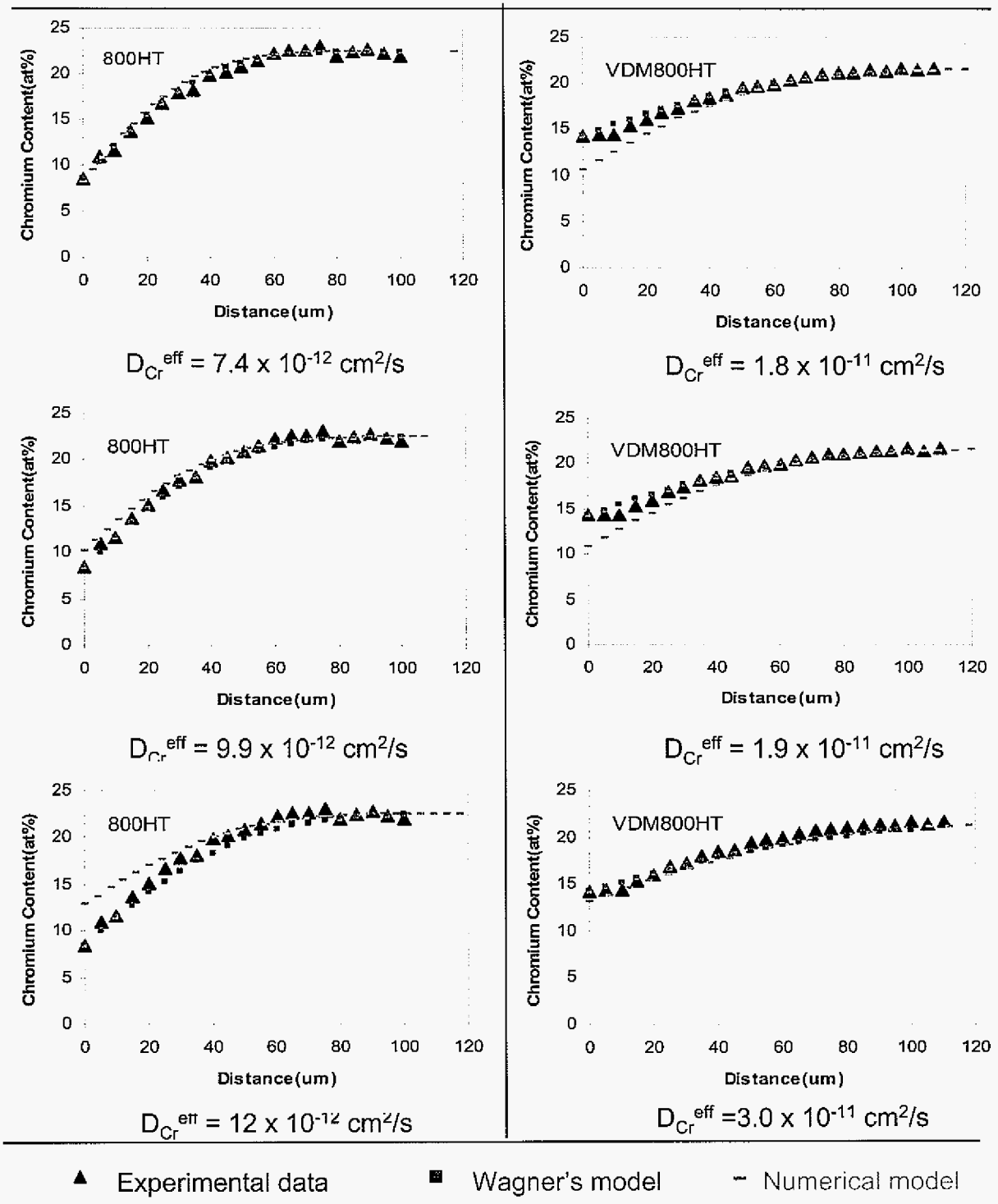
Figure 7.8. Calculated subsurface chromium depletion profiles after 7 days isothermal oxidation at 1000 °C.

numerically predicted Cr profiles using the different $\tilde{D}_{Cr}^{eff}$ values obtained using the three models, it is seen that the $\tilde{D}_{Cr}^{eff}$ obtained by Dayanada's model gave the best agreement between the measured and predicted Cr depletion profiles for 800HT, while the average-slope model gave the best agreement for VDM800HT. The $\tilde{D}_{Cr}^{eff}$ using the average-D model was intermediate for both alloys and, accordingly, the numerically predicted depletion Cr profiles were between those using the $\tilde{D}_{Cr}^{eff}$ values from the Dayananda and average-slope models.

For cyclic oxidation, a spallation constant, Q_o, of 0.008 was determined for 800HT and 0.002 for VDM800HT by matching the experimental cyclic oxidation kinetics curves with the fitted cyclic oxidation kinetics curves obtained by COSP (Figure 7.9). It is seen that the fitted kinetics curves deviated somewhat form the experimental kinetics curves, which indicates that the cyclic oxidation process was more complex than what it characterized using COSP. The fitted kinetics showed lower weight gain during early cyclic oxidation. As was shown in Fig. 7.3, the transient stage of oxidation for both alloys was more rapid than the steady-state about a factor of ten. The COSP does not consider transient oxidation, thus explaining a lower fitted weight gain in the early stages of cyclic oxidation.

800HT (Q$_o$=0.008)   VDM800HT(Q$_o$=0.002)
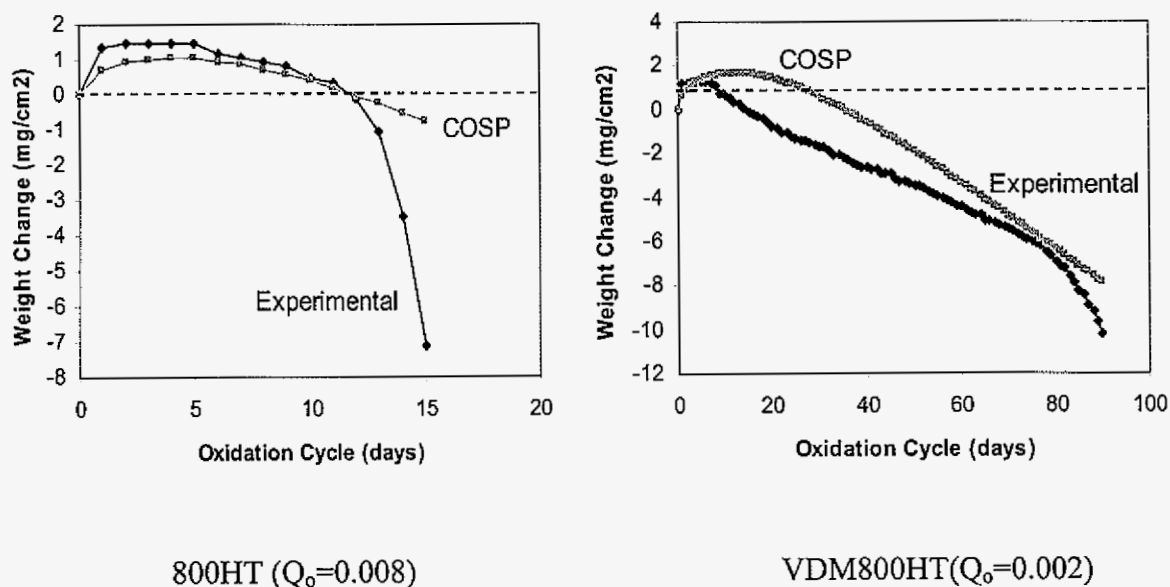
Figure 7.9. Fitting of the 1-day cyclic oxidation kinetics using COSP.

The COSP-TS fitting program was used for the cyclic oxidation VDM800HT (Figure 7.10). The transient oxidation kinetics was approximated to be a parabolic rate constant based on the TGA result (Table 4.1). The COSP fitted cyclic oxidation kinetics without considering transient oxidation is also shown in Fig. 7.10 for comparison. For the early stage of cyclic oxidation, it is seen that the agreement between the fitted and experimental kinetics curve is very good if the transient stage of oxidation is considered, while the fit is poor if the transient stage is not considered. The effect of transient oxidation on the prediction of Cr depletion and the lifetime of oxidation exceeds the aims of the current study, and is a target for the future study.

Transient oxidation not considered   Transient oxidation considered
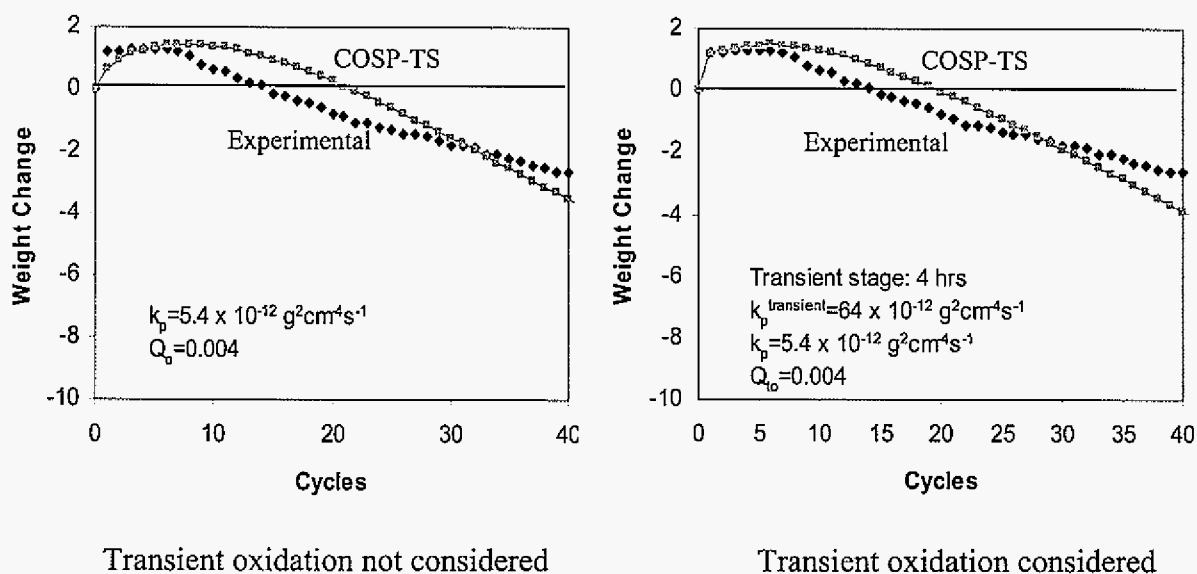
Figure 7.10. Fitted 1-day cyclic oxidation kinetics at 1000 °C of VDM800HT using COSP-TS.

Figure 7.11 shows the numerically predicted chromium depletion profiles in 800HT after different 1-day oxidation cycles at 1000 °C and using the differently obtained $\tilde{D}_{Cr}^{\textit{eff}}$ values. The measured chromium depletion profiles (scattered data in Fig. 7.11) are included for comparison. It is found that the best agreement between the predicted and measured Cr profiles was after 10 1-day cycles, followed by 3 cycles, 18 cycles, and finally 125 cycles. The prediction of chromium depletion profiles for VDM800HT (Figure 7.12) also showed
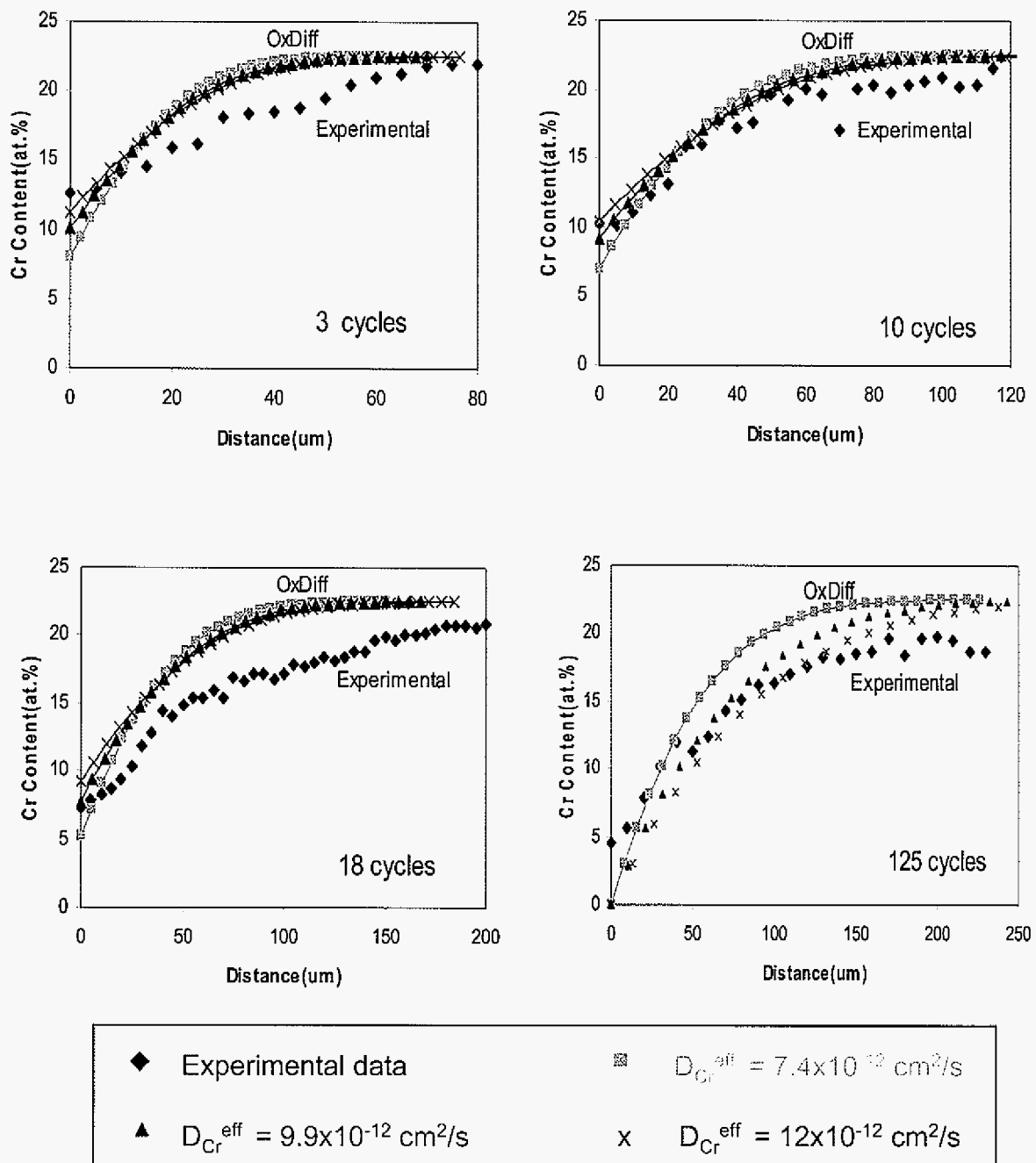
Figure 7.11. Calculated subsurface depletion profiles (lined data in the plots) of chromium of the 800HT alloy after 1-day cyclic oxidation at 1000 °C.
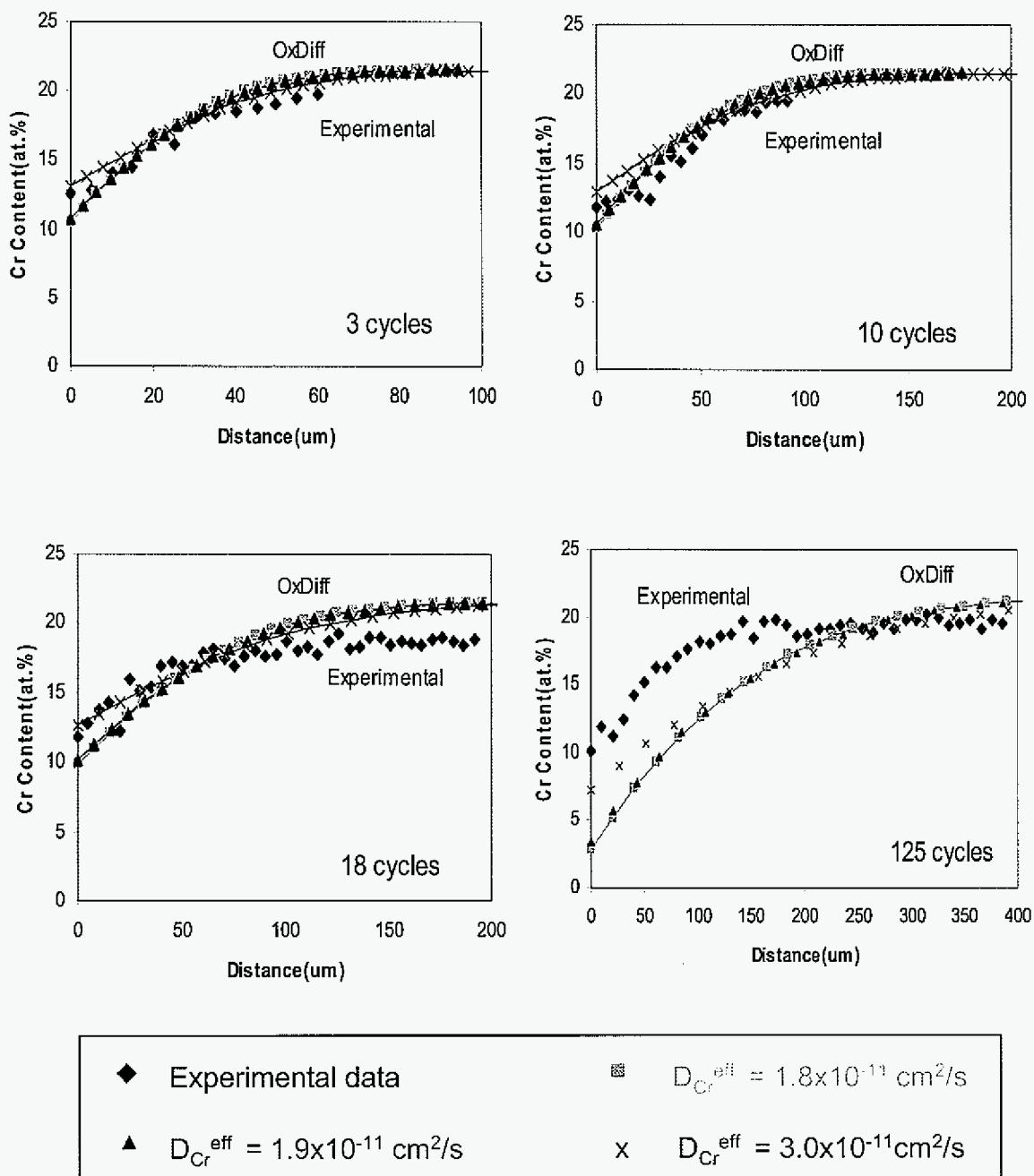
Figure 7.12. Calculated subsurface depletion profiles (lined data in the plots) of chromium of the VDM800HT alloy after 1-day cyclic oxidation at 1000 °C.

similar behavior with the sequence from the best to worst agreement: 10 cycles→3 cycles→18 cycles→125 cycles. The predicted Cr profiles for a given number of cycles showed similar depletion depths for the different $\tilde{D}_{Cr}^{eff}$ values. Moreover, the predicted Cr depletion depths were in good agreement with the experimental profiles. The predicted profiles obtained by applying different $\tilde{D}_{Cr}^{eff}$ showed different extent of deviation from the experimental profiles. It is noted that the largest difference between the Cr depletion profiles obtained form the different $\tilde{D}_{Cr}^{eff}$ was at the alloy/scale interface except for after 125 cycles.

Figure 7.13 shows the calculated interfacial chromium contents as a function of number of 1-day cycles oxidized at 1000 °C for both 800HT and VDM800HT. The calculated
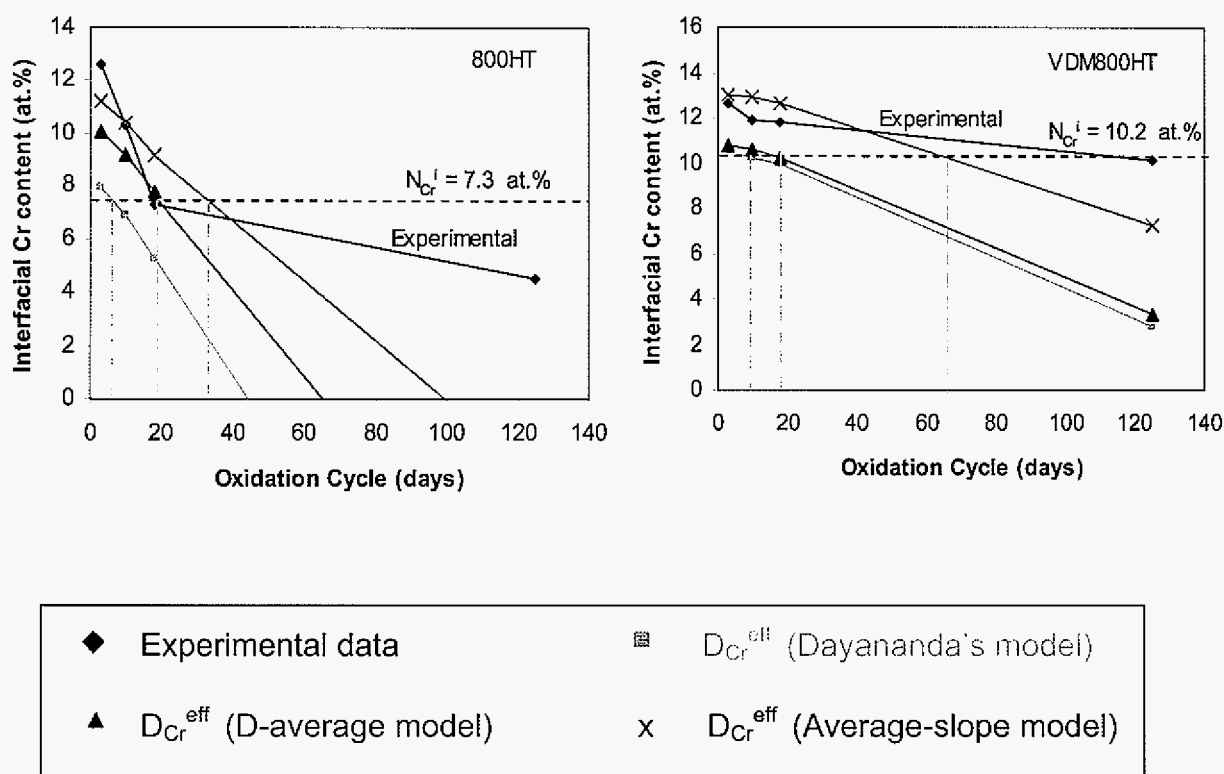
Figure 7.13. Predicted change in the interfacial chromium content during cyclic oxidation based on the numerical model.

interfacial chromium content showed an approximately linear decrease with oxidation time. It is seen that the decrease in the experimental interfacial chromium content after different oxidation cycles for 800HT was also approximately linear before breakdown oxidation (about 18 cycles). The dashed horizontal line at 7.3 at.% in Fig. 7.13 represents the inferred critical interfacial chromium content measured after 18 1-day cyclic oxidation of 800HT. Similarly, the dashed line at an interfacial Cr content of 10.2 at.% represents the critical interfacial Cr content for VDM800HT. For interfacial chromium contents below the dashed line, it would not be possible to reform the protective chromia oxide scale. Thus, the intersection of the calculated interfacial chromium content curve with the dashed line represents the predicted point of breakdown initiation. The predicted breakdown times for 800HT were about 7, 20, and 32 cycles when using the Dayananda, average-D, and average-slope models, respectively, while the predicted cycles to initiation of breakdown for VDM800HT were about 10, 18, and 65 cycles. The predicted number of cycles to breakdown initiation for the calculations based on the average-D $\tilde{D}_{Cr}^{\it eff}$ is in very close agreement with what was found experimentally for the 800HT alloy. After 18 cycles, the experimentally measured slower decrease in the interfacial chromium content was inferred to be due to the formation of the less-protective oxides. The prediction of breakdown for VDM800HT showed some disagreement with the experimental result. The $\tilde{D}_{Cr}^{\it eff}$ determined using the average-slope model produced the closest agreement, predicting initiation of breakdown at about 65 1-day oxidation cycles at 1000 °C. Experimentally, it was found that breakdown occurred starting at about 95 cycles for VDM800HT. Figure 7.13 shows the significant effect of $\tilde{D}_{Cr}^{\it eff}$ on the prediction. A difference of about a factor of two for $\tilde{D}_{Cr}^{\it eff}$ resulted in more than a factor of four difference in the predicted number of cycles to breakdown time.

Figures 7.14 and 7.15 show the effect of spallation constant and parabolic rate constant, respectively, on the predicted interfacial Cr content in VDM800HT after 1-day cyclic oxidation at 1000 °C using the $\tilde{D}_{Cr}^{\it eff}$ determined by the average-D model. The number of cycles to breakdown increases from 65 to 105 if the spallation constant decreases by a factor of two, while the cycles to breakdown would decrease to about 45 if the spallation constant

doubles (Fig. 7.14). The predicted rate of decrease in interfacial Cr content increased with increasing Q, as would be expected. Parabolic rate constant is seen in Figure 7.15 to have a much greater influence in affecting the rate of subsurface Cr depletion and, as a consequence, the number of predicted cycles to breakdown. VDM800HT is predicted to not breakdown until about 200 cycles if the parabolic rate constant halves, while it may not even form a protective oxide scale if the parabolic rate constant doubles.

7.5 Discussion

The 800HT alloy exhibited a short period of positive weight change during 1-day cyclic oxidation at 1000 °C, but then breakdown after about 18 cycles. The breakdown involved rapid and continuous weight loss and was associated with the formation of a less-protective scale rich in iron and nickel. As shown by Harper and Gleeson [110], who studied the same alloy exposed to 30-day oxidation cycles at 982 °C, breakdown commenced after about 5-6 cycles (150-180 days). The less-protective oxide was identified to be iron and nickel oxide $(Fe,Ni)_3O_4$. The VDM800HT alloy showed a longer protective period (about 95 cycles) compared to 800HT. The two alloys had very similar chemical compositions, but exhibited significantly different cyclic oxidation behaviors. The difference was attributed in the previous chapter to small difference in minority element content Ti, Al, and Si in particular. Notwithstanding, the occurrence of breakdown after a relatively few number of oxidation cycles provided good system for assessing life-prediction modeling.

7.5.1 Application of Experimental Result to Prediction

The TGA results showed that the transient oxidation stages for VDM800HT and 800HT were about 4-5 hours. Thus, one-day thermal cycling ensured the establishment of the slower growing steady-state scale during the first cycle. The measured parabolic rate constants are in agreement with literature [1], which shows that parabolic rate constant for chomia-scale growth at 1000 °C is in the range 1×10^{-12} - 5×10^{-11} $g^2cm^4s^{-1}$. However, the growth rate may change during cyclic oxidation, in which the protective scale is more prone to spall. The spallation of oxide scale generally involves the separation of cracked scale [143,219]. A
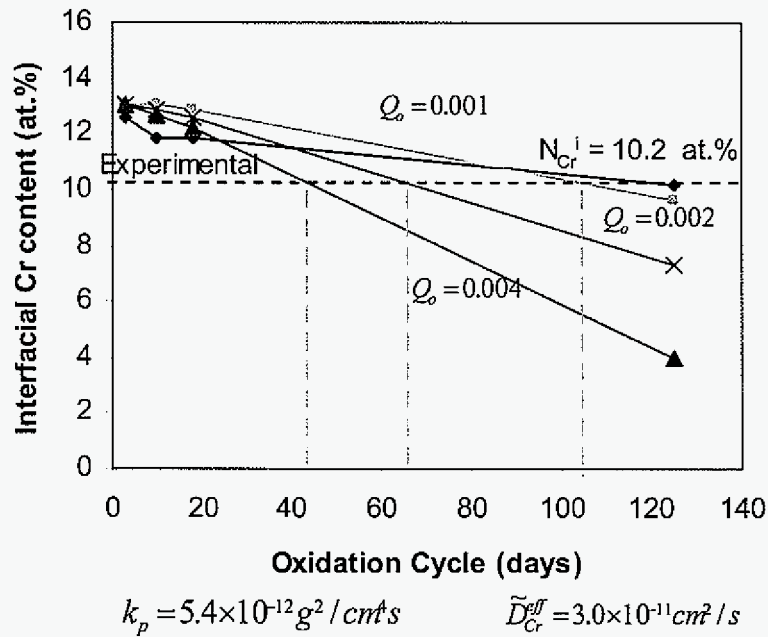
Figure 7.14. Sensitivity of the predicted interfacial chromium content on the spallation constant in VDM800HT during 1-day oxidation cycles at 1000 °C.
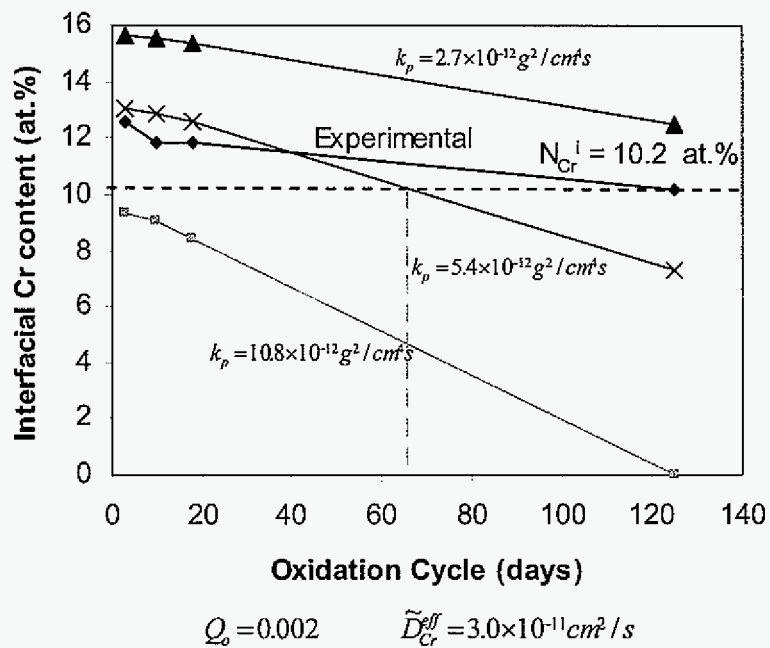
Figure 7.15. Sensitivity of the predicted interfacial chromium content on the parabolic scaling rate constant in VDM800HT during 1-day oxidation cycles at 1000 °C.

simplifying procedure in the current analysis was to use the isothermal parabolic rate constant to predict the cyclic oxidation behavior. Since oxidation was generally protective prior to breakdown, this was deemed a reasonable simplification.

The composition of the oxide layers determined the flux of alloying elements from the alloy matrix to the oxide scale. If the movement of the alloy/scale interface is neglected, more chromium depletion from the alloy subsurface would be predicted for a given parabolic rate constant, spallation constant, and amount of Cr in the scale. The amount of Cr in the scale was estimated form the scale that formed during isothermal testing. It is expected that such an estimation is not accurate during the period of cyclic oxidation; however, it is beyond the scope of this study to do anything more refined.

The present of an outer $NiFe_2O_4$ scale layer on the 800HT alloy after isothermal oxidation and the early stages of cyclic oxidation can be attributed to two possibilities. One is that $NiFe_2O_4$ mainly formed during transient oxidation, and the other possibility is that $NiFe_2O_4$ formed in conjunction with the growth of the inner chormia layer by diffusion of Fe^{2+} and Ni^{2+} ions through this chromia layer. For the first possibility, the largest thickness of $NiFe_2O_4$ layer can be calculated by using parabolic rate constant and time of transient oxidation. Doing this, it is found that the thickness of the $NiFe_2O_4$ layer should be about 2 μm (after 90 hours isothermal oxidation), which is less than the about 7 μm found in the cross-sectional image after the TGA test (Fig.7.4). Thus, the growth of $NiFe_2O_4$ spinel may be a combination of the two possibilities. Since $MnCr_2O_4$ has been reported to form by fast diffusion of Mn through chromia scale [111-114], the second case is likely apt to VDM800HT.

For 800HT, the interfacial chromium content was about 8 at.% of 7-day isothermal oxidation at 1000 °C; however, after 18 1-day cycles, the interfacial content was about 7.3 at.% and the alloy exhibited breakdown. In the study by Harper and Gleeson [110], the interfacial chromium content decreased to below about 11 at.% at the onset of breakdown after 6 30-day oxidation cycles (180 days) at 982 °C. It is apparent that the critical chromium level to re-form protective chromia scale varies on oxidation conditions, and makes the prediction of the cycles to breakdown very difficult. Whittle [64] treated the variation in the interfacial composition with time after a scale-spallation event (Fig. 2.27) and predicted an abrupt decrease and then increase in the interfacial content when the protective oxide layer

reforms immediately after spalling of the initial layer. If the interfacial concentration increases to a level that is below the critical concentration to form the protective oxide scale, then the protective oxide scale would not reform. Thus, an implication of Whittle's treatment is that cycling frequency affects the interfacial Cr content and, hence, the ability of the alloy to reform a protective scale. Generally, interfacial Cr concentration would decrease with increasing number of cycles because of spallation, and the time at temperature in a given cycle (*i.e.*, dwell time) may not be enough for the interfacial Cr content to approach the critical value. In such a case, the alloy could be prone to breakdown.

7.5.2 Implications of Predictions from Present Model

Wagner's model (Equation 7.6) showed better agreement with the measured Cr depletion profiles after 7-days isothermal oxidation at 1000 °C than the profiles calculated numerically. Wagner's model required the input of interfacial chromium content, thus causing the very close agreement with the measured depletion profile within the vicinity of the alloy/scale interface. However, Wagner's model is limited since it will be necessary in any life-prediction model to be able to predict the interfacial content. The numerical model showed good agreement with experimental profiles; however, $\tilde{D}_{Cr}^{eff}$ was found to be a critical input parameter. The $\tilde{D}_{Cr}^{eff}$ values obtained by the Dayananda and D-average models produced good agreement with experiment for Cr depletion profiles in the 800HT alloy, while the $\tilde{D}_{Cr}^{eff}$ obtained by the average-slope model gave the best agreement for VDM800HT. Generally, the average-slope model gave the largest $\tilde{D}_{Cr}^{eff}$, while the Dayananda model gave the smallest. The difference in the $\tilde{D}_{Cr}^{eff}$ values determined from the three models reflects the fact that the chromium interdiffusion is significantly composition dependent for the alloys studied. In spite of this, it was shown in current study that the numerical model could offer a good method to predict the interfacial chromium content if a proper interdiffusion coefficient of Cr was applied.

Cyclic oxidation exhibited more complex behavior than the simulated results. The experimental kinetics curves showed variation of weight change with cycles, and thus

increased the difficulty to fit the experimental kinetics curves. COSP did not consider the effect of transient oxidation, in which the oxidation rate was much larger than in the steady-state, thus resulting in a lower simulated weight gain during the early of cyclic oxidation for 800HT. VDM800HT showed relatively slow spallation between 20-70 cycles. It is possible that the relatively large weight loss before 20 cycles in VDM800HT came from the spallation of the less-protective $MnCr_2O_4$ spinel. With increasing of oxidation time, Mn would be depleted, and subsequently less weight loss was attributed to less $MnCr_2O_4$ formation. After about 70 cycles, another less-protective oxide, such as $NiFe_2O_4$, may form and result in a larger extent of spallation.

Cyclic oxidation increases the variation of oxide phases, oxide growth rate, spallation constant, and Cr interdiffusion coefficient. Thus, the prediction for cyclic oxidation will be much more complex than that for isothermal oxidation. In the numerical model, there are four main parameters which may be cycle dependent: k_p, Q_o, oxide scale phases, and $\tilde{D}_{Cr}^{eff}$. In the four parameters, k_p and Q_o may match each other by fitting cyclic oxidation kinetics in COSP program. Hence, the three parameters oxide phase, k_p, and $\tilde{D}_{Cr}^{eff}$ are required to be analyzed carefully. For the 800HT alloy, the two experimental Cr profiles after 3 and 10 cycles can be used to check the validation of the calculation because the two cycles were under protective period. The predicted chromium depletion was larger than the experimental result within the vicinity under the alloy/scale interface after 3 cycles, while it was less in the deeper region to matrix. It is noted that the more predicted chromium depletion within the vicinity under the alloy/scale interface should be balanced by the less predicted depletion in the deeper region for the same Cr consumption. However, the predicted Cr profile showed relatively less Cr consumption compared to the experimental Cr profile after 3 oxidation cycles. Thus, a less Cr consumption was estimated by the numerical model. The result is consistent with the less calculated weight gain by COSP program before first 10 cycles (Fig. 7.9). There are two possibilities for the less prediction of Cr consumption. One is the effect of the transient oxidation, which had much larger oxide growth rate than steady-state oxidation. The other may be related to varied parabolic rate contant, Cr interdiffusion behavior under cyclic oxidation. However, it is found that the Cr depletion was almost same for the predicted and experimental Cr profiles after 10 oxidation cycles. Hence, the transient

oxidation should mainly effect the prediction after 3 cycles. The 800HT alloy showed breakdown after about 18 cycles, which was associated with a faster Cr consumption, and the prediction, which was based on protective oxidation, resulted in a less Cr depletion. There is no meaning to evaluate the validation of the prediction for 125 cycles.

The VDM800HT alloy showed the good agreement between the predicted and experimental Cr profiles after 3, 10, and 18 oxidation cycles which were under protective period. For the three cycles, the predicted Cr profiles showed more Cr consumption within the vicinity under the alloy/scale interface and less Cr consumption deeper into the alloy than the experimental Cr profiles. It is seen that the total predicted Cr consumption was similar to the experimental Cr consumption for VDM800HT after the three cycles. Because VDM800HT did not form a large amount of spinel oxide, the most primary chromia scale enables that the oxide phases, parabolic rate constant, and Cr interdiffusion behavior obtained at isothermal oxidation provided a reasonable prediction for the Cr consumption during cyclic oxidation. The predicted Cr consumption after 125 cycles was not consistent with the experimental Cr consumption for VDM800HT due to its breakdown after about 95 oxidation cycles.

The experimental Cr depletion profiles after different oxidation cycles showed flat trend within the vicinity under the alloy/scale interface, while steeper in the alloy deeper from the vicinity. The fluctuation of the experimental Cr depletion profiles showed that the Cr interdiffusion behavior should be strongly composition-dependent during cyclic oxidation. Within the vicinity under the alloy/scale interface with larger chromium depletion, the interdiffusion coefficient of Cr should be large, which promoted the diffusion of chromium and resulted in the flat Cr concentration profile in the region. While the average effective interdiffsion coefficient of Cr used in the prediction may be smaller than the real interdiffusion coefficient of Cr in the vicinity under the scale/alloy interface, which resulted in steeper predicted Cr profiles in the region. The Cr depletion profiles of VDM800HT showed flatter behavior over entire depletion region than 800HT, which was attributed to the larger interdiffusion coefficient of Cr and slower growth rate of VDM800HT.

The interfacial Cr content can be used to predict the breakdown of cyclic oxidation, and also provide a method to evaluate the prediction. The best prediction for the breakdown of

800HT was obtained by applying the average effective interdiffusion coefficient of Cr of the average-D model. It is recalled that the average effective interdiffusion coefficient of Cr obtained from the Dayananda's model also produced the good agreement between the predicted and experimental Cr depletion profiles under isothermal condition; however, the prediction based on the Dayananda's model showed shorter breakdown time (about 7 oxidation cycles) for 800HT during cyclic oxidation. The explanation of the deviation of the Dayananda's model for the cyclic oxidation prediction is related to its spallation constant. As shown in Fig. 7.9, COSP program obtained a less weight gain before first 10 cycles for 800HT. If considering transient oxidation, which had much larger oxide growth rate, a smaller spallation constant would be obtained. Smaller spallation constant may increase the breakdown time.

The predicted and measured interfacial chromium contents before breakdown decreased linearly for 800HT and VDM800HT. Thus, it is postulated that interfacial chromium content after long-term cyclic oxidation could be derived by linearly fitting interfacial chromium contents obtained after short-term protective oxidation cycles. Further, the life-time of cyclic oxidation could be obtained based on short-term oxidation if the critical chromium content is known. However, more experiment and calculation are necessary to support this postulation, and the scattered results during short-term cyclic oxidation may increase the error in postulating the interfacial Cr content for long-term cyclic oxidation.

The VDM800HT alloy showed a large deviation of the predicted breakdown comparing with the experimental result. The average effective interdiffusion coefficient of Cr obtained by the three models predicted shorter breakdown time. It is found that VDM800HT showed a relatively smaller spallation trend between 20 and 70 cycles, while COSP program obtained an average spallation constant over entire 80 oxidation cycles, which had larger spallation trend during 20 to 70 cycles than the experimental kinetics. It is calculated that the predicted breakdown time would increase to about 105 cycles if a half spallation constant is applied (Fig. 7.14), which is close to the experimental breakdown time (about 95 cycles). It is noted that the closest prediction (65 cycles) for breakdown was obtained by using $\widetilde{D}_{Cr}^{avs}$, which also provided the best prediction for the isothermal oxidation (Fig. 7.8). Thus, it is concluded that

the average effective interdiffusion coefficient of Cr obtained under isothermal oxidation could be reasonably used to predict cyclic oxidation.

The critical interfacial chromium level, N_{Cr}*, is very important to predict the life-time of oxidation resistance. For the Fe-Cr alloy, this critical chromium content is about 14 wt. %. However, commercial chromia-forming alloys should have a lower value than 14 wt.% because small alloying additions, such as Mn and Si, are used to stabilize Cr_2O_3 scale [1,148]. Thus, the critical chromium level is dependent upon such variables as the alloy's composition and the oxidizing conditions, which make it difficult to predict. There is lack of mature method to predict the critical interfacial Cr content for chromia-forming alloys. The further work will be highly encouraged to determine the critical interfacial chromium concentration.

7.5.3 Sensitivity of Prediction to the Input Parameters

By analyzing the three models calculating average effective interdiffusion coefficient of Cr, it is seen that the Dayananda's model (Equation 7.1) uses the local position ($x-x_o$) in the numerator of Equation 7.4, while the average-slope model uses the depletion depth (x_m-x_o) in the numerator. Thus, the average-slope model produces a larger Cr interdiffusion coefficient than the Dayananda's model. The average-D model averages the local interdiffusion coefficient over entire depletion region, in which generally larger values are near the alloy/interface and smaller values in the front of depletion region, and obtains a medium Cr interdiffusion coefficient. Based on the prediction results, difference in a factor of two in the average effective interdiffusion coefficient of Cr produced at least a difference of a facor of three in the predicted breakdown time for VDM800, which is not tolerented in application.

As discussed above, cyclic oxidation showed complex oxidation kinetics, which is difficult to be simulated completely. The deviation of fitting between the experimental and simulated kinetics could result in estimation error in spallation constant. As shown in Fig.7.13, the spallation constant affected the prediction of long-term oxidation more than short-term because the different spalllation constant produced different slopes for the interfacial Cr content decrease. Thus, it is important to take into account the effect of spallation constant in long-term oxidation prediction.

Oxide growth rate also plays significant effect on the prediction (Fig. 7.15). The predicted interfacial Cr contents showed similar decrease trend for different parabolic rate constants. Thus, the oxide growth rate will significantly affect the prediction of interfacial Cr content for both of short-term and long-term oxidation. The significant effect of oxide growth rate on the prediction results increase the difficulty to the prediction of oxidation life-time because the growth rate depends on sample preparation, oxidation procedure, measurement of growth rate [100,220-223].

7.5.4 Key Point and Improvement in Application of the Current Model

It is complex to predict the depletion and lifetime of cyclic oxidation because the main parameters, such as oxide phases, oxide growth rate, spallation constant, and interdiffusion coefficient of Cr, may change with oxidation duration. However, reasonably prediction can be obtained if proper assumptions are built.

Constitution of oxide phases can be determined under isothermal oxidation. The phases would grow similarly during protective cyclic oxidation period. Average effective interdiffusion coefficient of Cr could be determined from Cr depletion profile under isothermal condition by the three models in the current stufy. The good agreement of the calculated and measured Cr depletion profile during isothermal oxidation produced the proper interdiffusion coefficient of Cr, which was successfully used to simulate Cr depletion under cyclic condition.

Spallation constant was obtained by fitting the experimental and simulated kinetics by COSP program. Based on the current study, transient oxidation should be considered in COSP program to obtain better fitting. Theorically, both of oxide growth rate and spallation constant can be simulated by COSP program; however, the reasonable results would be related to the ability to simulate complex behavior under cyclic oxidation for COSP program. From the prediction of VDM800HT, cyclic oxidation showed very complex kinetics behavior, which resulted in various spallation trend during protective period. Thus, various spallation should be considered in COSP and numerical model.

The critical Cr interfacial content is important to predict the life-time of cyclic oxidation. Unfortunately, it varies upon alloy and oxidation condition, such as alloy composition, Cr interdiffusion behavior, scale properties, spallation behavior, cyclic oxidation duration. And it is encouraged to predicting the critical interfacial Cr content for commercial chromia-forming alloys.

7.6 Conclusions

Chromia-forming commercial wrought 800HT and VDM800HT alloys were oxidized isothermally and cyclically at 1000 °C. The 1-day long-term cyclic oxidation showed breakdown after about 18 and 95 cycles for 800HT and VDM800HT, respectively. XRD and SEM analyses for 7 days isothermal oxidation identified two oxide layers of scale: an inner layer of Cr_2O_3 and an outer layer of $NiFe_2O_4$ for 800HT, and an inner layer of Cr_2O_3 and an outer layer of $MnCr_2O_4$ for VDM800HT.

Subsurface Cr depletion behavior during isothermal oxidation can, in general, be reasonably characterized using an average effective interdiffusion coefficient of Cr and an appropriate diffusion equation. Application of average effective interdiffusion coefficient of Cr on Wagner's and numerical calculation for subsurface Cr depletion profile could obtain good agreement with experimental result. The proper average effective interdiffusion coefficient of Cr obtained from isothermal oxidation can be applied to cyclic oxidation.

Kinetics of cyclic oxidation showed complex behavior, such as various oxide growth rate and spallation, which increases difficulty to simulate. COSP program offers a good way to simulate cyclic oxidation. However, there is a requirement to consider transient oxidation and variety of spallation constant in COSP program.

The numerical model provides an advanced method to predict the subsurface depletion profile during cyclic oxidation. The simulated results show good agreement with measured depletion profiles if proper parameters are obtained, such as average effective interdiffusion coefficient of Cr. The prediction of life-time of cyclic oxidation resistance has been obtained by comparing the predicted interfacial chromium content with the critical chromium content for the formation of protective chromia scale, and the results showed good agreement with experimental breakdown time.

The alloys studied showed complex characteristics during predicting the subsurface chromium depletion. Oxide phases, parabolic rate constant, spallation constant, and average effective interdiffusion coefficient of Cr play key effects on the prediction, and the effect varies on alloy structure, scale properties, spalltion behavior, and oxidation condition and duration. The interdiffusion coefficient of Cr showed strongly composition-dependent during cyclic oxidation, and produced complex chromium depletion profile. Based on the calculation of the numerical model, the life-time of oxidation resistance is very sensitive to oxide growth rate and interdiffusion coefficient of Cr.

The critical chromium level to re-form protective chromia scale would vary on alloy and oxidation condition for chromia-forming alloys. The variation of the value increases the difficulty to predict the life-time of oxidation resistance.

CHAPTER 8 SUMMARY

Commercial alloys for high-temperature applications require the formation of a protective scale to resist excessive degradation. The nature of the scale that forms can depend on the alloying composition and the oxidation condition. Most high-temperature alloys require a chromia scale for the protection. Concurrent with chromia scale growth are subsurface changes in the alloy, such as internal oxidation and chromium depletion. Subsurface changes can affect the properties of the scale and alloy, which is particularly evident during thermal cycling conditions.

It is shown in this study that the oxidation of commercial alloys is significantly affected by minor elements in the alloy, such as Si, Al, Ti, and Mn. It was further shown that variation of minor element contents within the specific rage of a given alloy can result in markedly different cyclic oxidation behavior.

The life-time of a chromia-forming alloy would end if no sufficient chromium diffuses to the alloy/scale interface for the re-formation of the chromia scale in the event of spallation. Thus, the prediction of oxidation resistance life-time requires the evaluation of subsurface Cr depletion. Many factors affect the subsurface Cr depletion, including oxide phases, oxide growth rate, spallation, and Cr interdiffusion coefficient. Those factors are difficult to predict under the conditions of cyclic oxidation.

The current study investigated the oxidation behavior of commercial wrought Fe-base and Ni-base alloys, which are extensively used in industries. The effects of alloying elements, especially the effect of minor amount of Si, were investigated. The behavior of oxide growth, oxide spallation, subsurface change, and chromium interdiffusion in the subsurface were studied in detail. A novel model was developed in the current study to predict the cyclic oxidation life-time by simulating oxidation kinetics and chromium interdiffusion in the subsurface of chromia-forming alloys.

From cyclic oxidation kinetics, Fe-base alloys generally showed poorer oxidation resistance than Ni-base alloys. All Fe-base alloys showed a large amount of spallation, even to the point of breakdown, during cyclic oxidation at 1000 °C. The Ni-base alloys also showed dramatic variability in their oxidation behavior, from negative weight change (large spallation) to stable positive weight gain (small spallation) during cyclic oxidation. The

variation in oxidation behavior is mainly attributed to variations in the alloy composition. The alumina-forming alloys, 214 and 602CA, showed excellent cyclic oxidation resistance at 1000 and 1100 °C. The chromia-forming alloy 45TM also showed excellent cyclic oxidation resistance which was attributed to the beneficial effect of SiO_2 particles within subsurface region formed during oxidation and to the presence of a minor amount of reactive element (*i.e.*, Ce).

Generally, the Fe-base chromia-forming alloys had larger parabolic rate constants than the Ni-base chromia-forming alloys. A large parabolic rate constant would help to establish the chromia scale, but would also result in a thicker chromia scale, which could develop large stresses and be prone to spallation during cyclic oxidation.

Nickel is more beneficial for oxidation resistance than iron. The following reasons may contribute to the beneficial effect of Ni: (1) Ni^{2+} doping in Cr_2O_3 decreases the cation vacancies concentration, and thus reduces the oxidation rate; (2) Ni may decrease the absorption of inwardly flowing cation vacancies and decrease the vacancy gradient across the scale; (3) Ni-base alloys may have better adhesion between oxide scale and subsurface alloy; and (4) Ni oxidizes more slowly than Fe and therefore it is kinetically easier for the Cr_2O_3 scale to establish itself on a Ni-base alloy.

Cycle duration was found to affect oxidation resistance. Generally, low cycle frequency could decrease induced thermal stress and thus be beneficial to spallation resistance. Under the cyclic oxidation conditions used in the current study, the dependence was about as $\Delta t^{(2/3)}$ (where Δt = cyclic duration) for the number of days to cross zero mass change.

Minor alloying elements play a significant role on cyclic oxidation behavior. Manganese is generally detrimental for oxidation resistance. Most alloys with a Mn content larger than 0.2 wt.% formed an $MnCr_2O_4$ outer oxide layer, which is less-protective and prone to spall. Silicon has different possible effects on oxidation resistance depending on its content. In general, silicon can facilitate the formation of Cr_2O_3 scale. A continuous SiO_2 layer at the alloy/scale interface makes the scale prone to spallation during cyclic oxidation. Titanium is generally detrimental to oxidation resistance. It trends to oxidize at the scale surface and the alloy/scale interface, and intergranularly in the subsurface region of the alloy. Aluminum is generally beneficial to oxidation resistance if an Al_2O_3 scale forms. A continuous internal

alumina network within the subsurface region of the alloy can reduce the diffusion of oxygen inward and chromium cations outward, which decreases the scale growth rate and the depletion of Cr within the subsurface region. Al-rich oxide particles combined with Si-rich oxide particles at the alloy/scale interface are also beneficial for oxidation resistance. However, internal alumina oxidation could be a problem from the standpoint of decreasing the mechanical properties of the alloy.

A more detailed analysis of the Si effect using Fe- and Ni-base alloys showed the Si can play a complex role that depended on alloy composition. Increasing the Si content in the Fe-base SM alloys (<1 wt.%) resulted in improved oxidation resistance. Formation of Si-rich oxide particles at the alloy/scale interface is believed to aid by impeding the diffusion of oxygen and chromium, thus decreasing oxidation kinetics of the 800 alloys. A higher silicon content facilitates the formation of oxide protrusions, such as Cr_2O_3 and TiO_2, at the alloy/scale interface of the Ti-containing alloys, which can result in larger stresses and poorer spallation resistance. Ti can oxidize at the alloy/scale interface, which induces complex stresses and initiates the formation of cracks along the alloy/scale interface. A higher minor alloying element content of Ti or Al also increases the extent of internal oxidation, which could offset the beneficial effect of silicon. Thus, the VDM800 alloy showed best oxidation behavior of the 800 series alloys due to its intermediate Si content and low Ti+Al content.

The high-Si (>2 wt.%) Ni-base alloys in the current study showed varied oxidation behavior. Silicon oxidized and formed what was inferred to be a continuous SiO_2 layer at the alloy/scale interface or a dispersion of SiO_2 particles in the subsurface region of the alloys. The formation of a disperse distribution of SiO_2 particle in the vicinity of the scale/alloy interface in the 45TM alloy apparently caused a decrease in the growth rate of the Cr_2O_3 scale. The silicon in 160-HR oxidized to form a continuous SiO_2 layer, which partially blocked oxygen diffusion inward and resulted in less internal oxidation attack. The development of a continuous silica layer initiated the formation of cracks within the scale and a general weakening of the scale during cyclic oxidation.

Addition of Fe and Co to a cast NiCr-based alloy increased oxidation growth rate and resulted in poorer cyclic oxidation resistance, while addition of Si decreased oxide growth rate, and thus improved cyclic oxidation resistance. The effect of Si on decreasing oxide

growth rate could eliminate the detrimental effect of Fe and Co on increasing oxide growth rate, and hence improved cyclic oxidation resistance.

It was found that the average effective interdiffusion coefficient, $\tilde{D}_{Cr}^{\mathit{eff}}$, is very sensitive to alloy composition. Higher Si content may increase the value of $\tilde{D}_{Cr}^{\mathit{eff}}$. Larger $\tilde{D}_{Cr}^{\mathit{eff}}$ could supply sufficient chromium to compensate the chromium consumption due to the selective formation of chromia scale, and thus facilitates the re-formation of chromia scale and improves oxidation resistance. Addition of Fe and Co in the NiCr-based alloy decreased the interdiffusion coefficient of chromium and increased the scaling kinetics, thus resulting in poorer oxidation behavior.

The cyclic oxidation kinetics showed complex behavior, such as variations in oxide growth kinetics and spallation, which made it difficult to simulate. COSP offers a good way to simulate cyclic oxidation; however, COSP is limited in that it does not consider transient oxidation and variation in the spallation constant.

Subsurface depletion behavior during isothermal oxidation can, in general, be reasonably characterized using an average effective interdiffusion coefficient and an appropriate diffusion equation. Application of an average effective interdiffusion coefficient in Wagner's model and in numerical calculations for subsurface depletion profiles could obtain good agreement with experimental result. The $\tilde{D}_{Cr}^{\mathit{eff}}$ obtained from isothermal oxidation could be applied to the treatment of cyclic oxidation.

The numerical model presented in this thesis gives an advanced method to predict the subsurface depletion profile under cyclic oxidation conditions. The results showed good agreement with measured depletion profiles; although, this agreement was highly dependent on the value of the Cr interdiffusion coefficient. The life-time prediction for oxidation resistance was obtained by comparing the predicted interfacial chromium content with the critical chromium level for the formation of protective scale, and the results could show good agreement with experiment.

The critical chromium content to re-form a protective chromia scale depends on the alloy's structure and composition, and on the oxidation condition. The variation of the N_{Cr}^{*}

value makes life-time prediction of oxidation resistance difficult. Clearly, methods are needed to predict the critical interfacial content.

APPENDIX A C++ COEFFDIF CODE TO CALCULATE THE AVERAGE EFFECTIVE INTERDIFFUSION COEFFICIENT OF CHROMIUM

```cpp
#include <iostream.h>
#include <fstream.h>

#define POINT 2000        // max profile point

void main(){

    float content[POINT];     // profile
    ifstream inFile;                    // profile file
    char fileName[20];               // profile file name
    char option;

    do {

    int dataNum=0;                    // profile data number

    cout<<"\n**********************************************************\n";
    cout<<"*   This is a program to calculate the average diffusion  *\n";
    cout<<"*   coefficient according to the concentration profile.   *\n";
    cout<<"**********************************************************\n\n";

    cout<<"Please input the profile file name: ";
    cin>>fileName;

    inFile.open(fileName);
    if (inFile.fail())
     { cout<<"CANNOT OPEN THE PROFILE FILE: "<<fileName;
      exit(1);
     }

    // Read the profile data
    while (!inFile.eof())
    {   inFile>>content[dataNum];
```

```
    dataNum++;
  }
inFile.close();

for (int i=0; i<dataNum; i++)
    cout<<content[i]<<endl;

float D[POINT];                    // average-D model

// Input the parameters
float bulkContent, interfaceContent, step;
int time;

if (content[0] > content[dataNum-2])
{ bulkContent = content[0];
  interfaceContent = content[dataNum-2]; }
  else
   { bulkContent = content[dataNum-2];
  interfaceContent = content[0]; }

cout<<"Please input the profile step(um): ";
cin>>step;
cout<<"Please input the test time(day): ";
cin>>time;

step /= 10000;                     // centimeter unit
time = time*24*60*60;              // second unit

// process the profile
float flux=0.0, slope=0.0, fluxDyn=0.0;        // flux-total flux, fluxDyn - Dayananda's flux

if (content[dataNum-2]< content[0])
{
 for (int i=1; i<dataNum-1; i++)
  { flux += (dataNum-i-1.5)*step*(fabs(content[i]-content[i-1]));
    slope += (fabs(content[i]-content[i-1]));
```

```
    if ( i != 1 && i!= dataNum-2 && (content[i-1]-content[i+1]) != 0.0 )
       D[i] = (flux*2*step) / (2*time*(fabs(content[i+1]-content[i-1])));
         else if (i == 1)
           { if (content[1] == content[2]) D[i]=0;
             else   D[i] = (flux*step) / (2*time*(fabs(content[i+1]-content[i])));
           }
         else if (i==dataNum-2)
           { if (content[i] == content[i-1]) D[i]=0;
             else   D[i] = (flux*step) / (2*time*(fabs(content[i-1]-content[i])));
           }
     else if ((content[i-1]-content[i+1]) == 0.0 ) D[i] = 0.0;


     fluxDyn += ((dataNum-i-1.5)*step)*((dataNum-i-1.5)*step)*
                fabs((content[i]-content[i-1]));
   }
   }
   else
   {
     for (int i= dataNum-2; i>0; i--)
     { flux += (i-0.5)*step*(fabs(content[i-1]-content[i]));
       slope += (fabs(content[i]-content[i-1]));
       if ( i != 1 && i!= dataNum-2 && (content[i-1]-content[i+1]) != 0.0 )
         D[i] = (flux*2*step) / (2*time*(fabs(content[i+1]-content[i-1])));
           else if (i==1)
             { if (content[1] == content[2]) D[i]=0;
               else   D[i] = (flux*step) / (2*time*(fabs(content[i+1]-content[i])));
             }
           else if (i==dataNum-2)
             { if (content[i] == content[i-1]) D[i]=0;
               else   D[i] = (flux*step) / (2*time*(fabs(content[i-1]-content[i])));
             }
         else if ((content[i-1]-content[i+1]) == 0.0 ) D[i] = 0.0;


     fluxDyn += ((i-0.5)*step)*((i-0.5)*step)*
                (fabs(content[i]-content[i-1]));
```

```
    }
  }

flux = flux/(2*time);

slope /= ((dataNum-3)*step);

float DiffMine=0;
for(int i=1; i< dataNum-2; i++)
  DiffMine += D[i];

DiffMine = DiffMine/(dataNum-3);

float diffusion, diffDyn;            // average-slope model and Dayananda's model
diffusion = (flux/slope);
diffDyn = (fluxDyn) /(2*time*(bulkContent-interfaceContent));

// output results

cout<<"\n\nThe average-slope interdiffusion coefficient is (cm^2/s): "<<diffusion;
cout<<"\nThe Dayananda's diffusion coefficient is(cm^2/s): "<<diffDyn;
cout<<"\nThe average-D interdiffusion coefficient is(cm^2/s): "<<DiffMine;

cout<<"\nDo you need a new calculation(Y/N)? ";
cin>>option;
} while (option == 'Y' || option == 'y');

} // end main()
```

APPENDIX B C++ COSP-TR CODE TO SIMULATE CYCLIC OXIDATION KINETICS

```cpp
#include <iostream.h>
#include <fstream.h>
#include <math.h>

#define POINT 5000        // max profile point

void main(){

  double OWeight[POINT];        // oxygen taken - weight gain
  double TWeight[POINT];        // total weight change
  ofstream outFile;     // output fit profile
  char option;

  do {

    int timeT;                      // transient time
    double rateT;                   // transient parabolic rate constant
    int time;             // oxidation duration
    double rate;          // parabolic rate constant
    double spall[POINT];            // spallation constant
    int cycle;            // cycling cycles
    double weight;                  // 1st weight gain for spallation constant calcu.

    cout<<"\n***********************************************************************\n";
    cout<<"*  This is a program to calculate the Kinetics of Cyclic Cr Oxidation.  *\n";
    cout<<"*  Assumption: kp keeps constant, non-uniform spallation each cycle (Qo*W). *\n";
    cout<<"***********************************************************************\n\n";

    cout<<"Please input the transient parabolic rate constant (10-6 mg2cm-4s-1): ";
    cin>>rateT;
    cout<<"Please input the transient time (hour): ";
    cin>>timeT;
```

```cpp
cout<<"Please input the parabolic rate constant (10-6 mg2cm-4s-1): ";
cin>>rate;
cout<<"Please input the estimated spallation constant ( <1 ): ";
cin>>spall[1];

cout<<"Please input the cycling duration time(hour): ";
cin>>time;
cout<<"Please input the cycles of oxidation: ";
cin>>cycle;

time = time*60*60;
timeT = timeT*60*60;
OWeight[0] = 0.0;
TWeight[0] = 0.0;

//first cycle
OWeight[1] = pow(((pow(OWeight[0],2)+0.000001*rate*(time-timeT))+(0.000001*rateT*timeT)),0.5);
weight = pow((pow(OWeight[0],2)+0.000001*rate*time),0.5);
cout<<OWeight[1]<<" ";
TWeight[1] = TWeight[0]+OWeight[1]-OWeight[0]-OWeight[1]*spall[1]*(OWeight[1]/weight)*152.0/48.0;
OWeight[1] = (1.0-spall[1]*OWeight[1]/weight)*OWeight[1];

for (int m = 2; m < cycle; m++)
{   OWeight[m] = pow((pow(OWeight[m-1],2)+0.000001*rate*time),0.5);
    spall[m] = spall[1]*pow((OWeight[m]/weight),1.7);
    TWeight[m] = TWeight[m-1]+OWeight[m]-OWeight[m-1]-
        OWeight[m]*spall[m]*152.0/48.0;
    OWeight[m] = (1.0-spall[m])*OWeight[m];
    cout<<OWeight[m]<<" "<<TWeight[m]<<endl;
    }

//output
outFile.open("out.txt");
for (int i = 0; i < cycle; i++)
  outFile<<TWeight[i]<<endl;
```

```
        outFile.close();

        cout<<"Do you want a new calculation(y/n)? ";
        cin>>option;

    } while (option != 'n' && option != 'N');

}  // end main()
```

REFERENCES

1. Brian Gleeson, Corrosion and Environmental Degradation of Materials, V.II: Materials Science and Technology V.19, Wiley-VCH, Weinheim, German, 2000.

2. George Y. Lai, High-Temperature Corrosion of Engineering Alloys, ASM International, Materials Park, OH, 1990.

3. S.N. Basu and G.J. Yurek, *Oxid. Met.*, 36(1991): p. 281.

4. F.H. Stott, *Mater. Sci. Forum*, 251-254, 19-32(1997).

5. G.C. Wood, F.H. Stott, *Mater. Sci. Technol.*, 3(1987): p. 519.

6. M. Schutze, *Oxid. Met.*, 44(1995): p. 29.

7. P. Kofstad, High Temperature Corrosion, San Diego, March 2-6, 1981, National Association of Corrosion Engineers, Houston, 123(1981).

8. P. Kofstad, High Temperature Oxidation of Metals, John Wiley and Sons, New York (1966).

9. N. Birks and G.H. Meier, Introduction to High Temperature Oxidation of Metals, Edward Arnold, 1983.

10. K. Hauffe and H. Pfeiffer, *Z. Electrochem.*, 56, 390(1952).

11. Samuel A. Bradford, Fundamentals of Corrosion in Gases, Metals Handbook, Ninth Edition, Vol. 13 Corrosion, ASM International, Metals Park, OHIO, 1987

12. L.L. Shreir, Corrosion II, Butterworth-Heinemann Ltd., Oxford, 1:280(1994).

13. O. Kubashewski and B.E. Hopkins, Oxidation of Metals and Alloys, 2nd ed., Butterworths, 1962.

14. Per Kofstad, High Temperature Corrosion, Elsevier Applied Science, London and New York, 54(1988).

15. C. Wagner, *Z. Phys. Chem.*, B21, 25(1931).

16. C. Wagner, Atom Movements, American Society Metals, Cleveland, OH, 153(1931).

17. C. Wagner, *Prog. Solid State Chem.*, 10, 3(1975).

18. G.M. Raynaud, W.A.T. Clark, R.A. Rapp, *Metall. Trans.*, 15A, 573(1984).

19. A. Atkinson, *Rev. Mod. Phys.*, 57, 437(1985).

20. S.R. Shatynski, R.A. Rapp, J.P. Hirth, *Acta Metall.*, 24, 1071(1976).

21. G. Garnaud, R.A. Rapp, *Oxid. Met.*, 11, 193(1977).

22. F. Gesmundo, F. Viani, *Corr. Sci.*, 18, 217(1978).

23. H.S. Hsu, *Oxid. Met.*, 26, 315(1986).

24. A.T. Fromhold, Jr., Theory of Metal Oxidation, V.I, Fundamentals, V.II, Space Charge, North-Holland, Amsterdam, 1980.

25. G.J. Yurek, Corrosion Mechanisms, Marcel Dekker Inc., New York, 397(1987).

26. A. Dravinieks, H. McDonald, *J. Electrochem. Soc.*, 94, 139(1948).

27. S. Mrowec, Proc. JIM Int. Sym. on High Temperature Corrosion of Metals and Alloys, Mt Fuji, Japan, 17-20 November, 115(1982).

28. M.I. Manning, In Corrosion and Mechanical Stress at High Temperatures, V. Guttmann, and M. Merz (Eds.), Applied Science, London, 323(1981).

29. U.R. Evens, An Introduction to Metallic Corrosion, Arnold, London, 1948.

30. H.E. Evens, In Mechanical Properties of Protective Oxide Scales, Special Issue Mater. High Temp., 12, 219(1994).

31. L. Brewer, High Strength Materials, V.F. Zackey, Ed., Wiley, New York, 1965.

32. P. Kofstad, Nonstoichiometry, Diffusion, and Electrical Conductivity in Binary Metal Oxides, Wiley, New York, 1972.

33. A. F. Wells, Structural Inorganic Chemistry, Oxford University Press, London, 3rd. Edition, 1982.

34. J.S. Armijo, *Oxid. Met.*, 1, 171(1969).

35. P. Hancock and R.C. Hurst, *Adv. Corr. Sci. Technol.*, 4, 1(1974).

36. D.J. Baxter and K. Natesan, *Rev. High Temp. Mater.*, 5, 149(1983).

37. J. Cathcart, Stress Effects and the Oxidation of Metals, TMS-AIME, New York, 1975.

38. Oxidation and Mechanical Properties, Special Issue *Mater. Sci. Techn.*, 6, 1990.

39. Mechanical Properties of Protective Oxide Scales, Special Issue *Mater. High Temp.*, 12, 1994.

40. H.E. Evans, G.P. Mitchell, R.C. Lobb, and D.R.J. Owen, Proc. R. Soc. London, A440, 1(1993).

41. A.G. Evens, G.B. Crumley, and R.E. Demaray, *Oxid. Met.*, 20, 193(1983).

42. M.I. Manning, Corrosion and Mechanical Stress at High Temperatures, Applied Science Publishers, London, 323(1981).

43. J. Robertson and M.I. Manning, *Mater. Sci. Technol.*, **6**, 81(1990).

44. Michael Schutze, *Oxid. Met.*, **44**, 29(1995).

45. Michael Schutze, Corrosion and Environmental Degradation of Materials, V.I: Materials Science and Technology V.19, Wiley-VCH, Weinheim, German, 2000.

46. N.B. Pilling and R.E. Bedworth, *J. Inst. Met.*, **29**, 529(1923).

47. Michael Schutze, Protective Oxide Scales and Their Breakdown, Institute of Corrosion and Wiley Series on Corrosion and Protection, John Wiley & Sons Ltd, England, 1991.

48. J. Stringer, *Corros. Sci.*, **10**, 513(1970).

49. F.N. Rhines and J.S. Wolf, *Metal. Trans.*, **1**, 1701(1970).

50. R.F. Tylecote, *J. Iron Steel Inst.*, **196**, 135(1960).

51. G.R. Rigby, G.H.B. Lowell and A.T. Green, Br. Ceram. *Soc. Trans.*, **45**, 137(1946).

52. C.I. Howe, B. McEnany and V.D. Scott, *Corr. Sci.*, **3**, 195(1985).

53. A.G. Goursat and W.W. Smeltzer, *Oxid. Met.*, **6**, 101(1973).

54. K. Kuroda, P.A. Labun, G. Welsh, and T.E. Mitchell, *Oxid. Met.*, **19**, 117(1983).

55. U.R. Evens, The corrosion and oxidation of metals, first supplementary volume, St. Martin's press, New York, 18(1968).

56. L.L. Shreir, R.A. Jarman, and G.T. G.T. Burstein, Corrosion (Volume 1), Butterworth-Heinemann Ltd., Oxford, 194.

57. C.S. Tedmon, *J. Electrochem. Soc.*, **113**, 766(1966).

58. D.W. Bridges, J.P. Baur, and W.M. Fassel, *J. Electrochem. Soc.*, **103**, 619(1956).

59. E.A. Gulbransen and W.S. Wysong, TAIME, **175**, 28(1948).

60. E.A. Gulbransen, K.F. Andrew, and F.A. Brassart, *J. Electrochem. Soc.*, **110**, 952(1963).

61. R.J. Jaffee, Proceedings on an international symposium on high temperature technology, Asilomar, California, 1959.

62. R.T. Dehoff, Thermodynamics in Materials Science, McGraw-Hill, New York, 1993.

63. C. Wagner, *J. Electrochem. Soc.*, **103**, 627(1956).

64. D.P. Whittle, *Oxid. Met.*, **4**, 171(1972).

65. B. Chattopadhyay, G.C. Wood, *Oxid. Met.*, **2**, 372(1970).

66. J. Oudar, High Temperature Corrosion: R.A. Rapp (Ed.), Houston, NACE, 8(1983).

67. G.C. Wood, Oxid. Met., **2**, 11(1970).

68. C. Wagner, *J. Electrochem. Soc.*, **99**, 369(1952).

69. C. Wagner, *J. Electrochem. Soc.*, **103**, 571(1956).

70. R.C. John, Corrosion/96, NACE, Houston, TX, Paper 171, 1996.

71. M.A. Harper, J.E. Barnes, G.Y. Lai, Corrosion/97, NACE, Houston, TX, Paper 132, 1997

72. B. Gleeson and M.A. Harper, *Oxid. Met.*, **49**, 373(1998).

73. D.L. Douglass, *Oxid. Met.*, **44**, 81(1995).

74. U. Bruce, K. Dohle, J. Putz, A. Rahmel, M. Schutze, K.D. Schuhmacher, Metallic Corrosion 1984 (Vol. III), Toronto, National Research Council Canada, 325(1984).

75. R.C. Rapp, *Corrosion* 21, 382(1965).

76. G.R. Laflamme and J.E. Morral, *Acta Met.*, **26**, 1791(1978).

77. F.I. Wei, F.H. Stott, *High Temp. Technol.*, **7**, 59(1989).

78. Bingtao Li and B. Gleeson, Cyclic Oxidation Behavior of 800 Series Chromia-Forming Alloys, Corrosion/2001, Paper 01163, Houston, TX, 2000.

79. A. Schnaas, H.J. Grabke, *Oxid. Met.*, **12**, 387(1978).

80. R.H. Kane, *Corrosion*, **37**, 187(1981).

81. C. Wagner, *Z. Elcktrochem.*, **63**, 772(1959).

82. D.R. Gaskell, Introduction to Metallurgical Thermodynamics, Hemisphere Publishing Corporation, New York, 1981.

83. F. Maak, *Z. Metallkde*, **52**, 545(1961).

84. R.H. Bricknell, D.A. Woodford, *Acta Metall.*, **30**, 257(1982).

85. D. Caplan, R.J. Hussey, G.I. Sproule, M.J. Graham, *Oxid. Met.*, **14**, 279(1980).

86. G. de Maria, J. Drowart and M.G. Inghram, *J. Chem. Phys.*, **30**, 318(1959).

87. J.R. Ligenza, *J. Electrochem. Soc.*, **109**, 73(1962).

88. S.N. Basu and G.J. Yurek, *Oxid. Met.*, **36**, 281(1991).

89. S. Leistikow, I. Wolf, H.J. Grabke, *Werkst. Korrs.*, **38**, 556(1987).

90. M.K. Hossain, *Corros. Sci.*, **19**, 1031(1990).

91. C.S. Giggins, F.S. Pettit, *Trans. AIME*, **245**, 2509(1969).

92. S.J. Allan, M.J. Dean, in Behavior of High Temperature Alloys in Aggressive Environment, 15-18 October 1979, JRC Petten Establishment, I. Kirman etc. eds., The Metals Society, London, 319(1980).

93. S. Leistikow, in Behavior of High Temperature Alloys in Aggressive Environment, 15-18 October 1979, JRC Petten Establishment, I. Kirman etc. eds., The Metals Society, London, 198(1980).

94. A.G. Evans, G.B. Crumley and R.R. Demaray, *Oxid. Met.*, **20**, 193(1983).

95. J.K. Wright, R.L. Williamson and R.M. Cannon, *Mater. Sci. Eng. A.*, **A238**, 411(1997).

96. M. Schutze, *Mater. Sci. Technol.*, **4**, 407(1988).

97. B.A. Pint, P.F. Tortorelli and I.G. Wright, *Mater. Corros.*, **47**, 663(1997).

98. V. Guttmann, F. Hukelmann, P.A. Beaven and G. Borchardt, in Cyclic Oxidation of High Temperature Materials, M. Schutze and W.J. Quadakkers eds., EFC, IOM Communications Ltd., **27**, 17(1999).

99. V.A.C. hannappel and M.F. Stroosnijder, in Cyclic Oxidation of High Temperature Materials, M. Schutze and W.J. Quadakkers eds., EFC, IOM communications Ltd., **27**, 225(1999).

100. K.P. Lillerud and P. Kofstad, in High Temperature Corrosion, R.A. Rapp, Ed., NACE, Houston, TX, 1983.

101. F.H. Stott, G.J. Gabriel, F.I. Wei, and G.C. Wood, *Werkst. Corrs.*, **38**, 521(1987).

102. A. Kumar and D.L. Douglass, *Oxid. Met.*, **10**, 1(1976).

103. A.W. Bowen and G.M. Leak, *Metall. Trans.*, **1**, 2767(1970).

104. C.J. Smithells, Metals Reference Book Vol II, Butterworths, London, 664(1967).

105. A.F. Smith and G.B. Gibbs, *Met. Sci. J.*, **3**, 93(1969).

106. K.P. Lillerud and P. Kofstad, *Oxid. Met.*, **17**, 487(1982).

107. F.H. Stott, *Mater. Charact.*, **28**, 311(1992).

108. F.H. Stott, F.I. Wei, *Oxid. Met.*, **31**, 369(1989).

109. F.H. Stott, *Mat. Sci. Tech.*, **5**, 734(1989).

110. M.A. Harper and B. Gleeson, Cyclic Oxidation of High Temperature Materials, M. Schutze and W.J. Quadakkers eds., EFC, IOM Communications Ltd., **27**, 273(1999).

111. D.L. Douglass and F. Rizzo-Assuncao, *Oxid. Met.*, **29**, 271(1988).

112. F.H. Stott, F.I. Wei, and C.A. Enahoro, *Werkst. Korros.*, **40**, 198(1989).

113. R.E. Lobnig, H.P. Scmidt, K. Hennesen and H.J. Grabke, *Oxid. Met.*, **37**, 81(1992).

114. D. Caplan and M. Cohen, *J. Electrochem. Soc.*, **112**, 471(1965).

115. D.E. Jones and J. Stringer, *Oxid. Met.*, **9**, 409(1975).

116. H.E. Evans, D.A. Hilton, R.A. Holm, and S.J. Webster, *Oxid. Met.*, **19**, 1(1983).

117. R.C. Lobb, J.A. Sasse, and H.E. Evans, *Mater. Sci. Technol.*, **5**, 828(1989).

118. J. Litz, A. Rahmel, and M. Schorr, *Oxid. Met.*, **30**, 95(1988).

119. D.R. Sigler, *Oxid. Met.*, **46**, 335(1996).

120. F.H. Stott and F.I. Wei, *Mater. Sci. Technol.*, **5**, 1140(1989).

121. C.L. Angerman, *Oxid. Met.*, **5**, 149(1972).

122. C.A. Barrett and C.E. Lowell, *Oxid. Met.*, **4**, 307(1975).

123. D.P. Whittle and J. Stringer, *Phil. Trans. R. Soc. Lond.* A., **295**, 309(1980).

124. T.N. Rhys-Jones, H.J. Grabke, and H. Kudielka, *Werkst. Korros.*, **38**, 65(1987).

125. P.Y. Hou and J. Stringer, *Oxid. Met.*, **29**, 45(1988).

126. J. Stringer, B.A. Wilcox, and R.I. Jaffee, *Oxid. Met.*, **5**, 11(1972).

127. J.L. Smialek, D.T. Jayne, J.C. Schaeffer, and W.H. Murphy, *Thin Solid Films*, **253**, 285(1994).

128. B.A. Pint, *Oxid. Met.*, **45**, 1(1996).

129. J.L. Smialek and B.K. Tubbs, *Metall. Mater. Trans.* A, **26A**, 427(1995).

130. F.S. Pettit and G.H. Meier, Processing and Design Issue in High-Temperature Materials, N.S. Stoloff and R.H. Jonesm (Eds). TMS, Warrendale, PA, 379(1997).

131. B.A. Pint, P.F. Tortorelli, and I.G. Wright, Cyclic Oxidation of High Temperature Materials, M. Schutze and W.J. Quadakkers eds., EFC, IOM communications Ltd., **27**, 111(1999).

132. G.H. Geiger and D.R. Poirier, Transport Phenomena in Metallurgy, Addison-Wesley Publishing Co., 1980.

133. L. Onsager, Annals, *New York Acad. of Sciences*, **46**, 241 (1945).

134. J.S. Kirkaldy, *Canadian Journal of Physics*, Vol.35, 435(1957).

135. M.A. Dayananda and C.W. Kim, *Metall.Trans*. A., **10A**, 1333(1979).

136. M.A. Dayananda, *Metall. Trans*. A., **14A**, 1851(1983).

137. J. Nesbitt, NASA report: NASA/TM-2000-209271, 08(2000).

138. J. Nesbitt, OxDiff – A Finite-Difference Computer Model to Predict Concentration Profiles Associated with Oxidation of Ternary, Single-Phase Alloys, High Temperature Corrosion, Gordon Research Conference, New London, NH, July 22-27, 2001

139. Carl E. Lowell, Charles A. Barrett, Raymond W. Palmer, Judith V. Auping, and Hubert B. Probst, *Oxid. Met.*, **36**, 81(1991).

140. Jim Smialek and Judy Auping, , COSP for Windows: The fun and easy way to analyze your cyclic oxidation weight change data, High Temperature Corrosion, Gordon Research Conference, New London, NH, July 22-27, 2001

141. C.E. Lowell, *Oxid. Met.*, **7**, 95(1973).

142. K.S. Chan, *Metall. Mater. Trans*. A, **28A**, 411(1997).

143. H.E. Evans, *Int. Mater. Rev.*, **40**, 1(1995).

144. C.O. Moon and S.B. Lee, *Oxid. Met.*, **39**, 1(1993).

145. J.L. Smialek, J.A. Nesbitt, C.A. Barrett and C.E. Lowell, Cyclic Oxidation of High Temperature Materials, M. Schutze and W.J. Quadakkers eds., EFC, IOM communications Ltd., **27**, 148(1999).

146. C.E. Lowell and D.D. Deadmore, *Oxid. Met.*, **14**, 325(1980).

147. Matthew J. Donachie, Superalloys – Source Book, ASM, 3(1984).

148. J.L. Smialek, C.A. Barrett, and J.C. Schaeffer, Design for Oxidation Resistance, ASM handbook, V.**20**, Materials Park, OH, 589(1997).

149. A. Weronski and T. Hejwowski, Thermal Fatigue of Metals, Marcel Dekker Inc., New York, 93(1991).

150. F.R. Morral, Metals Handbook, Ninth Edition, ASM, Vol.3, 209(1980).

151. I.G. Wright, Oxidation of Iron-, Nickel-, and Cobalt-Base Alloys, Metals and Ceramics Information Center 72-07, June, 1972.

152. J.C. Zhao and Michael F. Henry, JOM, 2002 January, 37(2002).

153. J.W. Brook and P.J. Bridges, in: Superalloys 1988, The Metallurgical Society, 33(1988).

154. C.T. Sims, N.S. Stoloff, and W.C. Hagel, Superalloys II, New York, John Wiley & Sons, 1987.

155. S.T. Wlodek, *Trans. Metall. Soc.*, AIME, **230**, 1078(1964).

156. Mark A. Harper and Larry R. Walker, Corrosion/2001, paper 01154, NACE, Huston, TX, 2001.

157. S.K. Rhee and A.R. Spencer, *Met. Trans.*, **1**, 2021(1970).

158. I.G. Wright, in Metals Handbook, 9th ed., Vol. **13**, Corrosion, ASM international, Metals Park, OH, 97(1987).

159. H.E. Eiselstein and E.N. Skinner, in ASTM STP No. 165, 162(1954).

160. A.S. Brasunas, J.T. Gow, and O.E. Harder, Proc. ASTM, Vol. **46**, 870(1946).

161. J.H. Chen, P.M. Rogers, and J.A. Little, *Mater. Sci. Forum.* 251-254, 57(1997).

162. S.B. Lasday, Industrial Heating, March 1979, 12(1979).

163. R.B. Herchenroeder, in Behavior of High Temperature Alloys in Aggressive Environments, Proceedings of the Petten International Conference, The Netherlands, 15-18 Oct. 1979, The Metals Society, London.

164. G.N. Irving, J. Stringer, and D.P. Whittle, *Corros. Sci.*, Vol. **15**, 337(1975).

165. B. Gleeson and M.A. Harper, in Lifetime Modeling of High Temperature Corrosion Processes, M. Schutze, W.J. Quadakkers, and J.R. Nicholls eds., EFC, IOM Communications Ltd., **23**, 167(2001).

166. A.J. Sedrickes, Corrosion of Stainless Steels, John Wiley & Sons, Inc, New York, 392(1996).

167. M.J. Bennet, B.A. Bellamy, C.F. Knight, N. Meadows, and N.J. Eyke, *Mater. Sci. Eng.*, **69**, 359(1985).

168. D.P. Whittle and J. Stringer, *Phil. Trans. R. Soc. London* A, **27**, 309(1979).

169. F.H. Stott, G.C. Wood, and J. Stringer, *Oxid. Met.*, **44**, 113(1995).

170. Anwar Ul-Hamid, *Mater. Chem. Phys.*, **80**, 135(2003).

171. F.H. Stott, P.K.N. Barlett, and G.C. Wood, *J. Mater. Sci. Eng.*, **88**, 163(1987).

172. C.S. Giggins and F.S. Pettit, *Trans. Metall. Soc.*, AIME, **245**, 2509(1969).

173. E.A. Gulbranson and K.F. Andrew, *J. Electrochem. Soc.*, Vol. **104**, 334(1957).

174. D.E. Jones and J. Stringer, *Oxid. Met.*, **9**, 409(1975).

175. B. Ahmad and P. Fox, *Oxid. Met.*, **52**, 113(1999).

176. G. F. Vander Voort, Metallography principles and practice, McGraw-Hill Book Company, New York, 1984.

177. J.L. Smialek and G.H. Meier, in Superalloys II, Chapter 11, C.T. Sims, N.S. Stoloff, and W.C. Hagel, eds., High-Temperature Oxidation, John Wiley & Sons, New York, 293(1987).

178. J.R. Nicholls and M.J. Bennett, *Materials at High Temperature*, **17**(3), 413(2000).

179. C.S. Giggins and F.S. Pettit, *Trans. TMS AIME*, **245**, 2495(1969).

180. G.M. Ecer and G.H. Meier, *Oxid. Met.*, **13**, 119(1979).

181. C.A. Barrett, A Statistical Analysis of Elevated Temperature Gravimetric Cyclic Oxidation Data of Ni- and Co-Base Superalloys Based on and Oxidation Attack Parameter, TM-105934, NASA Lewis Research Center, June 1987.

182. G.C. Wood and D.P. Whittle, *Corros. Soc.*, **4**, 263-293(1964).

183. D.L. Douglass, *Corros. Sci.*, **8**, 665(1968).

184. G.C. Wood and D.P. Whittle, *Corros. Sci.*, **7**, 763(1967).

185. V.R. Howes, *Corros. Sci.*, 8, 221, 729(1968).

186. P. Elliott and A.F. Hampton, *Oxid. Met.*, 14, 449(1980).

187. M.G. Hobby and G.C. Wood, *Oxid. Met.*, **1**, 23(1969).

188. H.J. Yearian, H.E. Boren, R.E. Warr, Corrosion, **12**, 561t(1956).

189. G.K. Bouse in, Superalloys 1996, R.D. Kissinger *et al.* eds, TMS, 163(1996).

190. H. Hindam and D.P. Whittle, *Oxid. Met.*, **18**, 245(1982).

191. M.D. Merz, *Metall. Trans.* A, **11A**, 71(1980).

192. F. Delaunay, C. Berthier, D. Galy, J.M. Lameille, M. Lenglet, Microscopy of Oxidation-3, The Institute of Materials, London, 587(1997).

193. M.P Brady, D.T. Hoelzer, E.A. Payzant, P.F. Tortorelli, J.A. Horton, I.M. Anderson, L.R. Walker, and S.K. Wrobel, *J. Mater. Res.*, **16**, 2784(2001).

194. U. Krupp and H.-J. Christ, *Metall. Mater. Trans.* A, **31A**, 47(2000).

195. J.L. Smialek, *Metall. Trans.*, **9A**. 309(1978).

196. C.E. Lowell, J.L. Smialek, and C.A. Barrett, Cyclic Oxidation of Superalloys, In: R.A. Rapp, editor. High Temperature Corrosion, Houston, NACE, TX, 219(1983).

197. J.L. Smialek, *Acta Materialia*, **51**, 469(2003).

198. J.H. Chen, P.M. Rogers, J.A. Little, *Oxid. Met.*, **47**, 381(1997).

199. J. Litz, A. Rahmel, M. Schorr, J. Weiss, *Oxid. Met.*, **32**, 167(1989).

200. Kiyoshi Kusabiraki and Yukimichi Nakao, High-Temperature Corrosion and Protection 2000, Toshio Narita et. al. (Eds.), Hokkaido, Japan, 105(2000).

201. A.G. Revsz and F.P. Fehlner, *Oxid. Met.*, **15**, 297(1981).

202. M.J. Bennett, J.A. Desport, and P.A. Labun, *Oxid. Met.*, **22**, 291(1984).

203. Y. Saito, T. Maruyama, and T. Amano, Proceedings of the International Symposium on High Temperature Corrosion, Marseille, France, 61(1986).

204. J.F. Radavich, *Corrosion*, **15**, 613t(1959).

205. D.L. Douglass and J.S. Armijo, *Oxid. Met.*, **2**, 207(1970).

206. Bingtao Li and B. Gleeson, Effects of Silicon on the Oxidation Behavior of Commercial Chromia-Forming Alloys, Corrosion/2002, Paper 02393, Denver, CO

207. R.C. Weast, Physical Constants of Inorganic Compounds, Handbook of Chemistry and Physics, 6th ed., The Chemical Rubber Company, B68(1984).

208. J. Rosler, M. Baker, and M. Volgmann, *Acta Mater.*, **49**, 3659(2001).

209. S.F. Frederick and I. Cornet, *J. Electrochem. Soc.*, June, 285(1955).

210. J.J. Petrovic and A.K. Vasudevan, High Temperature Silicides and Refractory Alloys, MRS, Boston, 7(1993).

211. J.L. Smialek, C.A. Barrett, and J.C. Schaeffer, Design for Oxidation Resistance, ASM handbook, V.**20**, Materials Park, OH, 599(1997).

212. C.A. Phalnikar, E.B. Evans, and W.M. Baldwin, *J. Electrochem. Soc.*, V.**103**, No. 8, 429(1956).

213. C. Wagner and K.E. Zimens, *Acta Chem. Scand.*, 1, 547(1947).

214. J.F. Shackelford, Introduction to Materials Science for Engineers, 4th ed., Prentice-Hall, Inc., 1996.

215. D.R.F. West and N. Saunders, Ternary Phase Diagrams in Materials Science, 3rd ed., Maney Publishing, 130(2002).

216. T.B. Massalski (Ed.), Binary Alloy Phase Diagrams, 2nd ed., ASM International, Ohio, 1990.

217. P. Villars (Ed.), Handbook of Ternary Alloy Phase Diagrams, ASM International, Ohio, 1994.

218. P.Y. Hou and J. Stringer, *Oxid. Met.*, **33**, 357(1990).

219. K.S. Chan, *Metall. Mater. Trans.*, **28A**, 411(1997).

220. F. Dettenwanger, E. Schumann, M. Ruhle, J. Rakowshi and G.H. Merier, *Oxid. Met.*, **50**, 269(1998).

221. V.A.C. Haanappel and M.F. Stroosnijder, The Importance of Relevant Experimental Parameters for High Temperature Cyclic Oxidation Experiments, in Cyclic Oxidation of High Temperature Materials, M. Schutze and W.J. Quadakkers eds., EFC, IOM Communications Ltd., **27**, 225(1999).

222. H.J. Grabke, E.M. Muller-Lorenz, S. Strauss, E. Pippel, and J. Woltersdorf, *Oxid. met.*, **50**, 241(1998).

223. Badrol Ahmad and Peter Fox, The Effect of Surface Contamination on the Transient Oxidation of Ni-20Cr, in Proceedings of the 4th International Conference on Microscopy of Oxidation, Eds. Gordon Tatlock and Simon Newcomb, Cambridge, 265(1999).

AKNOWLEDGEMENT